TOWARD AN IMPROVED MODEL OF

ASPHALT BINDER OXIDATION IN PAVEMENTS

A Dissertation

by

NIKORNPON PRAPAITRAKUL

Submitted to the Office of Graduate Studies of
Texas A&M University
in partial fulfillment of the requirements for the degree of

DOCTOR OF PHILOSOPHY

December 2009

Major Subject: Chemical Engineering

TOWARD AN IMPROVED MODEL OF

ASPHALT BINDER OXIDATION IN PAVEMENTS

A Dissertation

by

NIKORNPON PRAPAITRAKUL

Submitted to the Office of Graduate Studies of
Texas A&M University
in partial fulfillment of the requirements for the degree of

DOCTOR OF PHILOSOPHY

Approved by:

Chair of Committee,	Charles J. Glover
Committee Members,	Amy Epps Martin
	Eyad Masad
	Victor M. Ugaz
Head of Department,	Michael Pishko

December 2009

Major Subject: Chemical Engineering

ABSTRACT

Toward an Improved Model of Asphalt Binder Oxidation in Pavements.

(December 2009)

Nikornpon Prapaitrakul, B.E., Chulalongkorn University;

M.E., Texas A&M University

Chair of Advisory Committee: Dr. Charles J. Glover

Asphalt binder oxidation in pavements has been proven to be an ongoing process throughout a pavement's service life. Understanding the nature of the oxidation process is a critical step toward better pavement design to achieve greater pavement durability.

The main component in asphalt binder oxidation in pavements is binder oxidative hardening. As the aromatic compounds in asphalt binders are oxidized, more polar carbonyl compounds are created, which results in stronger associations between asphalt components and eventually leads to an increase in asphalt elastic modulus and viscosity. Consequently, the performance of pavements is affected directly by asphalt binder hardening.

Also, low levels of accessible air voids in pavements potentially relate to binder oxidation according to a recent research study. When the pavements have sufficiently high accessible air voids (4 percent or greater), the oxidation rate is largely determined by the temperature in the pavement. On the other hand, when the percentage of accessible air voids in the pavement is considerably lower (2 percent or less), the hardening rate of binders in pavements is reduced significantly.

Field evidence is mounting that asphalt binder oxidization in pavements produces a binder that is more susceptible to thermal and fatigue cracking. While the fundamentals of this oxidation process are fairly well known, predicting quantitatively the rate of oxidation as a function of depth in the pavement, is not straightforward. A thermal and oxygen transport model, coupled with binder reaction kinetics, provides the

basis for such calculations. A one-dimensional thermal transport model, coupled with site-specific model parameters and recent improvements in the availability of required input climate data, enables calculation of pavement temperatures throughout the year, which then is used in an asphalt binder oxidation and transport model to calculate binder properties in the pavement over time. Calculated binder property changes with depth and time are compared to measurements of binder oxidation in the field.

The work in this study is aimed at understanding the oxidation kinetics of asphalt binders in pavements, determining the impact of accessible air void levels on asphalt hardening, and ultimately developing an improved model of asphalt binder oxidation in pavements.

DEDICATION

I would like to dedicate all of my Ph.D. work and this dissertation to my beloved grandmother, who passed away while I was pursuing the degree and fulfilling my dream. I missed a chance to share the story of my success with her. Even though she could not physically celebrate this magnificent moment with me, she can be certain that all of her encouragement and support are gratefully appreciated.

From this point forward, she will always be my infinite source of inspiration in every aspect of my life. She will be remembered forever for her kindness and unconditional love that she gave to her grandson.

ACKNOWLEDGEMENTS

I would like to thank my research advisor, Dr. Charles J. Glover, for his guidance and support, not only on academic issues but also on general issues on a daily basis. I gratefully appreciate his passion in our research and his patience that encouraged me to move forward and overcome any difficulties that there might be throughout the course of my research work.

I would also like to thank all of my committee members, Dr. Richard R. Davison, Dr. Amy Epps Martin, Dr. Eyad Masad, and Dr. Victor Ugaz, for their invaluable advice and comments that were tremendously helpful to my research.

It would not have been possible to achieve the goal of my research without the support that I received from all my colleagues, Sung Hoon Jung, Won Jun Woo, Zachary Kraus, Tyner Devine, Erika Rios, Allex Alvarez Lugo, Rongbin Han, Xin Jin, Yuanchen Cui, Denise M. Hoyt, and James J. Lawrence. I thank all of them for the opportunity to share perspectives in research work and, more importantly, in life.

Also, my research work and administrative matters were assisted by Towanna Arnold from the Chemical Engineering Department, and Thomas J. Freeman and Richard Canatella from the Texas Transportation Institute (TTI).

Finally, I would like to thank my parents, Nopadol and Kanokpun, who are always there for me no matter what the situation. Being your son is the best thing that I could ever wish for. I am also in great debt to my sister, Arpaporn, who has taken on the responsibilities of serving our parents in my absence.

All the support from these precious people made my study and achievement possible. I appreciate all of them from the deepest feelings of my heart.

NOMENCLATURE

η_o	Original Viscosity
η_t	Viscosity at Time *t*
η'(ω)	Dynamic Shear Viscosity
r_η	Rate of Hardening
r_{CA}	Binder Oxidation Rate (Rate of Carbonyl Area Formation)
A	Frequency (Pre-Exponential) Factor
P	Pressure
α	Oxygen Reaction Order
E_a	Activation Energy
R	Gas Constant
G'(ω)	Elastic (Storage) Dynamic Shear Modulus
G'/(η'/G')	DSR Function
PAV	Pavement Aging Vessel

TABLE OF CONTENTS

CHAPTER Page

CHAPTER Page

Page

LIST OF FIGURES

Page

Page

Page

LIST OF TABLES

Page

Page

CHAPTER I
INTRODUCTION TO ASPHALT OXIDATION MODEL IN PAVEMENTS

Introduction

Asphalt pavements exist in human transportation history since 1,500 A.D. In the United States, the first asphalt roadways appeared in the early 1870s.[1] However, the use of hot mix asphalt (HMA) in pavement construction was not introduced until the beginning of the 20th century. According to the Federal Highway Administration (FHWA), approximately 60 percent of public roadways in the United States are paved roadways, which account for roughly 2.6 million miles of pavements.[2]

One of the main purposes of flexible asphalt pavements is to support the load of vehicles. Typically, these pavements are called flexible because the asphaltic pavement structure bends to support the traffic loads. However, if the asphalt materials become stiffer, the pavement structure loses its flexibility, making pavements more susceptible to cracking. In previous research studies, spanning the last 15 years, it was found that asphaltic binders experience oxidation and a consequent embrittlement over time that reduces the performance of flexible pavements. In addition, asphalt oxidation in pavements has been shown to be an ongoing process throughout a pavement's service life. Also, there is evidence that demonstrates that oxidation occurs through the depth of the pavement and has a significant effect on pavement performance.[3,4]

Pavement engineers have spent years of research to determine the nature of the oxidation process in pavements, focusing mainly on binder oxidation chemistry, reaction kinetics, and the effect of oxidation on binder rheology. Additionally, some studies have worked to gain an understanding of how deep into the pavement and how fast the oxidation occurs, as well as how differences in climate impact pavement performance, and how to appropriately implement maintenance programs on asphalt pavements. A key

---

The dissertation follows the style of the *AIChE Journal*.

concern in pavement engineering is that while pavements are designed for optimum performance initially, over time as asphalt binders oxidize the properties of binder change and lead to a decrease in pavement durability.

Yet, to address this concern experimentally requires an extended field study, extended in both the number of parameters that must be studied in different climates across the country, but also extended over years of time. Therefore, there is a need for a pavement durability predictive tool to assist pavement engineers in forecasting asphalt binder properties in pavements over time.

The goal of this dissertation is to develop a reliable transport computational model for use as a guide to designing field and laboratory experiments for the purpose of evaluating the impact of diffusion resistance on the oxidation rate of binders in pavements as a function of asphalt binder types, pavement air void structure, and weather climate zones. Ultimately, laboratory results and this proposed transport model could be used to benefit pavement engineers in improving pavement design protocols and pavement maintenance scheduling. This chapter presents introductory background information on elements of such a transport model including asphalt reaction kinetics, oxygen availability to pavements, and evidence of binder oxidation in pavements.

Asphalt Binder Oxidation and Hardening Kinetics

Binder oxidation greatly affects the physical and chemical properties of binders and over time makes binders harder and stiffer.[5,6,7] As binders oxidize, carbonyl (– C=O) groups are formed that increase the polarity of their host compounds and make them much more likely to associate with other polar compounds.[6,8] As they form these associations, they create less soluble asphaltene materials, the formation of which leads to asphalt hardening.

Without diffusion resistance, the asphalt binder hardening mechanism can be shown as:

$$\ln \eta_t = \ln \eta_o + \Delta(\ln \eta_{ot}) + \Delta(\ln \eta_j) + r_\eta (time) \tag{I-1}$$

where η_o is the original viscosity, η_t is the viscosity at any time, $\Delta(\ln \eta_{ot})$ is the hardening in the hot-mix plant simulated by an oven test, $\Delta(\ln \eta_j)$ is the hardening that occurs in an early rapid "initial jump" stage, and r_η is the subsequent constant rate of hardening. Equation I-1 is shown as the hardening progression in Figure I-1, where η_{ot} is the viscosity after the oven test and η_j is the viscosity after the initial jump defined by the intercept of the constant-rate line. Region A and B are time periods for the initial jump and constant-rate regions, respectively.

Asphaltene formation is the primary cause of binder hardening due to asphalt oxidation,[9,10,11] and the hardening rate is:

$$r_\eta = \frac{\partial \ln \eta}{\partial t} = \frac{\partial \ln \eta}{\partial AS} \cdot \frac{\partial AS}{\partial CA} \cdot \frac{\partial CA}{\partial t} \tag{I-2}$$

where $\partial \ln \eta / \partial AS$ is viscosity hardening due to asphaltene (AS) formation. $\partial AS / \partial CA$ is asphaltene formation due to increasing carbonyl area (CA), and $\partial CA / \partial t$ is the rate of CA production. It was found that CA formation has a linear correlation with oxidation.[6] Also, Equation I-2 can be rewritten as:

$$r_\eta = HS \cdot r_{CA} \tag{I-3}$$

where HS, hardening susceptibility, is the combination of the first two terms in Equation I-2. For oxidation temperature below 100 °C, HS can be considered as a constant.[5,12]

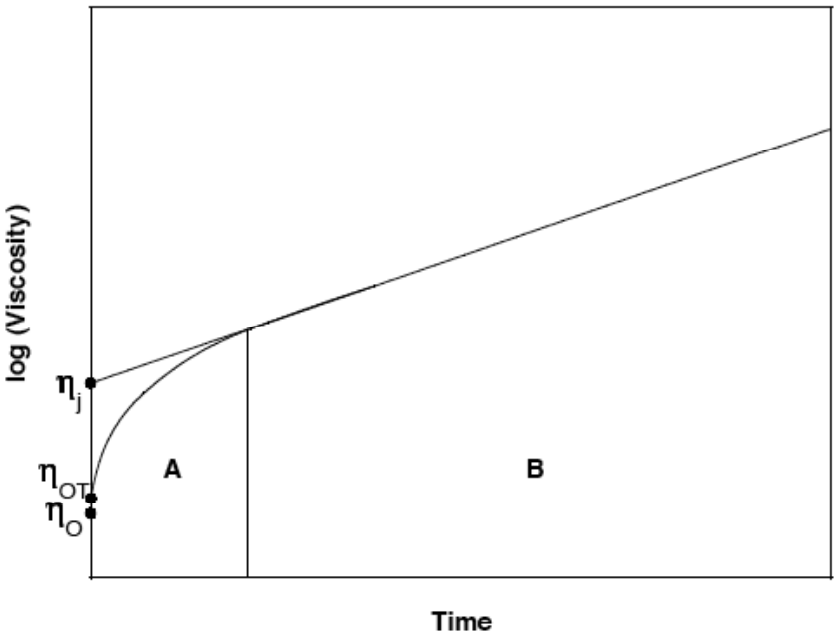

Figure I-1. Typical Hardening Response of an Unmodified Asphalt Binder to Oxidation[10]

Several studies have been conducted to explore basic binder oxidation chemistry.[5,13,14] From these reports, after an early, fast-rate period, the carbonyl compounds are formed at a rate that is a function of temperature and oxygen partial pressure. The rate of CA production can generally be described using an Arrhenius expression for temperature variation and pressure dependence as given in Equation I-4.[10,11,15,16]

$$r_{CA} = \frac{\partial CA}{\partial t} = AP^{\alpha} e^{-E_a/RT} \tag{I-4}$$

where A is the frequency (pre-exponential) factor, P is the pressure, α is the reaction order with respect to oxygen pressure. E_a is the activation energy, R is the gas constant, and T is the absolute temperature. Values of A, E_a, and, α depend on the type of asphalt

binder, while A and E_a are generally correlated.[15] Also, activation energy, E_a, depends on pressure and is a function of asphaltenes.[17] Equation I-5 summarizes these results as:

$$\ln \eta_t = \ln \eta_{ot} + \Delta\left(\ln \eta_j\right)[P] + r_{CA}[T,P] \cdot HS[P](time) \tag{I-5}$$

where [T, P] or [P] indicates that the property is a function of temperature and pressure or only pressure, respectively.

Asphalt binder oxidation in pavements has been proven to be an ongoing process throughout a pavement's service life. Also, there is evidence that demonstrates that oxidation occurs through the depth of the pavement and has a significant effect on pavement performance[3,4] Understanding the nature of the oxidation process and being able to predict the level of oxidation that occurs in pavements as a function of time and depth are critical to pavement design improvement that will provide greater pavement durability.

The important consequence of asphalt binder oxidation in pavements is oxidative hardening. As non-asphaltene polar aromatic compounds in asphalt binders oxidize, they become asphaltenes, associated species that act like solid particles suspended in the asphalt, thereby producing an increase in asphalt elastic modulus and viscosity.[5,7,9,12] Consequently, the performance of pavements is affected directly by asphalt binder oxidative hardening. Several studies by Walubita et al.[18,19,20,21] indicate that oxidation of asphalt binder in pavements leads to a decline in pavement fatigue resistance.

Also, low levels of accessible air voids in pavements potentially relate to binder oxidation.[22] When pavements have sufficiently high accessible air voids (4 percent or greater), the oxidation rate is largely determined by the temperature in the pavement. On the other hand, when the accessible air voids in the pavement is considerably lower (2 percent or less), the hardening rate of binders in pavements is reduced significantly.

According to the oxidative hardening discussed above, asphalt binders harden and become more brittle, which decreases the performance in terms of flexibility over time and eventually destroys the pavement. This embrittlement of binders can be

displayed through a correlation with binder ductility (measured at 15 °C, 1 cm/min) and binder DSR properties (dynamic shear modulus, G', and dynamic viscosity, η', equal to G''/ω), shown in Figure I-2. Binder ductility correlates very well with G'/(η'/G'), indicating a good relationship between elastic stiffness and the ability of the asphalt binder to flow. Such correlation can be represented on a "map" of G' versus (η'/G'), as shown in Figure I-3, which traces an asphalt binder as it ages.[23] On this map, as the binder ages over time, it moves from the lower right to the upper left as the result of the increase in elastic stiffness and viscosity. As observed from the map, G' increases more than η' since the movement is from right to left, toward smaller η'/G' values. Within this map, there are several different aged binders from SH-21 between Bryan and Caldwell, Texas (originally constructed in 1988). Samples were obtained in 1989, 1992, 1996, and 2002. It is clear from Figure I-3 that asphalt binders behave the same way as discussed above.

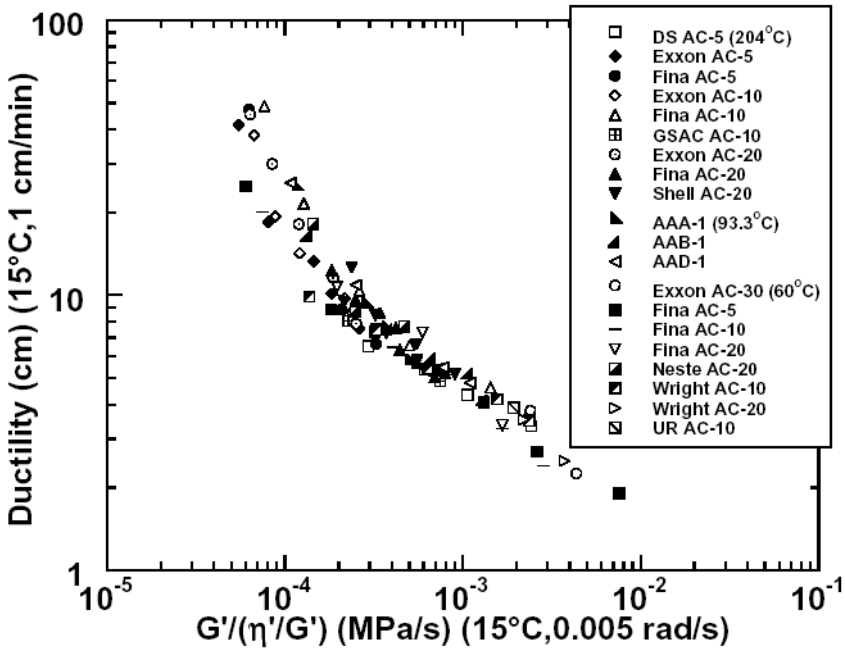

Figure I-2. Correlation of Aged-Binder Ductility with the DSR Function (G'/ (η'/G')) for Unmodified Binders[23]

These results are rather remarkable and strongly suggest, as noted above, that oxidative aging rates are remarkably constant over time and, beyond the very top portion of the pavement, proceed at remarkably uniform rates, at least to several inches below the surface of the pavement.

It should be noted that the literature reports that ductility values in the range of 2 to 3 cm for 15 °C at 1 cm/min appear to correspond to a critical level for age-related cracking .[24] Thus, the top left corner of the pavement aging map (Figure I-3) is a suspect region for adequate pavement performance. While this region has not yet been verified conclusively to be a critical zone, recent pavement data (from Texas Department of Transportation [TxDOT] Project 0-1872, including several Long Term Pavement Performance, LTPP, pavements) are consistent with this early conclusion.

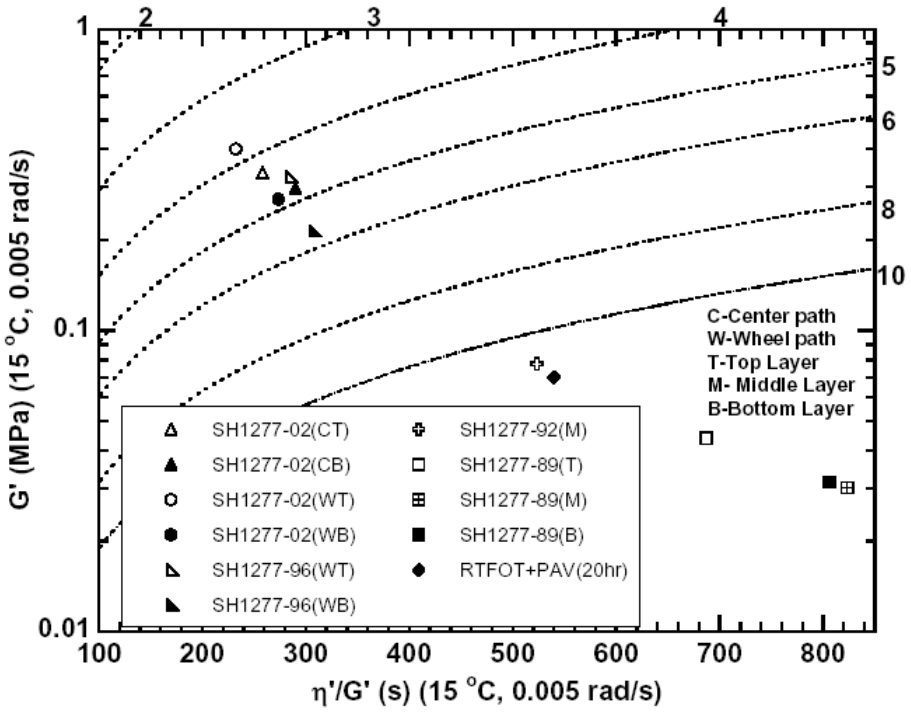

Figure I-3. Binder Aging Path on a G' versus η'/G' Map (Pavement-aged Binders)[3]

Binder Oxidation in Pavements

The oxidation of binders in asphalt pavements has been a subject of interest for a significant number of years, even decades.[3,4,5,12,14,20,25] A very well cited and accepted literature report by Coons and Wright[25] concludes that binder oxidation occurs only in the top 1.5 inch of the pavement and that below the top inch, the binder is left virtually unaffected by years of use and years of environmental exposure as shown in Figure I-4.

The conclusion by Coons and Wright[25] is formalized in a recently developed mechanistic-empirical pavement design guide (MEPDG)[26] that assumes in its calculation that binders oxidize only in the top inch. Parenthetically, calculations[18] using the MEPDG suggest that binder oxidation and the consequent increase in pavement stiffness (and the presumed decrease in deformation under load as a result of this stiffness) actually have a positive impact on pavement fatigue life.

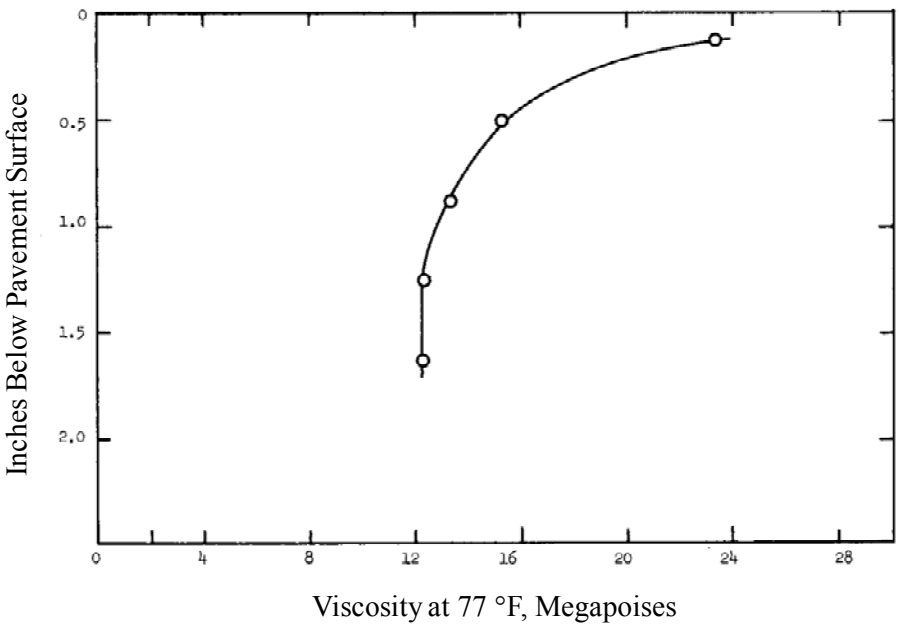

Figure I-4. Average Viscosity of Field Samples versus Depth[25]

These conclusions are adopted in the global aging model (GAM) of Mirza and Witczak[27] and subsequently incorporated into the National Highway Cooperative Research Program (NCHRP) mechanistic empirical design guide.[26] Mirza and Witczak[27] discussed the relationship between binder viscosity and pavement depth such that the greatest change in binder viscosity in pavements occurs only in the top few inches. Furthermore, the GAM assumes a hyperbolic aging function so that the great bulk of the hardening occurs in the first 10 years of service.

One difficulty with the data on which the assumptions above are based is that the solvent recovery process most likely left enough solvent in the recovered binder to soften its properties significantly.[28] Mirza and Witczak note that typically the recovery method for the materials in their master database was not included in the reference sources, with the implication that needed modifications were not employed. Residual solvent levels will be greater for the more heavily aged binders. Thus, stiffer binders will be more affected by residual solvent, leading to a compression of binder properties and thus erroneously small relative viscosity values when binder properties are tracked over time.

Oxygen Availability in Pavements

According to the asphalt binder oxidation kinetics described previously, a key element in asphalt oxidation is the oxygen availability in the pavements. Therefore, air void structure and pavement air permeability are crucial to the study of pavement oxidation. Since the measurement of air permeability in pavements is extremely difficult, the measurement of pavement water permeability and interconnected air void channels from top to bottom of the pavement should be adequate to ensure the availability of oxygen in the pavement under the assumption that the pavement is porous and ambient air can diffuse and/or flow into those air void channels in the pavements.

Several studies have shown that the air void content in asphalt pavement should not be lower than approximately 3 percent to prevent rutting and shoving or higher than

approximately 8 percent allowing water and air to penetrate into the pavement to prevent moisture damage in pavements.[29]

As for the relationship between pavement air void content and pavement water permeability, many researchers reported that when the in-place air void content increases, the water permeability of dense-graded pavements also increases.[30,31] In addition to air void contents in mixtures, it was also found that other factors such as aggregate gradation, aggregate shape, lift thickness, and compaction method influence the water permeability characteristics of asphalt mixtures.[32,33,34,35,36,37,38]

The relationship between in-place air voids and water permeability for 9.5 mm nominal maximum aggregate size (NMAS) is illustrated in Figure I-5 by Brown et al.[39] The water permeability values of coarse-graded and fine-graded mixtures were measured in the laboratory, and the air void contents of the corresponding mixtures were also measured using Corelok®.[40] The reported R^2 values for both coarse-graded and fine-graded mixes were relatively high (0.70 and 0.86, respectively) and both relationships are significant (p-value = 0.000). At 8 percent air voids, the pavement is expected to have a water permeability of 60×10^{-5} cm/s for a coarse-graded mix and 10×10^{-5} cm/s for a fine-graded mix. At lower void levels, the coarse-graded mixes are more permeable than fine-graded mixes.

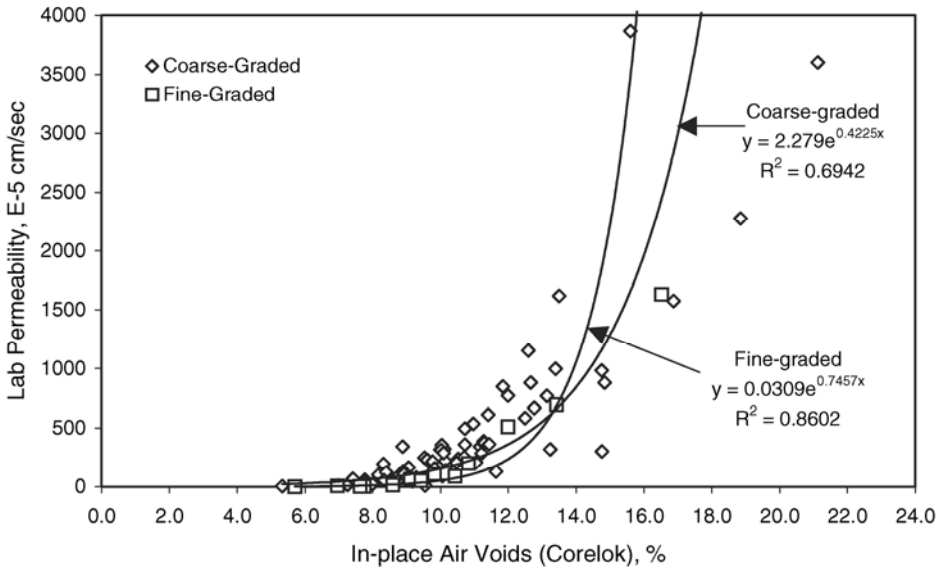

Figure I-5. Plot of Water Permeability versus In-Place Air Voids[26]

There were also several attempts to study the air void characteristics in pavements in further detail using imaging techniques. Al-Omari et al.[41] used X-ray computed tomography (CT) and image analysis techniques to measure the material properties. Their analysis demonstrated the complex distribution of air voids in asphalt mixes. The work by Masad et al.[42] used X-ray CT imaging techniques to study the moisture transport through the air void channels in asphalt mixtures and discovered that air void channels in pavement were connected from top to bottom of the specimen. Also, the paths of the connected voids can be determined by using a connectivity algorithm with the computer software.

According to these previous findings, the air void channels in pavements are accessible from top to bottom of the pavements and can be determined by the use of appropriate methods. Therefore, it should be possible for asphalt binder oxidation to occur well below the surface of the pavement.

Current Findings on Pavement Oxidation

Recent literature indicates that binder oxidation in pavements can have a very significant negative impact on pavement fatigue life.[20] While the mechanism of this fatigue life decline with oxidation is not yet well understood, it is believed to be a very important phenomenon, and early data indicate that there may be significant differences between different mixture designs.

Yet, the work of Coons and Wright[25] described above (Figure I-4) and the assumption of the MEPDG[26] on binder oxidation and hardening would appear to make any negative impact of binder oxidation on fatigue a moot point. If oxidation occurs in only the top inch of pavements, then any effects it might have below the top inch are irrelevant.

However, contradicting the work of Coons and Wright[25] and the assumptions of the MEPDG[26] are the extensive data reported in Glover et al.[3] in which a large number of Texas pavements were cored and the binder extracted and recovered and tested to determine binder stiffness as a function of age in the pavement. The results of this work indicate rather strongly that in fact binders can age in pavements well below the surface and that the hardening of binder in the pavement is virtually unabated over time. These data also are reported in a recent paper by Al-Azri et al.[4]

In addition, Woo et al.[22] discovered evidence of binder oxidation in pavements to extend to a depth of more than 3 inches. Table I-1 contains the information of field core samples collected from pavement sites in Minnesota. The MnRoad site is located in Minnesota near Minneapolis-St. Paul and is a suitable site for the scientific study of road pavements and their performance, including the performance of binder properties.[43] The MnRoad test site consists of a portion of I-94 in Minnesota with part of it being the main line interstate highway and part of it a test loop just off of the interstate highway. Cells 1 and 3 used an unmodified asphalt concrete (AC) 120-150 penetration grade binder, and Cells 33, 34, and 35 contain an unmodified base binder (Cell 33) and two levels of SBS (styrene-butadiene-styrene) modification to produce a performance graded (PG) 58-34

binder (Cell 34) and a PG 58-40 binder (Cell 35). Cells 1 and 3 were constructed in 1992, whereas Cells 33 through 35 were constructed in 1999. Coring of all of these cells occurred first in November of 2004 and the second coring was in July of 2006, thus giving 12 years of service for the first coring in Cells 1 and 3 and 5 years of service for the first coring of Cells 33 through 35.

Table I-1. Collected Cores from MnRoad[22]

MnRoad District	Highway	Thickness: Inch	PG (Modifier)	Construction Date	1st Coring	2nd Coring
Ce11 1	I 94	5.9	AC 120/150 (Un)	1992	11/2004	07/2006
Ce11 3		6.3				
Ce11 33		4.04	58-28 (Un)	1999		
Ce11 34		3.92	58-34 (SBS)			
Ce11 35		3.96	58-40 (SBS)			

The accessible or interconnected air voids of core samples from the MnRoad site, shown in Figure I-6, are particularly interesting and appear to bear on the binder oxidation. Cells 33, 34, and 35 all have a fairly uniform interconnected air void content from 3 to 5 percent. Cell 35 seems to have a significantly higher accessible air void percentage in the surface layer, but this higher level may be due to a surface roughness that might distort the actual interconnected air voids measurement. From the accessible air voids of cores from Cells 1 and 3, the interconnected air voids level is quite low, even below 1 percent for the layers in the top half of the core (top 3 inches), and then as the layers progress down deeper into the core, they increase to the 4 to 5 percent range of the other cores. The reason for these cells having such low interconnected air voids could be the result of binder content coupled with the mix design and compaction during construction.

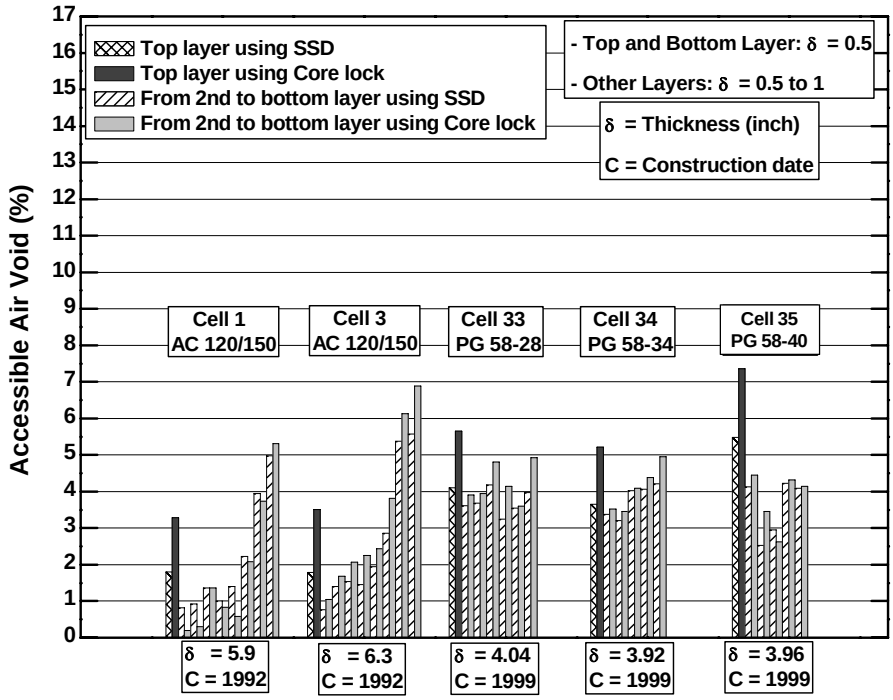

Figure I-6. MnRoad Accessible Air Voids[22]

Woo et al.[22] also reported the condition of extracted and recovered binder from the Cell 1 and 3 cores that were obtained in 2004 as shown in Figure I-7. The binders were extracted and recovered from the cores, which were sliced into layers of ½ inch thickness and then were tested for DSR properties to determine the level of oxidation. The G'/(η'/G') (DSR function) properties are plotted in Figure I-7 on the DSR map, which is a plot of G' versus the ratio of η' to G'. This plot of a binder's elastic modulus versus the ratio of its viscosity to elastic modulus shows the progression of a binder as it oxidatively hardens. As this hardening occurs, a binder moves from the vicinity of the lower right corner toward the top left corner.[23]

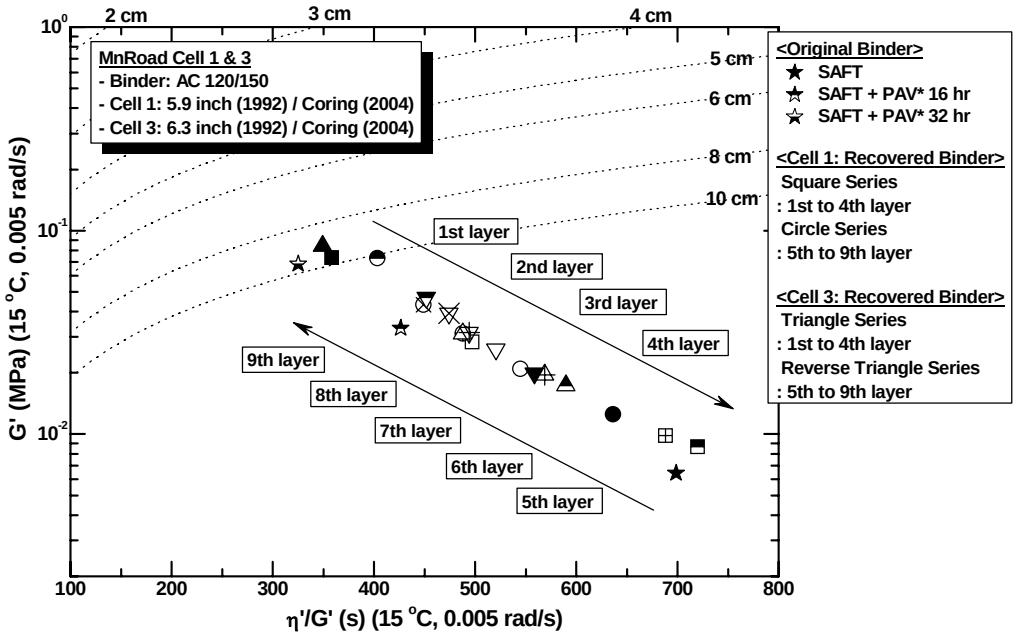

Figure I-7. MnRoad Aging Comparison of the Surface to the Bottom Layers[22]

For the top four layers from the top 2.5 inches of the pavement as shown in the DSR plot (Figure I-7), the binder that is deeper in the pavement is less aged. This finding follows the general trend that the progression from layer to layer is in a direction of the binder being less aged with depth into the pavement. The order of this progression would be expected if the temperature in the pavement with depth into the pavement is lower and if the access of oxygen to the binder at greater depths in the pavement is reduced.

However, the binder DSR data for the bottom five layers of the Cell 1 and 3 cores move in the opposite direction. That is, as binder is recovered from progressively greater depths into the pavement (from 2.6 to 6 inches deep into the pavement), the binder is progressively more aged, even to the extent that the binder that is recovered from the layer that is nearly 6 inches deep into the pavement is as aged as the binder at the surface of the pavement. One might attribute this range of binder DSR data that is covered in Figure I-7 to experimental variation except that the progression is so orderly, first decreasing monotonically in stiffness with increasing depth from the surface to the

middle of the core, and then increasing monotonically with increasing depth from the middle to the bottom of the core.

Referring back to the accessible air void contents, the Cell 1 and 3 cores had a significantly lower level of interconnected air voids than any of the others, and these lower levels were evident in the top layers of the pavement while the bottom layers were in the range of 2 to 5 percent interconnected air voids. A possible conclusion is that the variation in aging levels of that core with depth in the pavement is the result of these very low interconnected air voids. From Figure I-7, it can be seen that the air voids are less than 2 percent for the top five layers and then the sixth, seventh, eighth, and ninth layers increase progressively from 2 to 5 percent interconnected air voids. These data suggest that the progressively lower amount of aging deeper into the pavement could be due to this very low level of interconnected air voids and then that the increased aging towards the bottom of the pavement layer is a result of the increasing air voids with depth in that part of the pavement.

In addition to the recovered binder properties in Figure I-7, the original binder properties aged to different levels is also shown. These levels include the equivalent of a rolling thin film oven test aging procedure (designated Stirred-Air Flow Test, SAFT) and two aging states that were obtained in a Strategic Highway Research Program (SHRP) pressure aging vessel (PAV) apparatus. A stirred air flow test (SAFT) which simulates the hot mix process was used for short-term aging.[44] The standard pressure aging vessel (PAV) procedure was modified and is referred to as the PAV* procedure. This PAV* method was conducted at 90 °C and in 1 mm thick films and conducted for two test periods: 16 hr and 32 hr of aging, both at 20 atmospheres of air pressure. The thin film provides increased access of the binder to oxygen and thus enhancement to the binder aging rate, even at 20 atmospheres air pressure.

On the DSR map in Figure I-7, asphalt binder with SAFT aging originates at the lower right corner of the map, and the PAV* 32 hr aging is moved toward the top left corner near the dashed line that indicates a ductility of 10 cm. These dashed ductility lines are obtained from the correlation by Ruan et al.[23] and come from his correlation for

unmodified binders between the DSR function and ductility measured at 15 °C, 1 cm/min.

Dissertation Outline

With the background knowledge of asphalt oxidation, oxygen availability to pavements, and pavement oxidation in the field described in this chapter; the objective of this dissertation is to develop an improved asphalt binder oxidation model in pavements, which includes all the important elements of pavement oxidation, in order to predict asphalt binder properties in pavements as a function of service life. To further improve the model, the effects of local climate would also be incorporated into the model.

The approaches for each chapter to accomplish the goal of this dissertation are stated as follows:

Chapter II discusses the effects of different levels of air void contents in the pavements on asphalt binder oxidation. Several pavements in Texas were included in this study.

Chapter III presents the analysis of air void characteristics in pavement core samples determined using X-ray CT and image analysis. The stacked images obtained from the CT scans were analyzed by Image-Pro® Plus software to calculate the average size of air voids in the core samples. Then the average distance between air voids was calculated in the second stage using a Fortran-built algorithm. The results of the analysis from this chapter will be used as oxidation model inputs in the later chapters.

Chapter IV discusses the development of an improved pavement oxidation transport model, which is based on three interlinked processes: 1) diffusion of oxygen into the asphalt binder, 2) heat transfer into the pavement, and 3) asphalt binder oxidation. The improved oxidation model was developed in a more realistic cylindrical coordinate system that is able to capture the effects of air void structure in pavements and include such effects into model calculations.

Chapter V includes the extensive studies of the binder oxidation model developed in Chapter IV. In this chapter, the model was studied under the constant temperature condition. The oxidation rates calculated from the model were compared with the oxidation rates of asphalt binder recovered from core samples that undergo environmental room (ER) aging at 60 °C. Later in the chapter, the process for estimating model parameters with the least-squares method is discussed. This estimation process is used to determine unknown oxidation model parameters from known measured parameters together with measured ER mixture aging rates.

Chapter VI presents the discussion on integrating the pavement temperature prediction model with the pavement binder oxidation model. The oxidation rates calculated based on predicted pavement temperature are compared with available field oxidation rates.

Finally, Chapter VII provides an executive summary, conclusions, and recommendations based on the dissertation.

CHAPTER II
THE EFFECT OF ACCESSIBLE AIR VOIDS ON BINDER PROPERTIES AND AGING

Introduction

When the accessible air voids in a pavement are reduced, it might be expected that oxygen transport to the binder is also reduced and therefore that binder aging would be slowed. Similarly, to the extent an increased binder content results in a thicker binder film, the transport of oxygen throughout the binder could be reduced. Either of these effects conceivably could result in a reduction in hardening rates of binder in pavements.

The air void information and binder rheological properties reported in this chapter were from the study for seal treatment effectiveness in pavements.[45] In the study, the treatment did not have significant impact on binder rheological properties. Therefore, both treated and untreated samples in treatment study were used as core replicates.

Several Texas pavements were studied over a period of 2 years in order to understand the effects of different air void levels in pavements on binder oxidation. Tables II-1 and II-2 summarize the information on the pavement sites studied. In Tables II-1 and II-2, the site of the core is followed with a number in parentheses that indicates the number of cores that were taken at each site. Also included in Tables II-1 and II-2 is whether the site was an airport pavement, the original construction date of the pavement, and the coring date.

In this chapter, the impact of the accessible air voids – those that water can penetrate when the CoreLok® vacuum bag is opened underwater – to asphalt binder oxidation in pavements was determined. It was found that pavements with low level of accessible air voids (less than 3 percent) suffer less hardening than the pavements with high level of accessible air voids (more than 6 percent).

Table II-1. Site Information for the 1st Coring of the Study

1st Core (2004-2005)			
Site (# of cores)	**Location**	**Construction Date**	**Coring Date**
Abilene (18)	SH 36	1998	2004-2005
Carrizo Springs (6)	Airport	1995	2004-2005
Fort Worth 2000 (6)	FM 4	2000	2005
Fort Worth 2003 (6)	FM 4	2003	2005
Georgetown '89 (7)	Airport	1989	2004
Georgetown '95 (6)	Airport	1995	2004
Jacksonville (6)	Airport	2004	2004
Lufkin (6)	Bus 59	1995	2004
Pleasanton (6)	Airport	1985	2004

Table II-2. Site Information for the 2nd Coring of the Study

2nd Core (2006)			
Site (# of cores)	**Location**	**Construction Date**	**Coring Date**
Abilene (21)	SH 36	1998	2006
Atlanta CM (6)	IH 20	2001	2006
Atlanta DG (6)	IH 20	2001	2006
Atlanta SP (6)	IH 20	2001	2006
Atlanta 67 (6)	US 67	2003	2006
Carrizo Springs (6)	Airport	1995	2006
Fort Worth 2000 (6)	FM 4	2000	2006
Fort Worth 2003 (6)	FM 4	2003	2006
Georgetown '89 (6)	Airport	1989	2006
Georgetown '95 (9)	Airport	1995	2006
Jacksonville (6)	Airport	2004	2006
Lufkin (6)	Bus 59	1995	2006
Odessa SH 149 (6)	SH 191	1983	2006
Odessa SH 349 (6)	SH 349	1996	2006
Pleasanton (6)	Airport	1985	2006
Tyler (6)	US 79	2002	2006

Research Objectives

The objective of this chapter is to assess the effects of the accessible air voids and of binder content on binder aging by comparing asphalt binder physical properties extracted from Texas pavements with different levels of accessible air voids and binder content.

Methodology

The pavement cores were sliced into nominal ¼-inch layers through the top inch of the pavement. Then for each of the slices, the total air voids and the accessible air voids were determined. Additionally, the binder in each of these slices was extracted and recovered to provide the binder content, and measurement of the binder's DSR properties provided values for binder stiffness. The binder rheology was then assessed for each core as to its correlation to accessible air voids and binder content. Detailed information of the test methods are described subsequently.

Coring Plan

During the first year, coring locations for roadway sections were established that would provide one core from the inside edge of the wheelpath, one from the wheelpath, and one from the outside edge of the wheelpath. Figure II-1 illustrates this layout and the coring rig used during that first round of coring. The thought was that selecting the cores from the traveled area (wheelpath) and from the less traveled areas (inside and outside of the wheelpath) would provide a range of in-place densities and air voids.

Figure II-1. Layout of Coring Plan and Coring Rig

Core Preparation and Test Methods

The original sample preparation and test procedures are as shown in Figure II-2. Three core samples (replicates) were received from each site. At first, core samples were trimmed to approximately 3 inches thick and then the air void content of each core sample was measured. After air voids measurement, the specimen was sliced into ¼-inch disks for further testing. Figure II-3 shows a core being prepared for slicing, and Figure II-4 shows a set of slices being dried prior to additional testing. Due to the cutting blade thickness, the real thicknesses of slice samples needed to be estimated. Then, the binder from each slice was extracted and recovered for further testing. The extracted binders' properties were measured using the Dynamic Shear Rheometer (DSR) and Fourier transform-infrared (FT-IR) methods, which are discussed later in this chapter.

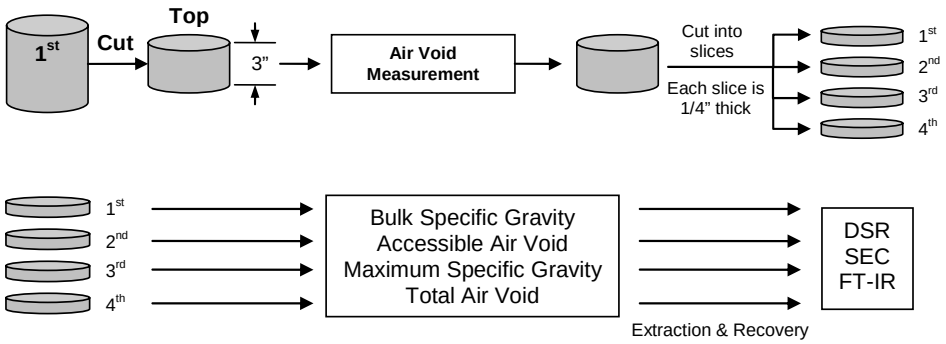

Remarks

DSR: Dynamic Shear Rheometer
SEC: Size Exclusion Chromatography
FT-IR: Fourier Transform Infrared Spectroscopy

Figure II-2. Test Plan Diagram

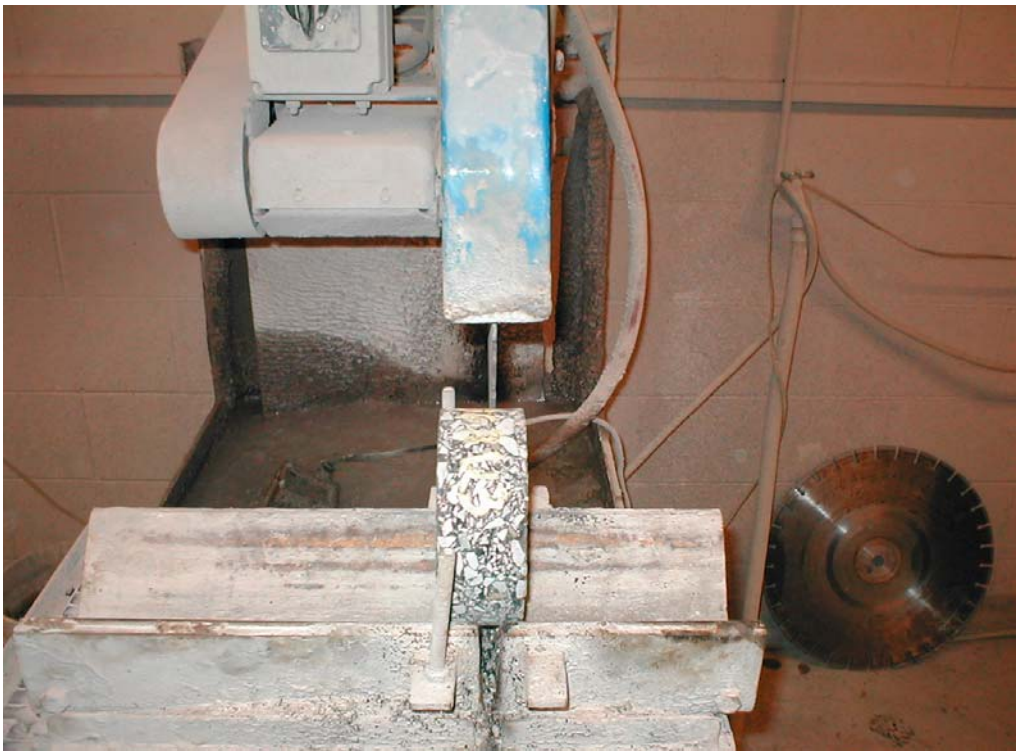

Figure II-3. Slicing Cores for Further Testing

Figure II-4. Core Slices Being Dried

Air Voids Measurement

A number of properties of intact pavement cores are of interest. These include the bulk and maximum specific gravities and the total and accessible air voids content. These properties are determined by a number of weight measurements including the weight of the dry core in air, the weight of the saturated core underwater, and the weight of the dry core underwater. Two methods were used to determine these weights, a saturated surface-dry (SSD) method[46] and the Corelok® method.[47,48] The Corelok® operating procedure can be found in the Corelok® Operator's Guide[49] The SSD method uses measurements of the unsealed core, while the Corelok® method uses underwater measurements of the evacuated core sealed in a plastic bag.

The measurements and the calculations for the two methods are given by the following equations and notation:

$$\text{Bulk Specific Gravity} = \frac{DA}{SaA\text{-}SaW} \quad \text{(SSD method)} \tag{II-1}$$

$$\text{Accessible Air Void} = \frac{SaA\text{-}DA}{SaA\text{-}SaW} \quad \text{(SSD method)} \tag{II-2}$$

$$\text{Bulk Specific Gravity} = \frac{DA}{SeA\text{-}SeW} \quad \text{(Corelok method)} \tag{II-3}$$

$$\text{Accessible Air Void} = \frac{SeA\text{-}SeW\text{-}\dfrac{BA}{B_{sg}} - (DA\text{-}SaW)}{SeA\text{-}SeW\text{-}\dfrac{BA}{B_{sg}}} \quad \text{(Corelok method)} \tag{II-4}$$

$$\text{MaximumSpecificGravity} = \frac{DA}{SeA\text{-}(SaW+BW)\text{-}\dfrac{BA}{B_{sg}}} \tag{II-5}$$

$$\text{Total Air Void} = 1 - \frac{\text{Bulk Specific Gravity}}{\text{MaximumSpecificGravity}} \tag{II-6}$$

where

DA = dry sample weight in air (g)

BA = bag weight in air (g)

BW = bag weight in water (g)

B_{sg} = bag specific gravity

SaA = saturated sample weight in air (g)

SaW = saturated sample weight in water (g)

SeA = sealed sample weight in air (g)

SeW = sealed sample weight in water (g)

Each of these methods of determining air voids has inherent measurement errors, and taken together, the two provide a useful check, and their comparisons provide an indication of the types of errors. For example, the SSD method is subject to greater error for more open, porous mixtures. This is because the SSD method relies on being able to obtain a weight of the saturated core that still contains all of the water inside the pores of the core. However, if the mixture is open enough, the water will tend to drain out, giving a lower saturated weight and also higher air voids. The Corelok® method will give higher air voids if the surface of the core has a rough texture because the bag cannot collapse around this texture completely and therefore, this texture appears as air voids in the pavement.

Binder Extraction and Recovery

Extraction and recovery of the binder in the cores is conducted based on the procedures outlined by Burr et al.[50] These procedures provide for a thorough wash and therefore extraction of the binder from the aggregate but with minimal hardening or softening of the binder in the solvent and with care taken to assure complete solvent removal during the recovery process.[28,50,51,52,53] For the extraction process, a solution of 15 percent by volume of ethanol in toluene was used to extract the asphalt binder from each sliced core. Before extraction, each core was broken into small pieces to increase contact surface with the solvent. After the crushed core was washed with the solvent mixture for 20 minutes, the asphalt solution was separated from aggregate using filtration and centrifugation. This step was repeated until there was practically no asphalt remaining in the aggregate – the aggregate can be seen through the solution. All of the

asphalt solutions from each wash were combined into one solution, and then passed to the recovery process.

In the recovery process, a Brinkman rotovap apparatus was used to evaporate all solvent from the asphalt. Asphalt solution was put into the evaporator for about 80 minutes under vacuum and with a nitrogen purge to assist solvent removal. The recovered asphalt binder was then subjected to further chemical and physical analyses. Figure II-5 shows the extraction/recovery process.

The binder content for each slice was calculated as the combined weight of asphalt binder from the recovery container, the filter, and the side of rotovap column (Figure II-5).

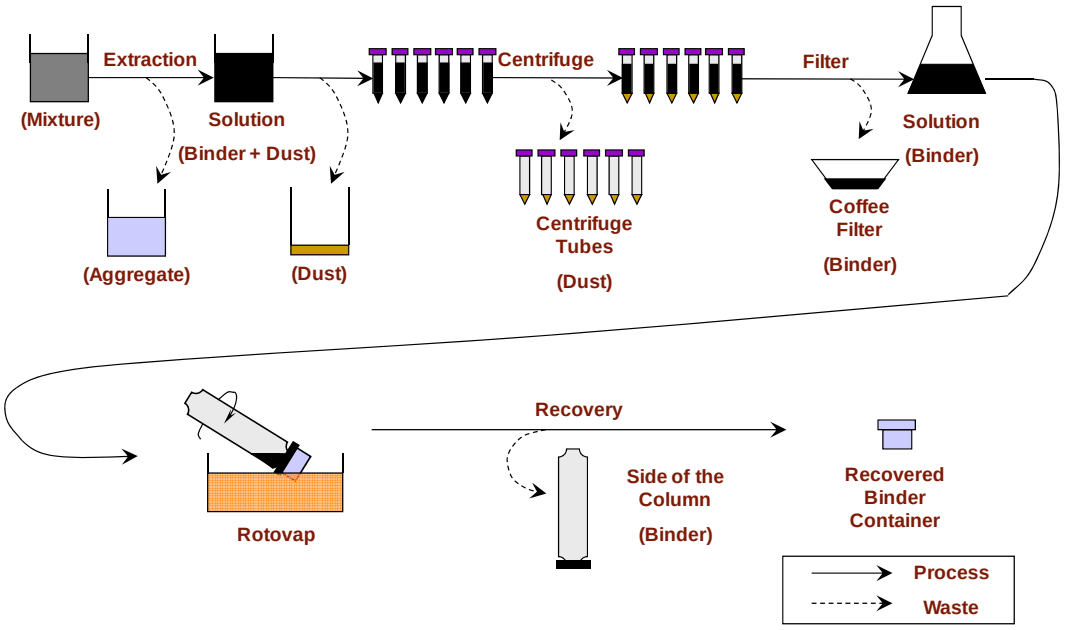

Figure II-5. Asphalt Binder Extraction and Recovery Process

Dynamic Shear Rheometer (DSR)

Two types of rheological property data were obtained from DSR measurements: the viscosity master curve at 60 °C and an estimated ductility of the asphalt binder. A 2.5 cm diameter parallel-plate geometry with a 500 μm gap was used for the measurements. To acquire the viscosity master curve at the 60 °C reference temperature, complex viscosity measurements were obtained in a controlled-stress mode by performing two frequency sweeps at 60 °C and 80 °C over a frequency range of 100 to 0.1 rad/s. Then, a shift factor was used to adjust the frequency range, moduli, and viscosities of 80 °C to match with 60 °C reference temperature data. As a result, a single master curve with wider range of frequency at 60 °C can be constructed. After this time-temperature superposition procedure, the viscosity master curve at 60 °C had a frequency range from 0.001 to 100 rad/s. At the lower end of the frequency range, the viscosity approaches a low shear rate limiting viscosity (also termed the "zero-shear" viscosity), a useful characteristic of the binder. An estimate of the binder's ductility at 15 °C and 1 cm/min extension rate can be calculated from the DSR value, G' and G" at 44.7 °C, and 10 rad/s.[23] The DSR function relationship is shown below:

$$\text{DSR Function} = \frac{G'}{\left(\eta'/G'\right)} = \frac{G'^{*}\omega}{\tan\delta} \qquad \text{(II-7)}$$

where $\eta' = \frac{G''}{\omega}$ and $\frac{G''}{G'} = \tan\delta$

ω = angular frequency (rad/s)

δ = phase angle (degree)

Then, G' versus (η'/G') can be plotted on the map with lines of constant ductility indicating the identified calculated ductility of each asphalt binder.

Fourier Transform-Infrared Spectrometer

The FT-IR spectrometer used in this research was a Mattson 5020 Galaxy Spectrometer, and the attenuated total reflectance method was used as described by Jemison et al.[54] Infrared spectra of asphalt binders coated on a zinc selenide prism were collected and analyzed over wavenumbers from 1800 to 700 cm^{-1}. The band from 1820 to 1650 cm^{-1} is the carbonyl band, and the area under the part of the spectrum is termed the carbonyl area and indicates the level of oxidation of the binder.

Results and Discussion

The bulk core properties are provided for each layer and for each site in Tables II-3 through II-19. Reported for layer-by-layer are the core bulk specific gravity, the maximum specific gravity, the total air voids, the accessible air voids, and the binder content. Note that not all of the data are reported for each of the slices. Also note that two methods were used for determining the air voids: the saturated surface-dry method (SSD)[46] and the Corelok®[47,48] methods discussed previously.

In addition, the descriptions of the abbreviations from Table II-3 through II-19 are given subsequently.

SH – State Highway	IH – Interstate Highway
BUS – Business Route	US – United States Highway
R1 – Southbound Outside Lane	L1 – Southbound Inside Lane
R2 – Northbound Outside Lane	L2 – Northbound Inside Lane
U, T – Sample Replicates	CM – Coarse Matrix Mixture
DG – Dense-Graded Mixture	SP – SuperPave Mixture

Table II-3. Properties of the Abilene L1 and L2 Cores

	Replicate	layer	Bulk S.G.		Maximum	Total A.V.		Accessible A.V.		Binder
			SSD	Corelok	S.G.	SSD	Corelok	SSD	Corelok	Content
	U3	1st	-	-	-	-	-	-	-	-
		2nd	-	-	-	-	-	-	-	-
1st Core		3rd	-	-	-	-	-	-	-	-
Abilene L1	T3	1st	2.27	2.05	2.54	10.84	19.28	6.35	14.57	5.06
		2nd	2.26	2.13	2.54	10.76	16.20	7.54	12.25	5.09
		3rd	2.25	2.09	2.51	10.48	16.83	7.64	13.25	5.37
	U1	1st	2.26	2.11	2.44	7.61	13.66	7.84	12.89	3.72
		2nd	2.25	2.15	2.44	8.00	11.99	7.54	10.61	4.40
		3rd	2.23	2.14	2.45	9.10	12.58	8.87	11.08	4.28
	U2	1st	2.22	2.11	2.47	10.12	14.47	10.37	13.01	3.79
		2nd	2.22	2.11	2.47	10.27	14.69	9.47	12.50	4.09
2nd Core		3rd	2.22	2.11	2.47	10.14	14.51	9.64	12.56	4.69
Abilene L1	T1	1st	2.22	2.07	2.45	9.36	15.49	8.39	13.47	4.55
		2nd	2.23	2.10	2.47	9.94	14.96	9.04	12.80	4.40
		3rd	2.23	2.06	2.48	10.15	16.96	9.58	15.01	4.35
	T2	1st	2.22	2.09	2.45	9.49	14.77	9.46	13.33	4.37
		2nd	2.21	2.06	2.46	10.21	16.20	9.87	14.36	5.05
		3rd	2.21	2.11	2.46	10.09	14.48	9.95	12.78	4.60
	U3	1st	-	-	-	-	-	-	-	4.22
		2nd	-	-	-	-	-	-	-	5.38
1st Core		3rd	-	-	-	-	-	-	-	4.90
Abilene L2	T3	1st	-	-	-	-	-	-	-	4.88
		2nd	-	-	-	-	-	-	-	5.42
		3rd	-	-	-	-	-	-	-	5.30
	U1	1st	2.20	2.07	2.45	10.00	15.61	10.65	14.46	4.07
		2nd	2.22	2.14	2.47	10.00	13.54	10.14	12.03	4.96
		3rd	2.24	2.11	2.50	10.69	15.55	8.68	12.44	3.84
	U2	1st	2.21	2.02	2.47	10.55	18.37	10.71	16.79	3.89
		2nd	2.22	2.03	2.43	8.69	16.74	9.39	16.02	4.64
2nd Core		3rd	2.26	2.21	2.47	8.55	10.76	7.88	9.05	4.35
Abilene L2	T1	1st	2.21	2.04	2.45	9.48	16.64	8.81	14.80	4.54
		2nd	2.23	2.09	2.44	8.70	14.48	7.75	12.62	4.82
		3rd	2.24	2.17	2.48	9.60	12.58	8.72	10.48	4.63
	T2	1st	2.20	2.04	2.44	9.94	16.60	7.82	13.66	4.17
		2nd	2.23	2.02	2.46	9.29	17.94	8.40	16.04	4.69
		3rd	2.26	2.21	2.49	9.29	11.41	8.60	9.50	4.13

Table II-4. Properties of the Abilene R1 and R2 Cores

	Replicate	layer	Bulk S.G.		Maximum	Total A.V.		Accessible A.V.		Binder
			SSD	Corelok	S.G.	SSD	Corelok	SSD	Corelok	Contents
	U3	1st	2.33	2.14	2.57	8.95	16.36	4.45	11.89	4.14
		2nd	2.32	2.15	2.54	8.77	15.17	5.26	11.43	4.86
1st Core		3rd	2.28	2.16	2.51	8.98	13.84	6.99	11.14	4.96
Abilene R1	T3	1st	2.29	2.07	2.51	8.76	17.57	4.96	13.74	4.68
		2nd	2.29	2.01	2.55	10.00	21.16	5.54	16.78	5.32
		3rd	2.27	2.09	2.52	10.04	17.02	7.41	13.71	5.15
	U1	1st	2.25	2.02	2.48	9.26	18.50	8.16	16.49	3.99
		2nd	2.23	2.05	2.46	9.30	16.81	8.66	15.05	4.36
		3rd	2.28	2.25	2.48	8.34	9.50	7.38	7.62	4.79
	U2	1st	2.26	2.07	2.46	8.14	15.85	6.52	13.68	3.94
		2nd	2.26	2.07	2.47	8.48	16.18	7.12	14.12	4.08
2nd Core		3rd	2.30	2.25	2.50	7.93	9.82	6.86	7.96	3.89
Abilene R1	T1	1st	2.24	2.04	2.46	8.78	17.07	7.45	14.98	4.17
		2nd	2.22	2.08	2.45	9.47	15.29	8.77	13.41	4.30
		3rd	2.28	2.26	2.48	7.87	8.90	6.50	6.80	4.65
	T2	1st	2.25	2.08	2.46	8.22	15.18	4.72	11.58	4.30
		2nd	2.24	2.09	2.45	8.48	14.76	7.97	13.26	4.51
		3rd	2.31	2.28	2.46	5.81	7.11	3.73	4.80	4.97
	U2	1st	-	-	-	-	-	-	-	-
		2nd	-	-	-	-	-	-	-	-
1st Core		3rd	-	-	-	-	-	-	-	-
Abilene R2	T2	1st	-	-	-	-	-	-	-	4.72
		2nd	-	-	-	-	-	-	-	4.60
		3rd	-	-	-	-	-	-	-	5.68
	U1	1st	2.22	1.97	2.48	10.48	20.46	10.66	18.95	3.65
		2nd	2.42	2.16	2.46	1.77	12.06	9.01	17.31	4.31
		3rd	2.27	2.12	2.44	6.86	13.02	0.45	7.04	4.96
	U2	1st	2.17	1.90	2.48	12.34	23.42	5.19	16.74	3.78
		2nd	2.23	2.17	2.45	9.06	11.35	8.61	9.68	5.06
2nd Core		3rd	2.28	2.27	2.45	6.92	7.13	5.46	5.14	5.02
Abilene R2	T1	1st	2.21	1.98	2.46	10.24	19.76	10.33	18.26	4.34
		2nd	2.24	2.16	2.46	8.73	12.16	7.71	10.18	5.07
		3rd	2.27	2.21	2.44	6.90	9.44	5.49	7.54	5.50
	T2	1st	2.23	1.98	2.48	10.10	20.16	9.44	18.24	3.62
		2nd	2.30	2.25	2.45	6.11	8.06	4.20	5.88	5.35
		3rd	2.29	2.27	2.38	3.84	4.66	2.02	2.78	7.05

Table II-5. Properties of the Atlanta IH 20 CM Cores

	Replicate	layer	Bulk S.G.		Maximum	Total A.V.		Accessible A.V.		Binder
			SSD	Corelok	S.G.	SSD	Corelok	SSD	Corelok	Contents
	U1	1st	2.26	1.88	2.48	8.80	24.00	10.69	24.00	2.92
		2nd	2.33	2.13	2.42	3.79	11.76	0.54	8.78	3.66
		3rd	2.28	2.14	2.28	0.00	5.89	6.49	11.56	3.55
	U2	1st	2.27	1.99	2.48	8.68	19.68	7.25	17.62	3.50
1st Core		2nd	2.24	2.12	2.42	7.45	12.47	5.04	9.75	4.48
Atlanta		3rd	2.27	2.15	2.44	6.89	11.96	6.59	10.95	4.29
IH 20 CM	T1	1st	2.25	2.05	2.41	6.81	14.96	7.54	14.72	3.71
		2nd	2.29	2.09	2.49	8.14	16.10	6.57	13.96	3.71
		3rd	2.32	2.07	2.49	6.81	16.56	5.39	14.82	3.59
	T2	1st	2.29	1.98	2.45	6.78	19.41	5.71	17.99	3.60
		2nd	2.29	2.13	2.48	7.73	14.31	6.33	12.34	3.63
		3rd	2.29	2.16	2.45	6.87	12.03	6.03	10.62	3.68

Table II-6. Properties of the Atlanta IH 20 DG Cores

	Replicate	layer	Bulk S.G.		Maximum	Total A.V.		Accessible A.V.		Binder
			SSD	Corelok	S.G.	SSD	Corelok	SSD	Corelok	Contents
	U1	1st	2.26	2.09	2.47	8.46	15.44	9.11	14.74	3.31
		2nd	2.33	2.23	2.50	7.12	10.87	6.26	9.37	4.11
		3rd	2.29	2.18	2.48	7.56	11.94	6.38	10.13	3.94
	U2	1st	2.28	2.06	2.51	9.31	18.15	7.93	15.92	3.48
1st Core		2nd	2.30	2.22	2.52	8.63	12.01	6.11	8.94	3.49
Atlanta		3rd	2.31	2.23	2.48	6.98	10.15	5.66	8.32	4.26
IH 20 DG	T1	1st	2.30	2.07	2.50	8.04	17.13	6.20	14.86	3.35
		2nd	2.28	2.17	2.49	8.47	12.66	7.22	10.59	3.59
		3rd	2.32	2.20	2.51	7.41	12.21	5.23	9.68	3.18
	T2	1st	2.29	2.04	2.49	8.02	18.13	6.73	16.27	3.77
		2nd	2.31	2.17	2.49	7.37	12.88	6.23	11.16	3.46
		3rd	2.32	2.21	2.50	7.08	11.77	5.95	10.09	3.66

Table II-7. Properties of the Atlanta IH 20 SP Cores

	Replicate	layer	Bulk S.G.		Maximum	Total A.V.		Accessible A.V.		Binder
			SSD	Corelok	S.G.	SSD	Corelok	SSD	Corelok	Contents
	U1	1st	2.34	2.20	2.53	7.51	13.02	5.52	10.62	3.44
		2nd	2.38	2.38	2.53	6.06	6.03	3.66	3.38	3.82
		3rd	2.37	2.34	2.52	5.96	7.06	3.85	4.70	4.40
	U2	1st	2.33	2.22	2.51	7.12	11.45	7.01	10.52	4.06
1st Core		2nd	2.36	2.30	2.52	6.19	8.72	4.76	6.92	4.31
Atlanta		3rd	2.35	2.32	2.50	6.24	7.46	5.46	6.16	4.20
IH 20 SP	T1	1st	2.35	2.11	2.53	7.01	16.34	5.54	13.96	3.99
		2nd	2.36	2.26	2.59	8.95	12.88	5.86	9.44	4.00
		3rd	2.38	2.28	2.54	6.39	10.48	4.65	8.38	4.15
	T2	1st	2.31	2.12	2.52	8.26	15.60	7.44	14.52	3.90
		2nd	2.35	2.25	2.53	6.84	10.90	5.96	9.33	3.85
		3rd	2.35	2.27	2.54	7.46	10.43	5.98	8.44	3.77

Table II-8. Properties of the Atlanta US 67 Cores

	Replicate	layer	Bulk S.G.		Maximum	Total A.V.		Accessible A.V.		Binder
			SSD	Corelok	S.G.	SSD	Corelok	SSD	Corelok	Contents
	U1	1st	2.26	2.19	2.43	7.06	9.96	6.30	8.54	4.04
		2nd	2.28	2.26	2.43	6.27	6.96	5.34	5.52	4.69
		3rd	2.28	2.25	2.43	6.16	7.23	5.74	6.23	4.64
	U2	1st	2.24	2.19	2.43	7.66	9.76	5.21	6.88	4.11
1st Core		2nd	2.27	2.26	2.45	7.32	7.66	5.38	5.21	4.35
Atlanta		3rd	2.27	2.26	2.44	6.85	7.28	5.85	5.68	4.69
US 67	T1	1st	2.27	2.22	2.45	7.32	9.15	5.18	6.57	4.40
		2nd	2.24	2.21	2.46	8.80	10.07	6.09	6.74	4.70
		3rd	2.24	2.23	2.45	8.60	8.90	7.40	6.75	4.58
	T2	1st	2.26	2.20	2.43	6.93	9.39	5.75	7.67	3.90
		2nd	2.28	2.22	2.42	6.11	8.49	5.42	7.30	4.45
		3rd	2.28	2.22	2.43	6.22	8.71	6.22	8.05	4.24

Table II-9. Properties of the Carrizo Springs Airport Cores

	Replicate	layer	Bulk S.G.		Maximum	Total A.V.		Accessible A.V.		Binder
			SSD	Corelok	S.G.	SSD	Corelok	SSD	Corelok	Contents
	U3	1st	2.31	2.30	2.59	10.80	11.23	5.06	5.05	4.38
1st Core		2nd	2.34	2.40	2.57	9.21	6.82	3.91	1.09	5.08
Carrizo		3rd	2.34	2.32	2.50	6.25	7.18	0.23	1.22	5.21
Springs	T3	1st	2.26	2.22	2.61	13.39	14.85	5.35	6.44	5.30
Airport		2nd	2.30	2.32	2.56	10.37	9.50	5.78	4.26	5.23
		3rd	2.31	2.32	2.57	9.96	9.74	4.40	3.81	5.05
	U1	1st	2.28	2.22	2.49	8.56	10.77	7.31	8.64	4.61
		2nd	2.32	2.31	2.46	5.87	6.36	4.79	4.87	4.86
		3rd	2.30	2.31	2.49	7.40	7.13	4.72	4.04	4.66
	U2	1st	2.28	2.21	2.51	8.83	11.80	7.61	9.64	4.48
2nd Core		2nd	2.32	2.31	2.49	6.76	7.32	4.68	4.85	4.41
Carrizo		3rd	2.32	2.32	2.47	5.99	6.12	4.37	4.15	4.45
Springs	T1	1st	2.29	2.28	2.46	6.68	7.29	5.98	5.96	4.60
Airport		2nd	2.33	2.34	2.48	6.08	5.51	3.98	3.11	4.83
		3rd	2.33	2.35	2.45	4.79	3.89	3.17	2.07	4.76
	T2	1st	2.27	2.25	2.48	8.73	9.46	7.77	7.46	4.20
		2nd	2.31	2.31	2.46	6.13	6.12	3.89	3.60	4.73
		3rd	2.32	2.33	2.46	5.83	5.40	3.79	3.08	4.72

Table II-10. Properties of the Fort Worth FM 4 (2000) Cores

	Replicate	layer	Bulk S.G.		Maximum	Total A.V.		Accessible A.V.		Binder
			SSD	Corelok	S.G.	SSD	Corelok	SSD	Corelok	Contents
	U1	1st	2.32	1.91	2.43	4.43	21.56	6.12	22.40	-
		2nd	2.24	2.08	2.25	0.40	7.65	3.63	10.42	-
		3rd	2.17	2.09	2.14	0.00	2.60	3.88	7.10	-
	U2	1st	2.33	1.85	2.55	8.76	27.70	2.04	22.31	-
		2nd	2.22	2.03	2.38	6.57	14.63	4.59	12.47	-
		3rd	2.17	2.05	2.31	5.94	11.18	3.78	8.89	-
	U3	1st	2.12	1.81	2.55	16.95	28.82	4.76	18.02	5.21
1st Core		2nd	2.18	2.01	2.34	6.71	14.03	5.21	12.19	9.61
Fort Worth		3rd	2.14	2.03	2.29	6.65	11.34	5.68	9.87	10.18
FM 4	T1	1st	2.27	1.87	2.50	9.34	25.07	7.73	22.89	-
(2000)		2nd	2.19	2.05	2.34	6.15	12.30	4.42	10.35	-
		3rd	2.13	2.08	2.23	4.55	6.91	3.63	5.77	-
	T2	1st	2.30	1.91	2.48	7.49	23.20	6.81	21.96	-
		2nd	2.22	2.01	2.37	6.31	15.20	4.03	12.87	-
		3rd	2.09	2.03	2.22	5.68	8.40	4.80	7.14	-
	T3	1st	2.26	1.94	2.45	7.54	20.60	5.46	18.35	5.69
		2nd	2.22	2.01	2.39	6.89	15.81	4.94	13.65	8.09
		3rd	2.12	2.03	2.23	5.11	8.93	3.22	6.92	13.77
	U1	1st	2.29	1.97	2.45	6.58	19.82	4.69	17.85	6.13
		2nd	2.24	2.03	2.36	5.20	14.00	2.99	11.83	8.37
		3rd	2.15	2.12	2.25	4.13	5.74	1.87	3.46	11.99
	U2	1st	2.32	1.95	2.46	5.52	20.68	5.48	20.20	4.94
		2nd	2.25	2.07	2.36	4.72	12.28	2.41	10.05	9.20
		3rd	2.18	2.13	2.27	3.90	5.97	1.80	3.85	10.66
	U3	1st	2.30	1.92	2.47	7.05	22.36	4.28	19.76	-
2nd Core		2nd	2.16	2.06	2.36	8.29	12.61	2.06	6.59	-
Fort Worth		3rd	2.17	2.08	2.28	4.95	8.76	2.85	6.60	-
FM 4	T1	1st	2.25	1.97	2.39	5.95	17.80	5.25	16.75	9.38
(2000)		2nd	2.19	2.06	2.31	5.35	10.80	4.04	9.28	9.07
		3rd	2.12	2.07	2.22	4.44	6.70	3.02	5.15	11.54
	T2	1st	2.26	1.95	2.36	4.21	17.49	5.55	18.17	6.95
		2nd	2.21	2.05	2.34	5.39	12.57	3.74	10.80	8.37
		3rd	2.10	2.07	2.24	6.01	7.74	0.67	2.48	11.25
	T3	1st	2.23	1.86	2.41	7.46	23.06	1.59	18.14	-
		2nd	2.19	2.09	2.31	5.10	9.52	3.48	7.76	-
		3rd	2.10	2.05	2.22	5.58	7.73	3.32	5.32	-

Table II-11. Properties of the Fort Worth FM 4 (2003) Cores

	Replicate	layer	Bulk S.G.		Maximum	Total A.V.		Accessible A.V.		Binder
			SSD	Corelok	S.G.	SSD	Corelok	SSD	Corelok	Contents
	U1	1st	2.10	2.00	2.20	4.60	9.23	2.36	7.00	-
		2nd	2.19	2.13	2.27	3.86	6.35	0.93	3.47	-
		3rd	2.34	2.24	2.56	8.38	12.54	3.36	7.55	-
	U2	1st	2.03	1.84	2.26	10.14	18.38	1.78	10.73	-
		2nd	2.02	1.98	2.07	2.49	4.40	0.59	2.54	-
		3rd	2.36	2.23	2.48	4.73	10.15	2.43	7.88	-
	U3	1st	2.15	1.96	2.28	5.55	13.99	1.93	10.63	14.93
1st Core		2nd	2.07	2.01	2.18	5.09	7.95	1.20	4.16	15.71
Fort Worth		3rd	2.36	2.28	2.49	4.98	8.11	1.66	4.84	6.80
FM 4	T1	1st	2.11	1.96	2.16	2.42	9.42	2.11	9.06	-
(2003)		2nd	2.11	2.08	2.19	3.77	5.36	0.95	2.57	-
		3rd	2.36	2.28	2.49	5.17	8.55	2.91	6.21	-
	T2	1st	2.12	1.94	2.23	5.15	13.22	0.21	8.71	-
		2nd	2.12	2.08	2.17	2.34	4.13	0.37	2.19	-
		3rd	2.36	2.29	2.48	4.62	7.55	2.10	5.03	-
	T3	1st	2.19	2.09	2.22	1.66	6.08	1.26	5.68	13.58
		2nd	2.16	2.15	2.25	3.75	4.46	1.78	2.44	12.36
		3rd	2.38	2.24	2.51	5.14	10.62	3.20	8.61	4.33
	U1	1st	2.14	1.97	2.24	4.19	11.94	2.92	10.62	13.08
		2nd	2.16	2.17	2.26	4.34	4.20	0.88	0.72	12.74
		3rd	2.41	2.37	2.51	4.15	5.77	2.35	3.91	4.14
	U2	1st	2.20	1.96	2.33	5.28	15.58	3.80	14.02	9.21
		2nd	2.18	2.16	2.24	2.86	3.63	1.57	2.30	12.16
		3rd	2.39	2.34	2.50	4.49	6.60	2.69	4.70	4.18
	U3	1st	2.10	2.00	2.17	3.35	7.84	2.01	6.49	-
2nd Core		2nd	2.30	2.21	2.40	4.28	8.08	1.59	5.44	-
Fort Worth		3rd	2.32	2.11	2.49	6.96	15.35	4.12	12.48	-
FM 4	T1	1st	2.09	2.03	2.16	3.42	6.04	1.60	4.22	15.45
(2003)		2nd	2.21	2.20	2.29	3.69	3.99	2.07	2.29	10.10
		3rd				-	-	-	-	4.05
	T2	1st	2.06	2.01	2.11	2.68	4.89	1.36	3.56	16.48
		2nd	2.21	2.20	2.28	3.08	3.53	1.16	1.59	10.54
		3rd	2.41	2.21	2.57	6.13	14.00	3.66	11.51	3.00
	T3	1st	2.05	1.95	2.12	3.45	7.92	1.29	5.83	-
		2nd	2.04	2.01	2.08	2.21	3.60	0.66	2.06	-
		3rd	2.39	2.25	2.53	5.44	11.02	3.70	9.14	-

Table II-12. Properties of the Georgetown Airport (1989) Cores

	Replicate	layer	Bulk S.G.		Maximum	Total A.V.		Accessible A.V.		Binder
			SSD	Corelok	S.G.	SSD	Corelok	SSD	Corelok	Contents
	U3	1st	2.19	2.12	2.50	12.69	15.30	10.95	11.71	5.18
1st Core		2nd	2.31	2.27	2.47	6.84	8.23	3.25	4.50	6.43
Georgetown		3rd	2.31	2.22	2.39	3.39	7.13	0.07	3.94	6.53
Airport	T3	1st	2.26	2.13	2.47	8.51	13.68	7.49	11.79	5.55
(1989)		2nd	2.32	2.27	2.51	7.58	9.56	4.31	6.02	5.65
		3rd	2.32	2.27	2.47	6.08	8.26	3.55	5.56	5.70
	U1	1st	2.21	2.09	2.49	11.10	16.17	10.46	13.86	4.59
		2nd	2.31	2.27	2.46	6.30	7.93	3.85	5.24	5.60
		3rd	2.34	2.32	2.48	5.65	6.44	2.05	2.79	6.13
	U2	1st	2.21	2.06	2.49	11.00	17.19	10.45	15.00	4.37
2nd Core		2nd	2.29	2.28	2.45	6.27	6.96	3.86	4.30	5.71
Georgetown		3rd	2.34	2.33	2.42	3.05	3.51	1.40	1.83	6.41
Airport	T1	1st	2.23	2.10	2.49	10.67	15.89	8.95	12.99	4.60
(1989)		2nd	2.31	2.31	2.45	5.67	6.00	3.08	3.24	5.22
		3rd	2.31	2.29	2.46	6.17	7.11	3.58	4.31	5.32
	T2	1st	2.22	2.07	2.51	11.46	17.53	9.24	14.12	4.94
		2nd	2.30	2.30	2.44	5.64	5.71	3.52	3.36	5.54
		3rd	2.31	2.29	2.46	5.85	6.82	2.81	3.67	6.03

Table II-13. Properties of the Georgetown Airport (1995) Cores

	Replicate	layer	Bulk S.G.		Maximum	Total A.V.		Accessible A.V.		Binder
			SSD	Corelok	S.G.	SSD	Corelok	SSD	Corelok	Contents
	U3	1st	2.23	2.14	2.54	12.02	15.64	8.67	11.19	5.19
1st Core		2nd	2.28	2.25	2.38	4.27	5.45	6.08	6.59	5.65
Georgetown		3rd	2.29	2.24	2.54	9.85	11.69	5.63	6.99	5.32
Airport	T3	1st	2.16	2.15	2.43	10.94	11.61	9.52	8.70	6.19
(1995)		2nd	2.25	2.28	2.59	12.92	11.99	7.03	5.16	5.70
		3rd	2.23	2.22	2.52	11.69	11.96	6.76	6.24	5.97
	U1	1st	2.25	2.16	2.47	9.25	12.89	2.54	6.33	4.68
		2nd	2.30	2.29	2.46	6.65	7.05	4.32	4.39	5.41
		3rd	2.32	2.32	2.44	4.91	4.87	2.46	2.30	5.77
	U2	1st	2.24	2.15	2.49	10.33	13.89	8.71	11.09	4.87
		2nd	2.26	2.25	2.46	7.82	8.53	6.46	6.44	5.19
		3rd	2.28	2.27	2.46	7.38	7.63	5.33	5.07	5.59
	T1	1st	2.22	2.19	2.45	9.38	10.52	7.59	7.77	5.49
2nd Core		2nd	2.28	2.28	2.48	7.96	8.14	5.32	5.00	5.39
Georgetown		3rd	2.29	2.29	2.47	7.43	7.26	4.62	4.06	5.63
Airport	T2	1st	2.21	2.00	2.44	9.47	17.98	0.62	9.95	5.40
(1995)		2nd	2.29	2.29	2.45	6.40	6.62	4.82	4.63	5.60
		3rd	2.32	2.31	2.45	5.61	5.84	3.59	3.59	5.69
	T1*	1st	2.24	2.13	2.44	8.34	12.91	7.84	11.42	5.47
		2nd	2.27	2.25	2.49	8.45	9.40	6.71	6.89	4.73
		3rd	2.27	2.27	2.47	8.19	8.34	6.25	5.71	5.40
	T2*	1st	2.22	2.16	2.45	9.39	11.82	8.94	10.06	4.76
		2nd	2.27	2.24	2.46	7.81	8.81	6.32	6.63	5.44
		3rd	2.31	2.29	2.48	6.98	7.82	4.94	5.36	4.73

Table II-14. Properties of the Jacksonville Airport Cores

	Replicate	layer	Bulk S.G.		Maximum	Total A.V.		Accessible A.V.		Binder
			SSD	Corelok	S.G.	SSD	Corelok	SSD	Corelok	Contents
	U3	1st	2.27	2.17	2.51	9.29	13.56	6.74	10.37	5.89
1st Core		2nd	2.33	2.26	2.44	4.48	7.48	1.93	4.94	7.48
Jacksonville		3rd	2.28	2.26	2.47	7.43	8.20	4.97	5.32	6.72
Airport	T3	1st	2.29	2.24	2.46	6.73	8.78	2.54	4.56	7.37
		2nd	2.35	2.32	2.45	3.82	5.37	1.49	3.04	6.74
		3rd	2.36	2.32	2.46	4.08	5.42	2.04	3.34	6.65
	U1	1st	2.28	2.19	2.50	8.80	12.21	8.18	10.51	5.50
		2nd	2.32	2.25	2.47	6.08	8.93	4.08	6.69	6.37
		3rd	2.30	2.24	2.47	6.87	9.24	4.48	6.56	6.43
	U2	1st	2.29	2.22	2.50	8.51	11.23	7.48	9.28	5.62
2nd Core		2nd	2.32	2.27	2.48	6.56	8.44	5.14	6.58	6.20
Jacksonville		3rd	2.33	2.30	2.47	5.98	7.04	5.02	5.64	6.39
Airport	T1	1st	2.23	2.14	2.45	9.02	12.65	8.76	11.14	5.76
		2nd	2.26	2.24	2.46	8.27	8.95	7.19	6.98	6.16
		3rd	2.26	2.22	2.46	8.40	9.74	7.75	8.08	6.09
	T2	1st	2.24	2.17	2.49	9.91	12.82	8.33	10.14	6.16
		2nd	2.24	2.20	2.47	9.04	10.70	8.03	8.63	6.20
		3rd	2.24	2.19	2.26	0.82	3.10	7.80	8.89	6.48

Table II-15. Properties of the Lufkin BUS 59 Cores

	Replicate	layer	Bulk S.G.		Maximum	Total A.V.		Accessible A.V.		Binder
			SSD	Corelok	S.G.	SSD	Corelok	SSD	Corelok	Contents
	U3	1st	-	-	-	-	-	-	-	3.89
1st Core		2nd	-	-	-	-	-	-	-	4.31
Lufkin		3rd	-	-	-	-	-	-	-	
BUS 59	T3	1st	-	-	-	-	-	-	-	4.50
		2nd	-	-	-	-	-	-	-	4.36
		3rd	-	-	-	-	-	-	-	4.20
	U1	1st	2.30	2.22	2.55	9.66	12.95	8.71	10.79	3.19
		2nd	2.29	2.25	2.56	10.31	12.11	8.04	8.79	4.06
		3rd	2.29	2.21	2.53	9.55	12.85	8.32	10.52	3.77
	U2	1st	2.32	2.21	2.56	9.33	13.44	8.01	11.12	3.21
2nd Core		2nd	2.30	2.23	2.58	10.72	13.52	8.13	9.91	3.53
Lufkin		3rd	2.29	2.23	2.52	9.27	11.76	7.00	8.72	3.69
BUS 59	T1	1st	2.30	2.28	2.50	8.04	8.91	6.26	6.46	3.88
		2nd	2.31	2.29	2.49	7.16	8.23	5.86	6.34	3.94
		3rd	2.28	2.19	2.47	7.71	11.31	7.83	10.40	4.48
	T2	1st	2.33	2.31	2.51	7.06	7.87	4.86	5.25	3.17
		2nd	2.32	2.31	2.51	7.40	7.80	5.62	5.47	3.93
		3rd	2.31	2.28	2.51	7.90	9.31	6.81	7.44	3.70

Table II-16. Properties of the Odessa SH 149 Cores

	Replicate	layer	Bulk S.G.		Maximum	Total A.V.		Accessible A.V.		Binder
			SSD	Corelok	S.G.	SSD	Corelok	SSD	Corelok	Contents
	U1	1st	2.14	2.03	2.11	0.00	3.77	0.86	6.05	11.38
		2nd	2.31	2.24	2.36	2.14	4.77	0.00	2.39	5.88
		3rd	2.35	2.35	2.43	3.27	3.23	0.67	0.62	4.95
	U2	1st	2.15	2.01	2.24	3.94	10.49	1.50	8.17	9.94
1st Core		2nd	2.30	2.29	2.34	1.91	2.31	0.64	1.04	6.60
Odessa		3rd	2.34	2.34	2.42	3.27	3.10	1.39	1.18	4.50
SH 149	T1	1st	2.13	2.00	2.22	3.87	9.98	2.07	8.21	11.00
		2nd	2.32	2.32	2.35	1.53	1.25	0.41	0.12	5.97
		3rd	2.32	2.32	2.43	4.56	4.41	2.10	1.86	4.62
	T2	1st	2.12	2.03	2.19	3.18	7.32	1.50	5.67	11.40
		2nd	2.32	2.34	2.36	1.83	1.12	0.71	0.00	5.86
		3rd	2.33	2.34	2.41	3.53	3.06	1.18	0.68	4.74

Table II-17. Properties of the Odessa SH 349 Cores

	Replicate	layer	Bulk S.G.		Maximum	Total A.V.		Accessible A.V.		Binder
			SSD	Corelok	S.G.	SSD	Corelok	SSD	Corelok	Contents
	U1	1st	2.10	2.02	2.17	3.39	6.93	1.92	5.45	8.95
		2nd	2.28	2.24	2.39	4.86	6.27	3.09	4.35	5.48
		3rd	2.27	2.24	2.40	5.26	6.64	3.45	4.65	5.76
	U2	1st	2.05	1.91	2.10	2.32	9.15	1.76	8.57	9.13
1st Core		2nd	2.27	2.20	2.44	6.93	9.91	4.69	7.35	5.00
Odessa		3rd	2.21	2.18	2.27	2.74	4.26	2.43	3.84	8.03
SH 349	T1	1st	2.16	2.01	2.26	4.38	11.22	2.34	9.23	10.85
		2nd	2.35	2.35	2.41	2.33	2.45	0.55	0.67	4.58
		3rd	2.30	2.29	2.32	1.04	1.18	0.81	0.93	6.42
	T2	1st	2.11	2.02	2.17	2.68	6.98	1.08	5.43	8.79
		2nd	2.31	2.30	2.23	0.00	0.00	1.30	1.92	5.91
		3rd	2.29	2.25	2.39	4.21	5.83	1.17	2.81	7.05

Table II-18. Properties of Pleasanton Airport Cores

	Replicate	layer	Bulk S.G.		Maximum	Total A.V.		Accessible A.V.		Binder
			SSD	Corelok	S.G.	SSD	Corelok	SSD	Corelok	Contents
	U3	1st	2.29	2.17	2.39	4.28	9.18	4.37	8.94	5.93
1st Core		2nd	2.34	2.38	2.45	4.21	2.54	1.76	0.00	6.30
Pleasanton		3rd	2.35	2.33	2.42	2.81	3.99	1.26	2.42	6.11
Airport	T3	1st	2.26	2.16	2.44	7.23	11.30	4.37	8.24	6.77
		2nd	2.30	2.16	2.49	7.76	13.18	5.06	10.20	5.53
		3rd	2.29	2.23	2.46	7.04	9.39	3.93	6.08	5.76
	U1	1st	-	-	-	-	-	-	-	-
		2nd	-	-	-	-	-	-	-	-
		3rd	-	-	-	-	-	-	-	-
	U2	1st	-	-	-	-	-	-	-	-
2nd Core		2nd	-	-	-	-	-	-	-	-
Pleasanton		3rd	-	-	-	-	-	-	-	-
Airport	T1	1st	2.24	2.19	2.42	7.31	9.50	5.22	6.98	6.54
		2nd	2.31	2.27	2.44	5.53	7.24	3.65	5.15	5.27
		3rd	2.32	2.30	2.45	5.34	6.12	3.06	3.68	5.05
	T2	1st	2.24	2.19	2.41	7.16	9.22	4.87	6.56	6.00
		2nd	2.31	2.26	2.45	5.77	7.91	3.40	5.38	5.12
		3rd	2.32	2.28	2.48	6.69	8.03	0.95	2.36	5.07

Table II-19. Properties of Tyler US 79 Cores

	Replicate	layer	Bulk S.G.		Maximum	Total A.V.		Accessible A.V.		Binder
			SSD	Corelok	S.G.	SSD	Corelok	SSD	Corelok	Contents
	U1	1st	2.30	2.17	2.55	9.98	14.77	8.30	12.07	2.90
		2nd	2.34	2.24	2.54	7.81	11.93	6.23	9.77	3.83
		3rd	2.36	2.28	2.52	6.65	9.78	5.51	8.15	3.50
	U2	1st	2.32	2.16	2.57	10.03	15.95	9.99	14.36	3.01
1st Core		2nd	2.34	2.24	2.55	8.10	12.13	6.66	10.00	3.67
Tyler		3rd	2.35	2.26	2.52	6.79	10.29	6.45	9.26	3.90
US 79	T1	1st	2.31	2.20	2.56	9.84	13.99	9.41	12.16	3.54
		2nd	2.32	2.26	2.55	8.90	11.27	8.32	9.55	3.37
		3rd	2.33	2.27	2.52	7.42	9.93	7.80	9.28	3.24
	T2	1st	2.33	2.21	2.54	8.47	13.26	8.21	11.91	3.16
		2nd	2.35	2.28	2.54	7.62	10.29	6.42	8.41	3.59
		3rd	2.37	2.31	2.52	6.09	8.28	5.89	7.47	3.60

Binder rheology measurements are reported in Appendix A in Tables A-1 through A-17. The binder rheology η* master curves are presented in Appendix B in Figures B-1 through B-29. The air voids results are presented in Appendix C in Figures C-1 through C-28b, and the data on binder content are presented graphically in Appendix D, Figures D-1 through D-19. The air voids results are presented two ways. The first comparison is in Figures C-1 through C-9 in which the accessible air voids in each figure are for a particular site, but are grouped according to layer so that all of the first-layer binders (first year, second year) are compared side by side as bar graphs; all of the second-layer binders are compared side by side; and the third-layer binders are compared side by side. The second comparison in Figures C-10a through C-28b presents the accessible air voids in one figure and the total air void in another figure for each site, but also the layers in each core are compared directly to each other. Thus the first, second, and third layers for one core are compared to each other, side by side, and then they are compared to each other for another core and so on. Again, this latter comparison is done for both the accessible air voids and the total air voids in Figures C-10a through C-28b. For the binder contents in Appendix D, the results are compared layer by layer for each core.

Figures II-6 and II-7 are comparisons of the DSR function to the accessible air voids for all sites and all slices. Figure II-6 presents the DSR function versus accessible air voids, with each site identified. Note that the range of accessible air voids is from nearly 0 percent to approximately 11 percent, a surprisingly wide range, with many data points at each value within this range. The DSR function, of course, increases as the binder stiffens with aging. Therefore, if accessible air voids is a factor in aging, the DSR function would tend to be less where there is low accessible air voids and higher where accessible air voids are higher. However, there is so much scatter to the data in Figure II-6 that such a correlation is not evident.

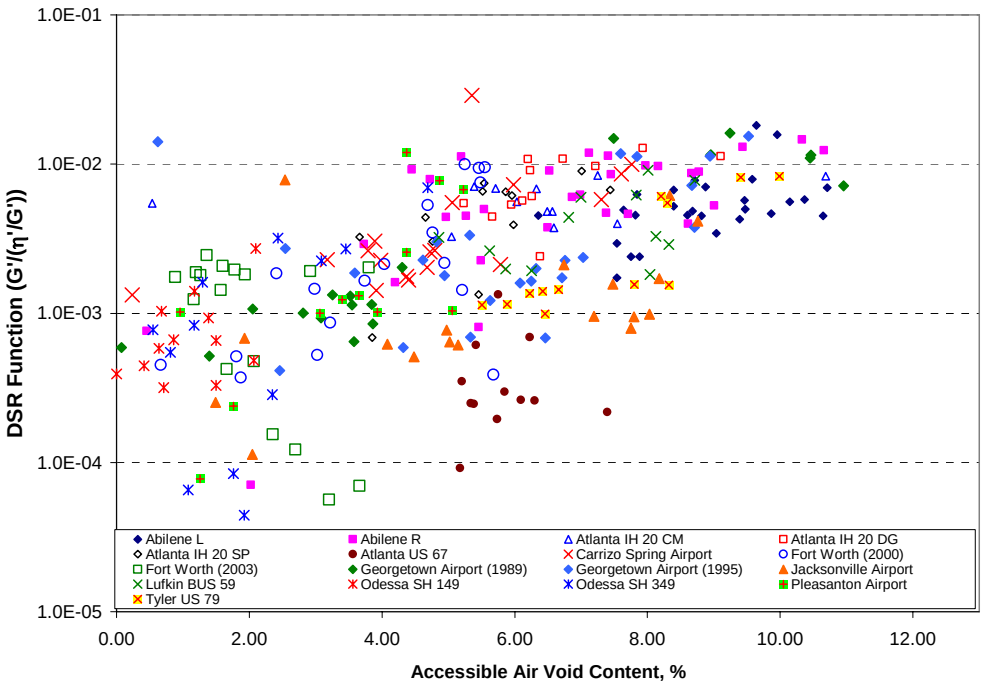

Figure II-6. DSR Function versus Accessible Air Voids Content for All Cores and Sites

Figure II-7 shows the data in a different way. This is a plot of the DSR function versus service life of the pavement with the data categorized by the accessible air voids level. Low accessible air voids (less than 3 percent) are identified by green diamond symbols, moderate accessible air voids (between 3 and 6 percent) are indicated by blue squares, and high accessible air voids (greater than 6 percent) are indicated by red triangles. In Figure II-7, binders that were in the portions of the pavements having low accessible air voids tended to be lower in binder stiffness throughout the service life of the pavement compared to those associated with high accessible air voids. Moderate accessible air voids appear to be in between. The separation appears better at longer service times, and very few of the high accessible air voids slices contained binders with low DSR function values. From these results, one might infer that lower accessible air voids can contribute to lower binder hardening rates.

Figure II-8 presents a similar comparison as that shown in Figure II-7, except the data are categorized by binder content. In this case the green symbols are low binder content (less than 3 percent), the blue symbols are moderate binder content (4-6 percent), and red symbols are high binder content (more than 6 percent). In this case, there appears to be much less, or no, correlation between binder content and DSR function.

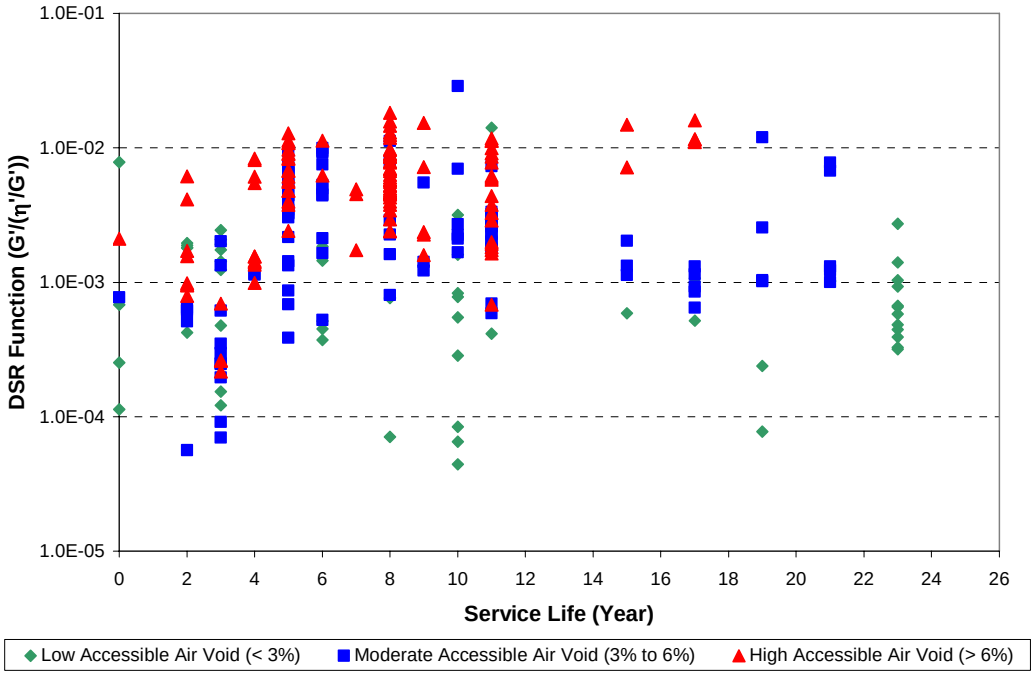

Figure II-7. DSR Function versus Service Life for Three Accessible Air Voids Intervals

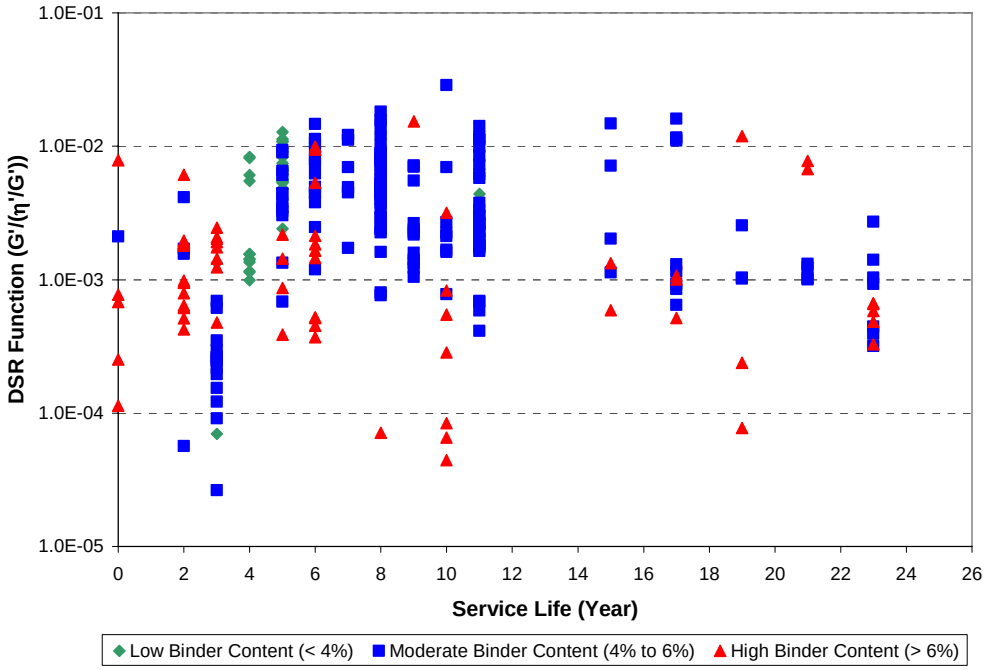

Figure II-8. DSR Function versus Service Life for Three Binder Content Intervals

Conclusions

Pavement core samples were collected from several locations throughout Texas, and their layer-by-layer air void contents from the top inch of the pavement were measured. After that asphalt binders from these core samples were extracted and recovered. Then the physical properties of these binders were compared with the air void contents from the corresponding slices. The results of this chapter support previous work that the aging rates of asphalt binders are affected by accessible air voids, especially at very low levels where there were thicker asphalt films.

CHAPTER III
X-RAY CT ANALYSIS OF LABORATORY/FIELD CORE SAMPLES

Introduction

A crucial element of the pavement aging models discussed previously is accessible air void influence on the pavement oxidation process. Cores obtained from field sections during the course of this research, in addition to core samples identified in Chapter II, were analyzed for total air voids (by the CoreLok®, the saturated surface dry methods-SSD, or X-ray computed tomography, CT), interconnected air voids (by X-ray CT), or accessible air voids (by CoreLok® or SSD).

Another important component in asphalt binder oxidation is the air voids characteristic of pavement samples. X-ray computed tomography and image analysis techniques were proposed to examine the internal microstructure of hot mix asphalt concrete (HMAC) mixtures, including air void (AV) distribution and interconnectivity and binder content and distribution in terms of film thickness. These factors are some of the HMAC mixture parameters to be identified in terms of the role they play in the aging mechanism. X-ray CT is a nondestructive technique used to visualize the interior characteristics of opaque objects.[42]

In this chapter, the technique to determine key air void structure characteristics from asphalt core samples and average air void radius of permeable friction course samples was developed.[55] Then the obtained technique was used to further determine average air void radius and minimum air void spacing for dense-graded mixture samples. Consequently, these two parameters were used as inputs for the binder oxidation model discussed in Chapter IV.

Research Objectives

The research work in this chapter aims to assess the air void characteristics in the pavement cores using the X-ray CT method, which is a nondestructive approach. The significant parameters that were investigated include the connectivity of air channels from top to bottom of the core, the average radius of air void channels, and the channel spacing within the pavement cores. These parameters were used as inputs in the binder oxidation model discussed subsequently in Chapter IV.

Methodology

The analysis in this chapter primarily involved X-ray CT scanning, which was performed on laboratory and field specimens to investigate the air void characteristics and structure. Table III-1 reports the details of laboratory mixed and laboratory compacted (LMLC) specimens. These specimens were fabricated using the mixture design from corresponding highway locations including asphalt type, optimum asphalt content (OAC), and aggregate type. For LMLC specimens, the cores that were fabricated using the mixture designs of US 281 and IH 35 in San Antonio, Texas, are porous friction course (PFC) mixtures that are usually placed on the top of dense-graded mixtures to reduce noise generated between tires and pavement surface. These high porosity PFC layers would also prevent water splash-spray and improve water drainage on the wet road surfaces. The last specimen from LMLC group was fabricated from the mixture design of US 59 in Yoakum, Texas. The specimen was a regular dense-graded mixture with an air void content much lower than the other two PFC mixtures.

Table III-1. Information of Laboratory Mixed-Laboratory Compacted (LMLC) Specimens

Mixture	Highway	Location	Asphalt Type	OAC (%)	Aggregate Type	Other Materials
US-281-AR	US 281	San Antonio, TX	AC-10 w/16% crumb rubber	8.1	Sandstone Limestone	None
I-35-PG	IH 35	San Antonio, TX	PG 76-22S	6.1	Sandstone Limestone	Lime (1%) Fibers (0.3%)
US 59	US 59	Yoakum, TX	Eagle PG 76-22	5.3	N/A	None

Table III-2 provides the information on plant mixture specimens. These cores were fabricated using the hot-mix samples from various construction sites in Texas and then compacted in the laboratory. All specimens in field mixed-laboratory compacted (FMLC) group were PFC mixtures.

Table III-2. Information of Field Mixed-Laboratory Compacted (FMLC or Plant Mixes) Specimens

Mixture	Highway	Location	Asphalt Type	OAC (%)	Aggregate Type	Other Materials
I-35-PG	IH 35	San Antonio, TX	PG 76-22S	6.1	Sandstone Limestone	Lime (1%) Fibers (0.3%)
US-83-PG	US 83/84	Abilene, TX	PG 76-22S	6.4	Limestone	Lime (1%) Fibers (0.3%)
IH-20-PG	IH 20	Abilene, TX	PG 76-22	6.5	Limestone	Lime (1%) Fibers (0.3%)
IH-30-PG	IH 30	Paris, TX	PG 76-22	6.6	Sandstone	Lime (1%) Fibers (0.3%)
US-59-PG	US 59	Lufkin, TX	PG 76-22	5.9	Granite	Lime (1%) Fibers (0.3%)
US-59Y-PG	US 59	Yoakum, TX	PG 76-22S	5.8	Limestone	Lime (1%) Fibers (0.3%)
US-281-AR	US 281	San Antonio, TX	AC-10 w/16% crumb rubber	8.1	Sandstone	None
US-288-AR	US 288	Houston, TX	AC-10 w/17% Type II rubber	8	Granite	None
US-290-AR	US 290	Austin, TX	AC-10 w/17 % crumb rubber	8.3	Sandstone	None

The last group of core specimens was taken directly from the field locations across Texas. Table III-3 shows the information of field mixed-field compacted (FMFC) specimens obtained for this research work. Note that all core specimens were PFC samples except the one from US 259, which was a regular dense-graded mixture.

Table III-3. Information of Field Mixed-Field Compacted (FMFC or Road Cores) Specimens

Mixture	Highway	Location	Asphalt Type	OAC (%)	Aggregate Type	Other Materials
I-35-PG	IH 35	San Antonio, TX	PG 76-22S	6.1	Sandstone Limestone	Lime (1%) Fibers (0.3%)
US-83-PG	US 83/84	Abilene, TX	PG 76-22S	6.4	Limestone	Lime (1%) Fibers (0.3%)
IH-20-PG	IH 20	Abilene, TX	PG 76-22	6.5	Limestone	Lime (1%) Fibers (0.3%)
IH-20-PG-TR	IH 20	Abilene, TX	PG 76-22TR	6.2	Limestone	Lime (1%) Fibers (0.3%)
IH-30-PG	IH 30	Paris, TX	PG 76-22	6.6	Sandstone	Lime (1%) Fibers (0.3%)
US-59-PG	US 59	Lufkin, TX	PG 76-22	5.9	Granite Limestone	Lime (1%) Fibers (0.3%)
US-59Y-PG	US 59	Yoakum, TX	PG 76-22S	5.81	Limestone	Lime (1%) Fibers (0.3%)
H-6-PG	SH 6	Houston, TX	PG 76-22 TR	Unknown	Traprock, Limestone	None
I-35-PG-W	IH 35	Waco, TX	PG 76-22 TR	6	Limestone Igneous	Lime (1%) Fibers (0.4%)
US-281-AR	US 281	San Antonio, TX	AC-10 w/16% crumb rubber	8.1	Sandstone Limestone	None
US-288-AR	US 288	Houston, TX	AC-10 w/17% Type II Rubber	8	Granite Limestone	None
US-290-AR	US 290	Austin, TX	AC-10 w/17 % Rubber	8.3	Sandstone	None
I-35-AR	I 35	San Antonio, TX	AC-10 w/17 % Type II Rubber	8.4	Sandstone Limestone	None
US-259-PG	US 259	Timpson, TX	Lion PG 70-22S	4.3	Limestone Sandstone	Lime (1%)

Core specimens that were identified in Table III-3 were tested in the CoreLok® machine to pre-calculate the air void content of the specimens as a necessary calibration of grayscale images for the X-ray CT method. As validation of the X-ray CT method,

CoreLok® was used to determine accessible air voids (AAV) (those that water can penetrate when the CoreLok® vacuum bag is opened underwater).

In order to pre-calculate the air void content of the specimens as discussed in Chapter II, bulk specific gravity and maximum specific gravity must be measured. The details of such measurements are described as follows.

Determination of Bulk Specific Gravity of the Compacted Mixture

As recommended by previous research, the Corelok® vacuum seal method discussed briefly in Chapter II was used to determine the bulk specific gravity of the core specimens in this study.[56] However, the procedure was adjusted due to the size and surface roughness of the specimens. Core specimens were tested in a double large bag[49] because sharp edges of the specimen frequently puncture the bag causing the seal to break if only one bag is used. The inner bag was 1.5 inch (38 mm) to 2 inch (51 mm) shorter than the external bag to best apply the seal. The bulk specific gravity of the compacted mixture was calculated as:

$$\text{Bulk Specific Gravity of Mixture} = \frac{DA}{BA + DA - SeW - \frac{BA}{CF}} \qquad \text{(III-1)}$$

where *DA* is the mass of the specimen in air (g), *BA* is the mass of the bag in air (g), *SeW* is the mass of the sealed bag and the specimen in water (g), and *CF* represents the double bag correction factor supplied by the manufacturer[49] In addition to bulk specific gravity, water accessible AV content can be calculated by determining the vacuum saturated sample mass in water (*SaW*) after completing all other measurements. Measuring *SaW* can be done by cutting the sealed bag under water and taking it out of the water and then allowing access to water until a stable mass is obtained. The minimum saturation time used to determine *SaW* was 4 minutes, but some mixes required up to 7 minutes before reaching stable saturated weights. This time is mix

dependent and requires evaluation for each particular mix. Water accessible AV is then calculated as follows:

$$Accessible\ AV_{vacuum} = \frac{BA + DA - SeW - \left(\frac{BA}{CF}\right) - (DA - SaW)}{BA + DA - SeW - \left(\frac{BA}{CF}\right)} * 100 \quad (\%) \qquad \text{(III-2)}$$

Analysis of X-Ray CT Images

An X-ray source emits a beam of known intensity through the specimen, and a detector on the opposite side of the specimen measures the attenuated beam intensity (Figure III-1). The specimen rotates 360° with respect to its center and moves at a specific fixed vertical interval to enable evaluation of the entire specimen volume.[42,57]

Figure III-1. Specimen Set-Up during X-Ray CT Scanning

Air Void Content, Air Void Pore Radius, and Air Void Connectivity

Image analysis consists of two phases. The first phase is to determine the AV distribution based on the total AV content established using the Corelok®, while the second phase is to determine the interconnected AV content and distribution based on the results of the first analysis. Interconnected AV is defined as the air void channels that connected from the top to the bottom of specimens. The first image analysis phase was carried out using a macro previously developed by Masad et al.[42] for Image-Pro® Plus software. The original images were converted into black and white by the assigned macro, where black areas represent the voids and white areas represent the aggregates and the mastic. An appropriate user-input threshold parameter was chosen between 0 and 56,000. The areas of the original images were converted to black (voids phase) if the gray intensity of the areas were less than the indicated threshold, and the areas were converted to white if the intensities were higher than the threshold (aggregate and mastic phase). The threshold selection process was repeated until the total AV content (black areas) computed from the set of analyzed images matches the AV content measured from Corelok®.

The initial image analysis, which excluded the surface irregularities, produced black-and-white images with low AV contents (black areas) when compared to the AV obtained from Corelok® method. In this case, when attempting to match the AV content from Corelok®, the required threshold generated the black-and-white images of which voids contours did not match the voids geometry of the original grayscale images. From this discrepancy, the surface irregularities must be included in the analysis. After the surface irregularities were included, the resulting AV content computed from black-and-white images matched with the AV geometry of the original grayscale images.

The total AV content of each image (AV_i) and the total AV content of the specimen (AV_s) were computed as follows using a macro previously developed by Masad et al.[42] using Image-Pro® Plus:

$$AV_i = \frac{A_{vi}}{A_T} \tag{III-3}$$

$$AV_s = \frac{\sum_{i=1}^{n} \%AV_i}{n} \tag{III-4}$$

where A_{vi} is the area of AV in image i, A_T is the cross-sectional area of the image i, and n is the total number of images. The average AV radius ($\bar{r}_i$) in image i is calculated as:

$$\bar{r}_i = \sqrt{\frac{A_{vi}}{\pi M_i}} \tag{III-5}$$

where M_i corresponds to the number of AVs in each image.

The second phase of image analysis determines the interconnected AV content and distribution using the threshold images obtained after the first analysis phase. These black-and-white images were converted to binary bit files using another set of macros developed by Masad et al.[42] These binary files were then analyzed to determine the connected paths from top to bottom of the specimen by using a FORTRAN-built algorithm.[42] As a result of this analysis, bit files containing the interconnected AV information were acquired as the output of the algorithm. Then the Image-Pro® Plus software was used to convert these bit files back to black-and-white images, and the interconnected AV content of these images was calculated.

Air Void Spacing in X-Ray CT Image Layers

In addition to the air void radius in core samples, average air void spacing in the specimens is also considered to be an important parameter in a binder oxidation model for pavements. After air void content was calculated by imaging techniques discussed

previously, the coordinate of each air void $(x, y)_i$ in each image slice was also identified. The average distance between air voids (air void spacing) in each image slice can then be determined by calculating the average of the minimum distance between two air voids, which is the distance between the adjacent air voids. The mathematical correlation of average distance between two adjacent air voids in the image layer that has a total of N air void locations can be shown as follows:

$$2 \cdot r_{NFB} = \frac{\sum_{i=1}^{N} \sqrt{\left(y_i - y_j\right)^2 + \left(x_i - x_j\right)^2}}{N} \qquad \text{(III-6)}$$

where j is the location of the air void closet to the air void at location i and r_{NFB} (radius distance of no-flux boundary) is the distance that an oxygen molecule can travel into the asphalt binder away from the air void surface. From the calculation, r_{NFB} is simply half of the average distance between two adjacent air voids. The significance of r_{NFB} is discussed in detail in Chapter IV.

Results and Discussion

Total Air Voids (AV) and Interconnected Air Voids

Figure III-2 shows one grayscale image and the outputs obtained after total AV and interconnected AV analyses. Figure III-2b corresponds to the image obtained after applying the threshold required to reproduce the total AV content computed by the Corelok® method, and Figure III-2c corresponds to the black-and-white image obtained after the analysis of interconnected AV performed as described previously. In the interconnected AV analysis, the voids that were in contact with the surface were excluded.

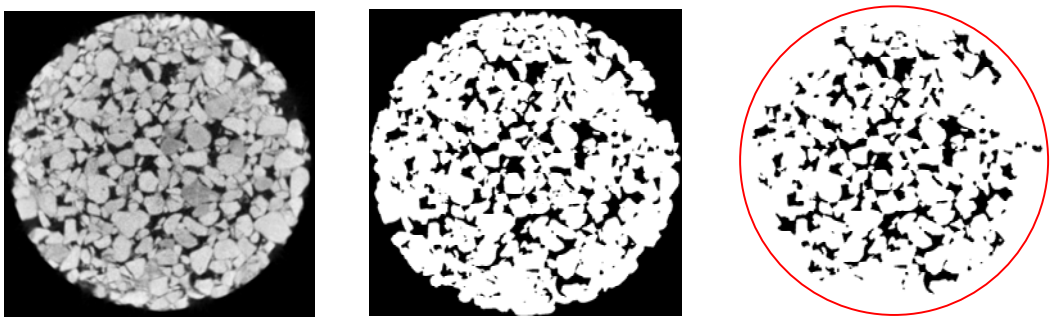

(a) (b) (c)

Figure III-2. X-ray CT Image Analysis. (a) Original Grayscale Image, (b) Black-and-White Image after Threshold and (c) Black-and-White Image after Interconnected AV Analysis[55]

The comparison of the total and accessible AV calculated based on the Corelok® method and the interconnected AV content calculated based on the analysis of X-ray CT images for the main mixtures (I-35-PG, US-59Y-PG, US-281-AR, and US-290-AR) that were used in this study is presented in Table III-4. The comparison shows that for most of the specimens, interconnected AV values were smaller compared to the water accessible AV values. While the accessible AV computation includes the AV that are accessible from all surfaces of the cylindrical specimen, the interconnected AV are computed including only the voids connected from the top to the bottom surface.

Table III-4. Comparison of Total, Water Accessible, and Interconnected Air Voids for FMLC Specimens[55]

Mix	Specimen	Vacuum, Total AV (%)	Vacuum, Accessible AV (%)	Dimensional Total AV (%)	Dimensional Accessible AV (%)	Total AV (X-Ray CT) (%)	Interconnected AV (X-Ray CT) (%)
I-35-PG	I35-C1D1	15.7	15.4	18.9	14.9	19.0	13.1
	I35-C2D1	16.0	16.1	19.1	15.5	19.0	14.2
US-59Y-PG	59Y-50C1D1	15.0	14.1	18.0	13.7	15.9	10.3
	59Y-50C2D1	15.8	15.2	18.6	14.5	17.1	11.1
	59Y-15C1D1	23.1	22.9	26.3	22.9	26.5	17.3
	59Y-15C2D1	22.6	22.0	25.7	22.1	25.7	16.8
US-281-AR	281-C1D1	17.5	17.6	21.5	18.3	21.5	15.0
	281-C2D1	17.8	18.5	21.7	18.9	21.8	15.2
US-290-AR	290-50C2D1	15.8	11.8	19.6	13.7	20.1	15.1
	290-50C1D2	15.3	11.0	20.0	15.3	19.4	15.1
	290-12C1D2	19.8	16.5	23.3	15.3	23.0	18.1
	290-12C1D1	19.4	14.2	23.0		23.3	17.1

In order to reproduce the road cores from FMLC for further pavement performance testing, the appropriate number of gyrations for compaction must be determined. Figure III-3 and Figure III-4 show the distribution of total and interconnected AV for FMLC specimens of the US-59Y-PG and US-290-AR mixtures. The set of FMLC specimens studied consists of samples that were compacted at 50, 12, and 10 gyrations using the SuperPave Gyratory Compactor (SGC) to reproduce the average total AV for corresponding road cores. As shown in Figures III-3 and III-4, the characteristic AV distribution resembles a “C” shape, which showed higher AV contents at the top and bottom portions of the specimen due to the restriction imposed by the top and bottom surfaces of the SGC during compaction. This characteristic AV distribution can be observed for both total and interconnected AV.

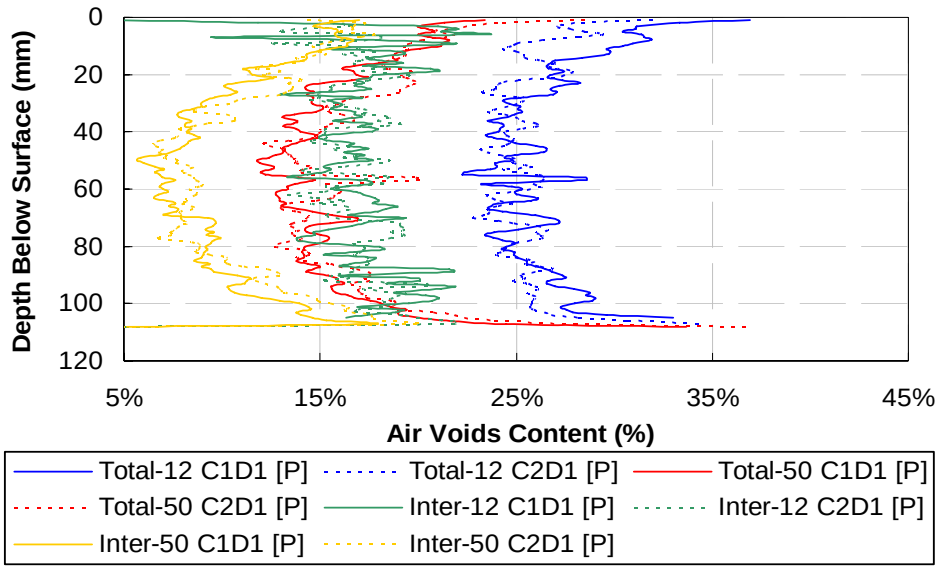

Figure III-3. Total and Interconnected Air Voids Distribution for FMLC Specimens and Road Cores of the US-59Y-PG Mixture[55]

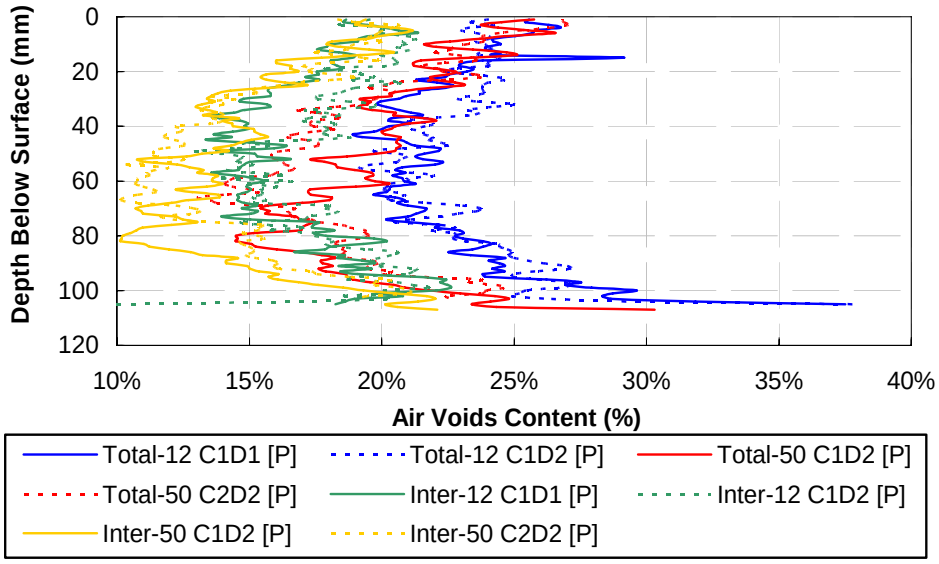

Figure III-4. Total and Interconnected Air Voids Distribution for FMLC Specimens of the US-290-AR Mixture[55]

Figure III-5 shows the distribution of total and interconnected AV for the road cores of both the US-59Y-PG and US-290-AR mixtures. These distributions suggest that the field compaction causes decreasing AV content, but the maximum AV contents are still at the pavement surface. The comparison of road cores and FMLC specimens compacted at small compaction effort (12 gyrations) shown in Figure III-6 indicates that the distribution and total AV content of road cores can be reproduced at the top portions of the SGC compacted specimens. This ensures that the FMLC specimens compacted with 12 gyrations can be used to represent the road cores for further pavement performance evaluations.

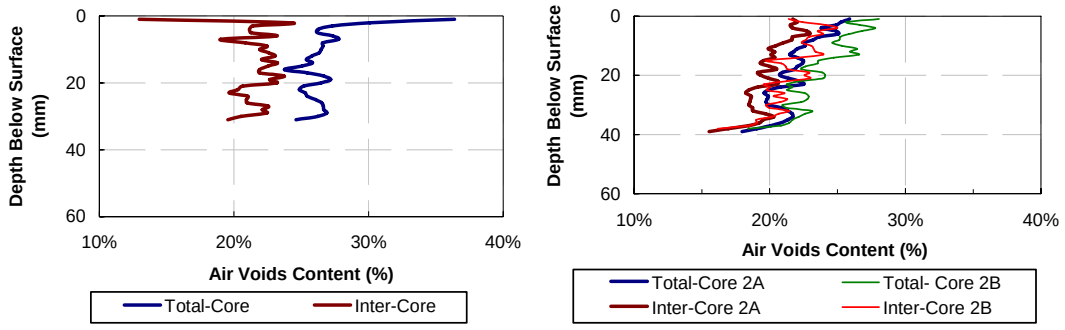

(a) (b)

Figure III-5. Total and Interconnected Air Voids Distribution for Road Cores. (a) US-59Y-PG and (b) US-290-AR Mixture[55]

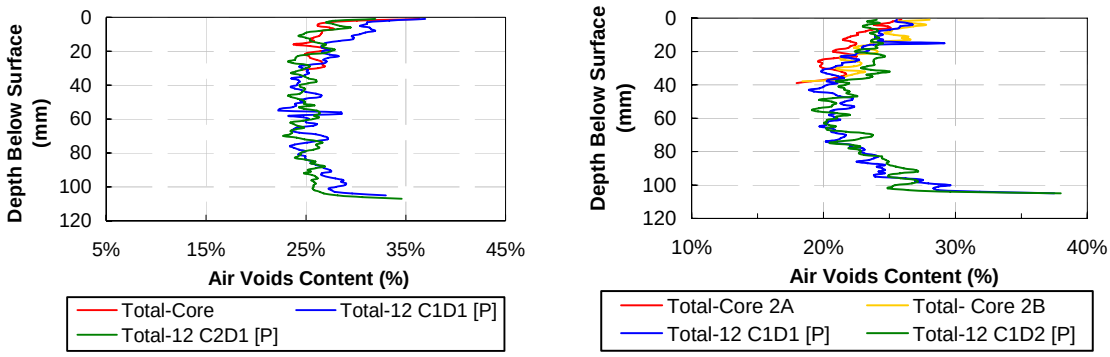

(a) (b)

Figure III-6. Comparison of Air Voids Distributions for FMLC Specimens and Road Cores. (a) US-59Y-PG and (b) US -290-AR Mixtures[55]

Air Void Radius and Air Void Spacing

Despite the total and accessible air void analysis that were performed on both PFC and dense-graded mixtures discussed previously, the air void spacings were evaluated only on the dense-graded mixtures because subsequent study on asphalt binder oxidation models in pavements is focused specifically on using dense-graded mixtures as a representative mixture in model calculations. The air void spacing results are shown in Table III-5. The air void spacing study was performed on two mixtures from two locations – US 259 (FMFC) and US 59 (LMLC). Although from the actual X-ray CT scan analysis, air void spacing data were reported for each of the scanned layers, the data that were reported in this section were the average values from the whole depth of the core sample. These average values were used in the calculations later in Chapters IV, V, and VI to reduce the complication of the oxidation model computations. The data of each replicate shown in Table III-5 are average air void content, average air void radius, r_{NFB}, and average distance between two adjacent air voids.

Table III-5. Air Void Radius and Air Void Spacing Summary for US 259 (FMFC) and US 59 (LMLC) Core Samples

Location	Replicate	Avg. Air Void Content (%)	Avg. Air Void Radius (mm)	r_{NFB} (mm)	Avg. Distance Between Two Adjacent Air Voids (mm)
US 259 (FMFC)	1-2	8.85	0.87	1.27	2.55
	1-3	10.43	1.02	1.43	2.86
	1-5	7.34	0.80	1.25	2.51
	1-17	9.13	0.91	1.32	2.63
	1-20	7.93	0.80	1.23	2.46
US 59 (LMLC)	1-1	8.58	0.87	1.51	3.02
	1-2	9.73	0.93	1.55	3.11
	1-3	9.04	0.97	1.68	3.35
	2-1	8.23	0.92	1.66	3.32
	2-2	8.81	0.90	1.58	3.16

Figure III-7 shows the results of X-Ray CT image analysis of US 259 road core 1-2. Additional parameters for the binder oxidation model that was introduced in this dissertation are the air void characteristics of asphalt mixtures, which are the average air void radius, r_{PS}, and the average half-distance between two adjacent air voids (the average distance to the no-flux boundary), r_{NFB}. The difference between r_{NFB} and r_{PS} determines the maximum distance oxygen molecules travel in the asphalt film, which directly affects oxygen diffusion. The air void spacing can be observed by X-ray CT scan, but the accuracy of the measurement depends on the scanning resolution of the equipment, which can be a time- and resource-consuming process for higher resolution. Figure III-7(a) shows X-ray CT image analysis results of air void radius, the r_{NFB}, and the average distance between two adjacent air voids distribution ($2r_{NFB}$) with depth of the core sample obtained from Highway US 259, Timpson, Texas. The average half-distance between two adjacent air voids can be calculated from the air void location schematic as shown in Figure III-7(b) together with Equation III-6.

From the data reported, r_{PS} and r_{NFB} through the depth of the core were estimated to be approximately 0.87 mm and 1.27 mm, respectively.

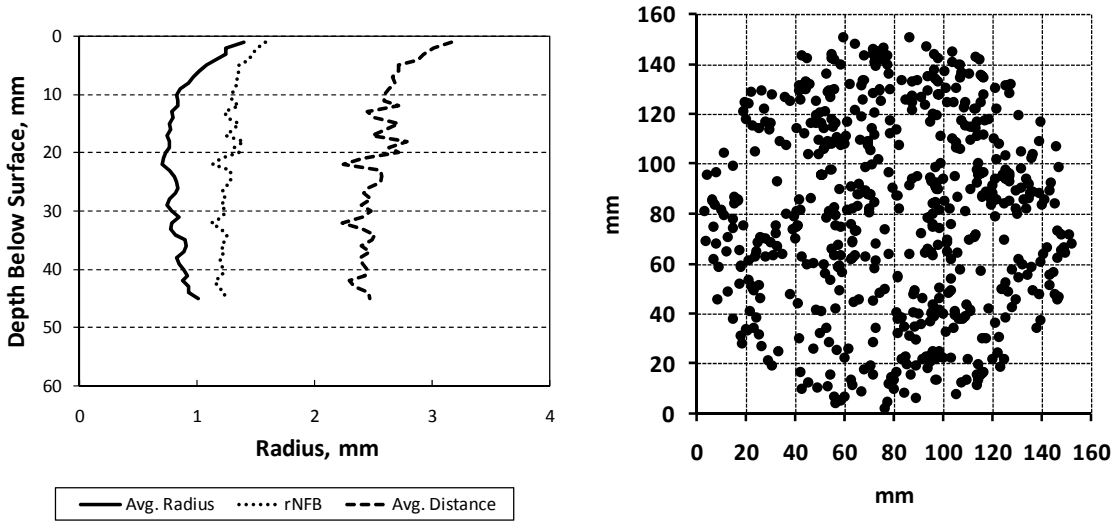

(a) **(b)**

Figure III-7. Results from X-Ray CT Scan and Additional Calculations for US 259 Core Sample (Road Core 1-2). (a) Average Air Void Radius, No-Flux Boundary Radius, and Average Distance between Two Adjacent Air Voids of Each X-Ray CT Scan Layer and (b) Air Void Locations in the Top Layer of the Core Sample 1-2

Figure III-8 shows results similar to that shown in Figure III-7. However the mixture design of the core sample was US 59 LMLC 1-1. Core samples that were fabricated in the laboratory were thicker than the road cores. The average air void radius, r_{NFB}, and the average distance between two adjacent air voids, in this case, have a pattern of "C" shape unlike the road cores that have only a half "C" shape as discussed previously.

From the data reported, r_{PS} and r_{NFB} through the depth of the core were estimated to be approximately 0.86 mm and 1.51 mm, respectively.

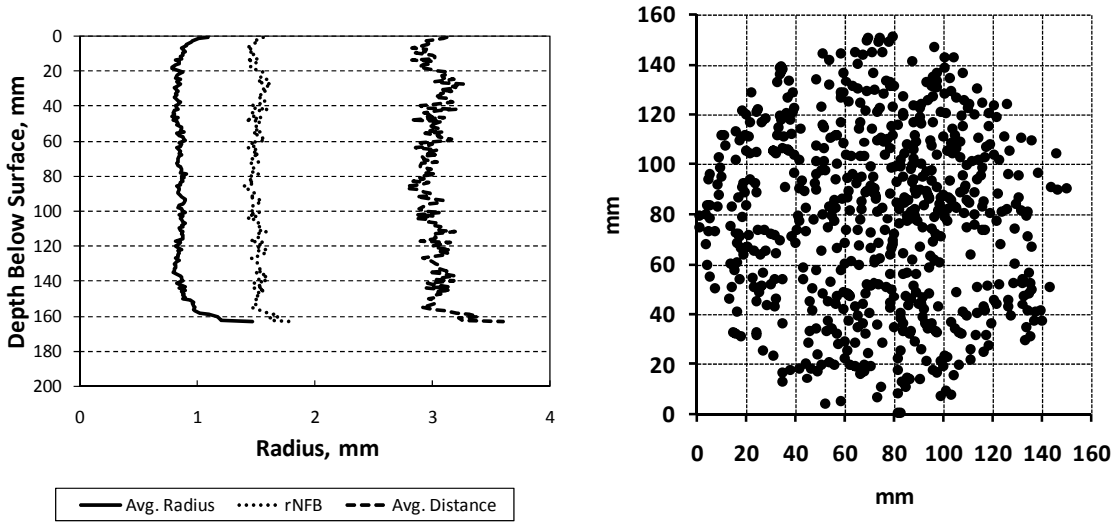

(a) **(b)**

Figure III-8. Results from X-Ray CT Scan and Additional Calculations for US 59 Core Sample (LMLC Core 1-1). (a) Average Air Void Radius, No-Flux Boundary Radius, and Average Distance between Two Adjacent Air Voids of Each X-Ray CT Scan Layer and (b) Air Void Locations in the Top Layer of the Core Sample 1-1

Additional X-ray CT results including the average air void radius, the r_{NFB}, and the average distance between two adjacent air voids for US 259 FMLC and US 59 LMLC specimens are reported in Appendix E.

Conclusions

The X-ray CT method is a nondestructive test that can be used to determine the total air void content as well as interconnected air voids in LMLC, FMLC, and FMFC samples. It was shown that the structure of air voids inside the core sample depends considerably on the compaction during construction or specimen fabrication process.

With additional imaging analysis techniques, more information on air void structure in samples can be obtained. The important parameters that are the results of image analyzing process are air void radius, r_{PS}, and the half-distance between two

adjacent pores, r_{NFB}. The r_{NFB} was calculated using the air void locations from the image analysis method. The difference of r_{NFB} and r_{PS} is the effective thickness that the oxygen molecule can diffuse into the asphalt-aggregate matrix. The detailed discussion of these air void characteristic parameters is included in Chapters IV and V.

CHAPTER IV
ASPHALT BINDER OXIDATION TRANSPORT MODEL DEVELOPMENT AND CALCULATED ASPHALT OXIDATION RATE UNDER CONSTANT TEMPERATURE CONDITION

Introduction

Previously, the asphalt oxidation model proposed by Lunsford[58] was based solely on asphalt binder kinetics that did not include the effects of air voids in pavements and pavement temperature, which are key factors in the binder oxidation process. The existing model, which was developed in Cartesian coordinates, also does not represent the geometry of the field pavement structure.

In order to understand oxidation phenomena in pavements, an improved model to predict the oxidation rate with the input of binder kinetics data, temperature profile of the pavement, and mixture characteristics was developed in this study. To reflect the geometry of asphalt pavements and their air voids structure, the asphalt oxidation model in pavements introduced in this study was developed under the cylindrical coordinate system assuming that there are air channels connecting from the top to the bottom of pavements.

An improved pavement oxidation transport model is also based on three interlinked processes: 1) diffusion of oxygen into the asphalt binder mastic in the pavement, 2) heat transfer into the pavement that results in temperature variations with depth and time, and 3) asphalt binder oxidation, which is a function of oxygen concentration and temperature in the binder. A fourth issue that affects the oxygen transport and concentration is the air voids distribution in the mixture because it affects the availability of oxygen to the binder. If the interconnected (or accessible) air voids are sufficiently low, then delivery of oxygen to the binder is hindered. The diffusion process is coupled to both temperature and the level of oxidation because both of these factors affect oxygen diffusivity.

The study in this chapter includes the development of asphalt binder oxidation model in pavements for a cylindrical coordinate system based on key the fundamentals: asphalt binder kinetics and oxygen transport in asphalt binder. The model was then used under the constant temperature condition to generate model outputs: oxygen pressure profile, carbonyl area, limiting viscosity, and oxygen diffusivity in asphalt binder.

Research Objectives

The objective of the work presented in this chapter was to develop a more realistic and more effective binder oxidation model that represents aging in pavements. The model must capture the key elements of asphalt oxidation including asphalt oxidation kinetics, pavement air void characteristics, and oxygen diffusion into asphalt binders.

Oxidation Model Development

In order to understand the complex pavement asphalt oxidation process, researchers have analyzed asphalt samples and proposed empirical asphalt oxidation (aging) models.[5,59,60] However, these proposed models do not include the effect of oxygen transport limitations (diffusion) into the asphalt binder. Lunsford[58] proposed a preliminary oxidation model with the oxygen diffusion effect included. However, the study used approximate values for diffusivity and did not include the effect of fines and aggregate on diffusion. In addition, previous work has not implemented a pavement temperature model that provides temperature as a function of depth. Thus a thermal and oxygen transport model, necessary for accurate predictions of binder oxidation in pavements, has not yet been developed.

The concept of approximating the binder film in the pavement as a thin film is probably reasonable for high air voids content where there are a large number of pores passing through the pavement so that the distance from any pore to the binder is not very

far. A more realistic model for a reduced number of air voids might be a cylindrical model that assumes that oxygen diffuses from the pore in a radial direction into a cylindrical shell of binder (Figure IV-1). The modeling concept was initiated from the X-ray CT study on air void connectivity in pavements (Chapter III). It was discovered that air void channels in pavements are positioned and connected from top to bottom.[42] In this case, the relevant parameter would be the thickness of this cylindrical shell, relative to the diameter of the pore containing the air. The smaller the air voids, the greater the ratio of this binder shell to the pore diameter and thus the more time required for oxygen to diffuse through the binder.

The initial assumption of the model is that there are only two phases in the pavement layers; asphalt-aggregate matrix and air void phases. This assumption eliminated the complexity in the determination of the oxygen diffusion path in a uniform asphalt phase. By combining asphalt and aggregate phases, the concept of effective diffusivity can be introduced and is discussed in a later section of this chapter.

Also from the figure, r_{PS} (pore surface) refers to air void pore radius and r_{NFB} (no-flux boundary) refers to the radius at the half distance between two adjacent air voids where there is no mass flux transfer across this boundary. The difference between r_{NFB} and r_{PS} is the effective distance that oxygen molecules need to diffuse through the asphalt-aggregate matrix.

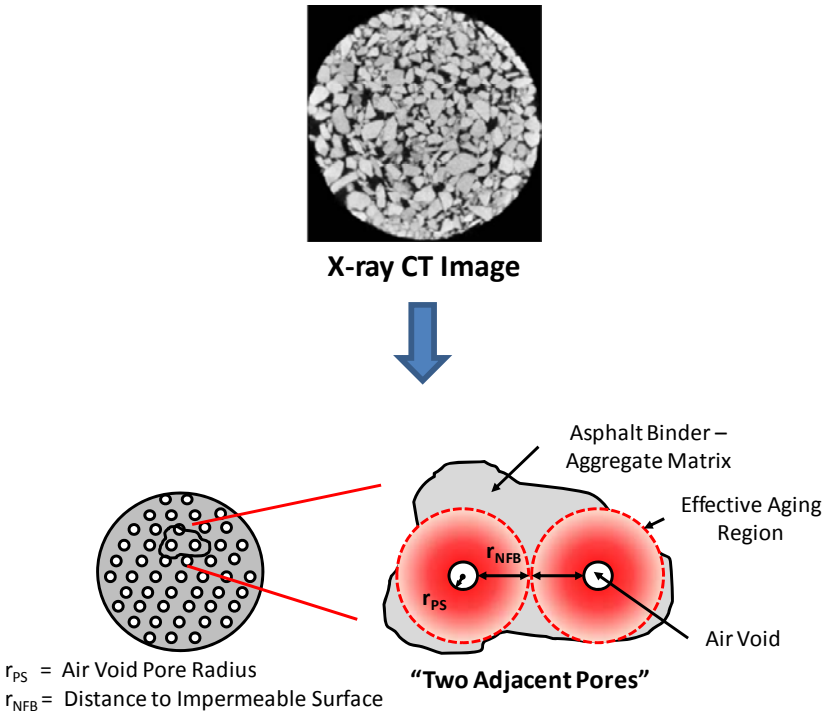

Figure IV-1. Initial Modeling Concept of Asphalt Binder Oxidation in Pavements

A mathematical equation accounting for oxygen diffusion and reaction in a differential volume is shown in Equation IV-1:[61]

$$\left(\frac{\partial C_{O_2}}{\partial t}\right) = -\nabla \cdot N_{O_2} - r_{O_2} \qquad \text{(IV-1)}$$

where, C_{O_2} is the oxygen concentration and r_{O_2} is the rate of oxygen consumption.

In asphalt, the molar flux of oxygen, N_{O_2}, can be expressed by Fick's first law of diffusion as given in Equation IV-2:

$$N_{O_2} = -\mathcal{D}_{O_2} \nabla C_{O_2} \qquad \text{(IV-2)}$$

where, $\mathcal{D}_{O_2}$ is the oxygen diffusivity in asphalt binder.

Lunsford[58] combined the mathematical model of asphalt oxygen diffusion and reaction described above and Fick's law of diffusion to propose a one-dimensional diffusion and reaction model in a flat thin asphalt film. However, to obtain oxygen partial pressure profiles in the pavement oxidation model, the partial differential equation (PDE) system was solved for the oxygen partial pressure as a function of time and distance away the from air void-binder interface in a cylindrical coordinate system. In principle the oxygen partial pressure profile can be used to calculate carbonyl area (CA) and viscosity profiles and histories in the pavement, which then can be combined with an appropriate performance model to estimate pavement durability and performance, taking into account binder oxidative hardening. With this modeling concept, the PDE system and boundary conditions can be written as follows:

$$\left(\frac{\partial P}{\partial t}\right) = \frac{1}{r}\frac{\partial}{\partial r}\left(r\mathcal{D}_{O_2}\frac{\partial P}{\partial r}\right) - \left(\frac{cRT}{h}\right)r_{CA} \tag{IV-3}$$

$\left(\frac{\partial P}{\partial r}\right) = 0$	at	$r = r_{NFB}$	No Flux Boundary
$P = P_{\text{gas}}$	at	$r = r_{PS}$	Air Void Surface
$P = 0$	at	$t = 0$	Initial Condition

where P is oxygen partial pressure, c is an experimental constant, r_{CA} is a rate of carbonyl formation, and h is the Henry's law constant.

In Equation IV-3, $\mathcal{D}_{O_2}$ is an unknown and needs to be estimated. Reid et al.[62] provides a model relating diffusivity to viscosity and temperature as given in Equation IV-4:

$$\mathcal{D}_{O_2} = \mathcal{D}_0\left(\eta_0^*\right)^B \tag{IV-4}$$

In Lunsford's study, $\mathcal{D}_0$ and B, estimated model constants, were estimated and reported.

Lau et al.[5] show that limiting viscosity, η_0^*, and carbonyl content are related by Equation IV-5:

$$\eta_0^* = \exp\{HS \cdot CA + m\} \tag{IV-5}$$

where HS is asphalt hardening susceptibility and m is an experimental parameter. HS and m are functions of temperature. Carbonyl content, CA, represents the level of oxidation of the binder and increases at rate r_{CA} so that the amount of oxidation can be represented by Equation IV-6:

$$CA(t) = \int_0^t r_{CA} d\theta + CA_0 \tag{IV-6}$$

where CA_0 is an integration constant and could be determined from experimental data.

Work has proceeded toward developing a combined heat and mass transport model for reaction of binders in compacted mixtures and pavements. Issues are the relative importance of diffusion and reaction rates in the binder as well as the accessibility of oxygen to the binder from the porous structures of the mixtures. The model that is being developed is conceived to provide oxygen to the binder radially from pores that pass through the mixture. The oxygen diffusivity in this model can be referred to as an effective diffusivity, $\mathcal{D}_e$, which is described as a function of the actual oxygen diffusivity in the asphalt binder, the asphalt volume fraction (ε), and the tortuosity (τ). In this discussion, the asphalt volume fraction is the volume fraction occupied by asphalt binder in the mixture and the tortuosity is the ratio of the oxygen diffusion path to the distance between two air voids. Complicating the model is the presence of aggregate that forces a tortuous path for the oxygen, thereby producing a reduced effective diffusivity. The extent to which diffusion resistance slows the oxidation process relates directly to

the ratio of the oxidation rate to the diffusion rate. The effective diffusivity can be expressed as follows:[63]

$$\mathcal{D}_e = \mathcal{D}_{O_2}\left(\frac{\varepsilon}{\tau}\right) \quad \text{(IV-7)}$$

The model is essential to guiding the efficient and effective use of both laboratory and field mixture aging data for assessing the rate of binder hardening in pavements and its impact on pavement durability.

Results and Discussion

Outputs from Developed Binder Oxidation Model

Typical results from model calculations are shown in Figures IV-2 through IV-5. The binder used for these calculations was an Ampet AC-20. The model cylindrical shell was 1 mm thick, spanning from a radius of 0.5 to 1.5 mm, and aging was simulated at a constant temperature of 333.3 K (60 °C) for 90 days to estimate the effect of aging on viscosity and diffusivity. As also discussed in the previous section, the pore surface (PS) refers to the air void-binder interface, whereas, the no-flux boundary (NFB) refers to the surface of the radius at the half-distance between two adjacent air voids.

Figure IV-2 shows oxygen partial pressure profiles calculated from the model. Oxygen partial pressure at the pore surface is assumed to be the oxygen partial pressure in air (approximately 0.2 atm) with no nitrogen film resistance. Another key assumption for the model calculation was that the oxygen in air channels throughout the pavement depth was replenished from the thermal cycle in the pavement which leads to excessive oxygen for the oxidation reaction. As the oxygen molecules diffuse through the asphalt matrix film, the oxygen concentration at the pore surface is assumed to be constant at approximately 0.2 atm and the concentration decreases across the film thickness toward

the no-flux boundary depending on reaction temperature and the thickness of the asphalt film.

Each solid line of the oxygen pressure profile in Figure IV-2 represents a radial increment of approximately 0.11 mm into the asphalt matrix film. The dotted horizontal line at 0.2 atm symbolizes the radial distance of 0.5 mm (at pore surface). The next solid line below represents the radial distance of 0.61 mm, 0.11 mm into the asphalt matrix film. The pattern continues until, eventually, the oxygen profile line reaches the no-flux boundary at the radial distance of 1.5 mm (the dotted line at the bottom of the oxygen profile). Note that a similar approach to that discussed above can be used to describe the carbonyl area, viscosity, and oxygen diffusivity profiles shown in Figures IV-3 through IV-5.

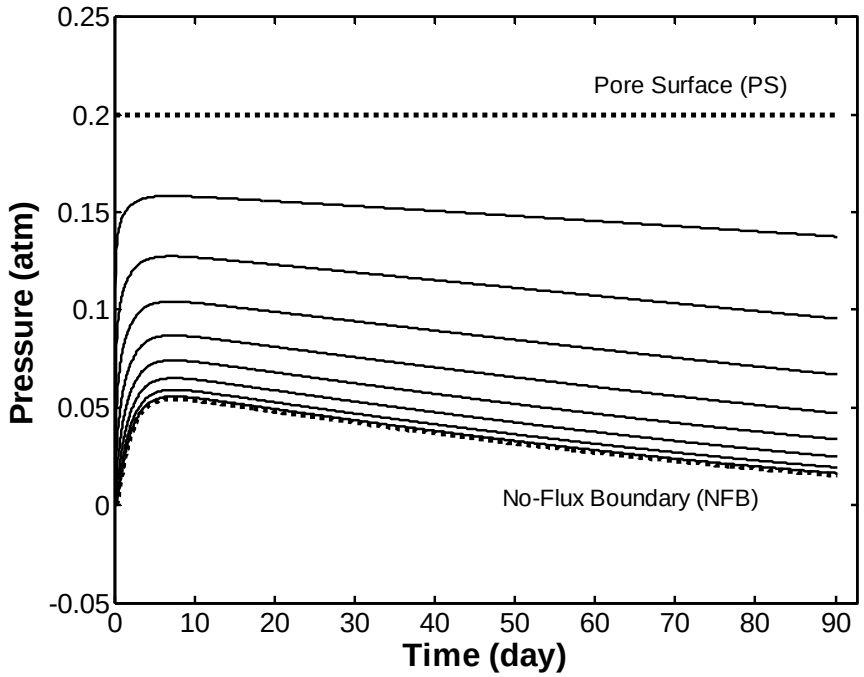

Figure IV-2. Calculated Oxygen Pressure Profile from Binder Oxidation Model

Oxygen molecules that diffuse into the asphalt-aggregate matrix are readily consumed to produce carbonyl compounds that create less soluble asphaltene materials,

which cause the hardening process in asphalt. Figure IV-3 presents the model calculations of carbonyl area that was simultaneously determined by using the resulting pressure profile obtained previously with Equations I-4, IV-4, IV-5, and IV-6.

The carbonyl growth rate follows the relationship given in Equation I-4. Due to higher oxygen concentration in the asphalt matrix, the carbonyl growth rate of the layer closer to the pore surface would be higher than the one closer to the no-flux boundary, where oxygen molecules experience more diffusion resistance in the asphalt-aggregate matrix. As shown in Figure IV-3, the carbonyl growth rate calculated at the pore surface was 0.096 CA/month, whereas the calculate rate at the no-flux boundary was 0.057 CA/month.

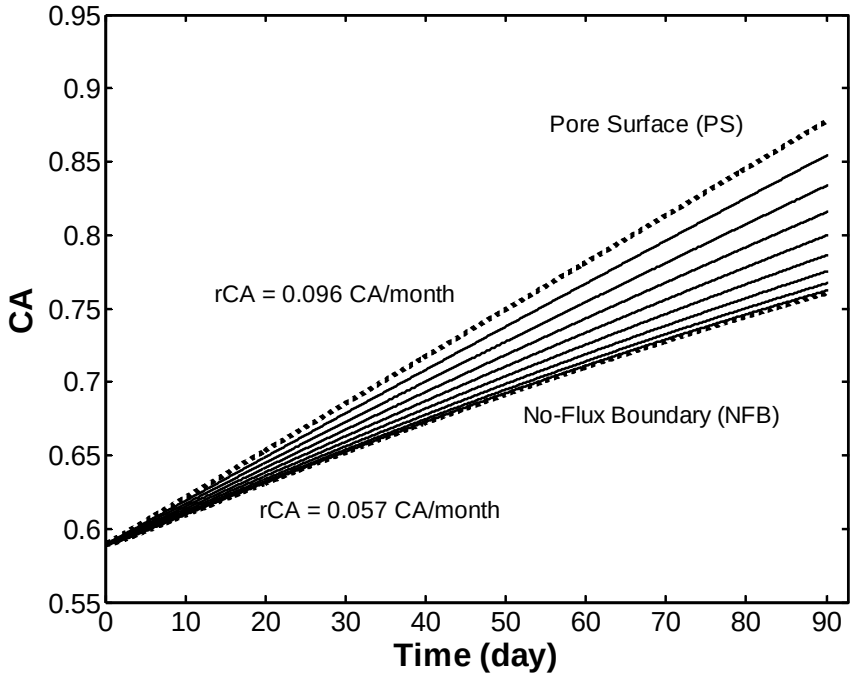

Figure IV-3. Calculated Carbonyl Area from Binder Oxidation Model

The viscosity of asphalt binder calculated from the oxidation model is shown in Figure IV-4. Again, the model calculation for asphalt viscosity (at a reference temperature of 60 °C) follows the mathematical correlation described in Equation IV-5,

where limiting viscosity (η_0^*) is a function of hardening susceptibility (HS), carbonyl area (CA), and model constant (m). Similar to calculated carbonyl area, the viscosity hardening rate at the pore surface was higher than the one at the no-flux boundary due to the higher level of carbonyl area. In this particular example, the viscosity hardening rate at the pore surface was 0.2915 ln(poise)/month, while the rate at the no-flux boundary was 0.1739 ln(poise)/month.

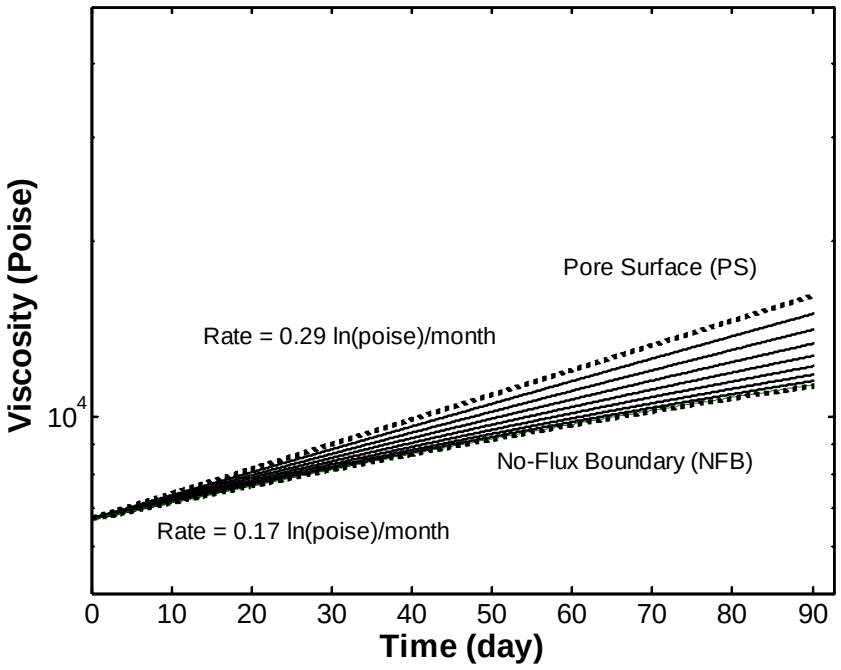

Figure IV-4. Calculated Viscosity from Binder Oxidation Model

The results for calculated oxygen diffusivity in the asphalt-aggregate matrix are presented in Figure IV-5. The oxygen diffusivity in asphalt is a function of limiting binder viscosity at 60 °C as discussed in Equation IV-4. Therefore, the oxygen diffusivity at the pore surface was lower than at the no-flux boundary forming a diffusion resistance region close to the pore surface. Also shown in Figures IV-4 and IV-5, as the asphalt viscosity increases with time due to accumulative oxidation, the overall

oxygen diffusivity would be decreased across the asphalt-aggregate matrix film, which would slowly hinder the oxygen diffusion into the asphalt-aggregate matrix over time.

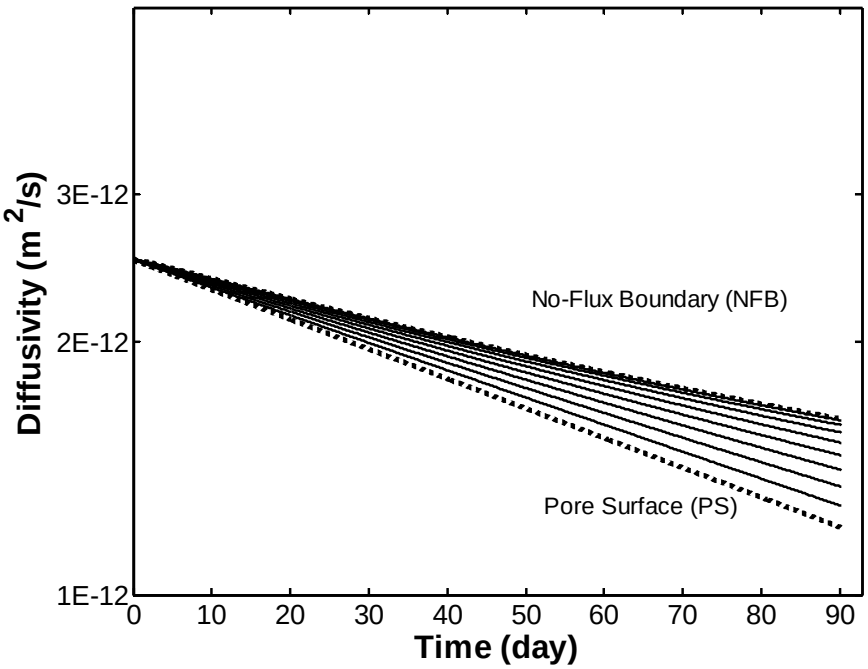

Figure IV-5. Calculated Oxygen Diffusivity from Binder Oxidation Model

Effects of Asphalt Matrix Film Thickness on Oxygen Pressure Profile

Figure IV-6 shows the results of calculated oxygen pressure profile for asphalt-aggregate matrix film thicknesses (Ampet AC-20) from 2 mm to 5 mm, 4 mm, and 3 mm, respectively. Therefore, the thicknesses of asphalt matrix films were 3 mm, 2 mm, and 1 mm, accordingly. In this calculation, the reaction temperature was held constant at 333.3 K (60 °C). Also, the two circles located at the top right corner of the profiles represent the pore surface region and no-flux boundary region as indicated by the arrows.

In this oxygen profile pattern, the asphalt matrix film was divided into 20 equivalent intervals. The solid lines marked by the asterisk (*) on the profile for 3 mm, 2

mm, and 1 mm thickness represent the increments of 0.15 mm, 0.1 mm, and 0.05 mm, respectively.

In these particular calculations, for a 3 mm asphalt matrix film thickness, it can be shown that at the radial distance of approximately 3.05 mm (1.05 mm into the asphalt matrix film, 35 percent of the film thickness), there was a small amount of oxygen molecule diffused past this radial distance. For a 2 mm asphalt matrix film thickness, the radial distance that the oxygen molecule diffused into the film was approximately 4 mm (1 mm into the asphalt film, 50 percent of the film thickness). Finally, for a 1 mm thickness, the oxygen molecule can diffuse through the thickness of asphalt matrix film and reach the no-flux boundary.

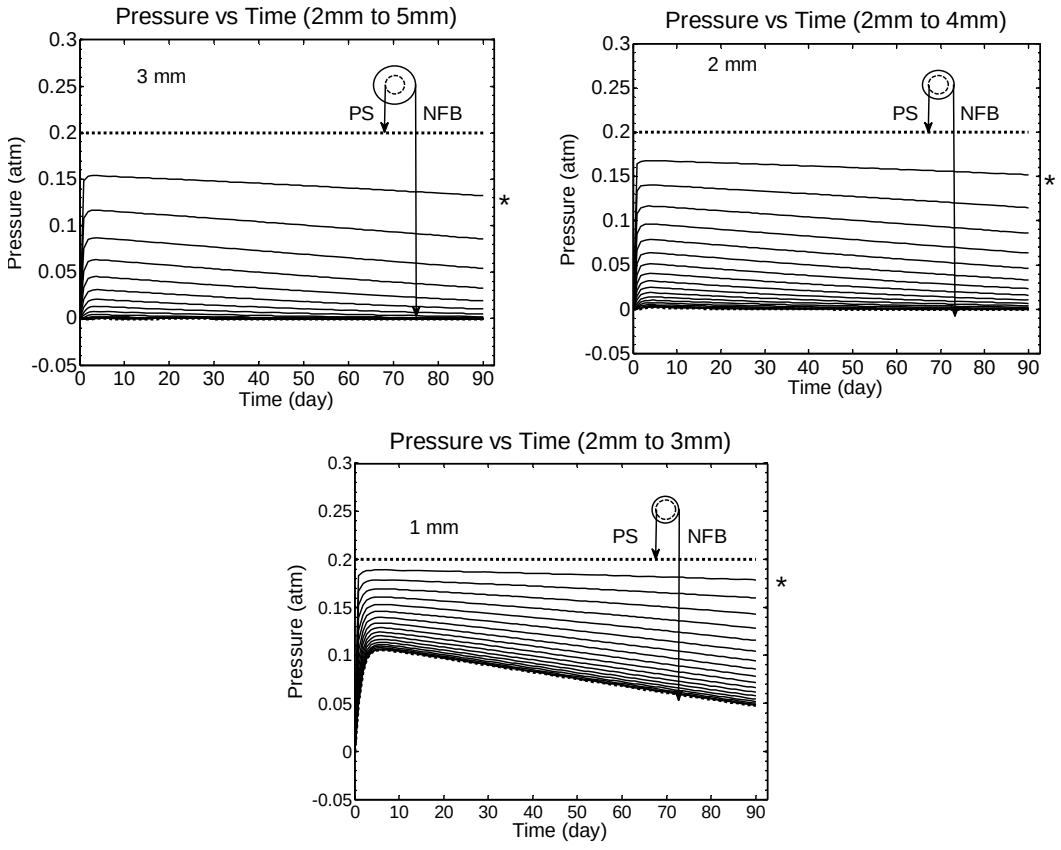

Figure IV-6. Effect of Asphalt Film Thickness on Calculated Oxygen Pressure Profile from Binder Oxidation Model

This effect of the asphalt matrix film thickness on oxidation model calculations shows that the thicker the asphalt matrix film, the harder it gets for the oxygen molecule to diffuse through. The similarity can be drawn that in pavements that have higher binder contents with thicker asphalt films, oxygen diffusion into the binder could be hindered, thus limiting the binder oxidation process.

Effects of Reaction Temperature on Oxygen Pressure Profile

According to the correlation discussed in Equation I-4, it was shown that the rate of carbonyl formation is an exponential function of reaction temperature, T. Figure IV-7 illustrates the oxygen pressure profiles at temperatures of 333 K, 320 K, 310 K, and 300 K, respectively, for 90 days. Note that the asphalt matrix film thickness, in this case, spans from the radial distance of 2 mm to 3 mm with the thickness divided into 20 equivalent intervals. At the higher reaction temperature, oxygen molecules were able to diffuse deeper into the asphalt matrix film. As discussed in Equation IV-4, the limiting viscosity of asphalt binder has a direct relationship with oxygen diffusivity in asphalt binder. The softer binder, which has lower viscosity, would result in higher oxygen diffusivity as shown in the early stage of each oxygen pressure profile where higher temperature caused the binder to soften. However, at the later stage of the model calculation, higher temperature leads to higher rate of oxidation that causes the viscosity of asphalt binder to increase continuously. Consequently, the oxygen diffusivity was quickly decreased and diminished the oxygen diffusion process in the asphalt-aggregate matrix film.

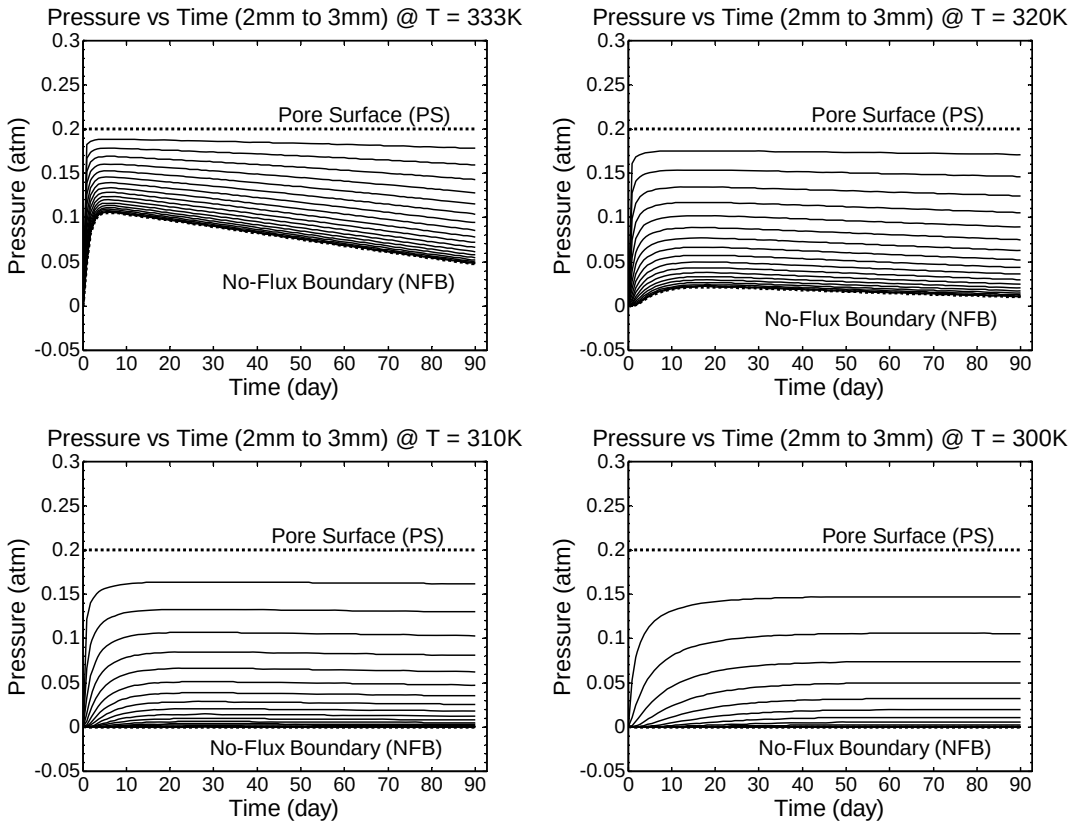

Figure IV-7. Effect of Reaction Temperature on Calculated Oxygen Pressure Profile from Binder Oxidation Model

Model Calculations in Rectangular versus Cylindrical Coordinates

Figure IV-8 shows the model schematic of both models. The previously proposed binder oxidation model in rectangular coordinates[58] was compared with the binder oxidation model developed in this study. The improved binder oxidation model was developed in cylindrical coordinates using a similar concept as in engineered cardiac tissue with parallel channel filled with oxygen carrier.[64] The model provides a more realistic approach to capture the structure of air void channels in the pavement that the oxygen diffuses into the asphalt matrix in the radial direction.

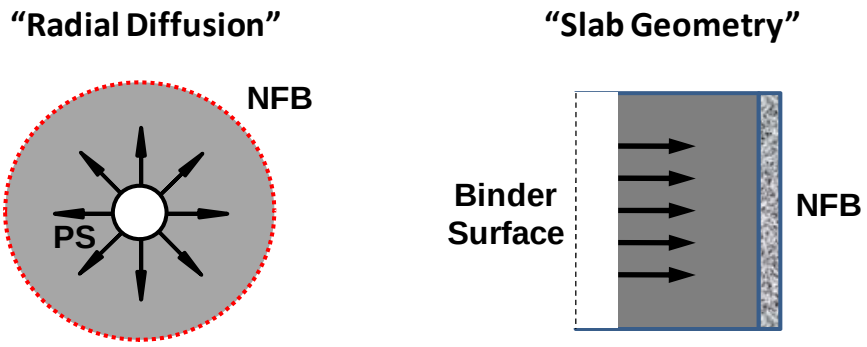

Figure IV-8. Schematic of Improved Binder Oxidation Model Compared with Previously Proposed (Slab) Model

Figure IV-9 shows the comparison between average oxygen pressure inside the asphalt film thickness of both models. The averages were calculated follow the correlation in Equation IV-8:

$$P_{av} = \sum_{i=1}^{n} P_i v_i \qquad \text{(IV-8)}$$

where P_i is the oxygen pressure profile of the interval i, v_i is the volumetric fraction of the interval i, and P_{av} is the average oxygen pressure of the asphalt matrix film. From Figure IV-9, the average pressure from the slab model was substantially higher than the average pressure from the cylindrical model probably because with the same air-asphalt surface area, the oxygen molecule in the cylindrical model had to diffuse into the larger asphalt volume, which would dilute the concentration of oxygen in the asphalt film.

This concept of average pressure profile was used to calculate the average binder properties throughout Chapters V and VI to estimate the overall binder properties in the pavement that can be compared with the extracted binder properties from core samples obtained from the field sections.

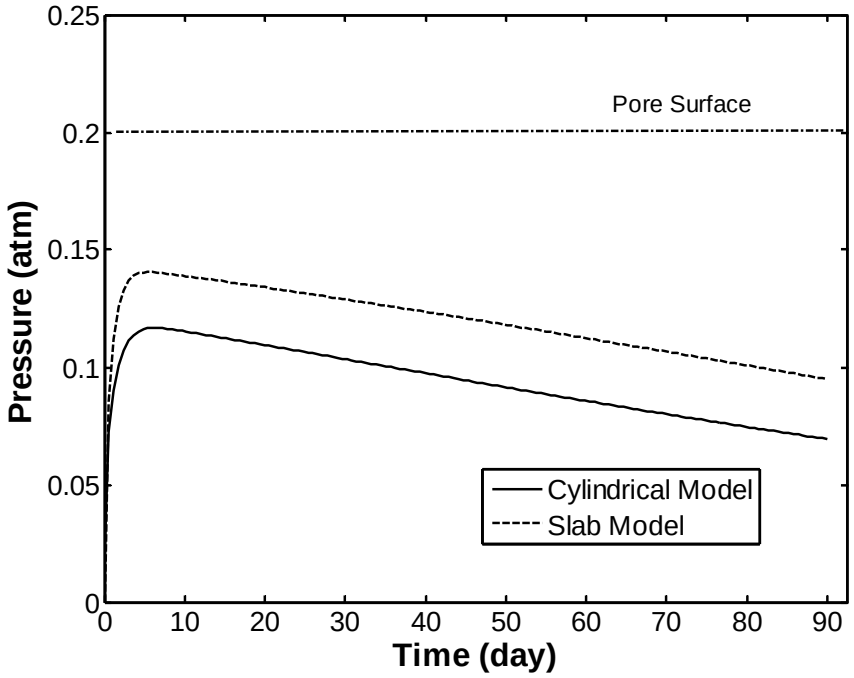

Figure IV-9. The Average Oxygen Pressure Profiles in Asphalt Film: Comparison between Cylindrical and Slab Model Calculation

Conclusions

This chapter provides the description of the development of an improved asphalt binder oxidation model in pavements. The model development was based on three significant processes, which are asphalt binder kinetics, air void characteristics in pavements, and pavement temperature profile. The binder oxidation model was developed in a cylindrical coordinate system to enable the model to capture the air void channel structures in pavement, which, in this case, were pore surface radius (r_{PS}) and no-flux boundary radius (r_{NFB}).

Key outputs from the model calculations were oxygen pressure profile, carbonyl area, limiting viscosity at 60 °C, and oxygen diffusivity in asphalt. These results, especially carbonyl area and limiting viscosity at 60 °C, can be used as indicators to assess the level of oxidation occurring in pavements.

CHAPTER V
A TRANSPORT MODEL OF ASPHALT BINDER OXIDATION IN PAVEMENTS*

Introduction

Field evidence is mounting that asphalt binder oxidization in pavements produces a binder that is more susceptible to thermal and fatigue cracking. While the fundamentals of this oxidation process are fairly well known, predicting quantitatively the rate of oxidation, and as a function of depth in the pavement, is not straightforward. A thermal and oxygen transport model, coupled with binder reaction kinetics, provides the basis for such calculations. A one-dimensional thermal transport model, coupled with site-specific model parameters and recent improvements in the availability of required input climate data, enables calculation of pavement temperatures throughout the year, which then is used in an asphalt binder oxidation and transport model to calculate binder properties in the pavement over time. Calculated binder properties change with depth and time are compared to measurements of binder oxidation in the field.

Asphalt Aging in Pavement

Several studies have been conducted to explore basic binder oxidation chemistry.[5,13,14] From these reports, after an early, fast-rate period, the carbonyl compounds are formed at a rate that is a function of temperature and oxygen partial pressure. Liu et al.[15] also found that the basic carbonyl (CA) reaction rate can generally be described using an Arrhenius expression for temperature variation and pressure dependence as given in Equation V-1.

$$\frac{dCA}{dt} = r_{CA} = AP^{\alpha} \exp\left(\frac{-E_a}{RT}\right) \qquad \text{(V-1)}$$

* Reprinted with permission from "A Transport Model of Asphalt Binder Oxidation in Pavements," by N. Prapaitrakul, R. Han, X. Jin and C.J. Glover. 2009 *International Journal of Road Materials and Pavement Design*, Vol. 10, pp. 95-113. Copyright 2009 by LAVOISIER and ICAM.

where A is the frequency (pre-exponential) factor, P is the absolute oxygen pressure, α is the reaction order with respect to oxygen pressure, E_a is the activation energy, R is the gas constant, and T is the absolute temperature. Values of A, E_a, and α are very asphalt dependent, though A and E_a are generally correlated.[15,17]

Asphalt binder oxidation in pavements has been proven to be an ongoing process throughout a pavement's service life. Also, there is evidence that demonstrates that oxidation occurs through the depth of the pavement and has a significant effect on pavement performance.[3,4] Understanding the nature of the oxidation process and being able to predict the level of oxidation that occurs in pavements as a function of time and depth are critical to pavement design improvement that will provide the greater pavement durability.

The important consequence of asphalt binder oxidation in pavements is oxidative hardening. As non-asphaltene polar aromatic compounds in asphalt binders oxidize, they become asphaltenes, associated species that act like solid particles suspended in the asphalt, thereby producing an increase in asphalt elastic modulus and viscosity.[5,7,9,12] Consequently, the performance of pavements is affected directly by asphalt binder oxidative hardening. Several studies by Walubita et al.[18-21] indicate that oxidation of asphalt binder in pavements leads to a decline in pavement fatigue resistance.

Also, low levels of accessible air voids in pavements potentially relate to binder oxidation.[22] As they report, when pavements have sufficiently high accessible air voids (4 percent or greater), the oxidation rate is largely determined by the temperature in the pavement. On the other hand, when the accessible air voids in the pavement is considerably lower (2 percent or less), the hardening rate of binders in pavements is reduced significantly.

In order to understand the complex pavement asphalt oxidation process, researchers have analyzed asphalt samples and proposed empirical asphalt oxidation (aging) models.[5,59,60] However, these proposed models do not include the effect of oxygen transport limitations (diffusion) into the asphalt binder. Lunsford[58] proposed a preliminary oxidation model with the oxygen diffusion effect included. However, the

study used approximate values for diffusivity and did not include the effect of fines and aggregate on diffusion. In addition, previous work has not implemented a pavement temperature model that provides temperature as a function of depth. Thus a thermal and oxygen transport model, necessary for accurate predictions of binder oxidation in pavements, has not yet been developed.

Pavement Temperature Prediction Model

One key environmental factor that influences asphalt pavement design and performance is pavement temperature, which varies with pavement site, time (day and seasonal), and depth. Accurate representation of pavement temperature is extremely important, particularly in predicting pavement performance such as thermal cracking and oxidative aging, issues that are highly sensitive to pavement temperature. The reaction kinetics of asphalt oxidation follow an Arrhenius activation energy relation; oxidation rates decrease exponentially with increasing inverse absolute temperature.[10] Thermal stress induced by rapid low-temperature changes has been widely accepted as the main cause of thermal cracking of asphalt pavement.

Many measurements of pavement temperature variations over time and depth have been reported in the literature. Also, fundamental early models of heat transfer in pavements, involving shortwave solar radiation, down-welling and upwelling long-wave radiation, and convective heat transfer at pavement surfaces and heat conduction inside the pavement have been thoroughly discussed.[65,66,67] Following these endeavors, a one-dimensional coupled heat and moisture simulation model, the enhanced integrated climate model (EICM), was developed and later integrated into the current mechanistic empirical pavement design guide (MEPDG) to couple pavement design with modeled pavement temperature.[68]

The model uses a finite difference approximation for calculating heat conduction within the pavement and underlying layers, subject to heat fluxes at the surface (shortwave solar radiation, long-wave radiation, and convective heat transfer) and a

constant-temperature boundary condition well below the pavement. Using required climatic input data including solar radiation, ambient temperature, and wind speed and constant model parameters such as albedo, emissivity, and thermal diffusivity, the model is solved numerically to obtain temperature as a function of time and depth.

Although temperatures predicted with the EICM model satisfy pavement design needs in general, there have been some large errors when compared to measured pavement temperature.[69] These errors are most likely caused by several factors: the assumption that heat fluxes at the pavement surface are exactly balanced by conduction into the ground well below the surface, and inaccuracy of climatic data (especially calculated solar radiation), plus the assumptions of the constant temperature boundary condition and site-independent model parameter values.

Recently, significant improvement over the EICM model has been achieved by several groups using a similar one-dimensional heat transfer model, but with an unsteady-state surface heat flux boundary condition, measured model input data, and site-specific model parameters that were optimized based on measured pavement temperatures.[70,71,72]

Research Objectives

The objective of this study is to develop an improved model to predict the oxidation rate of binders in pavements with the input of binder kinetics data, temperature profile of the pavement, and mixture characteristics such as average distance between air void pores. The specific objectives of this study are

- to analyze air void characteristics in pavements to categorize the mixture parameters used in this study;
- to improve the existing oxidation model based on the knowledge of oxidation kinetics, air void characteristics in pavement, oxygen diffusion into asphalt binders, and improved pavement temperature models;

- to estimate important parameters of the proposed oxidation model by using field oxidative aging data; and
- to develop a protocol and procedures for the proposed oxidation model to estimate real pavement oxidation rates using binder kinetics, oxygen diffusivity, pavement temperature profiles, and air void characteristics of the pavements.

Methodology

Analyzing Air Void Structure in the Pavement

A crucial element of the binder oxidation model developed in this study is the influence of accessible air voids on the pavement oxidation process. Cores obtained from field sites were analyzed for air voids (either by the Corelok® or the saturated surface dry methods-SSD), interconnected air voids (by X-ray CT), or accessible air voids (by Corelok® or SSD). Corelok® operating procedures can be found in the Operator's Guide[49] Then the binder was extracted and recovered using methodologies developed by the researchers.[28,50,51,52,53] The recovered binder was then analyzed for oxidation by infrared spectroscopy (FT-IR) and for physical properties by dynamic shear rheometry (DSR) to provide the binder aging and hardening rates corresponding to level of air voids in the pavements.

Another important component to verify the oxidation model is the air voids characteristic of pavement samples. X-ray CT and image analysis techniques are used to examine the internal microstructure of HMAC mixtures, including air void (AV) distribution and interconnectivity and binder content and distribution in terms of film thickness. These factors are some of the HMAC mixture parameters to be identified in terms of the role they play in the aging mechanism. X-ray CT is a nondestructive technique used to visualize the interior characteristics of opaque objects. An X-ray source emits a beam of known intensity through the specimen, and a detector on the opposite side of the specimen measures the attenuated beam intensity. The specimen

rotates 360° with respect to its center and moves at a specific fixed vertical interval to enable evaluation of the entire specimen volume. Then, a macro developed using the IPBasic capabilities of Image-Pro® Plus software can be used to process and analyze the X-ray CT images[41] in terms of air void size, number, and average overall percent. Based on a user-input grayscale threshold, the macro transforms the original images into black-and-white compositions with black representing AV and white representing the solid materials (binder and aggregate). The appropriate threshold value is obtained by matching the measured average percent AV to that output by the macro.

CoreLok® is used for determining total air voids of core specimens as a necessary calibration of grayscale for the X-ray CT method. As validation of the X-ray CT method, CoreLok® has been used to determine accessible air voids (AAV) (those that water can penetrate when the CoreLok® vacuum bag is opened underwater).

Binder Oxidation Model Development

The model proposed by Lunsford is a one-dimensional thin-film geometry in Cartesian coordinates. In addition, this model does not include the effect of air voids and mixture morphology on the oxidation rate determination.

In order to understand oxidation phenomena in pavements, an improved model to predict the oxidation rate with the input of binder kinetics data, temperature profile of the pavement, and mixture characteristics was developed in this study.

The oxygen transport limitations are also important in establishing binder hardening rates in pavements. If the interconnected (or accessible) air voids are sufficiently low, then delivery of oxygen to the binder is hindered.

An improved pavement oxidation transport model was based on three interlinked processes: 1) diffusion of oxygen into the asphalt binder mastic in the pavement, 2) heat transfer into the pavement that results in temperature variations with depth and time, and 3) asphalt binder oxidation, which is a function of oxygen concentration and temperature in the binder. A fourth issue that affects the oxygen transport and concentration is the air

voids distribution in the mixture because it affects the availability of oxygen to the binder. The diffusion process is coupled to both temperature and the level of oxidation because both of these factors affect oxygen diffusivity.

The concept of approximating the binder film in the pavement as a thin film is probably reasonable for high air voids content where there are a large number of pores passing through the pavement so that the distance from any pore to the binder, even to the farthest binder away, is not very far. A more realistic model for a reduced number of air voids might be a cylindrical model that assumes that the oxygen diffuses from the pore in a radial direction into a cylindrical shell of binder (Figure V-1). In this case, the relevant parameter would be the thickness of this cylindrical shell, relative to the diameter of the pore containing the air. The smaller the air voids, the greater the ratio of this binder shell to the pore diameter and thus the more time required for oxygen to diffuse through the binder.

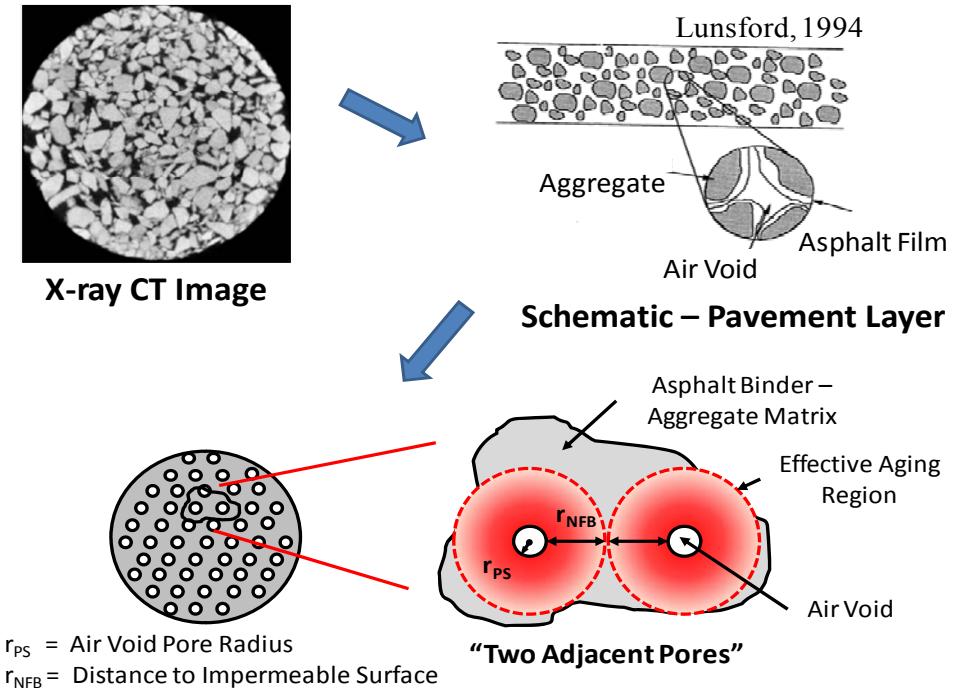

Figure V-1. Modeling Concept of Asphalt Binder Oxidation in Pavements

A mathematical equation accounting for oxygen diffusion and reaction in a differential volume is shown in Equation V-2.[61]

$$\left(\frac{\partial C_{O_2}}{\partial t}\right) = -\nabla \cdot N_{O_2} - r_{O_2} \tag{V-2}$$

In asphalt, the molar flux of oxygen, N_{O_2}, can be expressed by Fick's first law of diffusion as given in Equation V-3.

$$N_{O_2} = -\mathcal{D}_{O_2} \nabla C_{O_2} \tag{V-3}$$

Lunsford[58] combined the mathematical model of asphalt oxygen diffusion and reaction described above and Fick's law of diffusion to propose a one-dimensional

diffusion and reaction model in a flat thin asphalt film. However, to obtain oxygen partial pressure profiles in the pavement oxidation model, the PDE system was solved for the oxygen partial pressure as a function of time and distance away the from air void-binder interface in a cylindrical coordinate system. In principle the oxygen partial pressure profile can be used to calculate CA and viscosity profiles and histories in the pavement, which then can be combined with an appropriate performance model to estimate pavement durability and performance, taking into account binder oxidative hardening. With this modeling concept, the PDE system and boundary conditions can be written as follows;

$$\left(\frac{\partial P}{\partial t}\right) = \frac{1}{r}\frac{\partial}{\partial r}\left(r\mathcal{D}_{O_2}\frac{\partial P}{\partial r}\right) - \left(\frac{cRT}{h}\right)r_{CA} \tag{V-4}$$

$\left(\frac{\partial P}{\partial r}\right) = 0$	at	$r = r_{NFB}$	No Flux Boundary
$P = P_{\text{gas}}$	at	$r = r_{PS}$	Air Void Surface
$P = 0$	at	$t = 0$	Initial Condition

where c is an experimental constant and h is the Henry's law constant.

In Equation V-4, $\mathcal{D}_{O_2}$ is an unknown and needs to be estimated. Reid et al.[62] provides a model relating diffusivity to viscosity and temperature as given in Equation V-5.

$$\mathcal{D}_{O_2} = \mathcal{D}_0\left(\eta_0^*\right)^B \tag{V-5}$$

In Lunsford's study, $\mathcal{D}_0$ and B were estimated and reported.

Lau et al.[5] show that viscosity and carbonyl content are related by Equation V-6.

$$\eta_0^* = \exp\{HS \cdot CA + m\} \tag{V-6}$$

where *HS* is asphalt hardening susceptibility and *m* is an experimental parameter. *HS* and *m* are functions of temperature. Carbonyl content, CA, represents the level of oxidation of the binder and increases at rate r_{CA} so that the amount of oxidation can be represented by Equation V-7.

$$CA(t) = \int_0^t r_{CA} d\theta + CA_0 \tag{V-7}$$

where CA_0 is an integration constant and could be determined from experimental data.

Work has proceeded toward developing a combined heat and mass transport model for reaction of binders in compacted mixtures and pavements. Issues are the relative importance of diffusion and reaction rates in the binder as well as the accessibility of oxygen to the binder from the porous structures of the mixtures. The model that is being developed is conceived to provide oxygen to the binder radially from pores that pass through the mixture. The oxygen diffusivity in this model can be referred to as an effective diffusivity, $\mathcal{D}_e$, which is described as a function of the actual oxygen diffusivity in the asphalt binder, the asphalt volume fraction (ε), and the tortuosity (τ). In this discussion, the asphalt volume fraction is the volume fraction occupied by asphalt binder in the mixture and the tortuosity is the ratio of the oxygen diffusion path to the distance between two air voids. Complicating the model is the presence of aggregate that forces a tortuous path for the oxygen, thereby producing a reduced effective diffusivity. The extent to which diffusion resistance slows the oxidation process relates directly to the ratio of the oxidation rate to the diffusion rate. The effective diffusivity can be expressed as follows:[63]

$$\mathcal{D}_e = \mathcal{D}_{O_2}\left(\frac{\varepsilon}{\tau}\right) \tag{V-8}$$

The model is essential to guiding the efficient and effective use of both laboratory and field mixture aging data for assessing the rate of binder hardening in pavements and its impact on pavement durability.

Results and Discussion

Outputs from the Binder Oxidation Model

Typical results from model calculations are shown in Figure V-2. The binder used for these calculations is an Ampet AC-20. The model cylindrical shell was 1 mm thick, spanning from a radius of 0.5 to 1.5 mm, and aging was simulated at a constant temperature of 333.3 K for 90 days to estimate the size of the effect of aging on viscosity and diffusivity. The pore surface (PS) refers to the air void-binder interface, whereas the no-flux boundary (NFB) refers to the surface of the radius at the half-distance between two adjacent air voids.

Shown in the figure are carbonyl area and viscosity calculation, which were predicted to increase with aging time, and diffusivity, which is shown to decrease with aging time as the binder hardens.

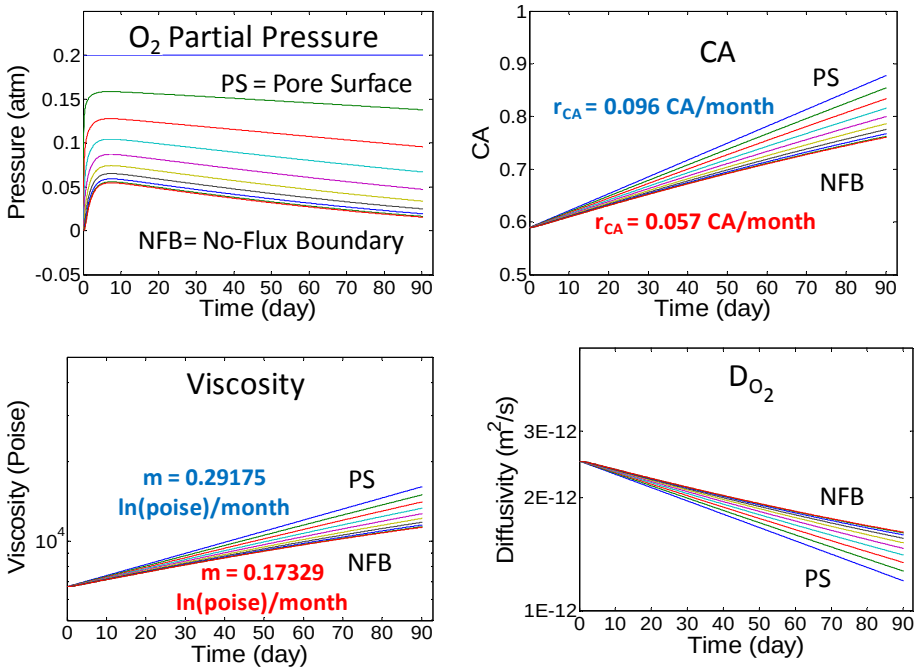

Figure V-2. Results from Transport Model of Binder Oxidation in Pavements for Binder Thickness of 1 mm at 333.3 K

Binder oxidation rates from field pavements in Texas (not shown) compare reasonably well to the calculated oxidation rates. However, additional field data and model calculation comparisons are required to adequately validate the oxidation model.

Model Parameter Estimation

This section discusses a parameter estimation process that may be used to determine unknown oxidation model parameters from known measured parameters together with measured environmental room (ER) mixture aging rates. However, due to the limited kinetics data and air void characteristics for the ER samples, ER aging rates were compared to mixture aging rates calculated using the oxidation kinetics parameters from previous research (and thus for a different binder) to demonstrate the model parameter estimation methodology and a potential important application of the model.

In the parameter estimation process, the results from oxidation model calculations were compared to asphalt mixture (PG 70-22) aging in the ER, at 60 °C and 25 percent humidity. Three laboratory mixture replicates were aged in the ER for 9 months and one core was sampled every 3 months. Then, carbonyl area of asphalt binder of each core, which was extracted and recovered by the method previously mentioned, was measured and the CA aging rate was calculated. The asphalt aging rate obtained from environmental room aging exhibits a linear relationship as shown in Figure V-3.

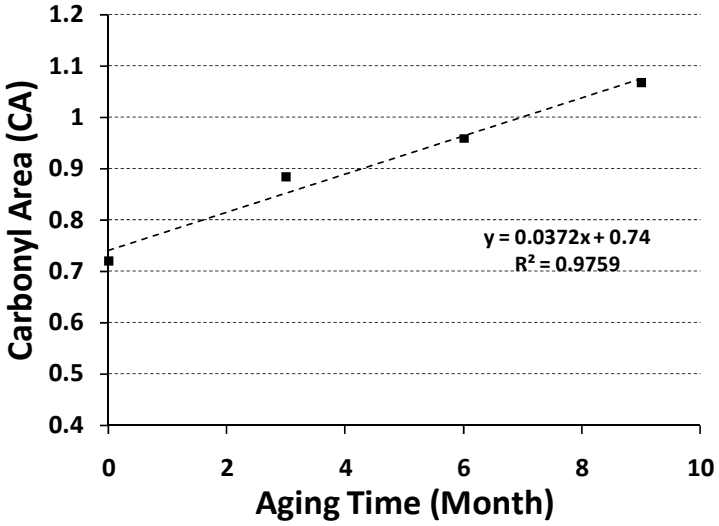

Figure V-3. Carbonyl Area Growth of Asphalt Mixture in Environmental Room (ER) Aging

The aging rate obtained was then used to compare to the model calculations, in a least-squares optimization sense. In this study, parameter estimation is categorized into two cases.

Case 1: Known mixture air void characteristics, unknown asphalt kinetic parameters

Additional parameters needed for the optimization process are the air void characteristics of asphalt mixtures, which are the average air void radius, r_{PS}, and the average half-distance between two air voids (the average distance to the no-flux boundary), r_{NFB}. The difference between r_{NFB} and r_{PS} determines the maximum distance oxygen molecules travel in the asphalt film, which directly affects the oxygen diffusion. The air void spacing can be observed by X-ray CT scan, but the accuracy of the measurement depends on the scanning resolution of the equipment, which can be a time- and resource-consuming process for higher resolution. Figure V-4 shows X-ray CT image analysis results of air void radius distribution with depth and the location of air voids at a single depth of the top layer of the core obtained from Highway US 59, Yoakum District, Texas. From the data, r_{PS} and r_{NFB} through the depth of the core were estimated to be approximately 0.87 mm and 1.27 mm, respectively.

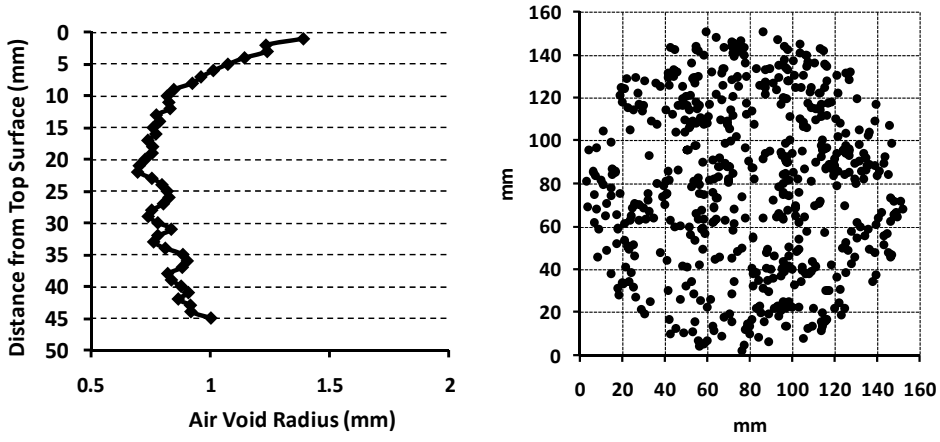

Figure V-4. Air Void Radius Distribution and Air Void Coordinates

From mixture design information, the asphalt volume fraction in the mixture of this study, which is the difference between voids in mineral aggregate (VMA) and air void content in the mixture, was reported to be 0.0735. In this case, the unknown

parameters in PDE, Equation V-4, were the binder oxidation kinetics pre-exponential factor (A), activation energy (E_a), and reaction order (α) and the mixture tortuosity (τ). The initial values used for parameter estimation were the Ampet AC-20 binder kinetics data reported by Lunsford (1994). After the least-squares parameter estimation process, the results for A, E_a, α, and τ were estimated to be 1.667×10^5 CA/s atm$^{\alpha}$, 81.1 kJ/mol, 0.285, and 2.33, respectively, as shown in Figure V-5. With these estimated values, the least-squares difference between the aging rate of model calculation and ER aging was 0.0057. In addition, these estimated kinetics parameters were within the range of kinetics data for asphalt binders reported by Lunsford.[58]

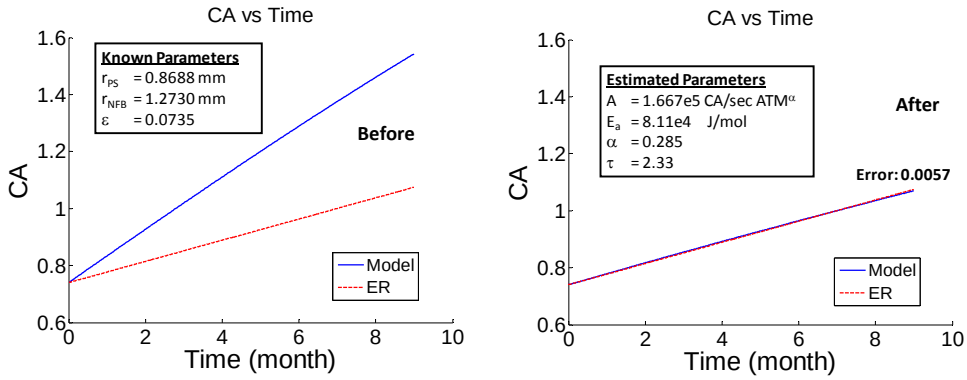

Figure V-5. Oxidation Model versus ER Aging Rate before and after Parameter Optimization Process: Case 1

The initial values of A, E_a, α, and τ used in this estimation were 3.105×10^4 CA/s atm$^{\alpha}$, 74.8 kJ/mol, 0.285, and 1, respectively. In order to decrease the carbonyl growth rate of the model to match the ER aging rate, A, E_a, and τ were adjusted to higher values. However, α remained the same as the initial value.

As demonstrated in this estimation process, researchers can use this approach to estimate kinetic information for an asphalt binder when the mixture information and the ER aging rate are known. Then, these estimated kinetics data together with mixture

characteristic can be used to calculate field aging rates using the pavement temperature profile.

Case 2: Known asphalt kinetic parameters, unknown mixture air void characteristics

In some cases, all asphalt kinetics data were known, but the mixture air void characteristics data were not available. Even though air void data can be determined with an X-ray CT scan, the machine might not be available for all laboratories or district locations. To be able to estimate the air void characteristics without X-ray CT scanning will enable subsequent asphalt binder oxidation rate calculations in a pavement, when used with the actual real pavement temperature profile and ER aging of field cores.

Figure V-6 shows the comparison between oxidation rate from model calculation and ER aging. The missing data, in this case, were mixture characteristic data: namely, r_{PS}, r_{NFB}, ε, and τ. As for the binder kinetics data, Coastal AC-20 data reported from Lunsford (1994) were used in oxidation model calculation. After least-squares estimation process, which had an error of 0.0017, the estimated values of r_{PS}, r_{NFB}, ε, and τ were 0.1375 mm, 3.875 mm, 0.1667, and 2.5, respectively.

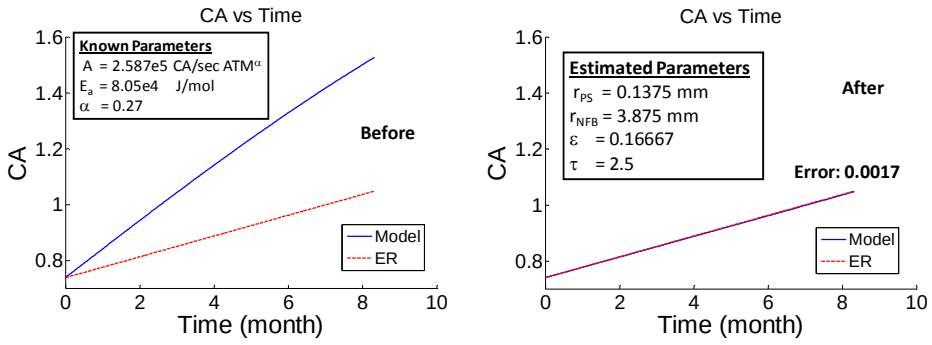

Figure V-6. Oxidation Model versus ER Aging Rate before and after Parameter Optimization Process: Case 2

The kinetics data of Coastal AC-20 used in this calculation had values of A, E_a, and α as 2.587×10^5 CA/s atm$^{\alpha}$, 8.05 kJ/mol, and 0.266[58] On the other hand, the initial values of mixture characteristic data used in the estimation process were the data for typical dense-graded mixtures obtained from the X-ray CT image analysis process. The set of initial values were 0.87 mm, 1.27 mm, 1, and 1 for r_{PS}, r_{NFB}, ε, and τ, respectively. From the estimation process, as τ and the difference between r_{NFB} and r_{PS} increased, indicating a thicker asphalt film and a longer path for oxygen to travel, the oxidation rate calculated from the model decreased. Also, as ε decreased, the oxidation rate decreased accordingly.

The parameter estimation process and results discussed in the above section were important examples of how to use the oxidation model at constant temperature to estimate the unknown model parameters. Although the asphalt kinetics data, mixture air void characteristics, and the ER mixture sample were not perfectly matched, the above cases demonstrate the capabilities of parameter estimation coupled with the binder oxidation model. Further analysis using complete and corresponding binder and mixture data will be used to more accurately assess and improve the transport model.

Binder Oxidation Model Calculation Using Temperature Profile from Pavement Temperature Prediction Model

An accurate model for pavement temperature prediction is critical to the study of pavement material properties as well as their changes over time. For example, for the prediction of both binder oxidation and thermal cracking in pavements, pavement temperature as a function of time and depth is crucial. A one-dimensional numerical model has been developed to predict pavement temperature based on heat transfer fundamentals.[65,66,67] The model employs commonly available hourly solar radiation, daily average wind speed, and imputed hourly air temperature based on site-specific daily pattern derived using time series analysis as climate input data. Three key site-specific model parameters were identified and the national distribution of their values

correlate with climatic patterns, suggesting possible interpolation strategies based on climate. The temperature model, proposed data sources, and methods provided calculations that agreed well with experimental measurements, suggesting a general approach to predicting pavement temperatures nationwide with acceptable accuracy.

Figure V-7 shows the hourly pavement temperature profiles generated by the pavement temperature prediction model for State Highway 21 located in Bryan, Texas. Temperature histories for three depths, 20, 80, and 160 mm from the pavement surface, are shown for July 1994. Pavement temperatures were estimated for the entire one-year period of 1994 and used in the transport oxidation model to estimate binder oxidation throughout the year as a function of depth.

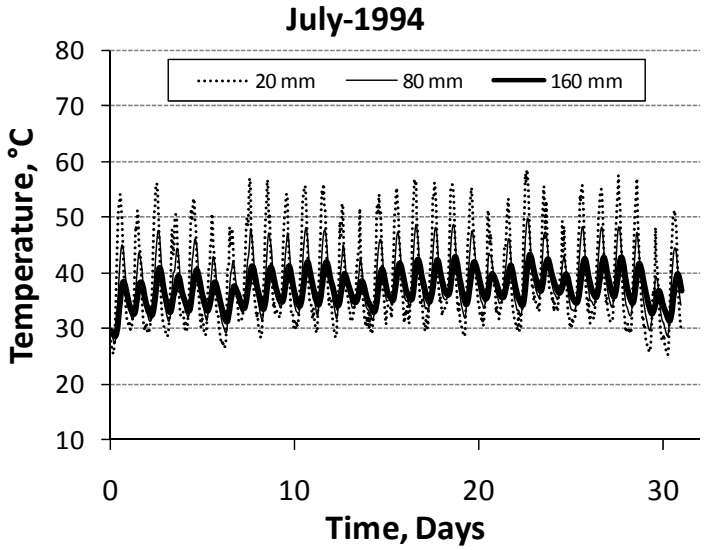

Figure V-7. Pavement Temperature Profile for SH-21 in Bryan, Texas, during July 1994

Table V-1 summarizes carbonyl area for each of the depths collected at various stations of State Highway 21 (SH-21 between Bryan and Caldwell) from 1989 to 1996.[3] Aging rates of binder from each depth also are shown in the table. Approximately, overall aging rates of top and bottom lifts for SH-21 can be estimated to be 0.05 CA/year. Glover et al.[3] also reported that asphalt binder used to construct SH-21

pavement was Exxon AC-20, whose binder kinetics data were reported by Domke et al.[17] However, the information for mixture air void characteristics was not available for this SH-21 pavement. The best available data for mixture air void characteristics at this time was the data from X-ray CT analysis of a comparable dense-graded mixture from US 59 pavement in Yoakum, Texas.

Each temperature profile as shown in Figure V-7 was used as reaction temperature in binder oxidation model calculation, Equation V-4. The carbonyl area growth of Exxon AC-20 for one-year period in pavement, from January to December, at various depths is shown in Figure V-8. According to the oxidation model calculation, asphalt binder aging rates in the pavement were rather slow during spring and winter. On the other hand, the rate increased significantly during the summer due to higher pavement temperatures, as would be expected.

Table V-1. Carbonyl Area of the Recovered Binder (Exxon AC-20) from SH-21, Texas

Station	Lifts	Depth Below Surface (in.)	Carbonyl Area			Aging rate (CA/Year)
			1989	1992	1996	
1277	Top	0 - 2	0.94	-	1.31	**0.053**
	Bottom	4 - 6	0.88	-	1.27	**0.056**
1394	Top	0 - 2	0.88	1.04	-	**0.053**
	Bottom	4 - 6	1.11	1.25	-	**0.047**

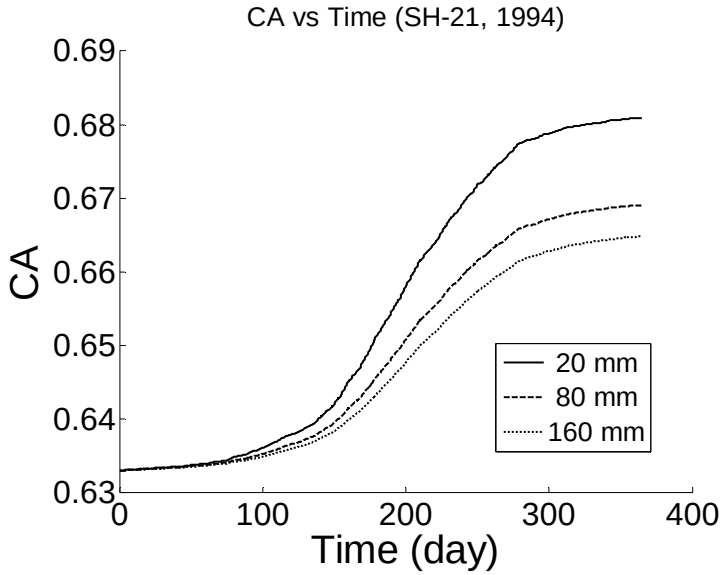

Figure V-8. Calculated Carbonyl Area from Binder Oxidation Model at Various Depths

Also from Figure V-8, after one year, the carbonyl area of binder in each depth increased from the initial carbonyl area of 0.633 to 0.681, 0.669, and 0.665 for the depths of 20, 80, and 160 mm, respectively. Thus the aging rates of Exxon AC-20 are 0.048, 0.036, and 0.032 CA/year at the corresponding depths. By comparing these aging rates with the data reported in Table V-1, the aging rate from top lifts agreed quite well with the model calculation, whereas the bottom lifts showed higher aging rates than values calculated by the model. The reason why the bottom lift calculation did not match the field measurement might come from the fact that mixture air void characteristic through the depth of pavement used in the model could be slightly different from actual SH-21 pavement structure. X-ray CT analysis should be performed on the original SH-21 pavement core to obtain a better match of mixture air void characteristics. However, with limited availability of air void characteristic data, the substituted values were able to produce reasonable aging rates to demonstrate the use of the binder oxidation model together with the pavement temperature prediction model to calculate the carbonyl area

growth of asphalt binder in selected pavement. Further mixture data would certainly improve the accuracy of the binder oxidation model prediction.

Conclusions

In this study, a binder oxidation model for pavements, which includes the effect of oxygen diffusion and pavement temperature as a function of time and depth, was developed in a cylindrical coordinate system. Input components for the oxidation model are pavement temperature profile, binder oxidation kinetics and diffusion parameters, and mixture air void characteristics. The one-dimensional thermal transport model, coupled with site-specific model parameters and recent improvements in the availability of required input climate data, enables calculation of pavement temperatures throughout the year to a surprisingly reliable extent. The asphalt binder kinetics data were gathered from existing literature and the mixture air void characteristics were obtained using X-ray CT image analysis. However, when either binder kinetics or mixture parameters were missing, a least-squares parameter estimation procedure at constant temperature can be applied to obtain reasonable parameter values. Despite the necessity of acquiring additional binder and mixture data, the binder oxidation model with available input data to date was able to calculate average asphalt aging rate for a pavement reasonably close to the actual average oxidation rate observed in the field.

The essential significance of this study is to introduce a mixture binder oxidation model as a cornerstone for subsequent research on asphalt oxidation in pavements and to demonstrate its applicability. Additional binder and mixture data are needed to assess the accuracy and validity of the model. Such a model is a critically important tool for pavement design and improvement and for maintenance scheduling.

CHAPTER VI
ANALYSIS OF THE EFFECT OF CLIMATE ZONES ON ASPHALT OXIDATION RATE IN PAVEMENTS

Introduction

Weather climate patterns throughout the country, even climates within Texas, can differ significantly. These different climates cause significant differences in pavement temperature profiles, which are key factors that influence the behavior of asphalt binder and pavement performance. For different pavement temperature profiles, asphalt binders in pavements experience unequal amounts of binder oxidation over time. Pavement engineers must understand these differences in order to design pavements to better withstand the binder hardening that occurs during its service life. In general, different pavement temperature profiles may lead to different binder hardening rates in pavements. Therefore, in pavement design, in order to obtain the desired level of pavement performance, the asphalt binders with appropriate rheological properties must be selected to compensate for binder hardening due to the diversity of climate zones. Unfortunately, such a selection study is a time- and resource-consuming process. A simple change in pavement designs, for example a change in binder PG grade, might take years in the field in order to detect any significant change in asphalt binder properties in the pavements. To overcome this major problem, integration of the asphalt binder oxidation model with a pavement temperature prediction model is critical to the study of binder oxidation in pavements under various climate conditions and thus to pavement performance modeling and maintenance planning.

In this chapter, the calculated binder oxidation rates of pavements in various climate locations are presented. The calculations are based on the binder kinetics information previously collected, the estimated pavement parameters from Chapter V, and predicted pavement temperature profiles. The calculated results show that the

climate zones play an important role in asphalt binder oxidation in pavements and therefore directly impact pavement performance.

Research Objectives

The purpose of the study presented in this chapter was to understand the effects of the climate zones on asphalt binder oxidation rates in the pavements. The temperature profiles throughout the United States and Texas were generated using a pavement temperature prediction model that has site-specific parameters in the binder oxidation model. The oxidation rates were calculated from the model as functions of time and pavement depth, keeping all pavement parameters constant (except climate) and then compared among themselves to determine the sole effect of the climate zone on binder oxidation rate. Then the calculated aging rates from the integrated model were compared to binder aging rates measured for actual pavements in Texas to verify that the calculated values were reasonable.

Methodology

Two model calculations that were used in this chapter were the pavement binder oxidation model and pavement temperature prediction model. The process of the calculations is shown in Figure VI-1. There are three key groups of input parameters: pavement temperature, pavement physical information, and asphalt binder information. First, the pavement temperature profiles of the selected pavement sites were generated to be used in pavement oxidation model. Then, the important parameters of the oxidation model were determined according to the methods discussed previously in Chapters IV and V. Using these model parameters and pavement temperature information, the asphalt aging rates were calculated and then compared to determine the effect of different climate zones on pavement oxidation. The calculation procedures for both the pavement

temperature prediction model and the pavement oxidation model are described substantially.

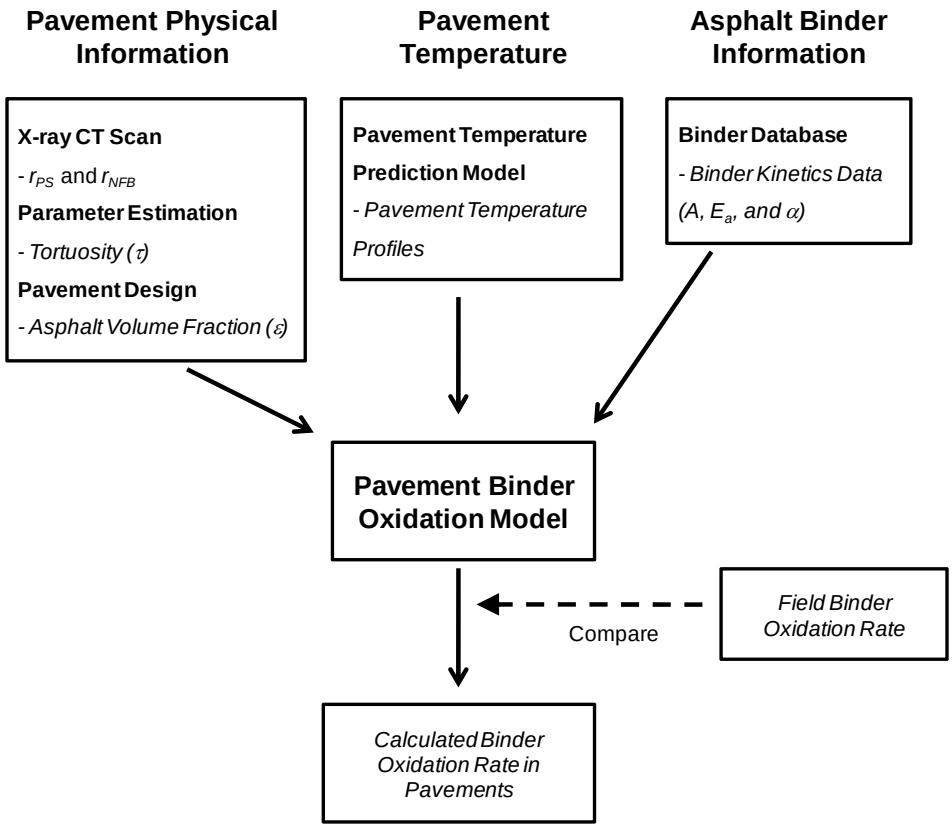

Figure VI-1. Workflow Schematic of the Binder Oxidation Rate Calculations

Binder Oxidation Model in Pavement

The pavement binder oxidation model was discussed in detail in Chapters IV and V. Key parameters of the pavement binder oxidation model are binder oxidation kinetics parameters and air voids characteristics of the pavement. Occasionally, these key parameters are estimated due to the limited availability of either binder kinetics or air voids data. The important parameters for the model were measured and estimated as discussed in Chapters III and V.

The asphalt binder that was used in the calculation in this chapter is an Exxon AC-20, of which the kinetics data were reported by Domke et al.[17] This Exxon AC-20 asphalt binder was used in the previously studied SH-21, which is located between Caldwell and Bryan, Texas. The reported values for the Exxon AC-20 of the frequency (pre-exponential) factor *(A)*, activation energy *(E_a)*, and oxygen reaction order *(α)* used for all calculations in this chapter were 1.696×10^6 CA/s atm^2, 86.4 kJ/mol, and 0.255, respectively.

For the air void related parameters that were obtained from X-ray CT image analysis results of the dense-graded mixture, the values of r_{PS} and r_{NFB} were approximately 0.87 mm and 1.27 mm, respectively. From mixture design information, the asphalt volume fraction (ε) for the mixture of this study, which is the difference between voids in mineral aggregate (VMA) and air voids content in the mixture, was reported to be 0.0735. Lastly, the mixture tortuosity (τ) was estimated in Chapter IV using least-squares parameter estimation method to be 2.33.

All the parameters mentioned above were for pavements using Exxon AC-20 in the same dense-graded mixture. These calculations use pavement temperature profiles generated for various locations throughout the country while holding every pavement structure-related parameter and binder kinetics parameter constant.

Pavement Temperature Prediction Model

Typically, pavement temperature varies with pavement location (climate), time (day and seasonal), and depth. As part of a pavement oxidation model, a reliable pavement temperature prediction model is also crucial to determine the change in asphalt binder properties due to oxidation.

The one-dimensional heat transfer model was developed and reported by Han et al.[73] and employs an unsteady-state heat flux boundary condition at the pavement surface, a depth-independent heat flux 3 m below the surface, and the ability to estimate site-specific model parameters using known measured pavement temperatures. First, a

general method to obtain or impute (if needed) hourly climatic data (solar radiation, ambient temperature, and wind speed) was developed. Then, with those input data and model calculations, optimal model parameters at 29 pavement sites across the country were estimated.

As shown in Figure VI-2a, the model employs commonly available hourly solar radiation, daily average wind speed, and imputed hourly air temperature based on site-specific daily patterns derived using time series analysis as climate input data. Three key site-specific model parameters: the albedo, the difference between the emissivity and absorption coefficients, and the absorption coefficient, were identified and the national distribution of their values correlated with climatic patterns, suggesting possible interpolation strategies based on climate. The temperature model, proposed data sources, and methods provided calculations that agreed well with experimental measurements, suggesting a general approach to predicting pavement temperatures nationwide with acceptable accuracy.

As shown in Figure VI-2b, the model uses a finite difference approximation for calculating heat conduction within the pavement and underlying layers, subject to heat fluxes at the surface (shortwave solar radiation, long-wave radiation, and convective heat transfer) and a constant-flux boundary condition well below the pavement. Using required climatic input data including solar radiation, ambient temperature, and wind speed and constant model parameters such as albedo, emissivity, and thermal diffusivity, the model calculates temperature as a function of time and depth.

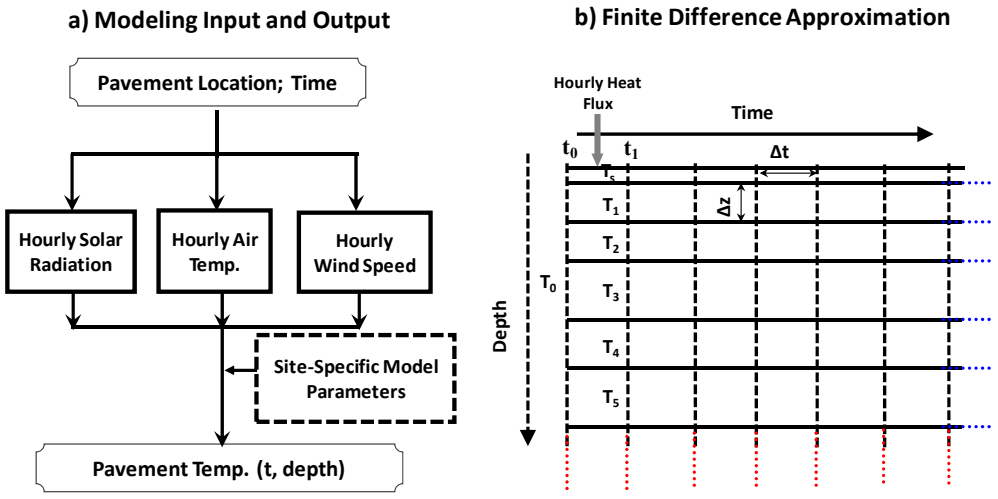

Figure VI-2. Pavement Temperature Prediction Model Diagram.
a) Modeling Input and Output, b) Finite Difference Approximation

The reaction kinetics of asphalt oxidation follow an Arrhenius activation energy equation (Equation I-4); these oxidation rates decrease exponentially with increasing inverse absolute temperature. Therefore, accurate representation of pavement temperature is critically important for predicting pavement oxidation as well as other issues that are highly sensitive to pavement temperature.

Results and Discussion

The pavement temperature prediction model with site-specific parameters and appropriate model inputs as discussed earlier was used to generate temperature profiles for various pavement locations over the course of one year. Then the profiles were used in the pavement binder oxidation model to calculate the asphalt oxidation rate, as it varies throughout the year, for each pavement location at several depths. In the calculations, although the pavement temperature profiles were changed to different locations, the model input data for pavement design were kept constant so as to isolate the effect of climate on binder oxidation rates in pavements. The calculated carbonyl

area growths of pavements in this study, both across the country and within Texas, are in Appendix F.

Typical Output from Pavement Temperature Prediction Model

Figures VI-3a and -3b show the yearly and monthly pavement temperature profiles generated by the pavement temperature prediction model for State Highway 21 located in Bryan, Texas. Temperature histories for three depths, 20, 80, and 160 mm from the pavement surface, are shown for the year 1994. The pavement temperature at the near surface has greater temperature fluctuation and somewhat higher average pavement temperatures than deeper into the pavement.

Later in this chapter, similar pavement temperature profiles are shown for sites throughout the country and within Texas. Asphalt oxidation rates were calculated based upon the temperature in each pavement layer.

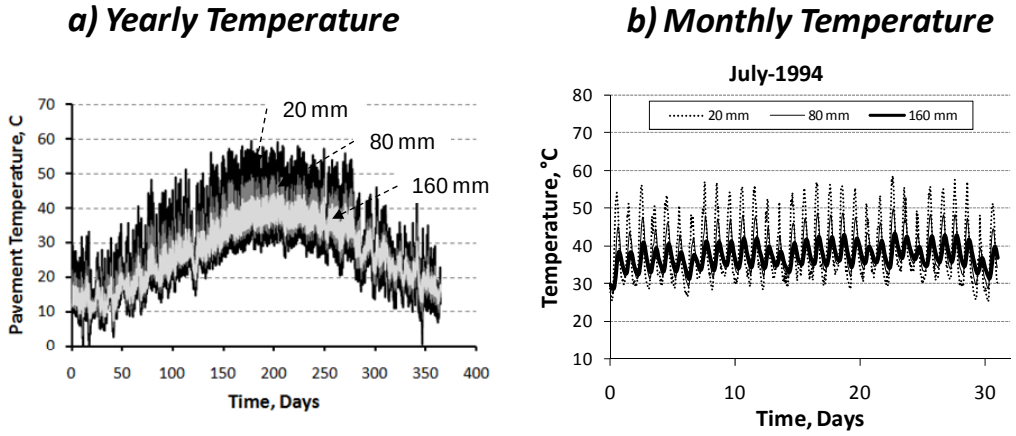

Figure VI-3. Typical Pavement Temperature Profile Output from the Model: a) Yearly Temperature and b) Monthly Temperature Profiles

Typical Output from Integrated Pavement Oxidation Model

As an example of the oxidation model calculations, the carbonyl area growth rates for Exxon AC-20 at three depths in Texas SH-21, located between Caldwell and Bryan, Texas, for the one-year period from January to December in 1994 are shown in Figure VI-4. The pavement used in the calculation utilized the parameters for a dense-graded mixture design, which has total air void content less than 10 percent, and used the model parameters as discussed previously. In this case, it is assumed that the initial carbonyl area values are the same throughout the pavement. The yearly carbonyl growth rates behave like a stair-step curve, corresponding to rather slow oxidation rates during spring and winter and then increasing significantly during the much warmer summer months. Also, the oxidation rate is higher at the surface, primarily because of the higher maximum temperature coupled with the exponential reaction activation energy effect, rather than because of a different average temperature.

According to the assumptions and parameters of these calculations, even as deep as 160 mm into the pavement, the oxidation rate is closer to that at the surface than it is to zero, that rate assumed by the mechanistic-empirical pavement design guide (MEPDG).

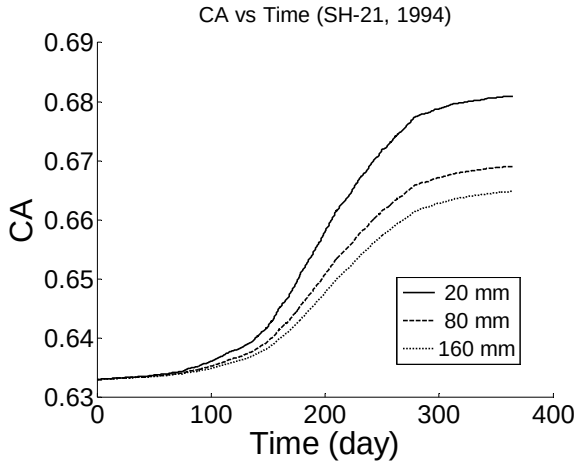

Figure VI-4. Calculated Carbonyl Area from Binder Oxidation Model at Various Depths

Predicted Temperature Profiles for Pavement Sites throughout the Country

Annual pavement temperature profiles as a function of depth for locations across the country were generated using available climate data coupled with the pavement temperature prediction model. Pavement temperatures as a function of time and depth were generated for locations in Arizona, Minnesota, Montana, New York, and Texas as shown in Figure VI-5. With these temperature profiles, binder oxidation rates in pavements were estimated using binder kinetics and pavement air void characteristic parameters.

The calculations indicate that, over a one-year cycle, the oxidation rate is slow during the fall and winter months when the average temperatures are low and daily pavement temperature fluctuations also are relatively small. Binder oxidation rates are significantly higher during the summer months, when the average temperatures are higher and daily pavement temperature fluctuations are also high.

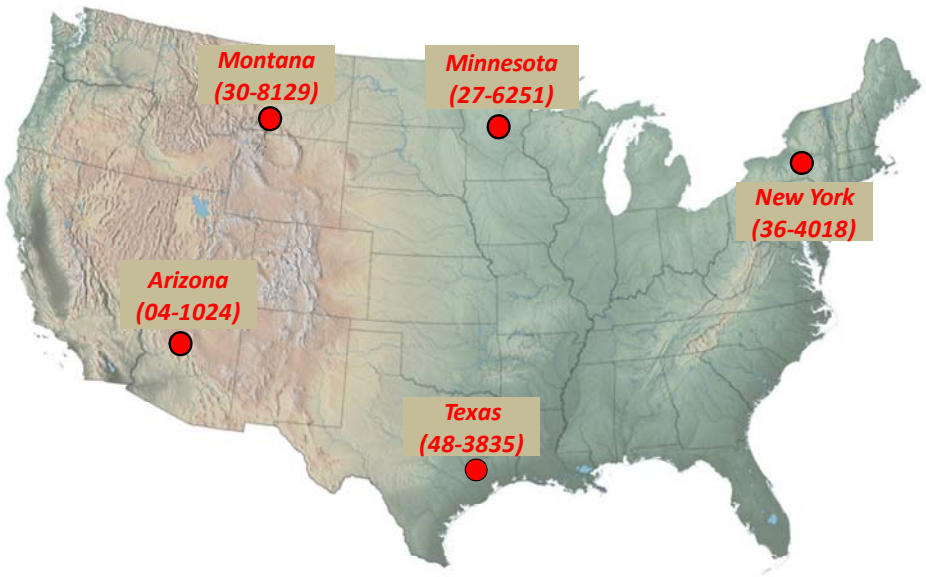

Figure VI-5. Selected Weather Station Sites throughout the Country

Table VI-1 contains the selected site information from the Long Term Pavement Performance (LTPP) database. These sites represent the climate regions throughout the country: Texas is in wet-no-freeze zone, Arizona and Montana are in dry-freeze zone, and Minnesota and New York are in wet-freeze zone. It should be noted that Arizona and Montana sites are located in the valley region as the elevation is comparably higher than the other sites. Also, the average number of days that air temperature exceed 32 °Cof each site , which indicates how hot the climate on that particular site, is reported.

Table VI-1. Selected Site Information from the LTPP Database

Site	County	Elevation (ft)	Climatic Region	Days Above 32 °C
Texas (48-3835)	Brazos	331	Wet No Freeze	96.22
Arizona (04-1024)	Yavapai	5,456	Dry Freeze	32.57
Montana (30-8129)	Golden Valley	4,440	Dry Freeze	10.61
Minnesota (27-6251)	Beltrami	1,364	Wet Freeze	3.44
New York (36-4018)	Otsego	1,070	Wet Freeze	2.48

Figures VI-6 and VI-7 show the 15-day intervals of pavement surface temperature profiles (at a depth of 20 mm) calculated by the pavement temperature prediction model for each location for the year 1994. The surface temperature profiles in colder months (January 1st to January 15th) are shown in Figure VI-6. The daily temperature fluctuations are quite similar for all pavement temperature profiles, approximately 20 °C. The daily average temperatures, however, are quite different from site to site; for example, the average temperatures in Texas and Arizona are generally higher than in Montana, Minnesota, and New York, as would be expected. Figure VI-7 shows the pavement temperature profiles of the pavements in the summer (July 16th to July 31st). The daily temperature fluctuations, approximately 30 °C, are significantly higher than for the colder month profiles. Also, during the warmer months, the daily average pavement temperatures are higher than during the colder months for all weather

stations. In addition, similar to the colder month profiles, Texas and Arizona generally have higher daily average temperatures than Montana, Minnesota, and New York.

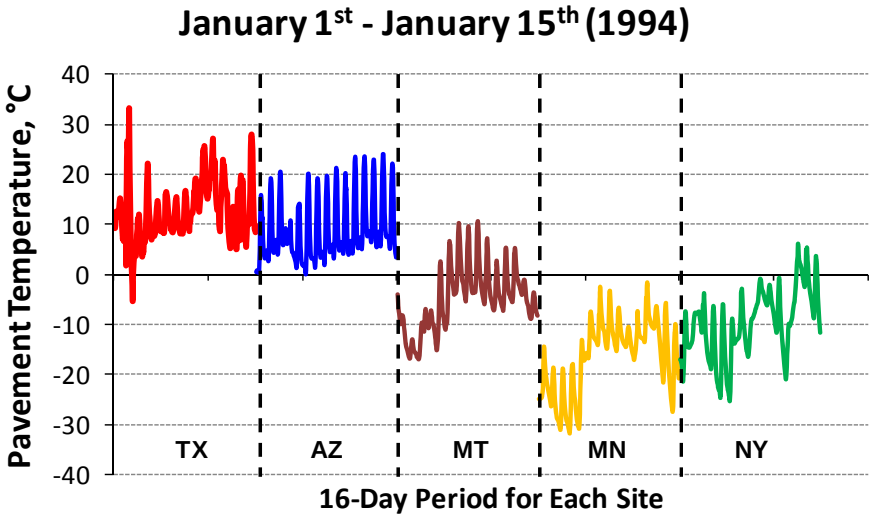

Figure VI-6. Pavement Surface Temperature Profiles of Colder Months (January 1st to January 15th)

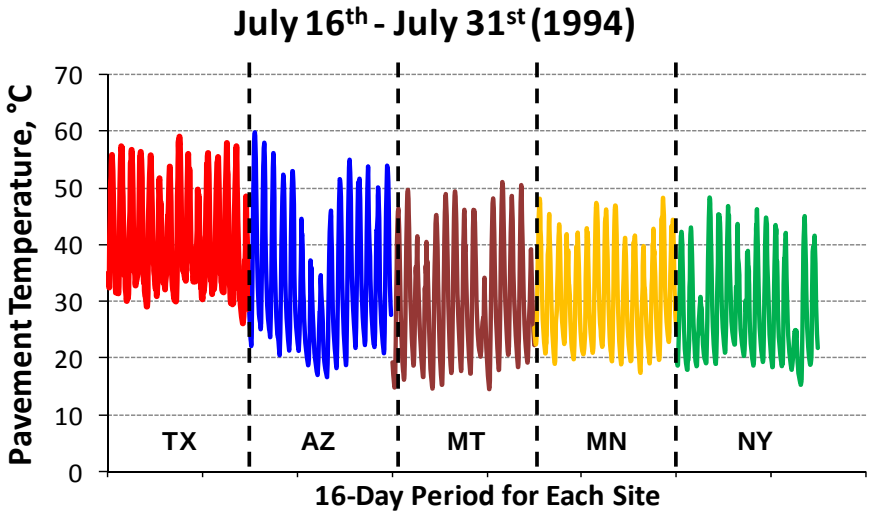

Figure VI-7. Pavement Surface Temperature Profiles of Warmer Months (July 16th to July 31st)

Asphalt Oxidation Rates Comparison throughout the United States

The study in this section used the asphalt oxidation model in pavements to study the effect of different climate zones on asphalt binder oxidation rates. Annual pavement temperature profiles as a function of depth for different locations across the country were generated using available climate data coupled with the pavement temperature prediction model. Then asphalt oxidation rates in pavements over 10 years were calculated. Due to the limitation of weather data to generate temperature profiles over 10 years, the assumption was made that each year each pavement has exactly the same temperature profile.

Figure VI-8 shows the carbonyl area growths at the pavements' top surface calculated for the five sites. The Texas site clearly has the highest oxidation rate, while Arizona's is the second highest followed by the fairly close-ranked Montana, Minnesota, and New York sites, respectively. All calculated carbonyl area growths have S-shaped curves indicating that aging practically stops during the fall, spring, and winter compared to the summer. In this case, although the carbonyl growth rates in colder months are slow and comparable for all sites, the carbonyl growth rates in the summer for the Texas and Arizona sites are significantly higher than the rest of the sites. Therefore, it is important to emphasize that the oxidation that occurs during the summer is critical to the overall oxidation rate in pavements.

An important assumption in these calculations is that the pavement structure and the reaction kinetic parameters of asphalt binder used in the calculations are the same throughout the study due to the limitation of binder and pavement structure data and in order to assess the effect of climate alone. In reality, different asphalt materials and different pavement designs are used to compensate for the effect of weather or climates on pavement performance in different parts of the country. For example, asphalt binders that are suitable for pavements in cold regions must a have high resistance to thermal cracking, while binders for pavements in warm regions must have good resistance to rutting at the higher pavement temperatures.

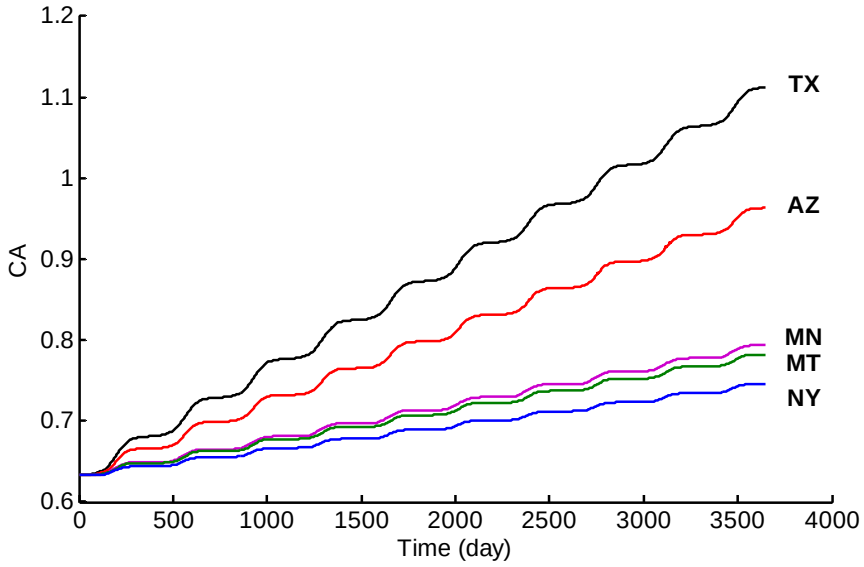

Figure VI-8. Calculated Asphalt Oxidation Rates at the Depth of 20 mm of the Pavements from Various Weather Stations throughout the Country

The results calculated by the asphalt oxidation model were compared to field binder aging rates. Table VI-2 summarizes carbonyl area (arbitrary units) growth rates measured for two depth ranges for binder recovered from Texas State Highway 21 (SH-21) between Bryan and Caldwell during the years 1989 and 1992.[3] These average aging rates for binder recovered from the top and bottom lifts were determined to be 0.053 and 0.047 CA/year, respectively, versus the calculated values of 0.048 and 0.032. Aging rates calculated for the five climate zones, and for the binder used in SH-21 (Exxon AC-20), are also reported. Because the same binder and mixture were assumed for the sake of comparison purposes, the rates vary from site to site only because of different temperature and solar radiation effects at the different locations. These rates are also shown as CA/year but a separate column also gives the oxidation rate relative to the rate for Texas. Note that the measured and calculated aging rates in Texas differ somewhat, perhaps because the air void characteristics used in the calculation were different from the air void characteristics of the actual pavement. In addition, due to the limitation of

weather parameter inputs for the pavement temperature prediction model, the generated pavement temperature profiles used in this study were for the year 1994.

Table VI-2. Carbonyl Area Growth Rates Comparison and Relative Aging Rates of Weather Station Sites throughout the Country

Site	Aging rate (CA/Year)		Aging rate relative to Texas pavement calculation at the top layer	Remark
	Top Layer*	Bottom Layer**		
TX SH-21	0.053	0.047	N/A	Average measured aging rate , 1989 to 1992
NY	0.012	0.007	0.25	Average aging rates calculated from pavement binder oxidation model and pavement temperature prediction model using the climate data from 1994
MT	0.015	0.008	0.31	
MN	0.016	0.010	0.34	
AZ	0.033	0.017	0.69	
TX	0.048	0.032	1.00	

* Top Layer. For TX SH-21 this refers to 0-2 inches below the pavement surface; for the calculations, it refers to 1 inch below the pavement surface

** Bottom Layer. For TX SH-21 this refers to 4-6 inches below the pavement surface; for the calculations, it refers to 6 inches below the pavement surface

Asphalt Oxidation Rates Comparison within Texas

The effect of climate on oxidation rates in pavements is important enough that differences in pavement oxidation rates are calculated even within the state of Texas. With the integrated model developed in this study, carbonyl growth rates of Exxon AC-20 were calculated for seven locations in five climate zones in Texas (Figure VI-9). The selected sites include Amarillo, Bryan, Dallas, El Paso, Hidalgo, Kingsville, and Lufkin. The pavement temperature prediction model was used together with site-specific parameters to calculate pavement temperature profiles and oxidation rates at three depths (20 mm, 80 mm, and 160 mm) for each site. For each pavement site, the calculated

binder oxidation rates for the top 20 mm is the highest and the rate decreases as the depth into the pavement increases. By comparing the binder oxidation rates from climate zones all across Texas, the results demonstrated that the regions where the climates were dry-warm and wet-warm have higher carbonyl growth rates than the dry-cold, wet-cold, and moderate weather regions. From Dallas to the lower Rio Grande Valley, these calculated rates varied by a factor of two, perhaps a surprisingly large difference.

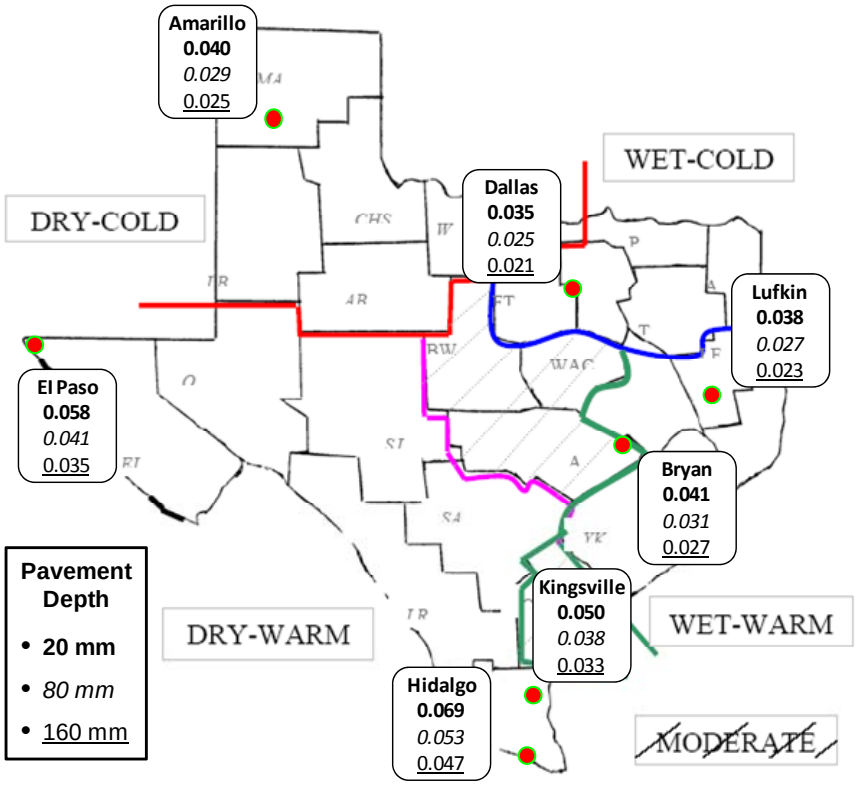

Figure VI-9. Calculated Asphalt Oxidation Rate of Three Pavement Depths for Several Pavement Sites in Texas

Conclusions

Based on model calculations to explore the effect of climates and the resulting pavement temperature profiles on binder oxidation in pavements, the following conclusions are made:

- The integrated binder oxidation model validation is still an issue. More measured pavement aging rates need to be compared to model calculations. Also, air void characteristic data of the corresponding pavements should be obtained or measured. In the case that these air void characteristic data are limited, parameter estimation methods were employed for necessary parameters.
- Temperature varies throughout the depth of a pavement and that affects the rate of binder oxidation as a function of depth.
- Diverse climates throughout different parts of the country greatly affect the pavement oxidation process. This effect should be taken into account in pavement design for improved durability.
- Climate zones within Texas show similar effects on binder oxidation in pavements, although not as extreme as, of course, the differences across the country. However, adjustments in pavement design are still important for constructing pavements with improved durability.
- With an adequate asphalt binder database, pavement air void characteristic data, and sufficient weather input data, the binder oxidation model integrated with the pavement temperature prediction model is an excellent combination of tools that enables pavement designers to be able to estimate binder oxidation and hardening rates in pavements.

CHAPTER VII
SUMMARY, CONCLUSIONS, AND RECOMMENDATIONS

Summary of Findings

Beginning with the background of asphalt oxidation in pavements in Chapter I, the discussions of findings in this dissertation on important elements of the oxidation model, oxidation model development, and oxidation model application were included in Chapters II through VI. After conducting research work to accomplish the objectives stated in each chapter, the summary of findings of each chapter was specifically discussed in a conclusion section.

The background information on binder oxidation in pavements provided in Chapter I provide the foundation of the research work necessary to develop the binder oxidation model in pavements. The important factors that influence the study of oxidation process of binder in pavements are asphalt binder kinetics, air void characteristics, pavement temperature, and the appropriate model that ties these factors together. In later chapters, the necessary model parameters was determined and estimated, and the desired oxidation model were carefully developed.

In Chapter II, the effects of accessible air void contents on asphalt binder properties were intensively studied. After the comparison between air void content and binder properties of pavement core samples, the general trend was discovered that the oxidation rates of asphalt binders are high when the accessible air void contents in pavement are high and the oxidation rates are low when there are low air void contents. The finding in this chapter supports the previous results that aging rates of asphalt binders are affected by accessible air voids.

Chapter III went further into the study to determine air void characteristics in pavements. The X-ray CT imaging technique, which is a nondestructive test, was used to obtain the information on total air void content as well as interconnected air voids in core samples. The results show that there are air void channels distributed in the

pavement core samples allowing the adequate availability of oxygen for the binder oxidation process. Also, with the additional image analysis process, key air void characteristic parameters, air void radius (r_{PS}) and the half-distance between two adjacent pores (r_{NFB}), were calculated and later used in the binder oxidation model developed in Chapter IV.

Once the fundamental elements of binder oxidation in pavements, binder kinetics, and air void characteristics were determined, these elements were used in Chapter IV together with the oxygen diffusion and reaction concepts to develop an improved binder oxidation model in pavements in a cylindrical coordinate system. Due to the unavailability of actual pavement temperature data, the preliminary outputs of the binder oxidation model were calculated using a constant temperature of 60 °C, which is the average temperature of pavements in Texas. The outputs, as a function of time, from the model include oxygen partial pressure profile, oxygen diffusivity in asphalt binder, binder viscosity, and carbonyl area of asphalt binder.

Chapter V includes extensive work on the binder oxidation model in pavements developed in Chapter IV. In addition to the detailed calculations of the oxidation model, least-squares parameter estimation methods were used to approximate the missing parameters such as binder kinetics information or air void characteristic parameters. The estimation was performed by comparing the calculated oxidation rate from the model with the oxidation rate obtained from the environmental room (ER) where the temperature of the room was held constant at 60 °C. Also, the pavement temperature prediction model was introduced and integrated with the binder oxidation model in pavements. The one-dimensional thermal transport model, coupled with site-specific model parameters and recent improvements in the availability of required input climate data, enables calculation of pavement temperatures throughout the year to a surprisingly reliable extent. With such an integrated model, the binder properties in pavements can be determined as a function of time and depth at the specific pavement locations where the required weather input data are available.

Chapter VI consists of the study on the effect of climates and pavement temperature profiles on binder oxidation in pavements. The pavement temperature profiles as a function of time and depth were generated for selected pavement sites and then used in the pavement oxidation model. It was found that diverse climates throughout the country greatly affect the oxidation process in pavements. Also, the difference of climate zones in Texas itself was enough to cause a significant difference in binder oxidation rates. As a general trend, the regions that have warm climates usually have higher carbonyl growth rates than the ones that have cold or moderate climates. Also from the model calculations, in a one-year cycle, the oxidation rate in pavements was highest during the summer months and the rates decreased substantially in fall, spring, and winter.

Conclusions

Asphalt binder oxidization in pavements is arguably one of the major causes for pavement thermal and fatigue cracking. Although binder oxidation fundamentals are well-documented, predicting binder oxidation rates in pavements is still a complicated matter.

The studies of the effects of air void content on binder oxidation and air void characteristics in pavements were the crucial steps toward the oxidation model development. Once the basic concept of binder oxidation in pavements was understood, the important elements of the model, including binder kinetics, air void characteristics, and pavement temperature profiles, were used in the development of an asphalt oxidation model in pavements. Occasionally, some input parameters were not available due to the limitation of the database and these parameters needed to be estimated by least-squares estimation methods. After obtaining all necessary input parameters, key outputs from the model, including carbonyl area of asphalt binder in pavements as a function of time and depth, can be predicted.

Lastly, the mixture binder oxidation model can be established as a crucial cornerstone for successive research on asphalt oxidation in pavements. Improving the accuracy and validity of the model by increasing the data availability of binder kinetics and air void characteristic in pavements is crucially important in order to utilize the model as a resource for pavement design and maintenance scheduling.

Recommendations

The research work completed in this dissertation was a proof of concept for binder oxidation in pavements. In addition to this work, which focused on the fundamental aspect of the model, there is much future research that could be studied in order to improve and/or extend the benefit of the binder oxidation model in pavements developed in this dissertation.

The calibration and validation of the asphalt oxidation model in pavements are still an ongoing process. Additional binder oxidation in pavements data from the field are required in order to validate the developed model. Therefore, field binder oxidation rates in pavements need to be monitored and reported.

As of now, the databases of model input parameters, asphalt kinetics and air void characteristics in pavements, are still very limited. In order to improve the accuracy of the model, the size of these input databases must be increased. It should be noted that the binder kinetics data measurement is a time-consuming process and needs to be done periodically as asphalt binder composition can be changed due to crude source. Also, the additional air void characteristic information of various types of mixture designs should be cataloged using either standard or high-resolution X-ray CT scans.

The additional development on oxygen diffusivity correlation could also be a crucial step toward the improvement of the binder oxidation model in pavements. Currently, the binder oxidation model uses oxygen diffusivity correlation that was developed as a general correlation for all asphalt binders. If the asphalt-specific oxygen diffusivity is developed, the accuracy of the model calculations can be improved.

The goal of this research was to develop the basic transport model for use as a guide to designing field and laboratory experiments for the purpose of evaluating the impact of diffusion resistance on the oxidation rate of asphalt binders in pavements as a function of air voids, asphalt binder content, and other parameters. Ultimately, laboratory results and this proposed transport model could be integrated into a prototype of pavement design software to be used as a time- and cost-effective pavement design tool.

LITERATURE CITED

1. Abraham H. *Asphalts and Allied Substances: Their Occurrence, Modes of Production, Uses in the Arts and Methods of Testing* (3rd edition). New York: D. Van Nostrand Co., Inc., 1929.

2. Federal Highway Administration (FHWA). *Highway Statistics 2007*. Washington D.C.: Office of Highway Policy Information, Federal Highway Administration, 2007. Accessed: 10 October 2009.
Available at: <http://www.fhwa.dot.gov/policyinformation/statistics/2007>.

3. Glover CJ, Davison RR, Domke CH, Ruan Y, Juristyarini P, Knorr DB, Jung SH. Development of a new method for assessing asphalt binder durability with field validation. Report FHWA/TX-03/1872-2. College Station, TX: Texas Transportation Institute, 2005.

4. Al-Azri NA, Jung SH, Lunsford KM, Ferry A, Bullin JA, Davison RR, Glover CJ. Binder oxidative aging in Texas pavements: hardening rates, hardening susceptibilities, and the impact of pavement depth. *Transportation Research Record*: *Journal of the Transportation Research Board*. 2006;1962:12-20.

5. Lau CK, Lunsford KM, Glover CJ, Davison RR, Bullin JA. Reaction rates and hardening susceptibilities as determined from POV aging of asphalts. *Transportation Research Record*: *Journal of the Transportation Research Board*. 1992;1342(50):50-57.

6. Liu M, Chaffin JM, Davison RR, Glover CJ, Bullin JA. Changes in Corbett fraction composition during oxidation of asphalt fractions. *Transportation Research Record*: *Journal of the Transportation Research Board*. 1998;1638:40-46.

7. Martin KL, Davison RR, Glover CJ, Bullin JA. Asphalt aging in Texas roads and test sections. *Transportation Research Record*: *Journal of the Transportation Research Board*. 1990;1269:9-19.

8. Liu M, Ferry MA, Davison RR, Glover CJ, Bullin JA. Oxygen uptake as correlated to carbonyl growth in aged asphalts and asphalt Corbett fractions. *Ind. Eng. Chem. Res.* 1998;37:4669-4674.

9. Lin MS, Lunsford KM, Glover CJ, Davison RR, Bullin JA. The Effects of asphaltenes on the chemical and physical characteristics of asphalts. *Asphaltenes: Fundamentals and Applications*. New York: Plenum press, 1995:155-176.

10. Lin MS, Chaffin JM, Liu M, Glover CJ, Davison RR, Bullin JA. The effect of asphalt composition on the formation of asphaltenes and their contribution to asphalt viscosity. *Fuel Sci. and Technol. Intl*. 1996;14(1&2):139-162.

11. Lin MS, Chaffin JM, Davison RR, Glover CJ, Bullin JA. A new suspension viscosity model and its application to asphaltene association thermodynamics and structures. In *Structures and Dynamics of Asphaltenes*. New York: Plenum press, 1998: 267-302

12. Domke CH, Davison RR, GloverCJ. Effect of oxidation pressure on asphalt hardening susceptibility. *Journal of the Transportation Research Board*. 1999;1661:114-121.

13. Lee DY, Huang RJ. Weathering of asphalts as characterized by infrared multiple internal reflection spectra. *Applied Spectroscopy.* 1973;27(6):419-490.

14. Petersen JC, Branthaver JF, Robertson RE, Harnsberger PM, Duvall JJ, Ensley EK. Effects of physicochemical factors on asphalt oxidation kinetics. *Transportation Research Record*: *Journal of the Transportation Research Board*. 1993;1391:1-10.

15. Liu M, Lunsford KM, Davison RR, Glover CJ, Bullin JA. The kinetics of carbonyl formation in asphalt. *AIChE Journal*. 1996;42(4):1069-1076.

16. Liu M, Chaffin JM, Davison RR, Glover CJ, Bullin JA. Reactivity of asphalt supercritical fractions. *Ind. Eng. Chem. Res*. 1997;36(6):2177-2183.

17. Domke CH, Davison RR, Glover CJ. Effect of oxygen pressure on asphalt oxidation kinetics. *Ind. Eng. Chem. Res.* 2000;39(3):592-598.

18. Walubita LF, Martin AE, Jung SH, Glover CJ, Park ES, Chowdhury A, Lytton RL. Comparison of fatigue analysis approaches for two hot mix asphalt concrete (HMAC) mixtures. FHWA/TX-05/0-4468-2. College Station, TX: Texas Transportation Institute, 2005.

19. Walubita LF. Comparison of fatigue analysis approaches for predicting fatigue lives of hot mix asphalt concrete mixtures (HMAC). Ph.D. Thesis. Texas A&M University, College Station, TX, 2006.

20. Walubita LF, Martin AE, Jung SH, Glover CJ, Park ES. Application of calibrated mechanistic fatigue analysis with aging effects. Report FHWA/TX-06/0-4468-3. College Station, TX: Texas Transportation Institute, 2006.

21. Walubita LF, Martin AE, Cleveland GS. Application of the new M-E Pavement Design Guide software for fatigue characterization of three Texas asphalt mixtures.

Paper accepted for presentation at the 10th ICAP Conference 2006, 12-17 August 2006, Quebec, Canada, 2006.

22. Woo WJ, Ofori-Abebresse E, Chowdhury A, Hilbrich J, Kraus Z, Martin AE, Glover CJ. Polymer modified asphalt durability in pavements. Publication FHWA/TX-07/0-4688-1, FHWA/TX-07. College Station, TX: Texas Transportation Institute, 2007.

23. Ruan Y, Davison RR, Glover CJ. An investigation of asphalt durability: relationships between ductility and rheological properties for unmodified asphalts. *Pet. Sci. & Tech.*, 2003;21(1-2):231-254.

24. Vallerga BA, Halstead WJ. Effects of field aging on fundamental properties of paving asphalts. *Highway Research Record*. 1971;361:71-92.

25. Coons RF, Wright PH. An investigation of the hardening of asphalt recovered from pavements of various ages. *Journal of Association of Asphalt Paving Technologists*. 1968;37:510-528.

26. NCHRP. *Guide for Mechanistic-Empirical Design of New and Rehabilitated Pavement Structures.* Final NCHRP Report 1-37A., Part 2. Design Inputs, Chapter 2. Material Characterization. www.trb.org/mepdg/Part2_Chapter2_Materials.pdf. Accessed July 05, 2007.

27. Mirza MW, Witczak MW. Development of a global aging system for short and long term aging of asphalt cements. *Journal of Association of Asphalt Paving Technologists*. 1995;64:393-430.

28. Burr BL, Davison RR, Glover CJ, Bullin JA. Solvent removal from asphalt. *Transportation Research Record*: *Journal of the Transportation Research Board*. 1990;1269:1-8.

29. Roberts FL, Kandhal PS, Brown ER, Lee DY, Kennedy TW. *Hot Mix Asphalt Materials, Mixture Design, and Construction* (2nd edition). Lanham, MD: NAPA Education Foundation, 1996.

30. Zube E. Compaction Studies of Asphalt concrete pavements as related to the water permeability test. *Highway Research Board, Bulletin*. 1992;358.

31. Brown ER, Collins R, Brownfield JA. Investigation of segregation of asphalt mixtures in the state of Georgia. *Transportation Research Record*: *Journal of the Transportation Research Board.* 1989;1217:1-8.

32. Hudson SB, Davis RL. relationship of aggregate voidage to gradation. *Journal of the Association of Asphalt Paving Technologists*. 1965;34:574-593.

33. Mallick RB, Cooley Jr. LA, Teto MR, Bradbury RL, Peabody D. An evaluation of factors affecting permeability of superpave designed pavements. Presented at the 80th Annual Meeting of the Transportation Research Board, Washington, D.C., 2001.

34. Cooley Jr. LA, Brown ER. Selection and evaluation of a field permeability device for asphalt pavements. *Transportation Research Record*: *Journal of the Transportation Research Board.* 2000;1723:73-82.

35. Maupin Jr. GW. Asphalt permeability testing in Virginia. *Transportation Research Record: Journal of the Transportation Research Board*. 2000;1723:83-91.

36. Musselman JA, Choubane B, Page GC, Upshaw PB. Superpave field implementation: Florida's early experience. *Transportation Research Record*: *Journal of the Transportation Research Board*. 1998;1609:51-60.

37. Westerman JR. AHTD's Experience with Superpave Pavement Permeability. <http://www.utexas.edu/research/superpave/articles/jrw10a.html>, January 21, 1998.

38. Cecheitini JA. Vibratory compaction of asphalt concrete pavements. *Journal of the Association of Asphalt Paving Technologists.* 1974;43:384-416.

39. Brown ER, Hainin MR, Cooley A, Hurley G. Relationship of Air Voids, Lift Thickness, and Permeability in Hot Mix Asphalt Pavements. NCHRP Report 531. Washington D.C.: Transport Research Board, 2004.

40. Cooley Jr. LA, Prowell BD, Hainin MR, Buchanan MS, Harrington J. Bulk specific gravity round robin using the corelok vacuum sealing device. Report No. 02-11. National Center for Asphalt Technology (NCAT), 2002.

41. Al-Omari A, Tashman L, Masad E, Cooley Jr. LA, Harman T. Proposed methodology for predicting HMA permeability. *Journal of the Association of Asphalt Paving Technologist.,* 2002;71:30-58.

42. Masad E, Arambula E, Ketcham R, Abbas A, Martin AE. Nondestructive measurements of moisture transport in asphalt mixtures. *Asphalt Paving Technology.* 2007;76:919-952.

43. Palmouist D, Worel B, Zerfas W. Mn/Road hot-mix asphalt mainline test cell condition report. Publication Minnesota Road Research Project, U.S. Minnesota Department of Transportation, 2002.

44. Vassiliev N, Davison RR, Glover CJ. Development of a stirred air-flow test procedure for short-term aging of asphaltic materials. *Transportation Research Record*: *Journal of Transportation Research Board.* 2002;1810:25-32.

45. Prapaitrakul N, Freeman TJ, Glover CJ. Assessing the ability of fog seal pavements to rejuvenate in situ binder, and to retard binder oxidation. Publication FHWA/TX-06/0-5091-3, FHWA/TX-07. College Station, TX: Texas Transportation Institute, 2007.

46. ASTM D 2041, Standard test method for theoretical maximum specific gravity and density of bituminous paving mixtures. 2003 Annual Book of ASTM Standards, 04.03, ASTM, 2003.

47. ASTM D 6752, Standard test methods for bulk specific gravity and density of compacted bituminous mixtures using automatic vacuum sealing method. 2004 Annual Book of ASTM Standards, 04.03, ASTM, 2004.

48. ASTM D 6857, Standard test methods for maximum specific gravity and density of bituminous paving mixtures using automatic vacuum sealing method. 2003 Annual Book of ASTM Standards, 04.03, ASTM, 2003.

49. Instrotek Incorporated. *Corelok® Operator's Guide*, Version 20, Raleigh, NC, 2003.

50. Burr BL, Glover CJ, Davison RR, Bullin JA. New apparatus and procedure for the extraction and recovery of asphalt binder from pavement mixtures. *Transportation Research Record*: *Journal of the Transportation Research Board*. 1993;1391:20-29.

51. Burr BL, Davison RR, Jemison HB, Glover CJ, Bullin JA. Asphalt hardening in extraction solvents. *Transportation Research Record: Journal of the Transportation Research Board*. 1991;1323:70-76.

52. Burr BL, Davison RR, Glover CJ, Bullin JA. Softening of asphalts in dilute solutions at primary distillation conditions. *Transportation Research Record*: *Journal of the Transportation Research Board.* 1994;1436:47-53.

53. Cipione CA, Davison RR, Burr BL, Glover CJ, Bullin JA. Evaluation of solvents for the extraction of residual asphalt from aggregates. *Transportation Research Record*: *Journal of the Transportation Research Board*. 1991;1323:47-52.

54. Jemison HB, Burr BL, Davison RR, Bullin JA, Glover CJ. Application and use of the ATR, FTIR method to asphalt aging studies. *Fuel Sci. & Tech. Int*. 1992;10(795):490-495.

55. Alvarez AE, Martin AE, Estakhri CK, Button JW, Kraus Z, Prapaitrakul N, Glover CJ. Evaluation and recommended improvements for mix design of permeable friction courses. Publication FHWA/TX-08/0-5262-3, FHWA/TX-08. College Station, TX: Texas Transportation Institute, 2008.

56. Crouch LK, Badoe D, Cates M, Borden TA, Copeland A, Walker CT, Dunn T, Maxwell R, Goodwin W. Bulk specific gravity of compacted bituminous mixtures: finding a more widely applicable method. Final Report, Project Number TNSPR-RES1153. Tennessee Department of Transportation, 2003.

57. Masad E. X-Ray Computed Tomography of Aggregates and asphalt mixes. *Materials Evaluation.* 2004:775-783.

58. Lunsford KM. The effect of temperature and pressure on laboratory oxidized asphalt films with comparison to field aging. Ph.D. Thesis. Texas A&M University, College Station, TX, 1994.

59. Brown AB, Sparks JW, Larsen O. Rate of change of softening point, penetration, and ductility of asphalt in bituminous pavement. *Proceedings of the Association of Asphalt Pavement Technologists*. 1957;26:66-76.

60. Lau CK. Photo- and moderate-temperature oxidation reactions and their impacts on the properties and performance on asphalt as a pavement binder. MS Thesis. Texas A&M University, College Station, TX, 1991.

61. Bird RB, Stewart WE, Lightfoot EN. *Transport Phenomena*. New York: Wiley, 1960.

62. Reid RC, Prausnitz JM, Sherwood TK. *The Properties of Gases and Liquids* (4^{th}edition). New York: McGraw-Hill, 1983.

63. Basmadjian D. *Mass Transfer: Principles and Applications*. Boca Raton: CRC Press LLC., 2004.

64. Radisic M, Deen W, Langer R, Vunjak-Novakovic G. Mathematical model of oxygen distribution in engineered cardiac tissue with parallel channel array perfused with culture medium containing oxygen carriers. *American Journal of Physiology - Heart and Circulatory Physiology*. 2005;288: H1278-H1289.

65. Rumney TN, Jimenez RA. Pavement temperatures in the southwest. *Highway Research Record*. 1969;361:1-13.

66. Dempsey BJ. A heat transfer model for evaluating frost action and temperature related effects in multilayered pavement systems. *Highway Research Record*. 1970;342:39-56.

67. Solaimanian M, Kennedy TW. Predicting maximum pavement surface temperature using maximum air temperature and hourly solar radiation. *Transportation Research Record*: *Journal of the Transportation Research Board*. 1993;1417:1-11.

68. Lytton RL, Pugahl DE, Michalak CH, Liang HS, Dempsey BJ. An integrated model of the climatic effects on pavements. Report FHWA-RD-90-033. College Station, TX: Texas Transportation Institute, 1989.

69. Ahmed Z, Marukic I, Zaghloul S, Vitillo N. Validation of enhanced integrated climatic model predictions with New Jersey seasonal monitoring data. *Transportation Research Record*: *Journal of the Transportation Research Board.* 2005;1913:148-161.

70. Gui J, Phelan PE, Kaloush KE, Golden JS. Impact of pavement thermophysical properties on surface temperature. *Journal of Materials in Civil Engineering*. 2007;19:683-690.

71. Hermansson A. Simulation model for calculating pavement temperatures, including maximum temperature. *Transportation Research Record*: *Journal of the Transportation Research Board.* 2000;1699:134-141.

72. Hermansson A. Mathematical model for paved surface summer and winter temperature: comparison of calculated and measured temperatures. *Cold Regions Science and Technology*. 2004;40:1-17.

73. Han R, Jin X, Glover CJ. Modeling of pavement temperature history for use in binder oxidation models and pavement performance prediction. *Journal of Materials in Civil Engineering*. 2009. Submitted: Under Review.

APPENDIX A

ASPHALT BINDER RHEOLOGY MEASUREMENTS

FOR CHAPTER II

Table A-1. Recovered Binder Properties for the Abilene SH 36 L1 and L2 Cores [a]

	Replicate	layer	η* (poise) @ 60 °C 0.1 rad/s	η'/G' (s) @ 15 °C 0.005 rad/s	G' (MPa) @ 15 °C 0.005 rad/s	G'/(η'/G') (MPa/s) @ 15 °C 0.005 rad/s	Calculated Ductility (cm) -	Carbonyl Area -
	U3	1st	-	-	-	-	-	-
		2nd	-	-	-	-	-	-
1st Set		3rd	-	-	-	-	-	-
Abilene L1	T3	1st	262550	148.0	0.66774	0.0045129	2.48	-
		2nd	120880	206.8	0.35748	0.0017287	3.78	-
		3rd	217080	148.7	0.73146	0.0049181	2.38	-
	U1	1st	369380	119.4	0.74978	0.0062787	2.14	-
		2nd	155150	177.9	0.52384	0.0029445	2.99	-
		3rd	289250	120.8	0.84814	0.0070234	2.04	-
	U2	1st	307120	120.9	0.69988	0.0057897	2.22	-
		2nd	256120	131.9	0.65822	0.0049903	2.37	-
2nd Set		3rd	690860	71.5	1.30160	0.0182066	1.34	-
Alilene L1	T1	1st	370230	120.3	0.80918	0.0067258	2.08	-
		2nd	192200	162.1	0.55548	0.0034261	2.80	-
		3rd	547540	113.2	0.89858	0.0079386	1.93	-
	T2	1st	345500	127.5	0.72838	0.0057126	2.23	-
		2nd	244940	143.1	0.66484	0.0046461	2.44	-
		3rd	514760	82.5	1.29540	0.0156998	1.43	-
	U3	1st	488110	98.2	1.04100	0.0105994	1.70	1.555
		2nd	146010	195.7	0.48314	0.0024694	3.23	1.275
1st Set		3rd	337410	114.3	0.90158	0.0078887	1.94	1.331
Abilene L2	T3	1st	221010	162.8	0.61846	0.0037980	2.67	1.533
		2nd	91086	254.9	0.30442	0.0011941	4.44	1.104
		3rd	415790	87.7	1.28680	0.0146650	1.47	1.394
	U1	1st	260000	143.3	0.64532	0.0045028	2.48	-
		2nd	207050	143.2	0.80072	0.0055914	2.25	-
		3rd	145920	149.6	0.72414	0.0048421	2.40	-
	U2	1st	384280	117.1	0.81104	0.0069232	2.05	-
		2nd	200950	157.9	0.67396	0.0042671	2.54	-
2nd Set		3rd	86846	208.4	0.50010	0.0024003	3.27	-
Abilene L2	T1	1st	259220	149.6	0.67092	0.0044839	2.48	-
		2nd	148870	188.3	0.45086	0.0023939	3.27	-
		3rd	237560	123.2	0.95754	0.0077728	1.95	-
	T2	1st	242590	149.4	0.67942	0.0045470	2.47	-
		2nd	243990	139.7	0.72868	0.0052167	2.32	-
		3rd	142750	155.0	0.70338	0.0045378	2.47	-

[a] η' and G' are measured at 44.7 °C, 10 rad/s and converted by TTSP to 15 °C, 0.005 rad/s

Table A-2. Recovered Binder Properties for the Abilene SH 36 R1 and R2 Cores [a]

	Replicate	layer	η* (poise) @ 60 °C 0.1 rad/s	η'/G' (s) @ 15 °C 0.005 rad/s	G' (MPa) @ 15 °C 0.005 rad/s	G'/(η'/G') (MPa/s) @ 15 °C 0.005 rad/s	Calculated Ductility (cm) -	Carbonyl Area -
	U3	1st	425090	99.1	0.91202	0.0092040	1.81	-
		2nd	155620	162.7	0.73120	0.0044945	2.48	-
1st Set		3rd	213830	132.6	0.82550	0.0062235	2.15	-
Abilene R1	T3	1st	244960	137.9	0.61002	0.0044229	2.50	-
		2nd	237160	138.8	0.68938	0.0049674	2.37	-
		3rd	387680	97.8	1.10900	0.0113357	1.65	-
	U1	1st	415790	103.3	0.99738	0.0096561	1.77	-
		2nd	363730	103.0	0.89194	0.0086605	1.86	-
		3rd	144280	162.7	0.76628	0.0047106	2.43	-
	U2	1st	407320	101.4	0.91828	0.0090597	1.82	-
		2nd	428810	95.0	1.12780	0.0118739	1.62	-
2nd Set		3rd	169100	140.7	0.84640	0.0060149	2.18	-
Abilene R1	T1	1st	376870	110.1	0.93800	0.0085190	1.87	-
		2nd	318920	108.6	0.96608	0.0088951	1.84	-
		3rd	120360	175.1	0.65842	0.0037595	2.68	-
	T2	1st	369090	104.0	0.82460	0.0079324	1.93	-
		2nd	399960	96.9	0.94728	0.0097805	1.76	-
		3rd	105660	195.8	0.56900	0.0029058	3.01	-
	U2	1st	-	-	-	-	-	-
		2nd	-	-	-	-	-	-
1st Set		3rd	-	-	-	-	-	-
Abilene R2	T2	1st	672460	91.9	1.11280	0.0121091	1.60	-
		2nd	292380	128.5	0.89180	0.0069428	2.05	-
		3rd	403490	104.7	1.16860	0.0111574	1.66	-
	U1	1st	625320	89.2	1.10620	0.0124080	1.59	-
		2nd	183730	147.9	0.77932	0.0052682	2.31	-
		3rd	48292	312.2	0.23772	0.0007614	5.42	-
	U2	1st	615090	90.7	1.01606	0.0112054	1.66	-
		2nd	142610	171.0	0.68296	0.0039943	2.61	-
2nd Set		3rd	45139	300.4	0.24168	0.0008046	5.29	-
Abilene R2	T1	1st	795480	79.3	1.15720	0.0145892	1.48	-
		2nd	168710	150.1	0.69274	0.0046163	2.45	-
		3rd	88568	212.5	0.48030	0.0022602	3.36	-
	T2	1st	798450	81.6	1.06100	0.0129967	1.55	-
		2nd	74877	241.4	0.38888	0.0016108	3.90	-
		3rd	15901	607.5	0.04309	0.0000709	15.39	-

[a] η' and G' are measured at 44.7 °C, 10 rad/s and converted by TTSP to 15 °C, 0.005 rad/s

Table A-3. Recovered Binder Properties for the Atlanta IH 20 CM Cores [a]

	Replicate	layer	η* (poise) @ 60 °C 0.1 rad/s	η'/G' (s) @ 15 °C 0.005 rad/s	G' (MPa) @ 15 °C 0.005 rad/s	G'/(η'/G') (MPa/s) @ 15 °C 0.005 rad/s	Calculated Ductility (cm) -	Carbonyl Area -
Atlanta IH 20 CM	U1	1st	1886200	105.6	0.87602	0.0082974	1.89	-
		2nd	837260	128.5	0.69968	0.0054433	2.28	-
		3rd	748980	139.5	0.66972	0.0048020	2.41	-
	U2	1st	1783500	101.6	0.85266	0.0083953	1.88	-
		2nd	629330	148.7	0.48604	0.0032687	2.85	-
		3rd	647580	151.8	0.56948	0.0037516	2.69	-
	T1	1st	745790	142.5	0.56650	0.0039765	2.62	-
		2nd	738040	140.8	0.67632	0.0048043	2.41	-
		3rd	1090000	112.7	0.79788	0.0070782	2.03	-
	T2	1st	1504400	107.6	0.74070	0.0068814	2.06	-
		2nd	1001500	120.3	0.81866	0.0068058	2.07	-
		3rd	852270	128.3	0.71786	0.0055940	2.25	-

[a] η' and G' are measured at 44.7 °C, 10 rad/s and converted by TTSP to 15 °C, 0.005 rad/s

Table A-4. Recovered Binder Properties for the Atlanta IH 20 DG Cores [a]

	Replicate	layer	η* (poise) @ 60 °C 0.1 rad/s	η'/G' (s) @ 15 °C 0.005 rad/s	G' (MPa) @ 15 °C 0.005 rad/s	G'/(η'/G') (MPa/s) @ 15 °C 0.005 rad/s	Calculated Ductility (cm) -	Carbonyl Area -
Atlanta IH 20 DG	U1	1st	2373400	84.7	0.95704	0.0113055	1.65	-
		2nd	1099000	120.2	0.73168	0.0060861	2.17	-
		3rd	485730	178.9	0.43102	0.0024091	3.26	-
	U2	1st	3060100	80.7	1.03380	0.0128104	1.56	-
		2nd	1012900	129.2	0.73284	0.0056709	2.24	-
		3rd	512220	88.3	0.39318	0.0044504	2.49	-
	T1	1st	2074700	89.7	0.96692	0.0107801	1.69	-
		2nd	1752500	94.8	0.91668	0.0096729	1.77	-
		3rd	959760	128.2	0.70002	0.0054615	2.28	-
	T2	1st	2077800	96.4	1.04840	0.0108779	1.68	-
		2nd	1693700	98.5	0.89534	0.0090855	1.82	-
		3rd	1151200	120.1	0.64038	0.0053333	2.30	-

[a] η' and G' are measured at 44.7 °C, 10 rad/s and converted by TTSP to 15 °C, 0.005 rad/s

Table A-5. Recovered Binder Properties for the Atlanta IH 20 SP Cores [a]

	Replicate	layer	η* (poise) @ 60 °C 0.1 rad/s	η'/G' (s) @ 15 °C 0.005 rad/s	G' (MPa) @ 15 °C 0.005 rad/s	G'/(η'/G') (MPa/s) @ 15 °C 0.005 rad/s	Calculated Ductility (cm) -	Carbonyl Area -
Atlanta IH 20 SP	U1	1st	1706300	105.5	0.69292	0.0065708	2.10	-
		2nd	635160	157.1	0.50900	0.0032406	2.86	-
		3rd	180200	226.2	0.15508	0.0006856	5.67	-
	U2	1st	2131300	94.5	0.84744	0.0089666	1.83	-
		2nd	672120	150.8	0.45770	0.0030354	2.95	-
		3rd	358440	188.3	0.25116	0.0013336	4.23	-
	T1	1st	1507100	111.4	0.82980	0.0074469	1.99	-
		2nd	1278900	117.4	0.76616	0.0065277	2.10	-
		3rd	882580	136.7	0.60176	0.0044023	2.50	-
	T2	1st	1324600	112.2	0.75448	0.0067267	2.08	-
		2nd	1185300	119.5	0.73682	0.0061677	2.16	-
		3rd	928920	136.7	0.53664	0.0039269	2.63	-

[a] η' and G' are measured at 44.7 °C, 10 rad/s and converted by TTSP to 15 °C, 0.005 rad/s

Table A-6. Recovered Binder Properties for the Atlanta US 67 Cores [a]

	Replicate	layer	η* (poise) @ 60 °C 0.1 rad/s	η'/G' (s) @ 15 °C 0.005 rad/s	G' (MPa) @ 15 °C 0.005 rad/s	G'/(η'/G') (MPa/s) @ 15 °C 0.005 rad/s	Calculated Ductility (cm) -	Carbonyl Area -
Atlanta US 67	U1	1st	62856	327.7	0.08516	0.0002599	8.69	-
		2nd	58530	354.9	0.08859	0.0002496	8.85	-
		3rd	51932	365.1	0.07132	0.0001953	9.86	-
	U2	1st	70528	321.3	0.11212	0.0003489	7.64	-
		2nd	53257	356.1	0.08763	0.0002461	8.91	-
		3rd	65126	341.6	0.10168	0.0002976	8.19	-
	T1	1st	31275	348.6	0.03191	0.0000915	13.76	-
		2nd	58231	354.1	0.09313	0.0002630	8.65	-
		3rd	57627	351.7	0.07638	0.0002172	9.41	-
	T2	1st	198630	218.3	0.29114	0.0013335	4.23	-
		2nd	107110	275.2	0.16914	0.0006145	5.95	-
		3rd	109230	273.9	0.18948	0.0006918	5.65	-

[a] η' and G' are measured at 44.7 °C, 10 rad/s and converted by TTSP to 15 °C, 0.005 rad/s

Table A-7. Recovered Binder Properties for the Carrizo Springs Airport Cores [a]

	Replicate	layer	η* (poise) @ 60 °C 0.1 rad/s	η'/G' (s) @ 15 °C 0.005 rad/s	G' (MPa) @ 15 °C 0.005 rad/s	G'/(η'/G') (MPa/s) @ 15 °C 0.005 rad/s	Calculated Ductility (cm) -	Carbonyl Area -
	U3	1st	899570	111.7	0.61624	0.0055190	2.27	1.505
1st Set		2nd	216370	182.7	0.25916	0.0014183	4.12	1.298
Carrizo		3rd	180880	190.3	0.25316	0.0013303	4.24	1.234
Springs	T3	1st	4042600	52.0	1.50060	0.0288352	1.09	1.999
Airport		2nd	303470	171.7	0.36346	0.0021169	3.45	0.930
		3rd	236010	184.5	0.30800	0.0016691	3.84	1.182
	U1	1st	780050	112.3	0.64966	0.0057838	2.22	-
		2nd	317180	157.1	0.41498	0.0026409	3.13	-
		3rd	323710	156.6	0.40464	0.0025839	3.16	-
	U2	1st	1329400	91.1	0.78130	0.0085778	1.87	-
2nd Set		2nd	294550	167.5	0.33892	0.0020229	3.52	-
Carrizo		3rd	254890	177.4	0.31284	0.0017630	3.74	-
Springs	T1	1st	920540	102.2	0.74354	0.0072721	2.01	-
Airport		2nd	308890	154.1	0.34830	0.0022599	3.36	-
		3rd	380430	149.4	0.34174	0.0022881	3.34	-
	T2	1st	1452400	82.3	0.81868	0.0099465	1.75	-
		2nd	309000	153.5	0.46710	0.0030430	2.94	-
		3rd	350370	149.5	0.39176	0.0026201	3.15	-

[a] η' and G' are measured at 44.7 °C, 10 rad/s and converted by TTSP to 15 °C, 0.005 rad/s

Table A-8. Recovered Binder Properties for the Fort Worth FM 4 (2000) Cores [a]

	Replicate	layer	η* (poise) @ 60 °C 0.1 rad/s	η'/G' (s) @ 15 °C 0.005 rad/s	G' (MPa) @ 15 °C 0.005 rad/s	G'/(η'/G') (MPa/s) @ 15 °C 0.005 rad/s	Calculated Ductility (cm) -	Carbonyl Area -
1st Set Fort Worth FM 4 (2000)	U1	1st	-	-	-	-	-	-
		2nd	-	-	-	-	-	-
		3rd	-	-	-	-	-	-
	U2	1st	-	-	-	-	-	-
		2nd	-	-	-	-	-	-
		3rd	-	-	-	-	-	-
	U3	1st	381620	145.1	0.50398	0.0034727	2.78	-
		2nd	155690	202.8	0.29034	0.0014318	4.10	-
		3rd	59988	310.4	0.12024	0.0003874	7.29	-
	T1	1st	-	-	-	-	-	-
		2nd	-	-	-	-	-	-
		3rd	-	-	-	-	-	-
	T2	1st	-	-	-	-	-	-
		2nd	-	-	-	-	-	-
		3rd	-	-	-	-	-	-
	T3	1st	1014500	92.5	0.86926	0.0093991	1.79	-
		2nd	236220	178.5	0.38708	0.0021683	3.42	-
		3rd	95660	229.1	0.19806	0.0008644	5.12	-
2nd Set Fort Worth FM 4 (2000)	U1	1st	706550	125.6	0.66642	0.0053048	2.31	-
		2nd	140390	210.9	0.30672	0.0014543	4.08	-
		3rd	48833	285.9	0.10612	0.0003712	7.43	-
	U2	1st	823710	106.6	0.80296	0.0075352	1.98	-
		2nd	205190	183.1	0.33814	0.0018464	3.67	-
		3rd	67656	261.9	0.13478	0.0005145	6.44	-
	U3	1st	-	-	-	-	-	-
		2nd	-	-	-	-	-	-
		3rd	-	-	-	-	-	-
	T1	1st	1052000	91.6	0.91402	0.0099746	1.75	-
		2nd	228760	186.5	0.39724	0.0021301	3.45	-
		3rd	64421	262.3	0.13746	0.0005241	6.39	-
	T2	1st	1050100	94.9	0.89972	0.0094851	1.79	-
		2nd	185120	194.7	0.32154	0.0016518	3.85	-
		3rd	58434	280.3	0.12622	0.0004503	6.83	-
	T3	1st	-	-	-	-	-	-
		2nd	-	-	-	-	-	-
		3rd	-	-	-	-	-	-

[a] η' and G' are measured at 44.7 °C, 10 rad/s and converted by TTSP to 15 °C, 0.005 rad/s

Table A-9. Recovered Binder Properties for the Fort Worth FM 4 (2003) Cores [a]

	Replicate	layer	η* (poise) @ 60 °C 0.1 rad/s	η'/G' (s) @ 15 °C 0.005 rad/s	G' (MPa) @ 15 °C 0.005 rad/s	G'/(η'/G') (MPa/s) @ 15 °C 0.005 rad/s	Calculated Ductility (cm) -	Carbonyl Area -
	U1	1st	-	-	-	-	-	-
		2nd	-	-	-	-	-	-
		3rd	-	-	-	-	-	-
	U2	1st	-	-	-	-	-	-
		2nd	-	-	-	-	-	-
		3rd	-	-	-	-	-	-
	U3	1st	464000	170.2	0.30868	0.0018140	3.70	-
1st Set		2nd	334330	170.8	0.32232	0.0018870	3.63	-
Fort Worth		3rd	58147	270.1	0.11410	0.0004225	7.02	-
FM 4	T1	1st	-	-	-	-	-	-
(2003)		2nd	-	-	-	-	-	-
		3rd	-	-	-	-	-	-
	T2	1st	-	-	-	-	-	-
		2nd	-	-	-	-	-	-
		3rd	-	-	-	-	-	-
	T3	1st	347080	179.8	0.32270	0.0017949	3.71	-
		2nd	289000	172.4	0.33770	0.0019584	3.58	-
		3rd	12609	500.2	0.02825	0.0000565	17.02	-
	U1	1st	477900	167.6	0.32066	0.0019138	3.61	-
		2nd	245030	172.3	0.30052	0.0017444	3.76	-
		3rd	22439	379.9	0.05860	0.0001542	10.94	-
	U2	1st	601030	164.4	0.33266	0.0020238	3.52	-
		2nd	223260	190.2	0.27232	0.0014321	4.10	-
		3rd	21087	391.6	0.04774	0.0001219	12.13	-
	U3	1st	-	-	-	-	-	-
2nd Set		2nd	-	-	-	-	-	-
Fort Worth		3rd	-	-	-	-	-	-
FM 4	T1	1st	492590	161.9	0.33664	0.0020789	3.48	-
(2003)		2nd	75378	264.3	0.12592	0.0004764	6.66	-
		3rd	7147	601.8	0.01594	0.0000265	23.75	-
	T2	1st	536880	157.5	0.38560	0.0024486	3.24	-
		2nd	173220	199.5	0.24718	0.0012388	4.37	-
		3rd	12834	406.6	0.02836	0.0000698	15.51	-
	T3	1st	-	-	-	-	-	-
		2nd	-	-	-	-	-	-
		3rd	-	-	-	-	-	-

[a] η' and G' are measured at 44.7 °C, 10 rad/s and converted by TTSP to 15 °C, 0.005 rad/s

Table A-10. Recovered Binder Properties for the Georgetown Airport (1989) Cores [a]

	Replicate	layer	η* (poise) @ 60 °C 0.1 rad/s	η'/G' (s) @ 15 °C 0.005 rad/s	G' (MPa) @ 15 °C 0.005 rad/s	G'/(η'/G') (MPa/s) @ 15 °C 0.005 rad/s	Calculated Ductility (cm) -	Carbonyl Area -
1st Set Georgetown Airport (1989)	U3	1st	790130	114.0	0.81358	0.0071358	2.02	1.507
		2nd	118480	221.9	0.29498	0.0013294	4.24	1.164
		3rd	80630	259.8	0.15328	0.0005899	6.06	1.079
	T3	1st	1206800	76.2	1.13040	0.0148375	1.47	1.805
		2nd	214240	177.4	0.35942	0.0020263	3.52	1.329
		3rd	121990	222.9	0.25286	0.0011342	4.55	1.192
2nd Set Georgetown Airport (1989)	U1	1st	1507900	88.3	1.01540	0.0114974	1.64	-
		2nd	123010	221.9	0.25406	0.0011448	4.53	-
		3rd	118470	223.4	0.23918	0.0010708	4.66	-
	U2	1st	1690900	79.6	0.87482	0.0109914	1.67	-
		2nd	104340	228.7	0.19442	0.0008503	5.16	-
		3rd	62569	275.5	0.14244	0.0005170	6.42	-
	T1	1st	1542500	84.5	0.97814	0.0115763	1.64	-
		2nd	123770	221.4	0.20618	0.0009314	4.96	-
		3rd	77549	258.7	0.16742	0.0006472	5.82	-
	T2	1st	2173100	72.7	1.16880	0.0160762	1.42	-
		2nd	144630	207.1	0.27072	0.0013070	4.27	-
		3rd	122310	221.4	0.22234	0.0010045	4.80	-

[a] η' and G' are measured at 44.7 °C, 10 rad/s and converted by TTSP to 15 °C, 0.005 rad/s

Table A-11. Recovered Binder Properties for the Georgetown Airport (1995) Cores [a]

	Replicate	layer	η* (poise) @ 60 °C 0.1 rad/s	η'/G' (s) @ 15 °C 0.005 rad/s	G' (MPa) @ 15 °C 0.005 rad/s	G'/(η'/G') (MPa/s) @ 15 °C 0.005 rad/s	Calculated Ductility (cm) -	Carbonyl Area -
1st Set Georgetown Airport (1995)	U3	1st	965240	105.0	0.75512	0.0071934	2.02	1.498
		2nd	181930	190.8	0.30408	0.0015939	3.91	1.207
		3rd	150970	201.7	0.24604	0.0012199	4.40	1.169
	T3	1st	1422100	64.9	0.99586	0.0153463	1.45	1.815
		2nd	256470	167.3	0.39716	0.0023734	3.29	1.289
		3rd	243840	164.7	0.37316	0.0022661	3.35	1.234
2nd Set Georgetown Airport (1995)	U1	1st	371850	156.9	0.42576	0.0027143	3.10	-
		2nd	80971	246.1	0.14460	0.0005876	6.07	-
		3rd	60333	276.8	0.11452	0.0004138	7.09	-
	U2	1st	500030	140.7	0.52998	0.0037672	2.68	-
		2nd	89043	240.4	0.16408	0.0006824	5.69	-
		3rd	88002	246.5	0.17084	0.0006929	5.65	-
	T1	1st	1510400	81.0	0.95328	0.0117640	1.62	-
		2nd	433840	145.9	0.48566	0.0033290	2.83	-
		3rd	303210	163.2	0.37096	0.0022728	3.35	-
	T2	1st	2272900	74.5	1.05040	0.0141085	1.50	-
		2nd	398220	151.6	0.45634	0.0030109	2.96	-
		3rd	242610	173.7	0.32246	0.0018560	3.66	-
	T1*	1st	1334400	84.7	0.95346	0.0112511	1.66	-
		2nd	281610	170.9	0.29530	0.0017275	3.78	-
		3rd	189090	183.5	0.30020	0.0016364	3.87	-
	T2*	1st	1426400	83.8	0.94650	0.0112948	1.65	-
		2nd	235480	176.6	0.35208	0.0019938	3.55	-
		3rd	206870	179.6	0.32116	0.0017886	3.72	-

[a] η' and G' are measured at 44.7 °C, 10 rad/s and converted by TTSP to 15 °C, 0.005 rad/s

Table A-12. Recovered Binder Properties for the Jacksonville Airport Cores [a]

	Replicate	layer	η* (poise) @ 60 °C 0.1 rad/s	η'/G' (s) @ 15 °C 0.005 rad/s	G' (MPa) @ 15 °C 0.005 rad/s	G'/(η'/G') (MPa/s) @ 15 °C 0.005 rad/s	Calculated Ductility (cm) -	Carbonyl Area -
1st Set Jacksonville Airport	U3	1st	164390	184.3	0.38792	0.0021050	3.46	1.408
		2nd	58562	284.2	0.19324	0.0006799	5.69	1.134
		3rd	61745	278.0	0.21472	0.0007723	5.38	1.098
	T3	1st	436970	106.9	0.83726	0.0078325	1.94	1.702
		2nd	28963	394.1	0.09951	0.0002525	8.80	0.929
		3rd	20391	472.7	0.05347	0.0001131	12.54	0.800
2nd Set Jacksonville Airport	U1	1st	114270	206.9	0.35354	0.0017087	3.80	-
		2nd	55221	291.5	0.18108	0.0006211	5.93	-
		3rd	45784	302.7	0.15494	0.0005118	6.45	-
	U2	1st	113480	211.1	0.33018	0.0015640	3.95	-
		2nd	57882	281.9	0.17314	0.0006142	5.95	-
		3rd	53273	293.8	0.18836	0.0006411	5.84	-
	T1	1st	275430	145.6	0.60354	0.0041454	2.57	-
		2nd	69099	258.3	0.24572	0.0009513	4.91	-
		3rd	71689	279.5	0.22194	0.0007940	5.32	-
	T2	1st	352760	127.2	0.78138	0.0061419	2.16	-
		2nd	71116	253.0	0.24968	0.0009869	4.83	-
		3rd	71191	258.4	0.24542	0.0009496	4.92	-

[a] η' and G' are measured at 44.7 °C, 10 rad/s and converted by TTSP to 15 °C, 0.005 rad/s

Table A-13. Recovered Binder Properties for the Lufkin BUS 59 Cores [a]

	Replicate	layer	η* (poise) @ 60 °C 0.1 rad/s	η'/G' (s) @ 15 °C 0.005 rad/s	G' (MPa) @ 15 °C 0.005 rad/s	G'/(η'/G') (MPa/s) @ 15 °C 0.005 rad/s	Calculated Ductility (cm) -	Carbonyl Area -
	U3	1st	159280	208.5	0.30096	0.0014437	4.09	-
1st Set		2nd	261990	178.9	0.47496	0.0026552	3.13	-
Lufkin		3rd	-	-	-	-	-	-
BUS 59	T3	1st	396920	119.5	0.83934	0.0070233	2.04	-
		2nd	127470	233.9	0.24554	0.0010497	4.70	-
		3rd	241870	187.2	0.40656	0.0021715	3.42	-
	U1	1st	767840	112.6	0.87468	0.0077687	1.95	-
		2nd	164000	200.1	0.36488	0.0018234	3.69	-
		3rd	288760	161.3	0.46630	0.0028905	3.01	-
	U2	1st	1089600	96.2	0.87620	0.0091053	1.82	-
2nd Set		2nd	310130	159.1	0.52024	0.0032708	2.85	-
Lufkin		3rd	541820	125.8	0.75250	0.0059817	2.19	-
BUS 59	T1	1st	204350	182.8	0.35196	0.0019252	3.60	-
		2nd	210750	183.1	0.36366	0.0019856	3.55	-
		3rd	597050	123.5	0.76314	0.0061814	2.16	-
	T2	1st	296510	158.1	0.50882	0.0032176	2.87	-
		2nd	241000	173.1	0.45370	0.0026211	3.14	-
		3rd	396470	142.8	0.62634	0.0043876	2.51	-

[a] η' and G' are measured at 44.7 °C, 10 rad/s and converted by TTSP to 15 °C, 0.005 rad/s

Table A-14. Recovered Binder Properties for the Odessa SH 149 Cores [a]

	Replicate	layer	η* (poise) @ 60 °C 0.1 rad/s	η'/G' (s) @ 15 °C 0.005 rad/s	G' (MPa) @ 15 °C 0.005 rad/s	G'/(η'/G') (MPa/s) @ 15 °C 0.005 rad/s	Calculated Ductility (cm) -	Carbonyl Area -
	U1	1st	59280	282.9	0.18842	0.0006659	5.75	-
		2nd	35333	337.8	0.13264	0.0003927	7.25	-
		3rd	59228	256.3	0.26510	0.0010345	4.73	-
	U2	1st	38470	344.2	0.11294	0.0003281	7.85	-
		2nd	46071	295.9	0.17214	0.0005818	6.10	-
Odessa		3rd	52603	265.2	0.24654	0.0009297	4.96	-
SH 149	T1	1st	49228	310.9	0.15010	0.0004828	6.62	-
		2nd	42024	316.5	0.14068	0.0004445	6.87	-
		3rd	133420	174.8	0.47526	0.0027182	3.09	-
	T2	1st	61504	284.4	0.18676	0.0006567	5.78	-
		2nd	34323	340.9	0.10790	0.0003165	7.97	-
		3rd	83301	220.7	0.31088	0.0014086	4.13	-

[a] η' and G' are measured at 44.7 °C, 10 rad/s and converted by TTSP to 15 °C, 0.005 rad/s

Table A-15. Recovered Binder Properties for the Odessa SH 349 Cores [a]

	Replicate	layer	η* (poise) @ 60 °C 0.1 rad/s	η'/G' (s) @ 15 °C 0.005 rad/s	G' (MPa) @ 15 °C 0.005 rad/s	G'/(η'/G') (MPa/s) @ 15 °C 0.005 rad/s	Calculated Ductility (cm) -	Carbonyl Area -
Odessa SH 349	U1	1st	13634	517.8	0.02292	0.0000443	18.94	-
		2nd	116640	198.7	0.44624	0.0022462	3.37	-
		3rd	134760	179.8	0.48686	0.0027075	3.10	-
	U2	1st	19724	445.6	0.03742	0.0000840	14.29	-
		2nd	293770	124.7	0.86702	0.0069535	2.05	-
		3rd	184210	162.0	0.51488	0.0031785	2.89	-
	T1	1st	36527	361.9	0.10314	0.0002850	8.35	-
		2nd	51192	285.4	0.22170	0.0007767	5.37	-
		3rd	46099	304.5	0.16690	0.0005481	6.26	-
	T2	1st	17991	476.7	0.03113	0.0000653	15.96	-
		2nd	93448	218.0	0.35120	0.0016108	3.90	-
		3rd	56594	278.1	0.23078	0.0008298	5.22	-

[a] η' and G' are measured at 44.7 °C, 10 rad/s and converted by TTSP to 15 °C, 0.005 rad/s

Table A-16. Recovered Binder Properties for the Pleasanton Airport Cores [a]

	Replicate	layer	η* (poise) @ 60 °C 0.1 rad/s	η'/G' (s) @ 15 °C 0.005 rad/s	G' (MPa) @ 15 °C 0.005 rad/s	G'/(η'/G') (MPa/s) @ 15 °C 0.005 rad/s	Calculated Ductility (cm) -	Carbonyl Area -
1st Set Pleasanton Airport	U3	1st	321790	165.5	0.42332	0.0025577	3.18	1.203
		2nd	40917	329.7	0.07858	0.0002383	9.03	0.805
		3rd	18239	430.0	0.03333	0.0000775	14.81	0.645
	T3	1st	2051100	76.3	0.91082	0.0119345	1.61	1.366
		2nd	155790	211.8	0.21972	0.0010374	4.73	0.990
		3rd	124980	219.0	0.22292	0.0010180	4.77	0.957
2nd Set Pleasanton Airport	U1	1st	-	-	-	-	-	-
		2nd	-	-	-	-	-	-
		3rd	-	-	-	-	-	-
	U2	1st	-	-	-	-	-	-
		2nd	-	-	-	-	-	-
		3rd	-	-	-	-	-	-
	T1	1st	1055800	108.8	0.73324	0.0067367	2.08	-
		2nd	176090	200.3	0.26320	0.0013143	4.26	-
		3rd	128100	215.1	0.21536	0.0010014	4.80	-
	T2	1st	1356700	98.4	0.76246	0.0077513	1.95	-
		2nd	156370	203.1	0.24982	0.0012302	4.39	-
		3rd	135670	210.6	0.21524	0.0010218	4.76	-

[a] η' and G' are measured at 44.7 °C, 10 rad/s and converted by TTSP to 15 °C, 0.005 rad/s

Table A-17. Recovered Binder Properties for the Tyler US 79 Cores [a]

	Replicate	layer	η* (poise) @ 60 °C 0.1 rad/s	η'/G' (s) @ 15 °C 0.005 rad/s	G' (MPa) @ 15 °C 0.005 rad/s	G'/(η'/G') (MPa/s) @ 15 °C 0.005 rad/s	Calculated Ductility (cm) -	Carbonyl Area -
Tyler US 79	U1	1st	2008400	116.9	0.64078	0.0054820	2.27	-
		2nd	492840	189.0	0.25632	0.0013563	4.20	-
		3rd	440750	197.8	0.22548	0.0011398	4.54	-
	U2	1st	2592600	103.2	0.85716	0.0083050	1.89	-
		2nd	534150	188.2	0.27072	0.0014384	4.10	-
		3rd	428190	200.9	0.19908	0.0009908	4.82	-
	T1	1st	2590800	99.6	0.81124	0.0081409	1.91	-
		2nd	568700	181.5	0.28150	0.0015506	3.96	-
		3rd	553310	181.7	0.28272	0.0015562	3.96	-
	T2	1st	1981400	114.7	0.69816	0.0060855	2.17	-
		2nd	529270	184.7	0.25966	0.0014061	4.14	-
		3rd	461200	187.0	0.21538	0.0011517	4.52	-

[a] η' and G' are measured at 44.7 °C, 10 rad/s and converted by TTSP to 15 °C, 0.005 rad/s

APPENDIX B

VISCOSITY MASTER CURVES OF RECOVERED ASPHALT BINDERS

FROM CHAPTER II

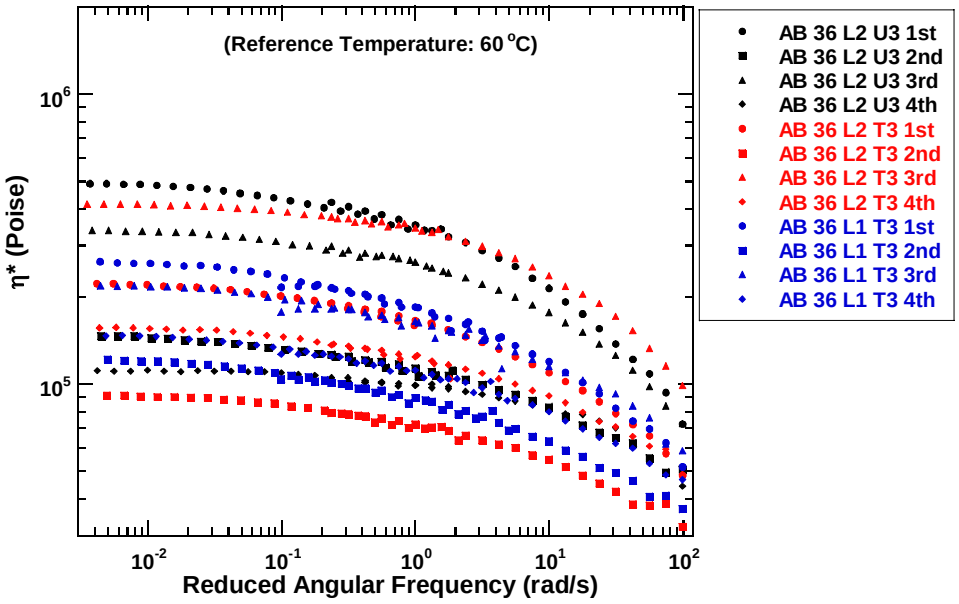

Figure B-1. Complex Viscosity Master Curves

Abilene SH 36 L1 T3, Abilene SH 36 L2 U3 and T3

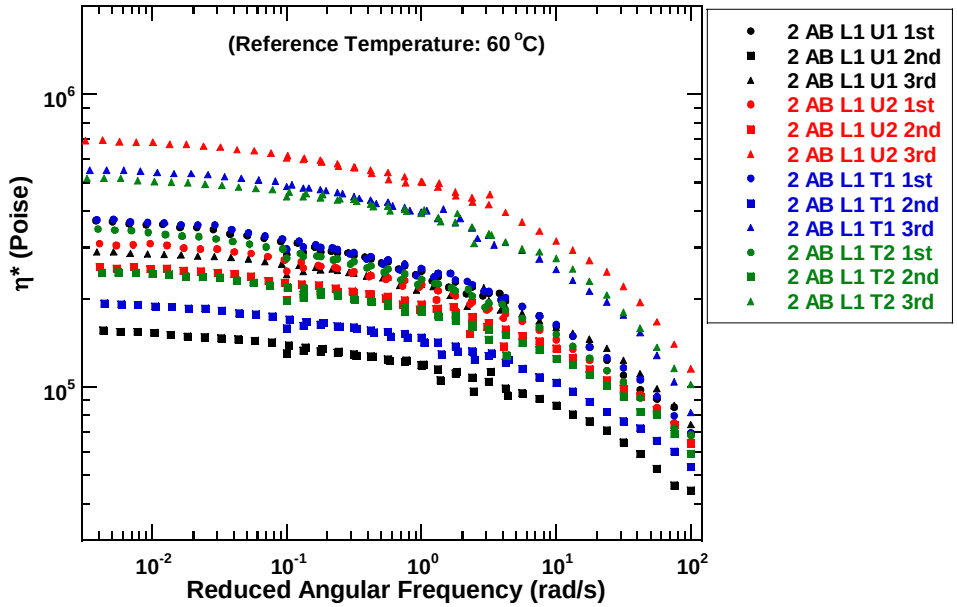

Figure B-2. Complex Viscosity Master Curves 2nd Set

Abilene SH 36 L1 U1, U2, T1, and T2

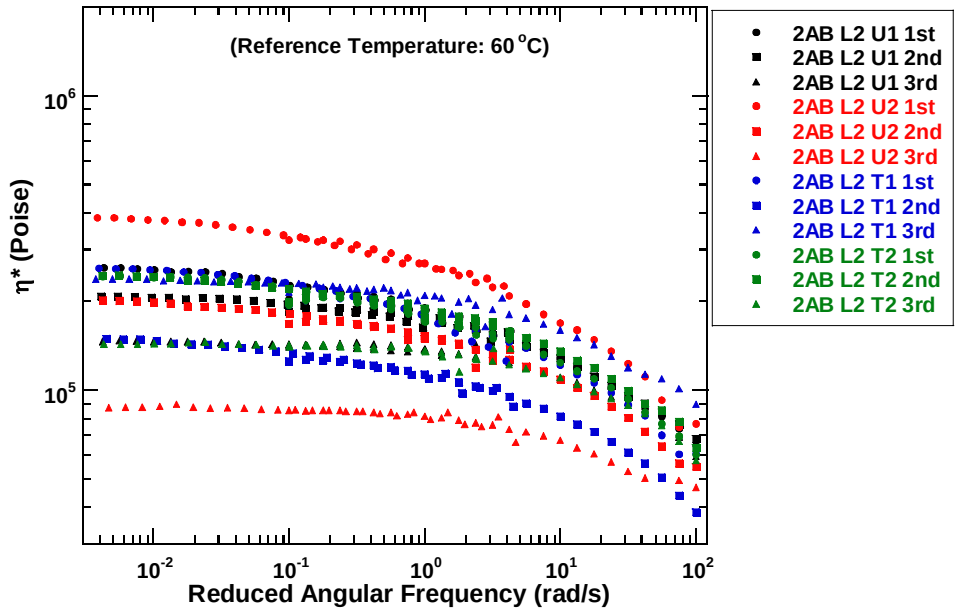

Figure B-3. Complex Viscosity Master Curves 2nd Set

Abilene SH 36 L2 U1, U2, T1, and T2

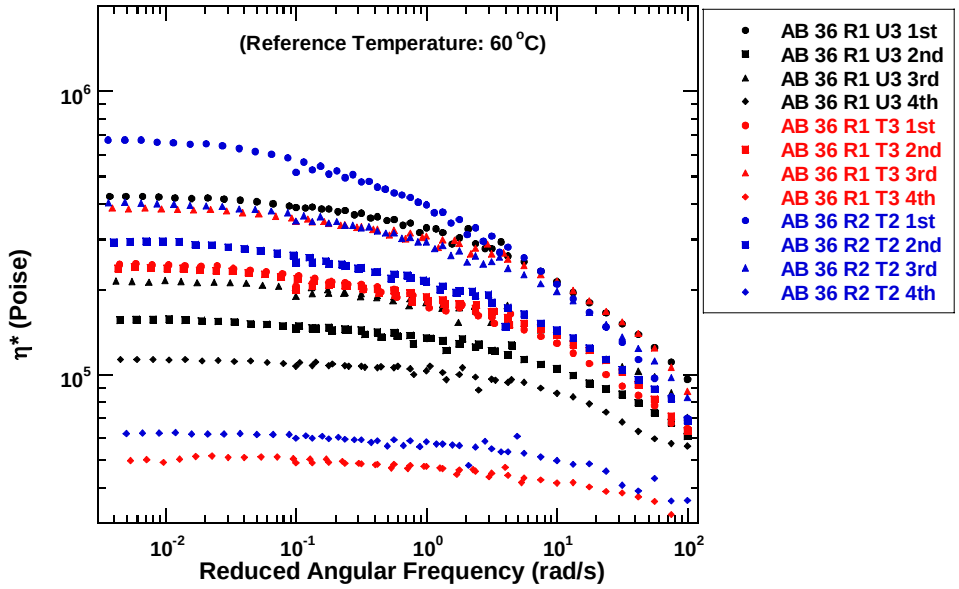

Figure B-4. Complex Viscosity Master Curves

Abilene SH 36 R1 U3 and T3, Abilene SH 36 R2 T2

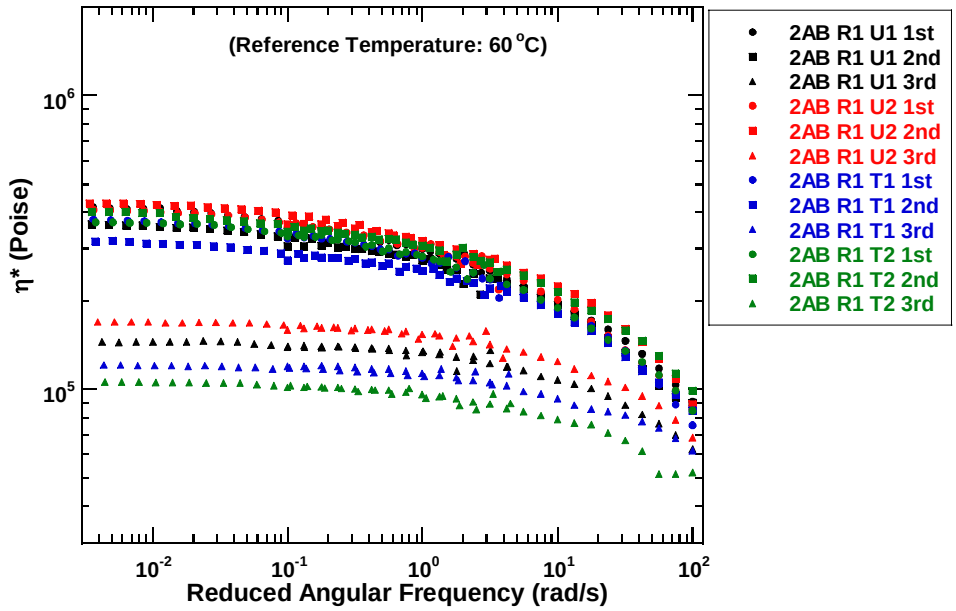

Figure B-5. Complex Viscosity Master Curves 2nd Set

Abilene SH 36 R1 U1, U2, T1, and T2

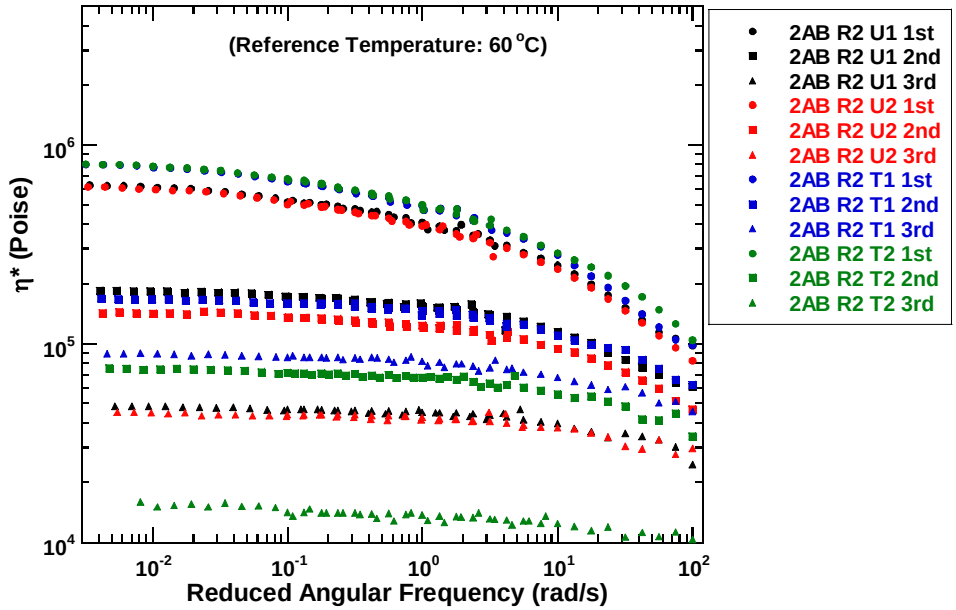

Figure B-6. Complex Viscosity Master Curves 2nd Set

Abilene SH 36 R2 U1, U2, T1, and T2

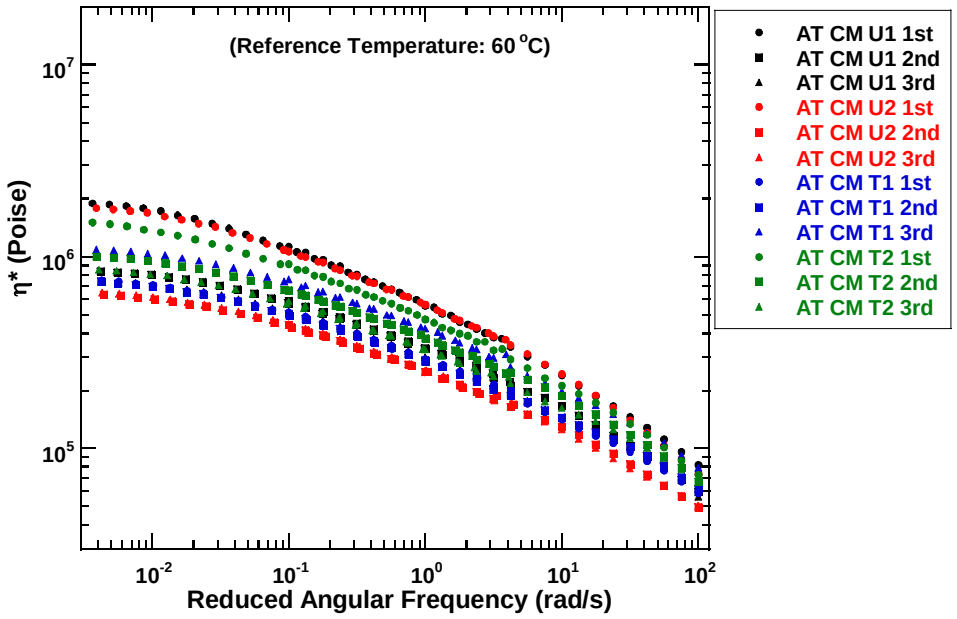

Figure B-7. Complex Viscosity Master Curves

Atlanta IH 20 CM U1, U2, T1, and T2

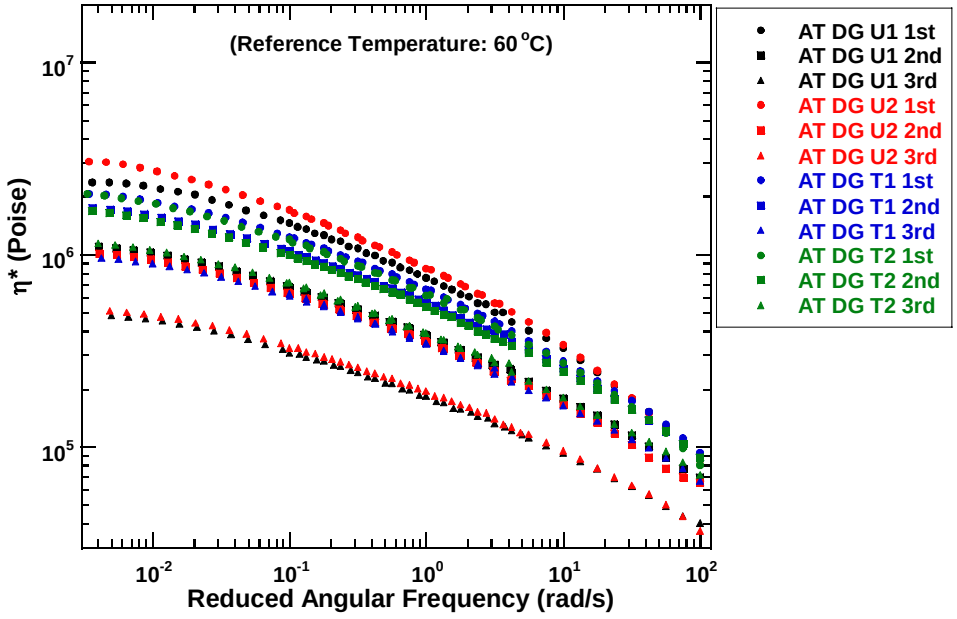

Figure B-8. Complex Viscosity Master Curves

Atlanta IH 20 DG U1, U2, T1, and T2

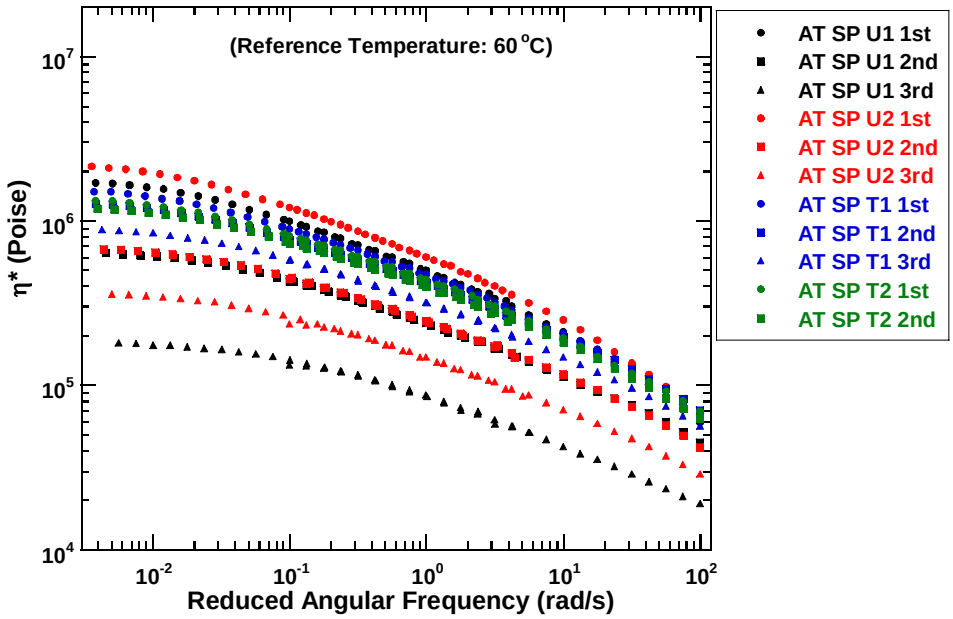

Figure B-9. Complex Viscosity Master Curves

Atlanta IH 20 SP U1, U2, T1, and T2

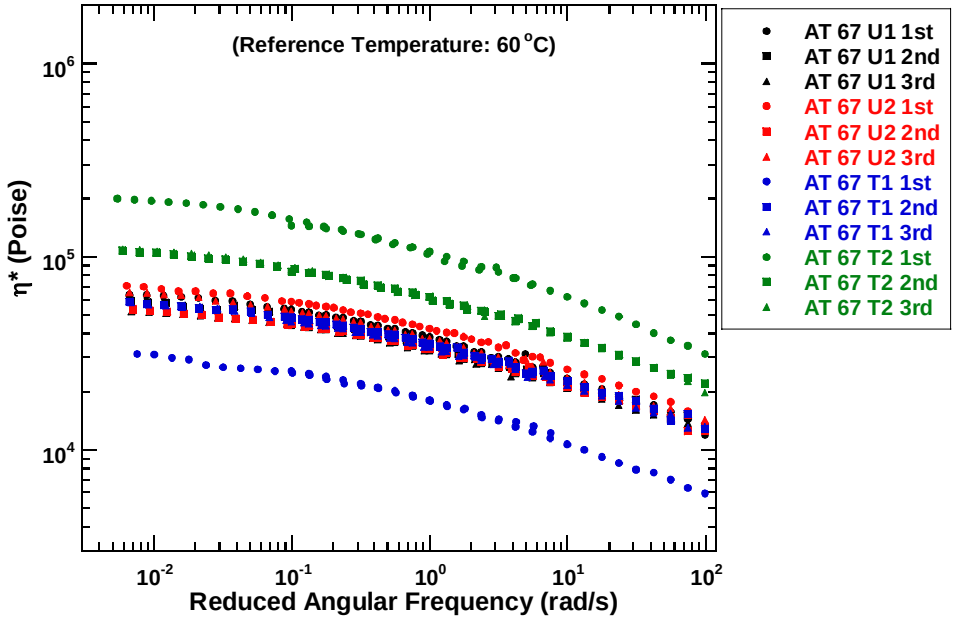

Figure B-10. Complex Viscosity Master Curves

Atlanta US 67 U1, U2, T1, and T2

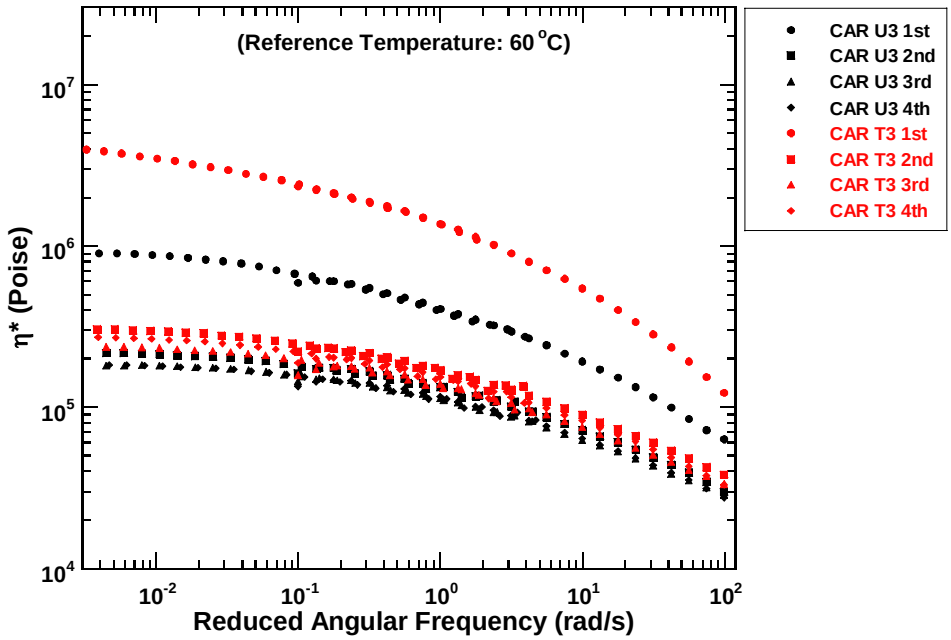

Figure B-11. Complex Viscosity Master Curves

Carrizo Springs Airport U3 and T3

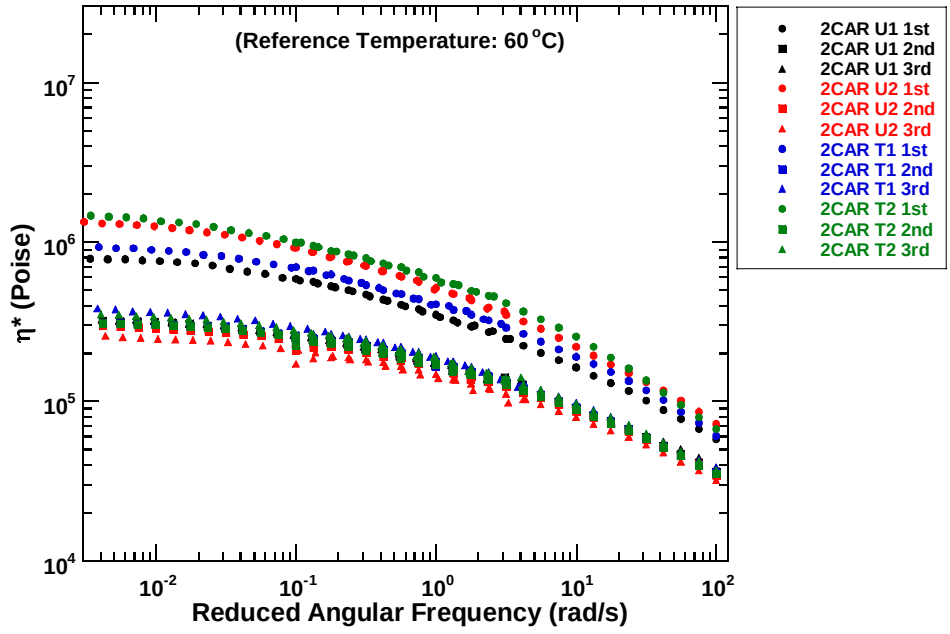

Figure B-12. Complex Viscosity Master Curves 2nd Set

Carrizo Springs Airport U1, U2, T1, and T2

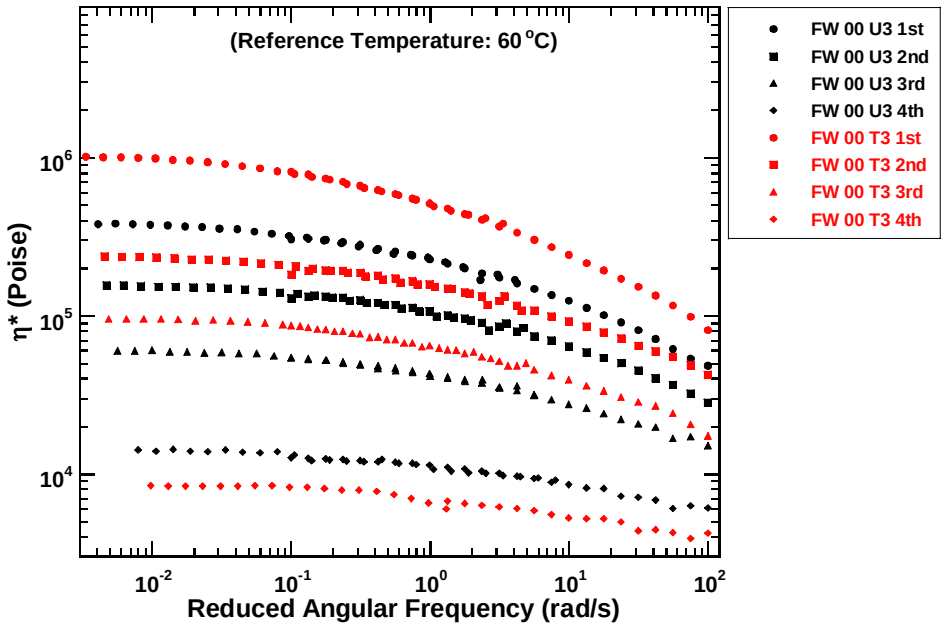

Figure B-13. Complex Viscosity Master Curves

Fort Worth FM 4 (2000) U3 and T3

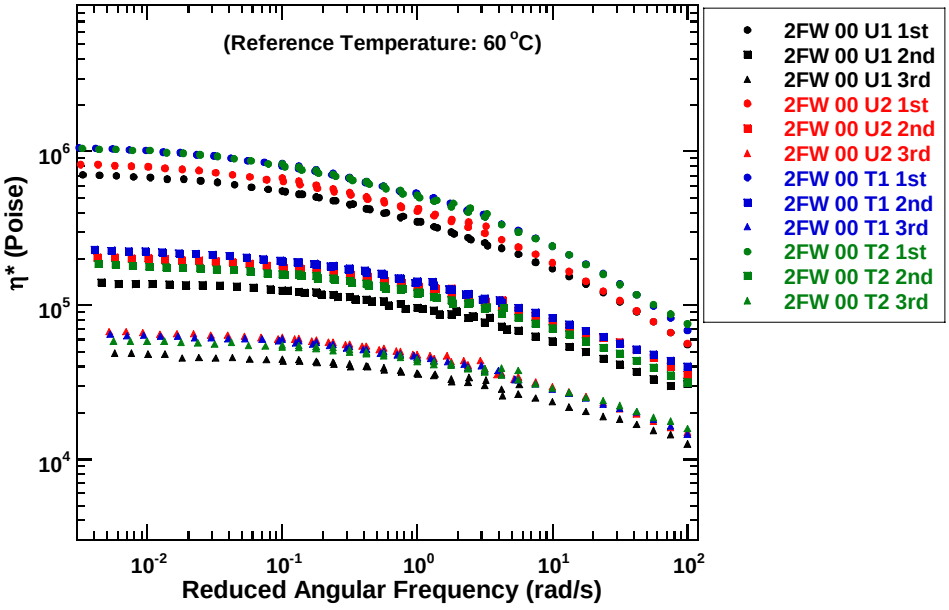

Figure B-14. Complex Viscosity Master Curves 2nd Set

Fort Worth FM 4 (2000) U1, U2, T1, and T2

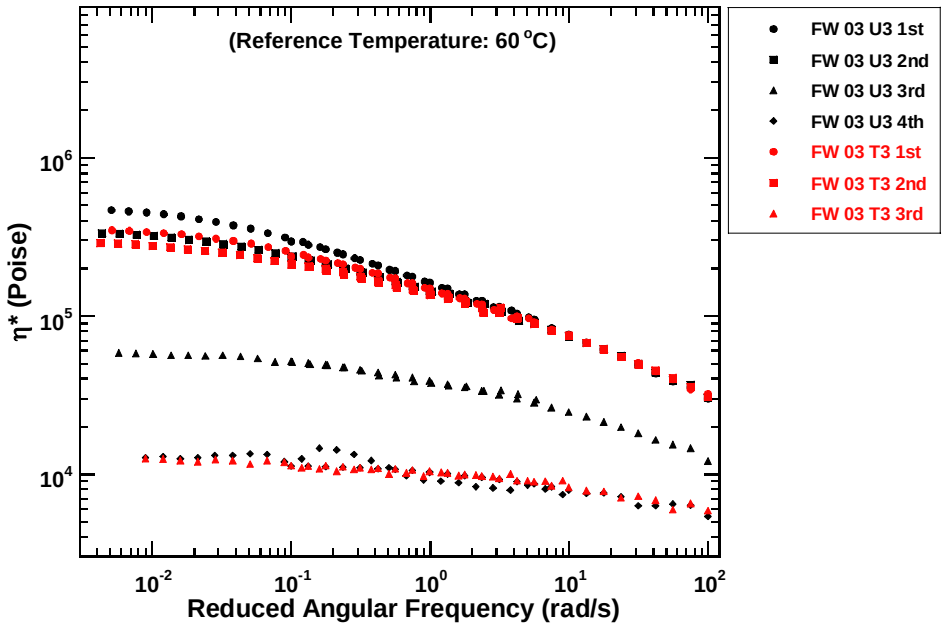

Figure B-15. Complex Viscosity Master Curves

Fort Worth FM 4 (2003) U3 and T3

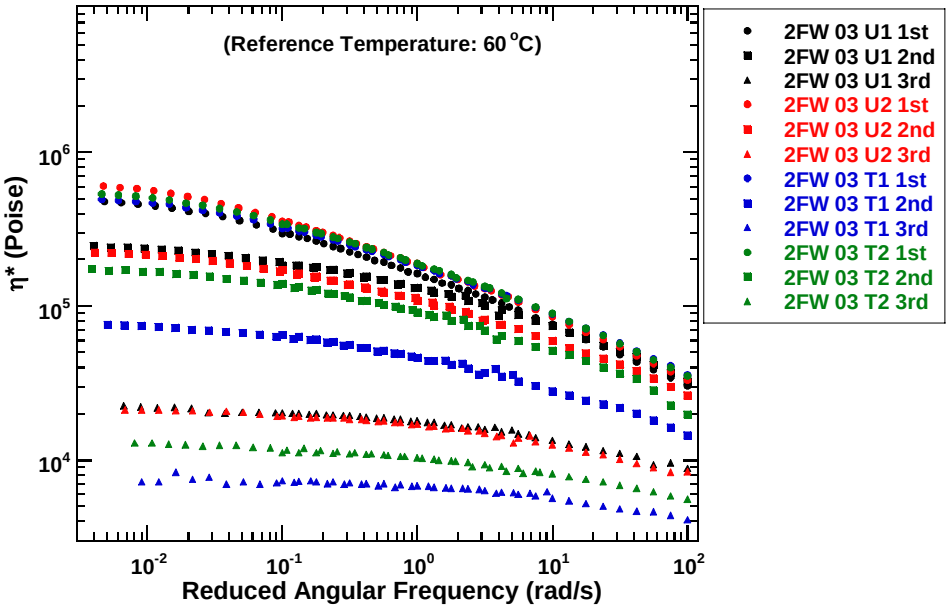

Figure B-16. Complex Viscosity Master Curves 2nd Set

Fort Worth FM 4 (2003) U1, U2, T1, and T2

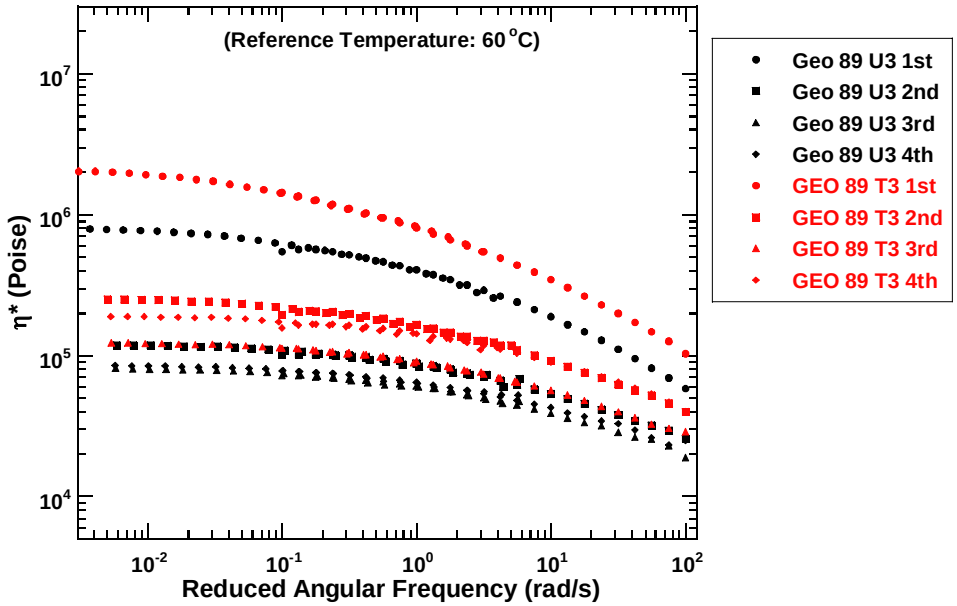

Figure B-17. Complex Viscosity Master Curves

Georgetown Airport (1989) U3 and T3

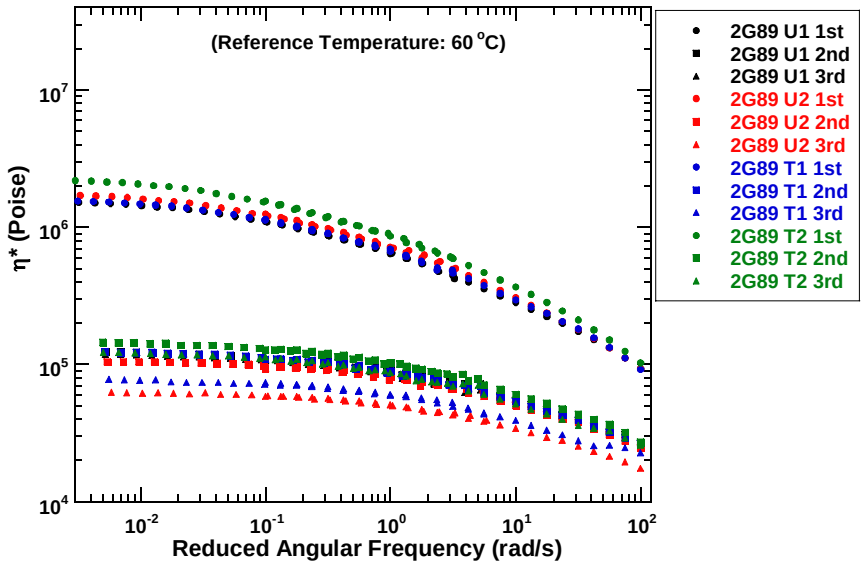

Figure B-18. Complex Viscosity Master Curves 2nd Set

Georgetown Airport (1989) U1, U2, T1, and T2

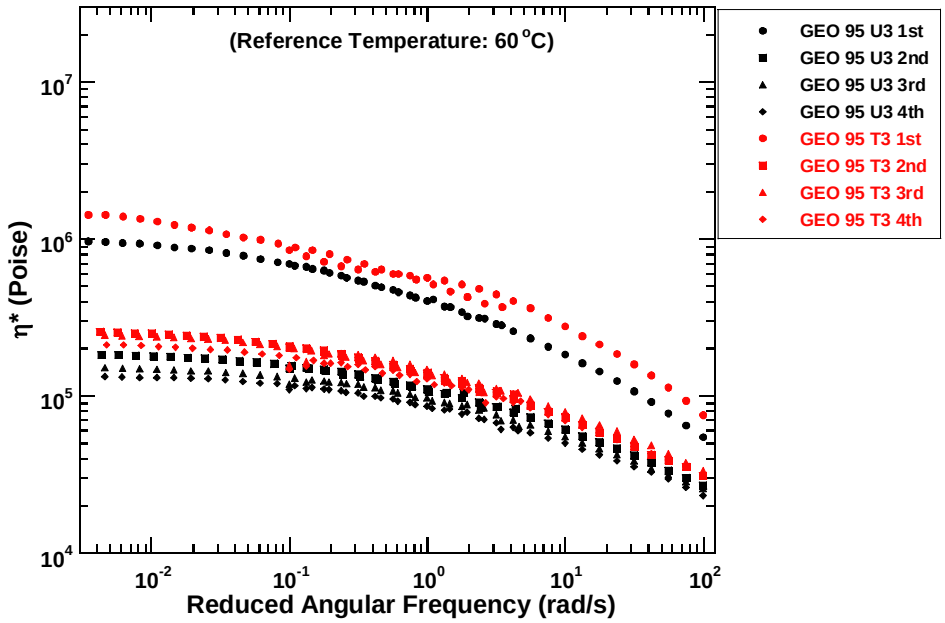

Figure B-19. Complex Viscosity Master Curves

Georgetown Airport (1995) U3 and T3

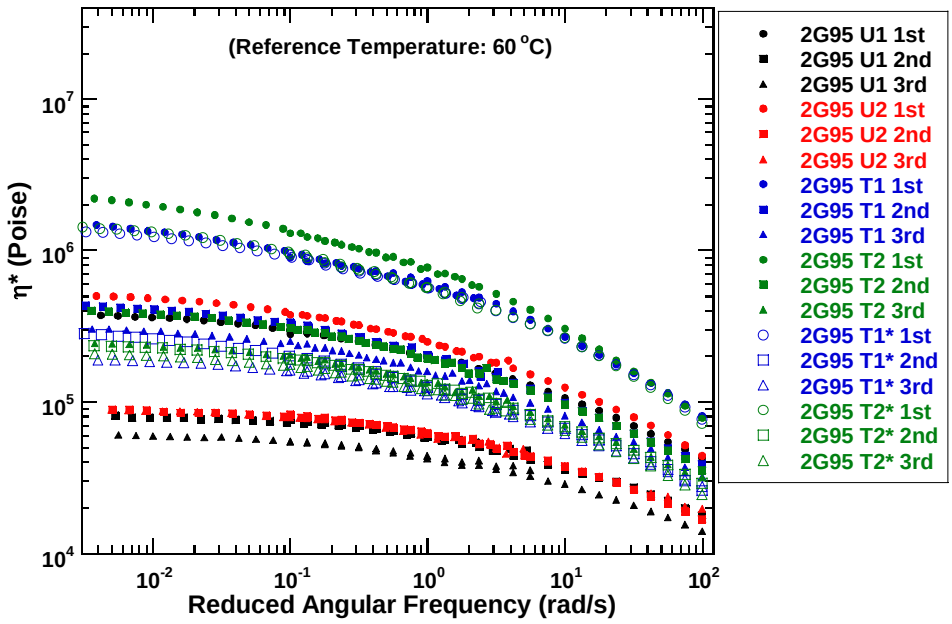

Figure B-20. Complex Viscosity Master Curves 2nd Set

Georgetown Airport (1995) U1, U2, T1, T2, T1*, and T2*

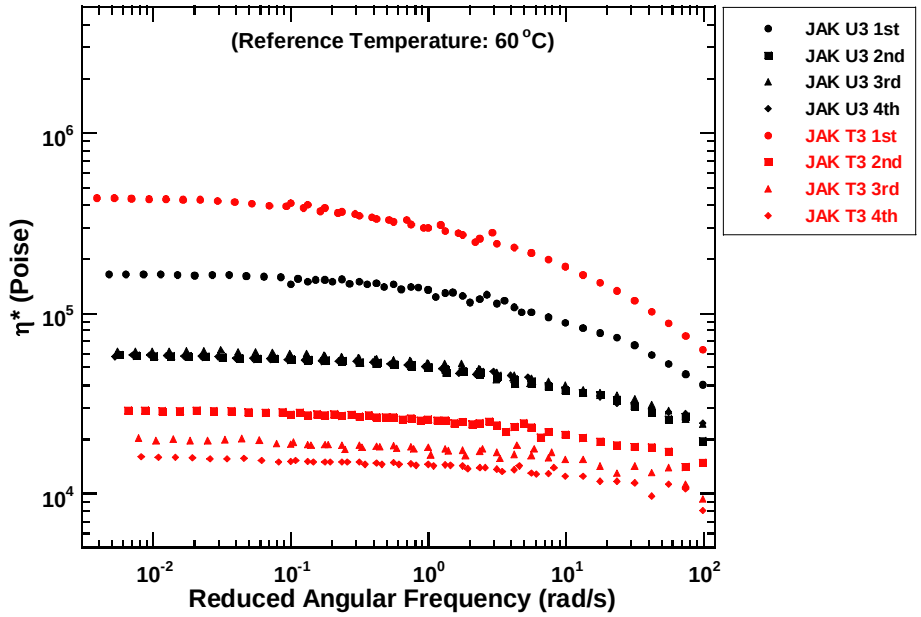

Figure B-21. Complex Viscosity Master Curves

Jacksonville Airport U3 and T3

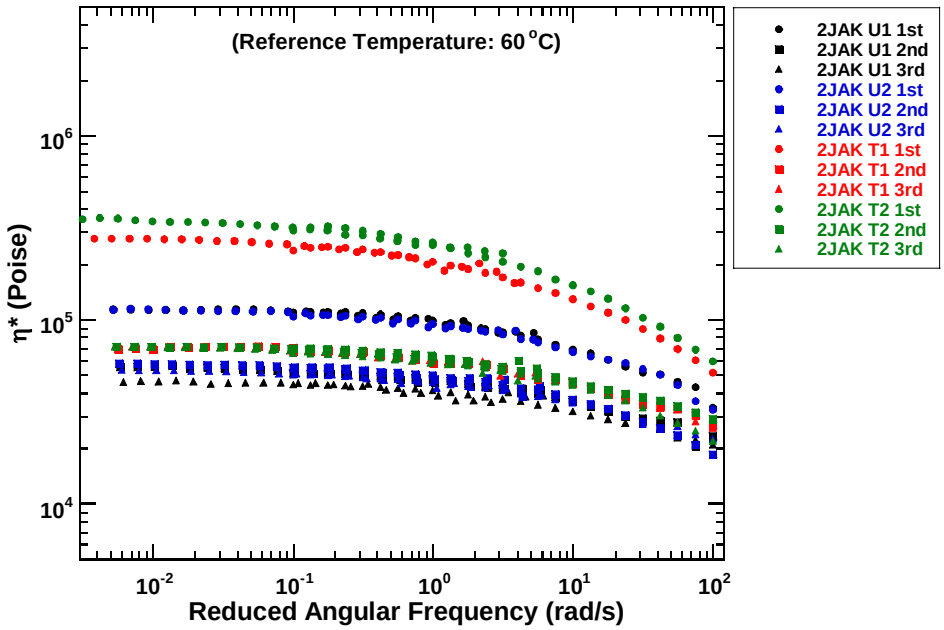

Figure B-22. Complex Viscosity Master Curves 2nd Set

Jacksonville Airport U1, U2, T1, and T2

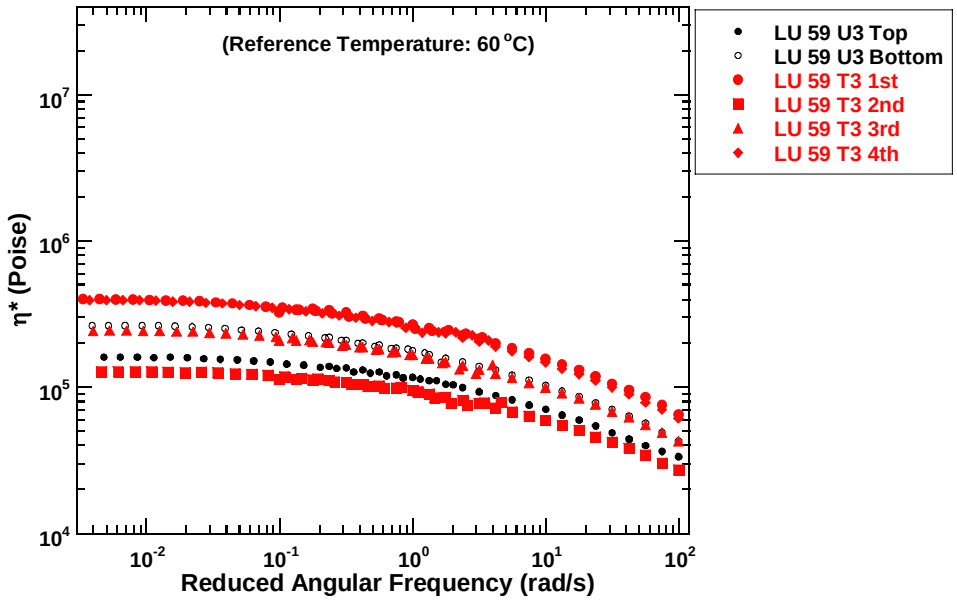

Figure B-23. Complex Viscosity Master Curves

Lufkin BUS 59 U3 and T3

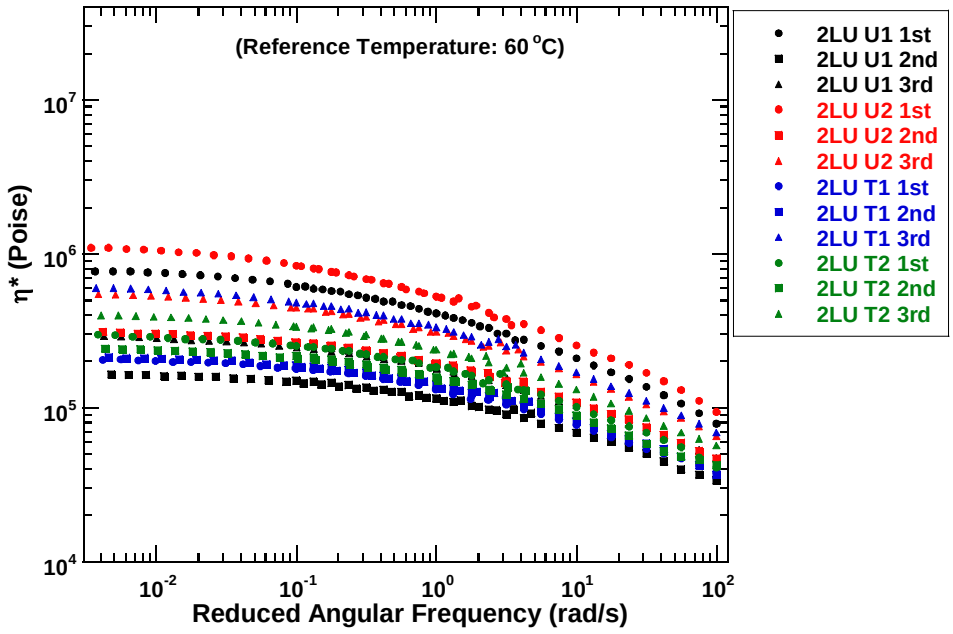

Figure B-24. Complex Viscosity Master Curves 2nd Set

Lufkin BUS 59 U1, U2, T1, and T2

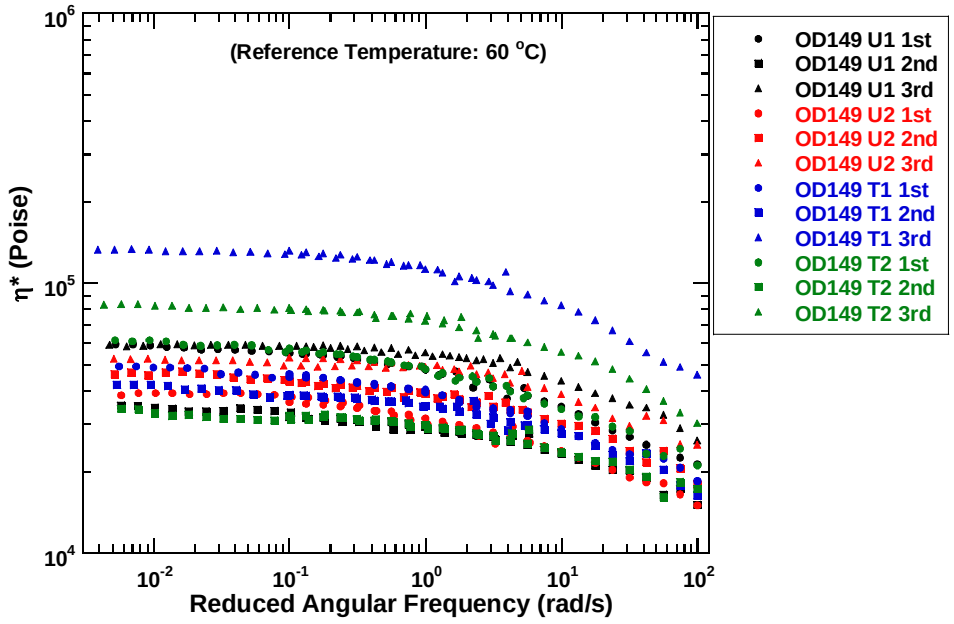

Figure B-25. Complex Viscosity Master Curves

Odessa SH 149 U1, U2, T1, and T2

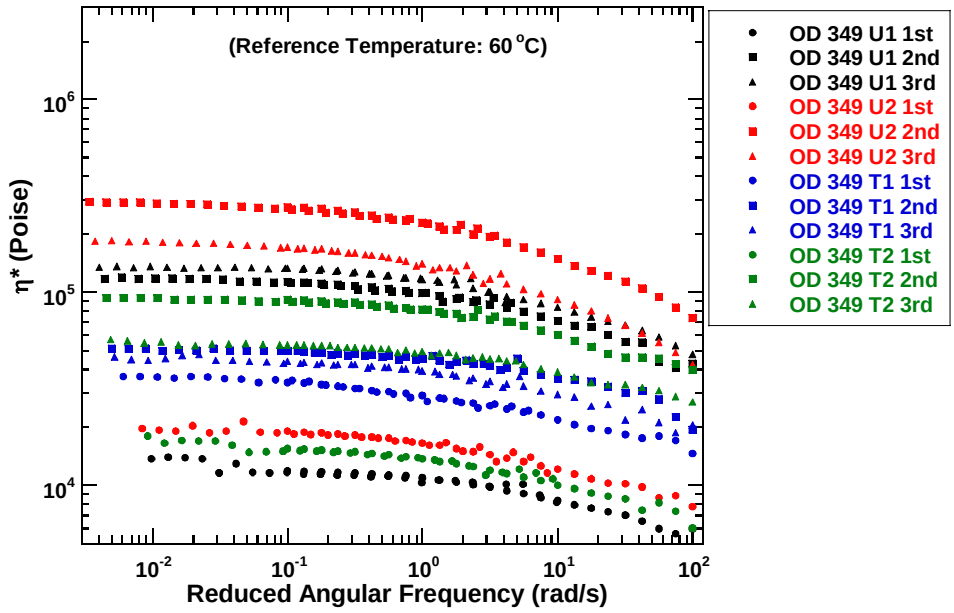

Figure B-26. Complex Viscosity Master Curves

Odessa SH 349 U1, U2, T1, and T2

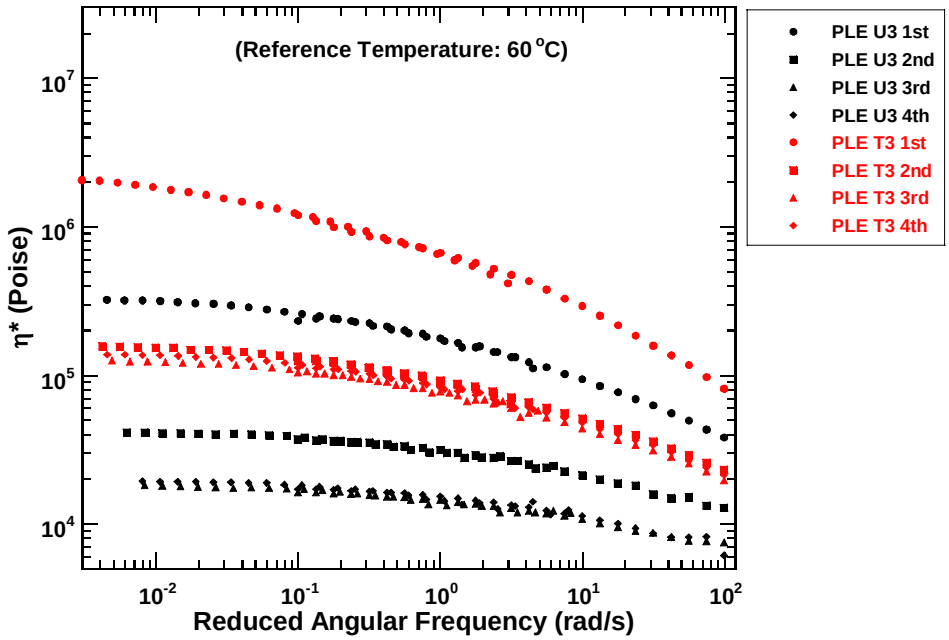

Figure B-27. Complex Viscosity Master Curves

Pleasanton Airport U3 and T3

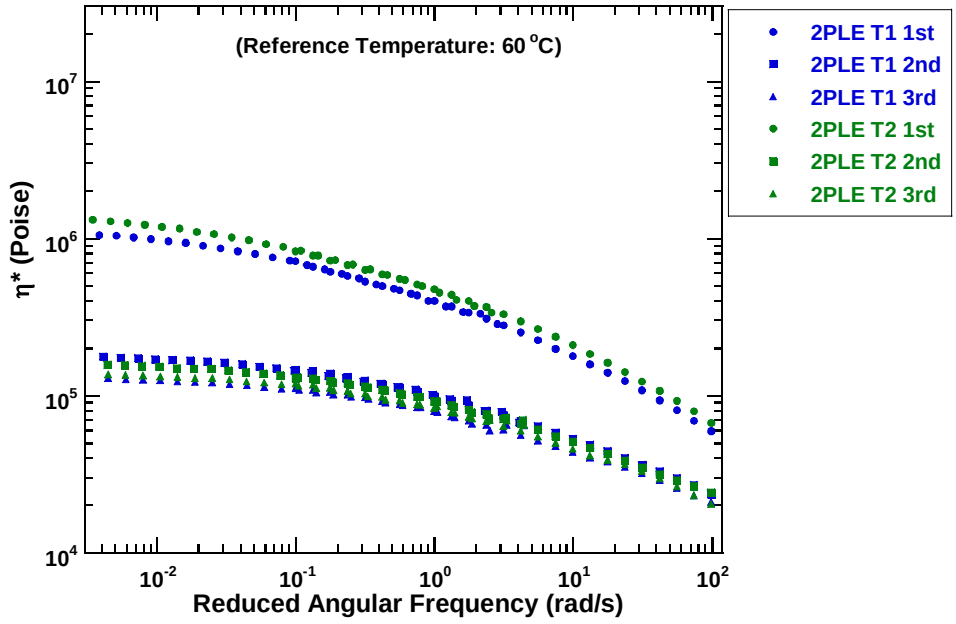

Figure B-28. Complex Viscosity Master Curves 2nd Set

Pleasanton Airport T1 and T2

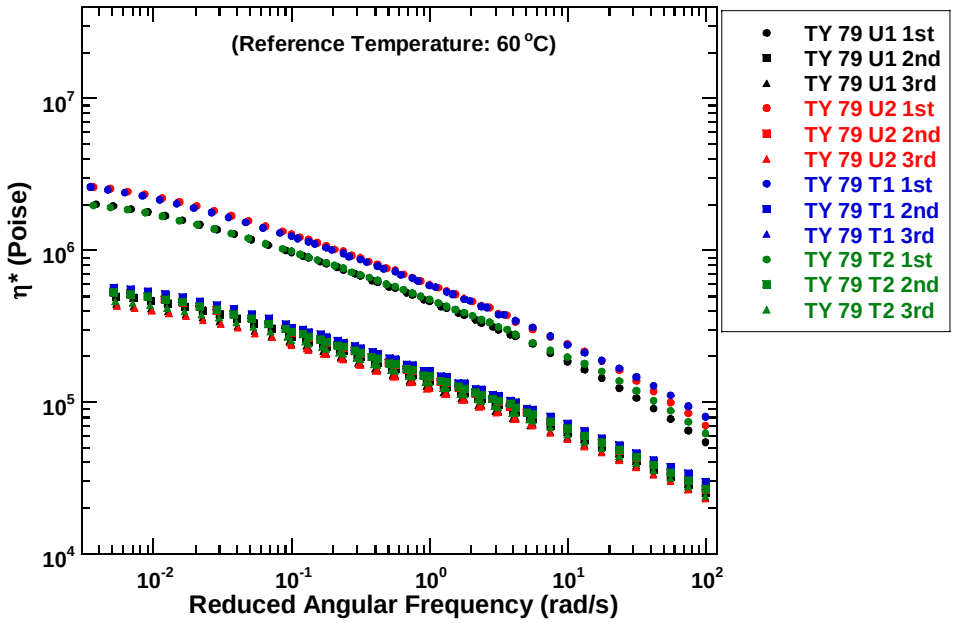

Figure B-29. Complex Viscosity Master Curves

Tyler US 79 U1, U2, T1, and T2

APPENDIX C

ACCESSIBLE AIR VOIDS DATA COMPARISON BY LAYERS AND ACCESSIBLE/TOTAL AIR VOIDS DATA COMPARISON BY TEST SITES FROM CHAPTER II

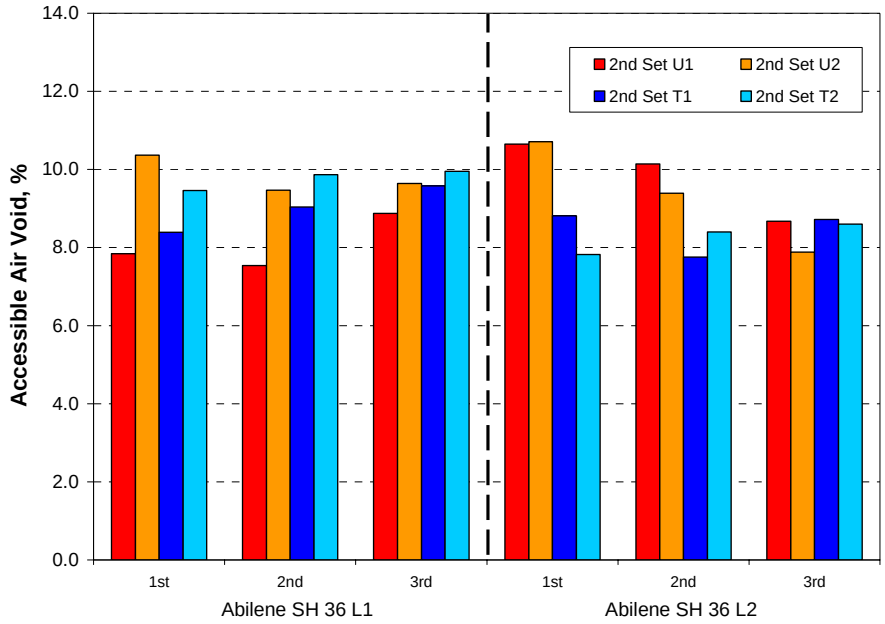

Figure C-1. Abilene SH 36 L Series Accessible Air Void Comparison by Layers

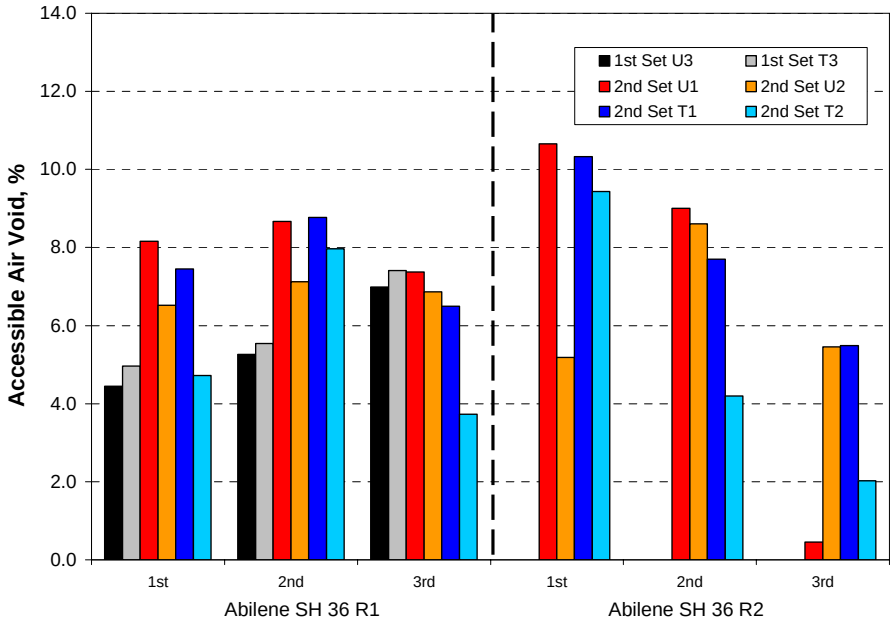

Figure C-2. Abilene SH 36 R Series Accessible Air Void Comparison by Layers

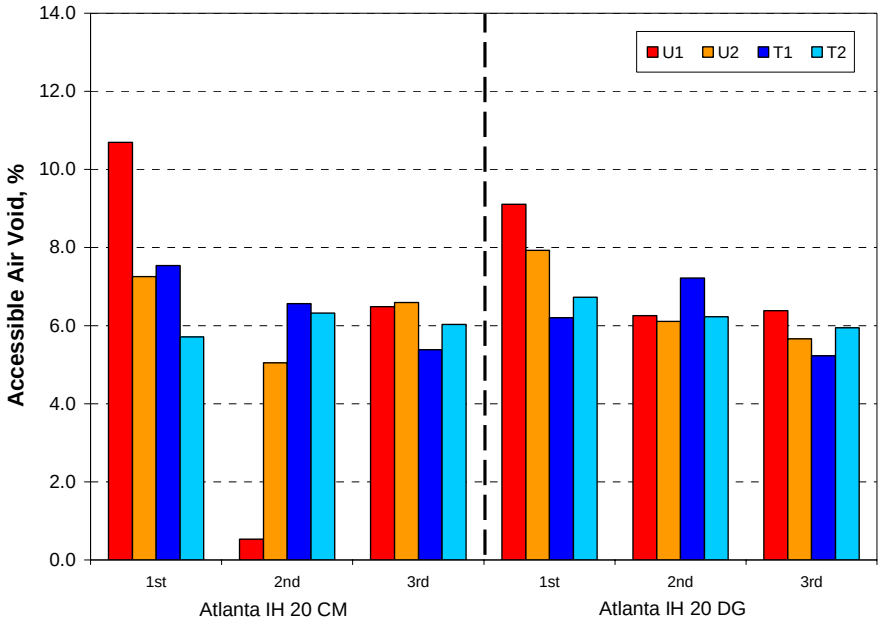

Figure C-3. Atlanta IH 20 CM and DG Accessible Air Void Comparison by Layers

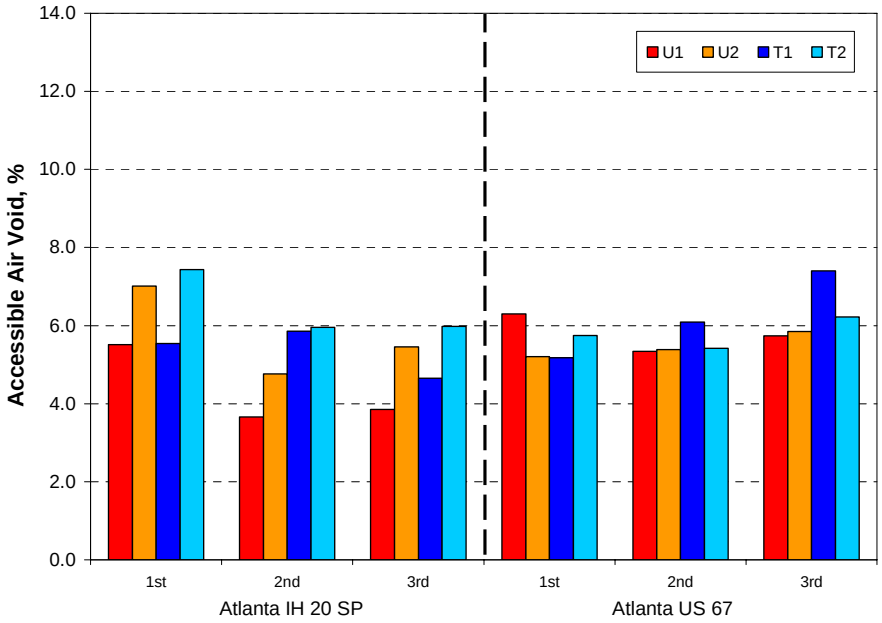

Figure C-4. Atlanta IH 20 SP and Atlanta US 67 Accessible Air Void Comparison by Layers

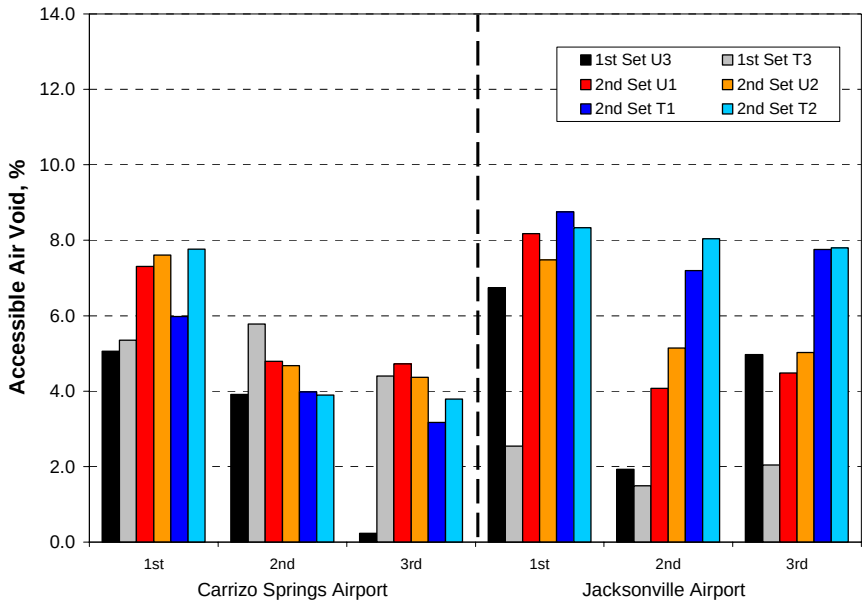

Figure C-5. Carrizo Springs Airport and Jacksonville Airport Accessible Air Void Comparison by Layers

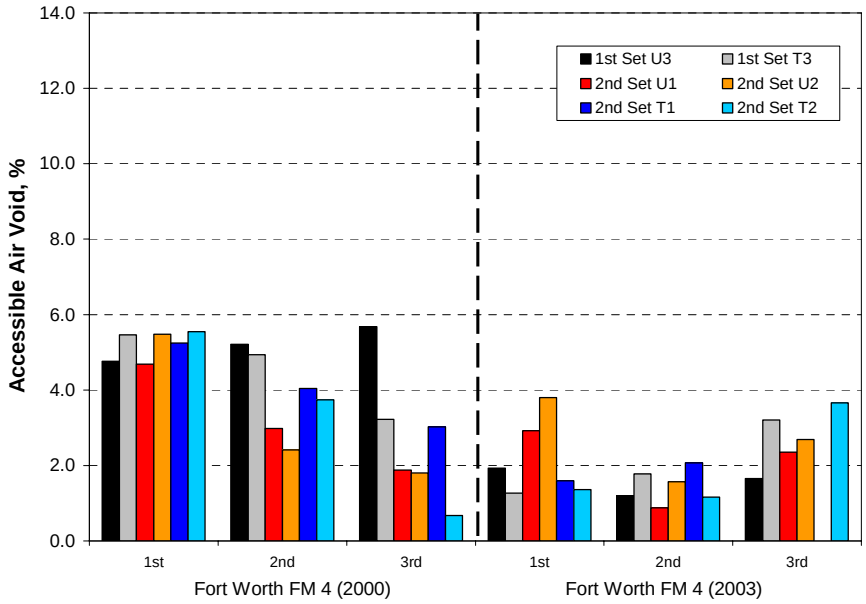

Figure C-6. Fort Worth FM 4 (2000) and (2003) Accessible Air Void Comparison by Layers

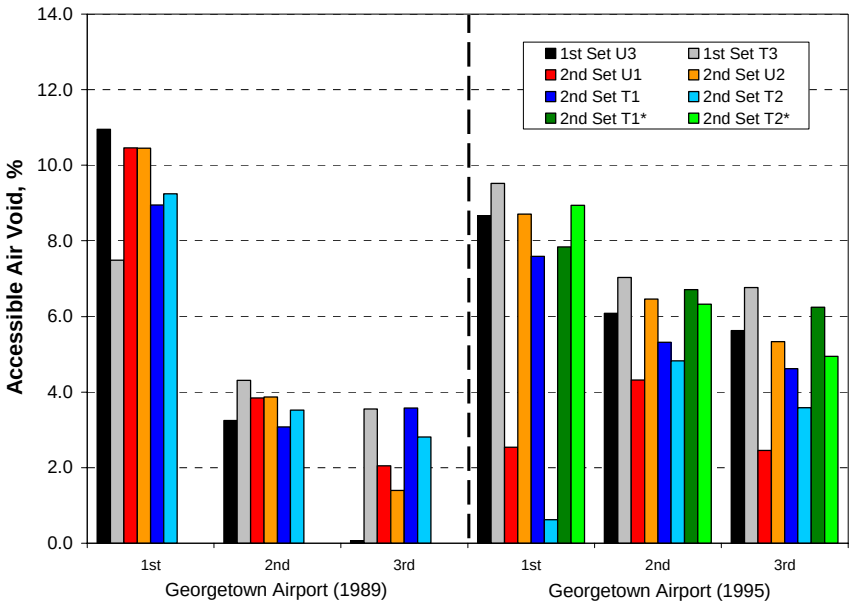

Figure C-7. Georgetown Airport (1989) and (1995)
Accessible Air Void Comparison by Layers

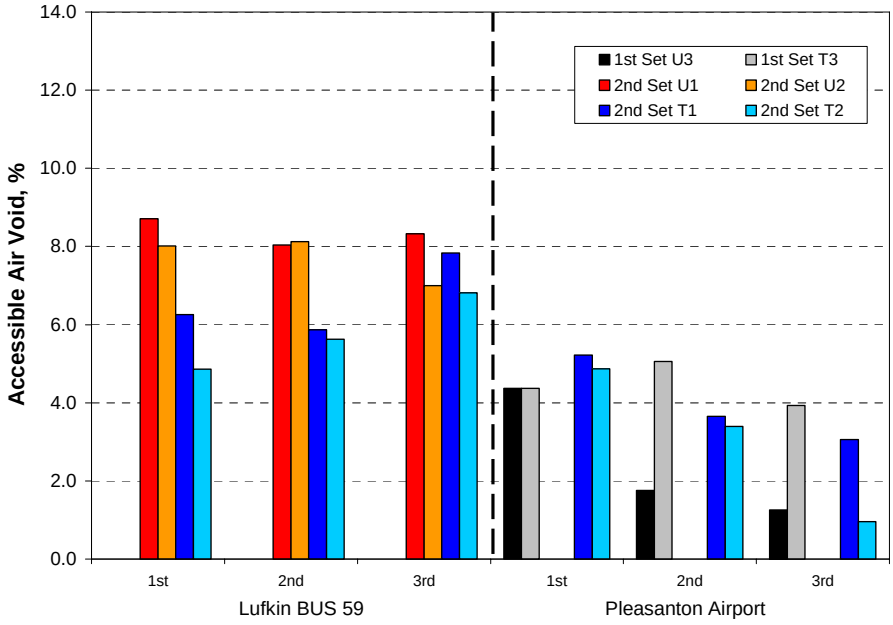

Figure C-8. Lufkin BUS 59 and Pleasanton Airport
Accessible Air Void Comparison by Layers

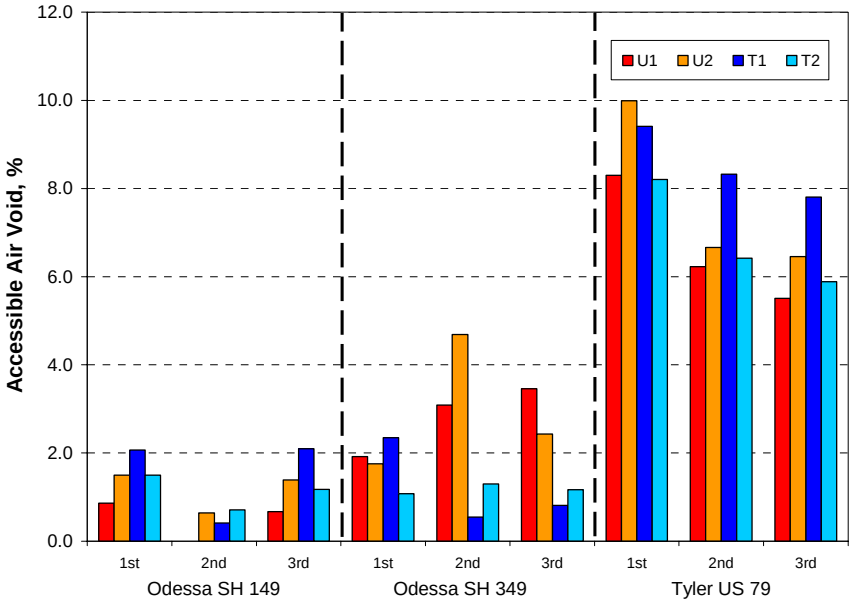

Figure C-9. Odessa SH 149, SH 349, and Tyler US 79 Accessible Air Void Comparison by Layers

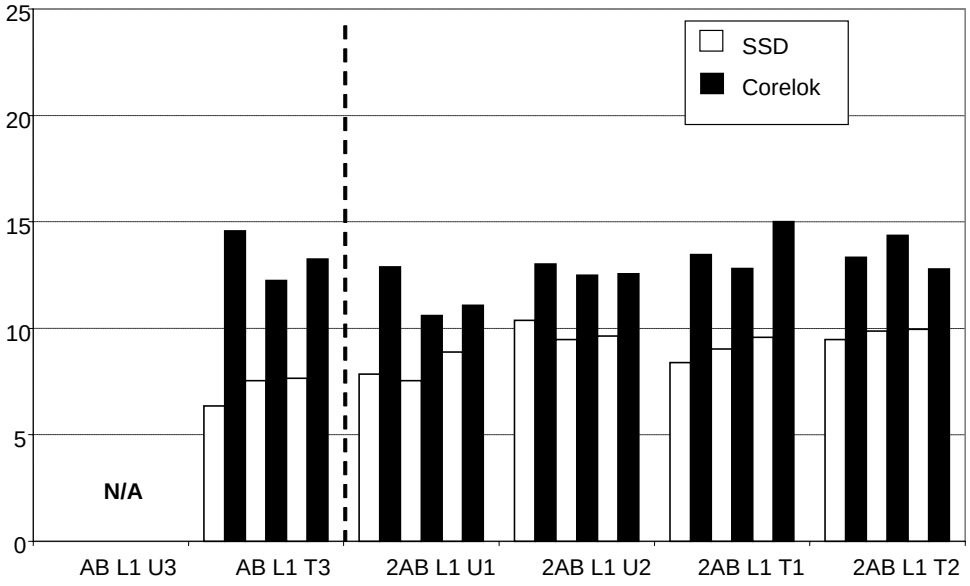

Figure C-10a. Accessible Air Void of 1st and 2nd Set Abilene SH 36 L1, %

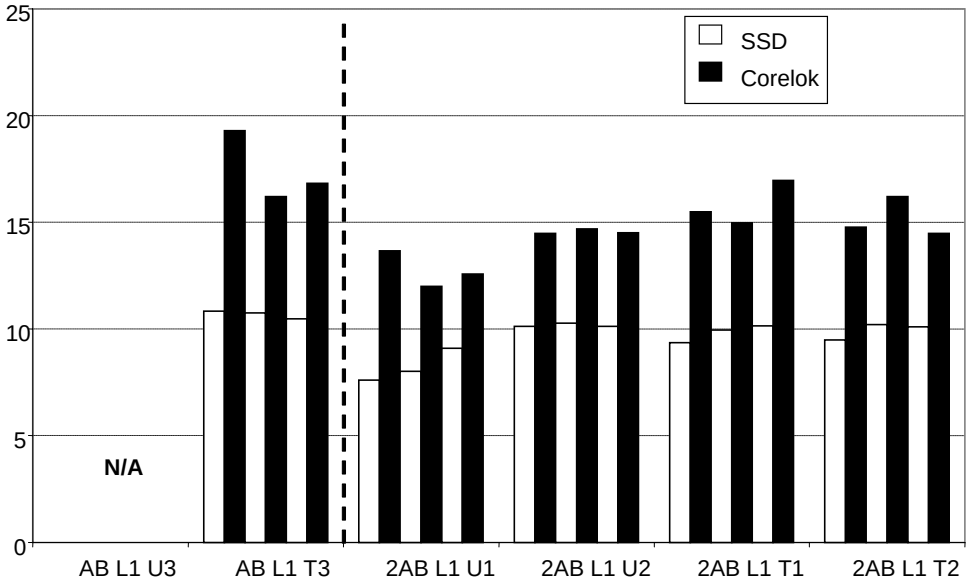

Figure C-10b. Total Air Void of 1st and 2nd Set Abilene SH 36 L1, %

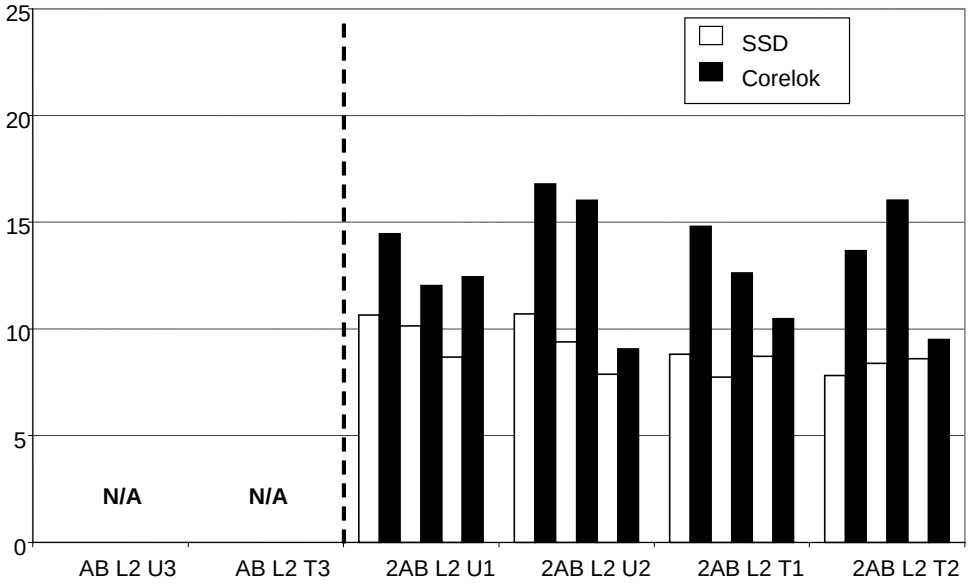

Figure C-11a. Accessible Air Void of 2nd Set Abilene SH 36 L2, %

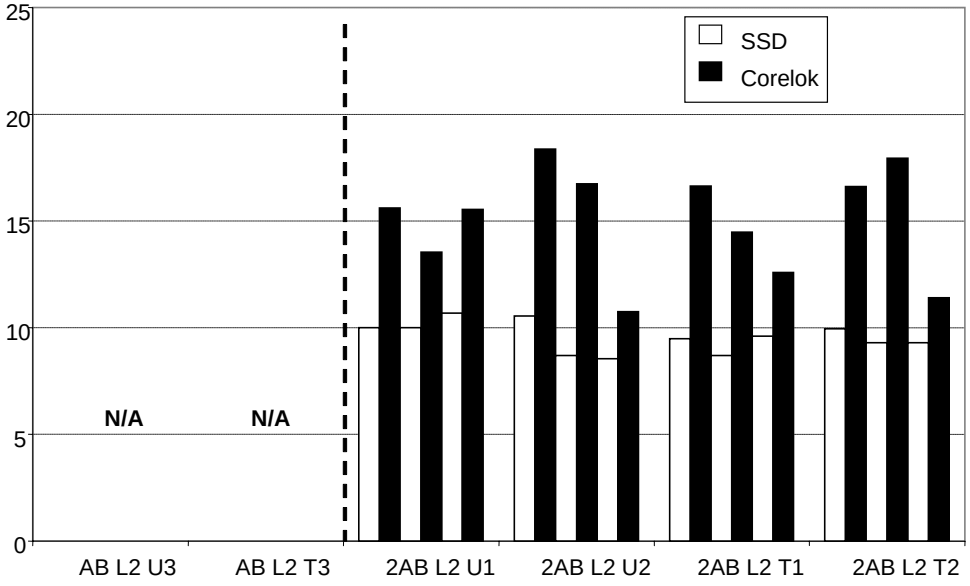

Figure C-11b. Total Air Void of and 2nd Set Abilene SH 36 L2, %

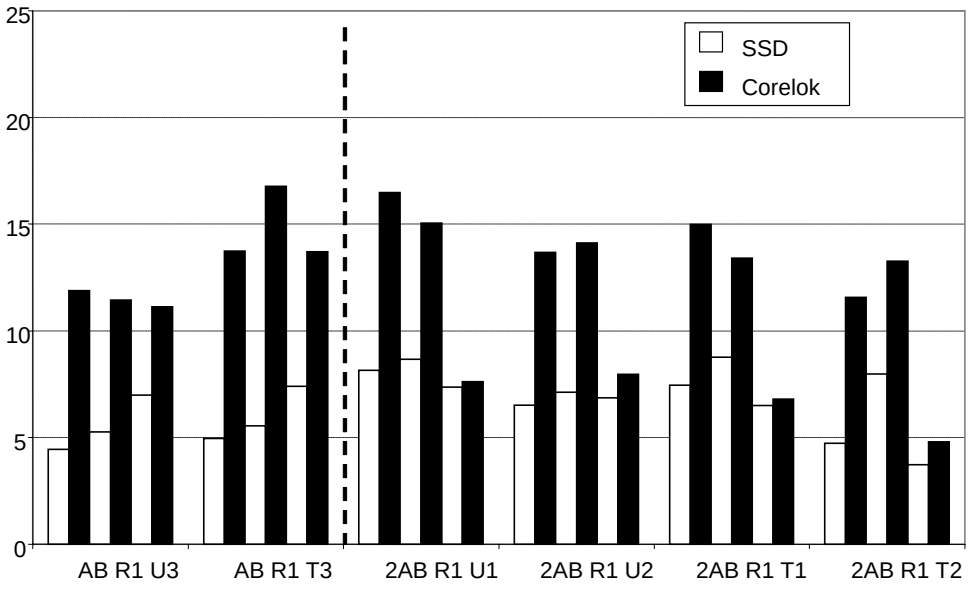

Figure C-12a. Accessible Air Void of 1st and 2nd Set Abilene SH 36 R1, %

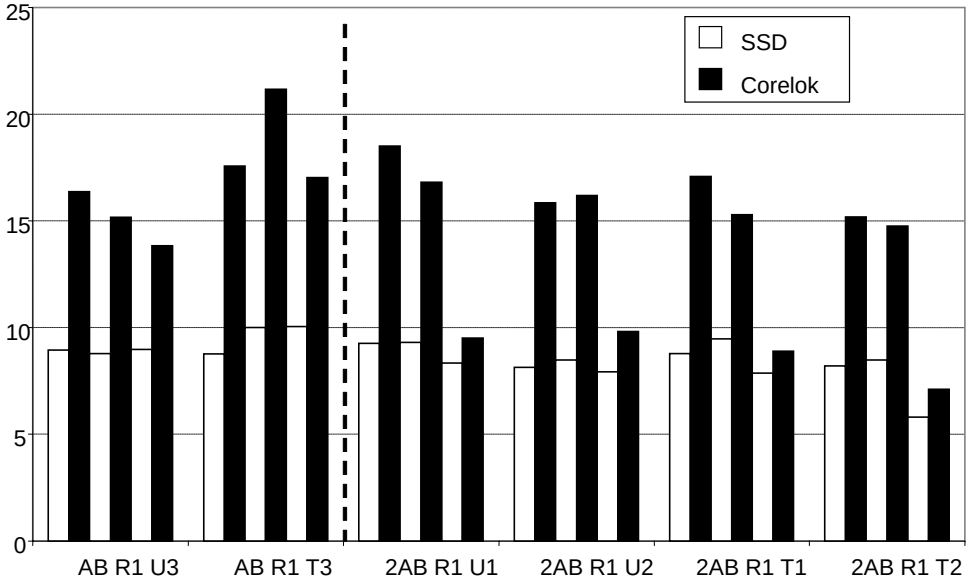

Figure C-12b. Total Air Void of 1st and 2nd Set Abilene SH 36 R1, %

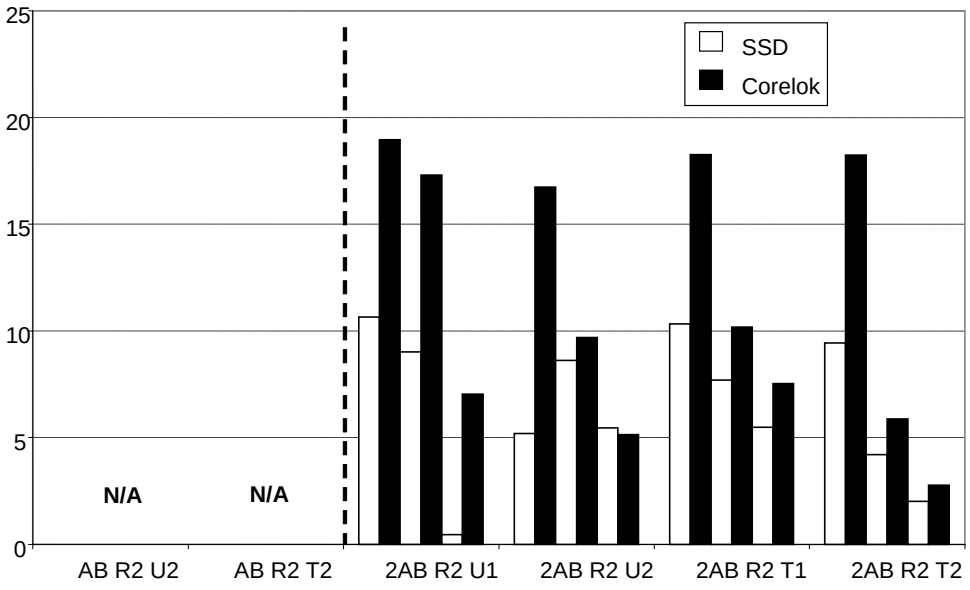

Figure C-13a. Accessible Air Void of 2nd Set Abilene SH 36 R2, %

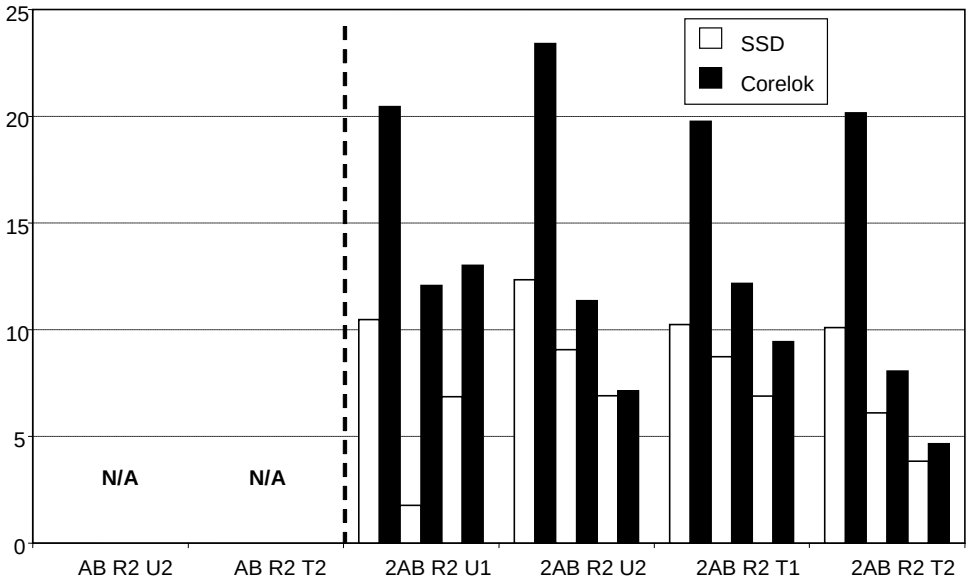

Figure C-13b. Total Air Void of 2nd Set Abilene SH 36 R2, %

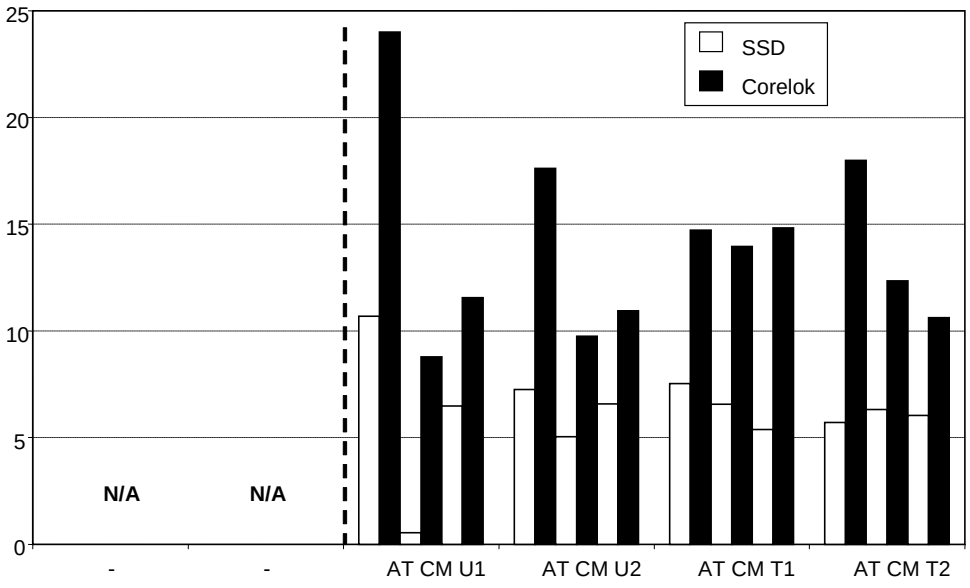

Figure C-14a. Accessible Air Void of Atlanta IH 20 CM, %

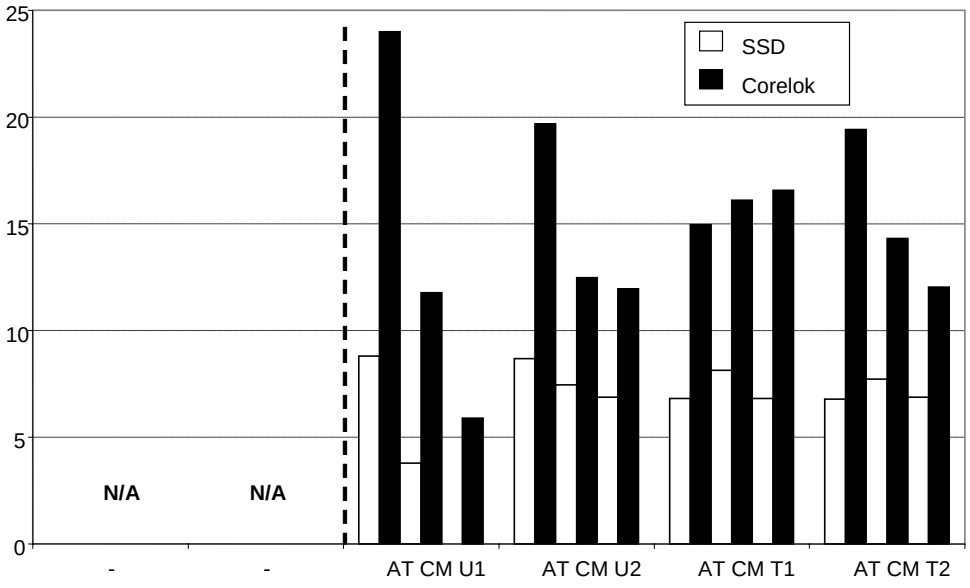

Figure C-14b Total Air Void of Atlanta IH 20 CM, %

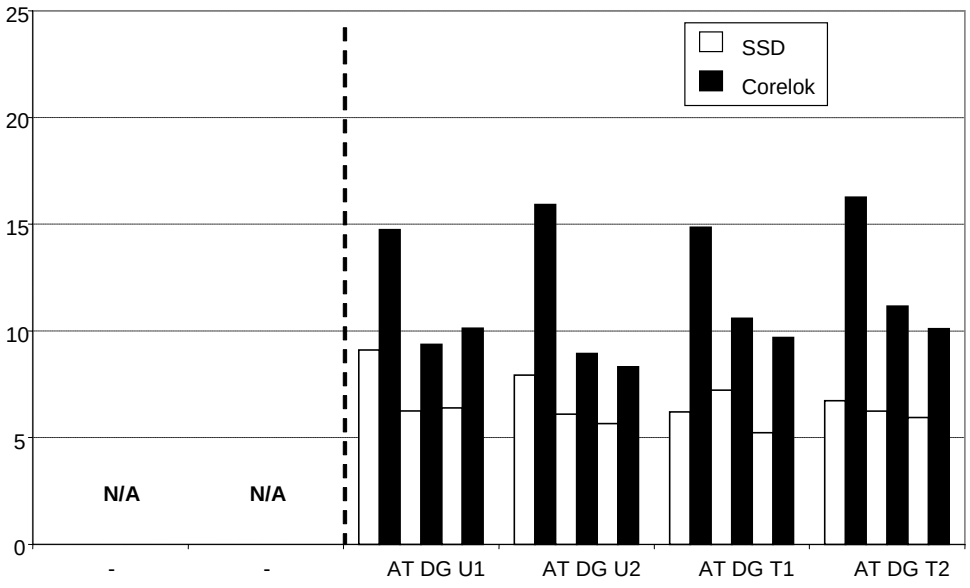

Figure C-15a. Accessible Air Void of Atlanta IH 20 DG, %

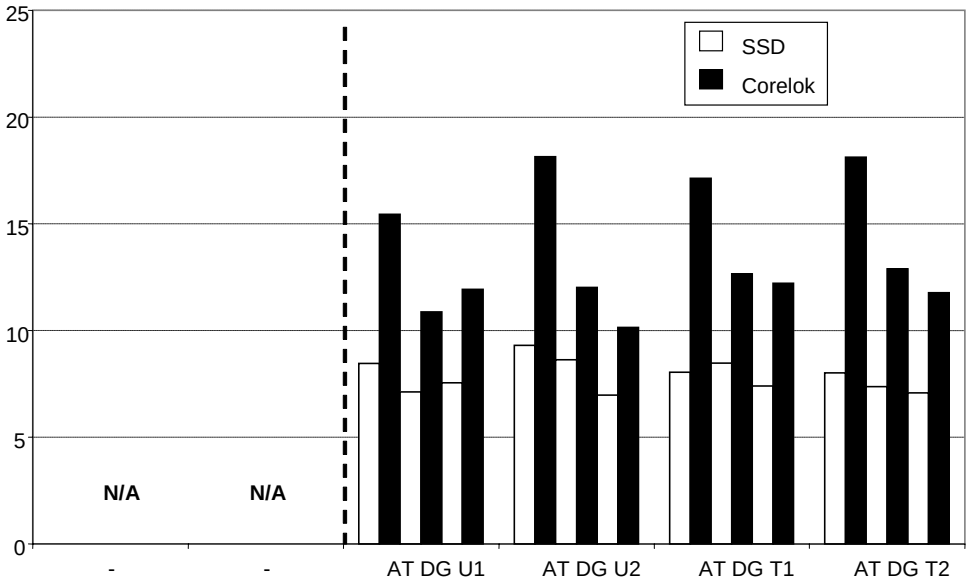

Figure C-15b. Total Air Void of Atlanta IH 20 DG, %

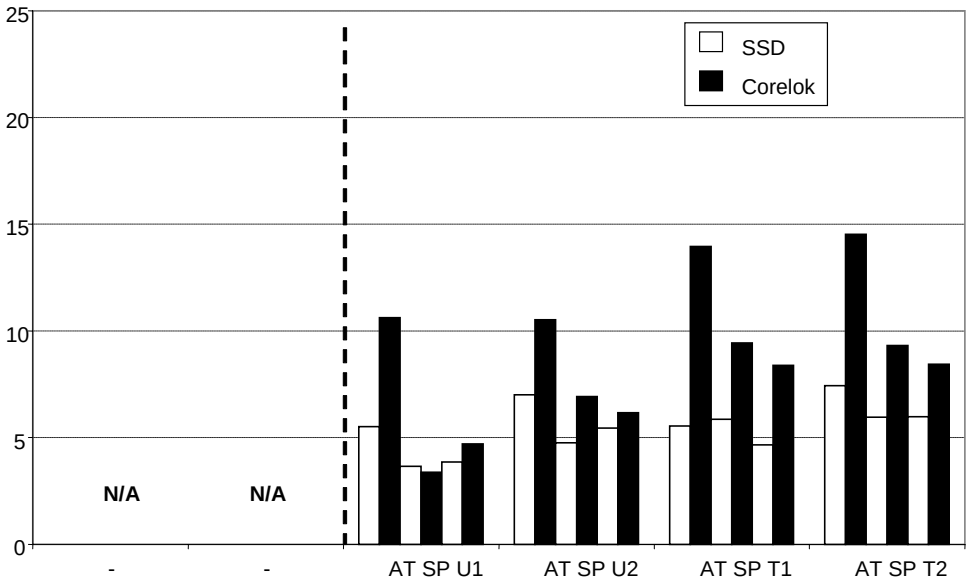

Figure C-16a. Accessible Air Void of Atlanta IH 20 SP, %

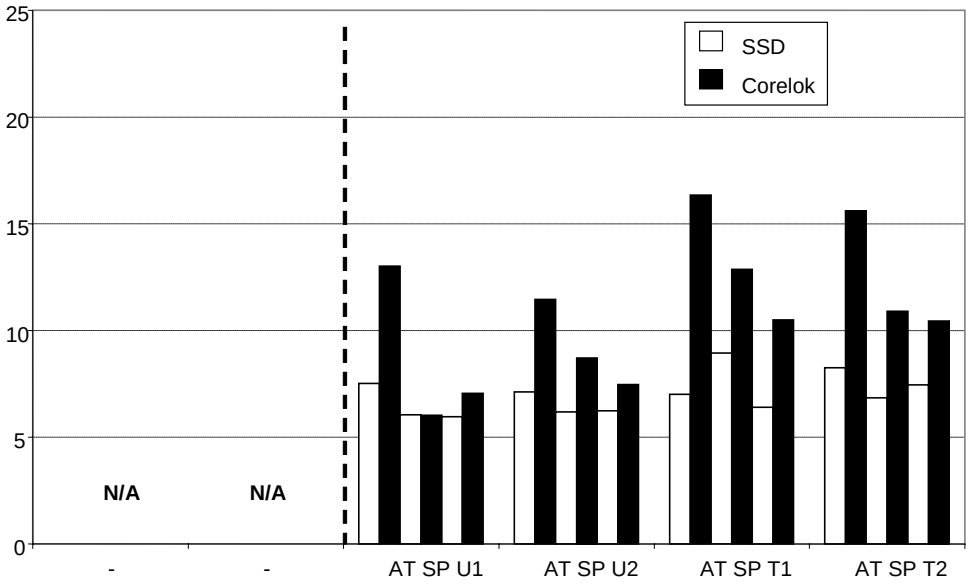

Figure C-16b. Total Air Void of Atlanta IH 20 SP, %

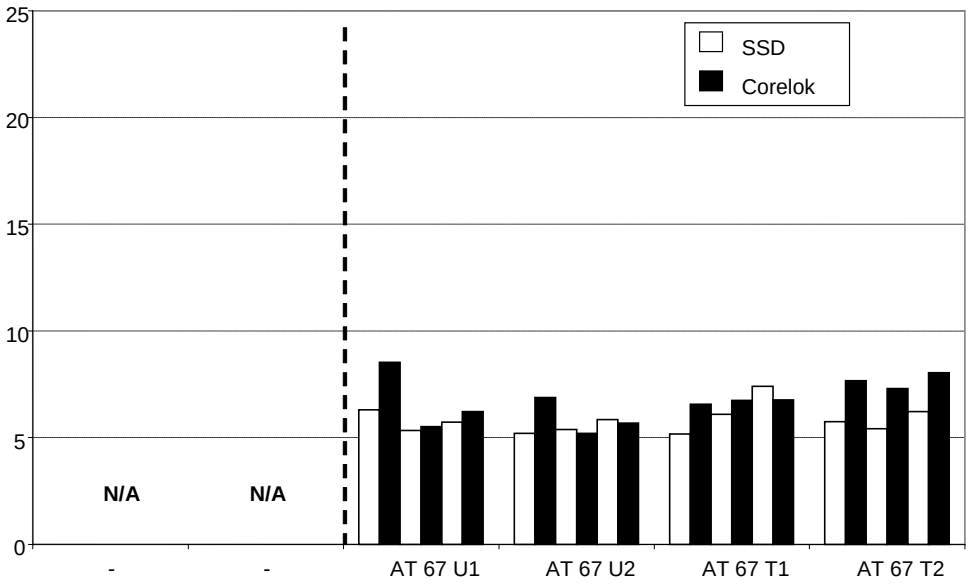

Figure C-17a. Accessible Air Void of Atlanta US 67, %

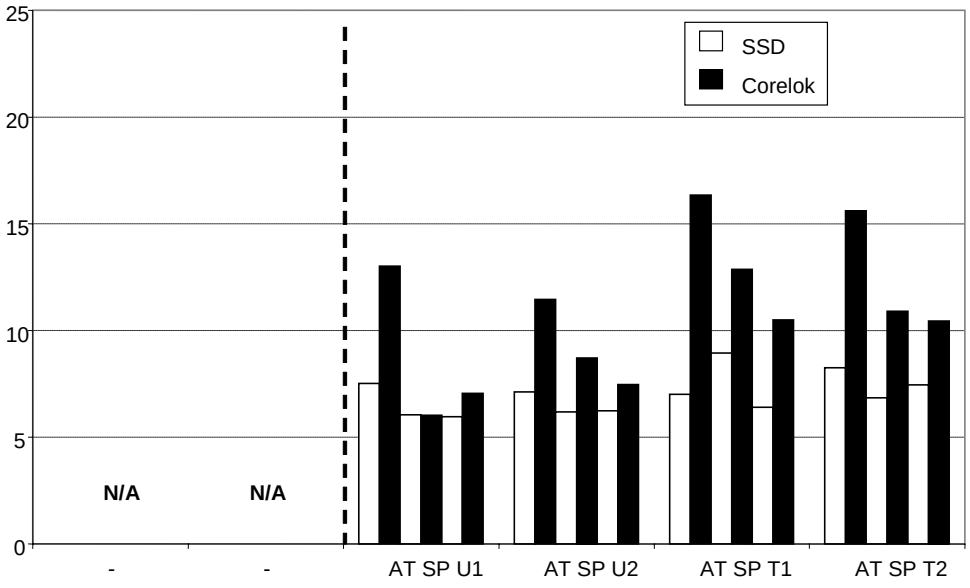

Figure C-17b. Total Air Void of Atlanta US 67, %

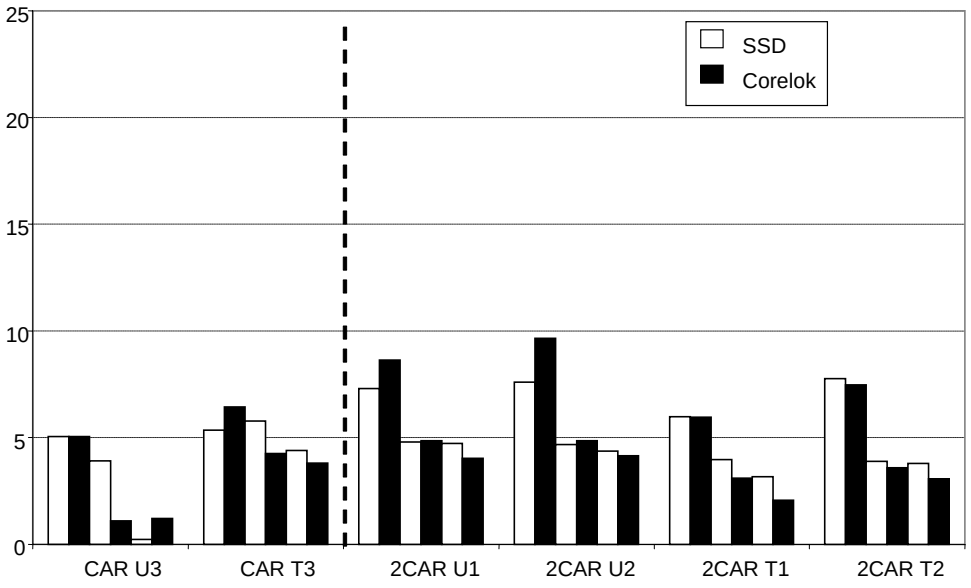

Figure C-18a. Accessible Air Void of 1st and 2nd Set Carrizo Springs Airport, %

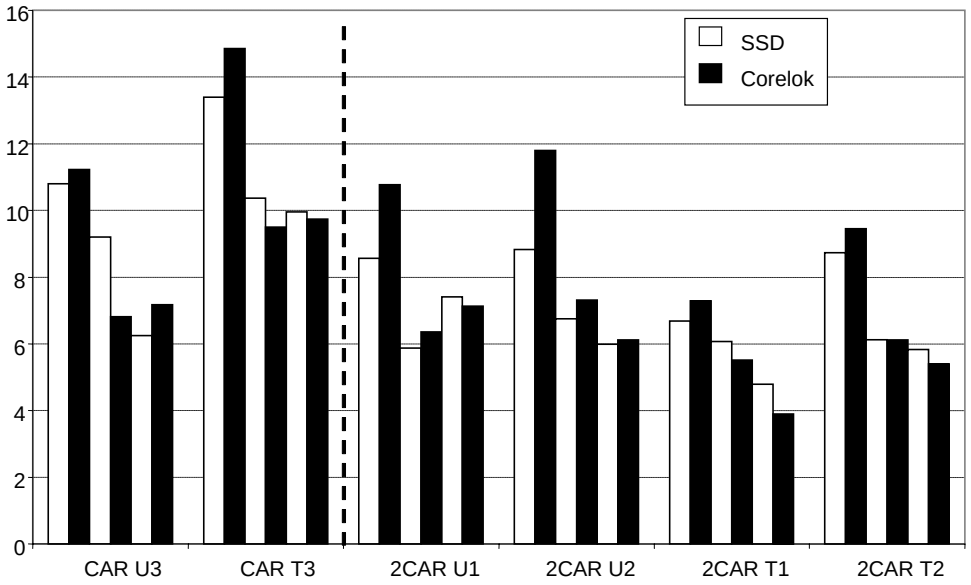

Figure C-18b. Total Air Void of 1st and 2nd Set Carrizo Springs Airport, %

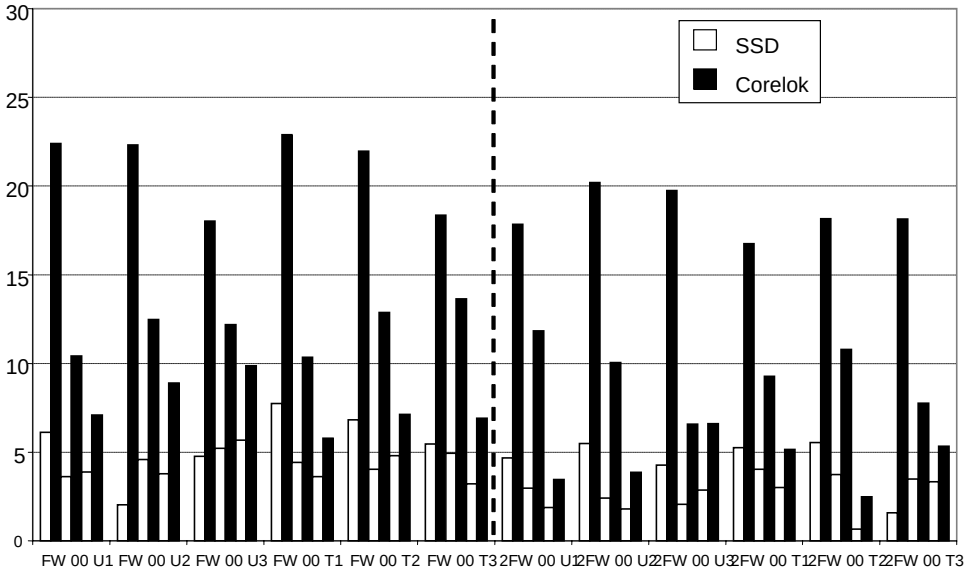

Figure C-19a. Accessible Air Void of 1st and 2nd Set Fort Worth FM 4 (2000), %

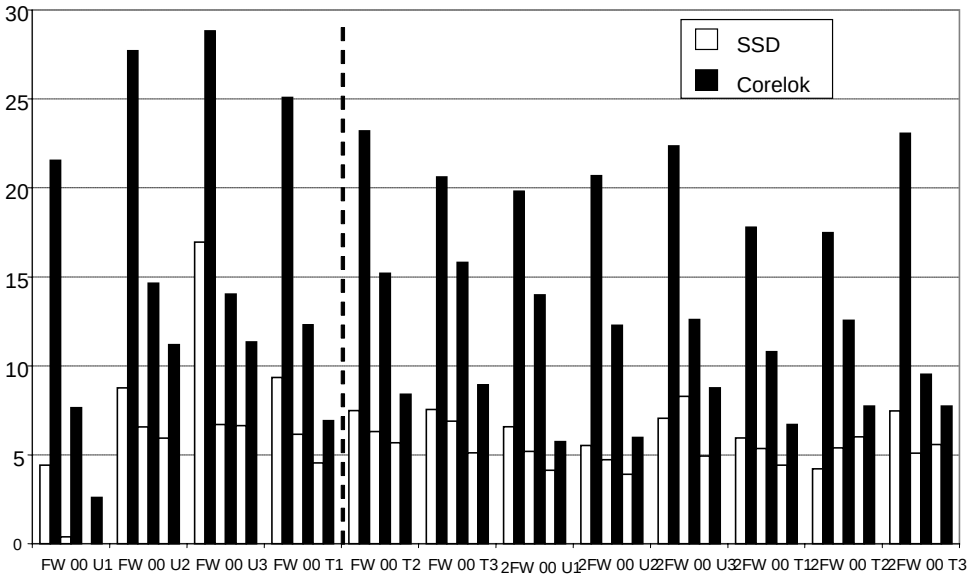

Figure C-19b. Total Air Void of 1st and 2nd Set Fort Worth FM 4 (2000), %

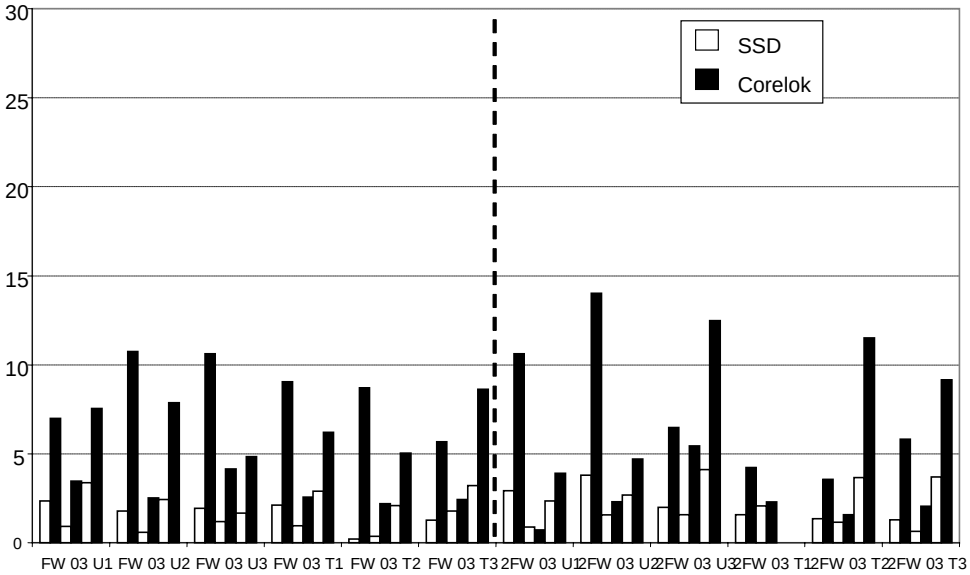

Figure C-20a. Accessible Air Void of 1st and 2nd Set Fort Worth FM 4 (2003), %

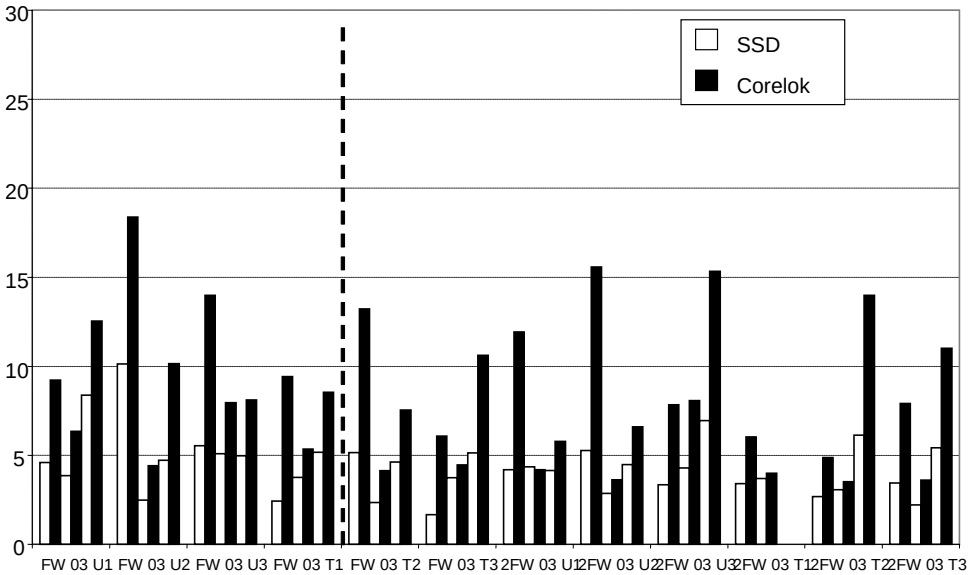

Figure C-20b. Total Air Void of 1st and 2nd Set Fort Worth FM 4 (2003), %

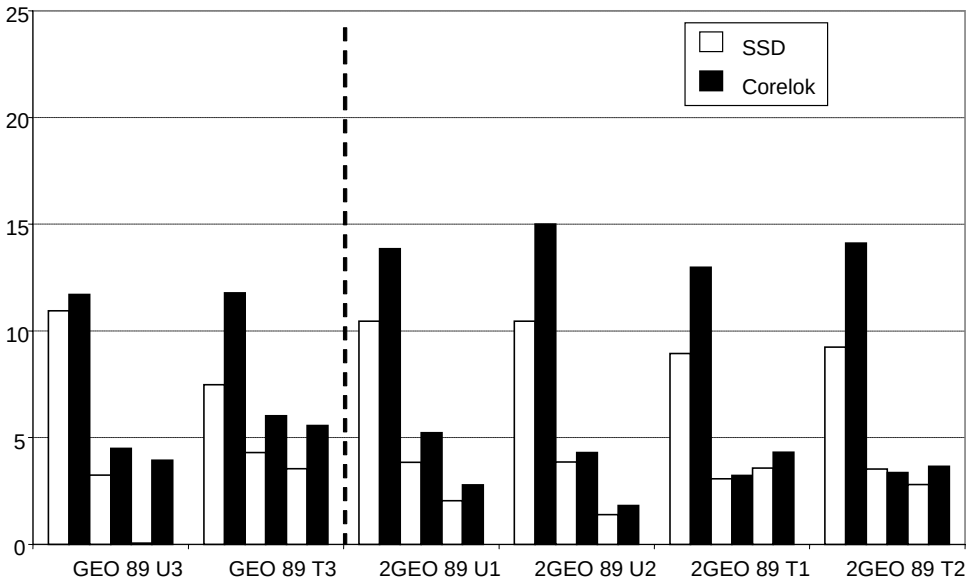

Figure C-21a. Accessible Air Void of 1st and 2nd Set Georgetown Airport (1989), %

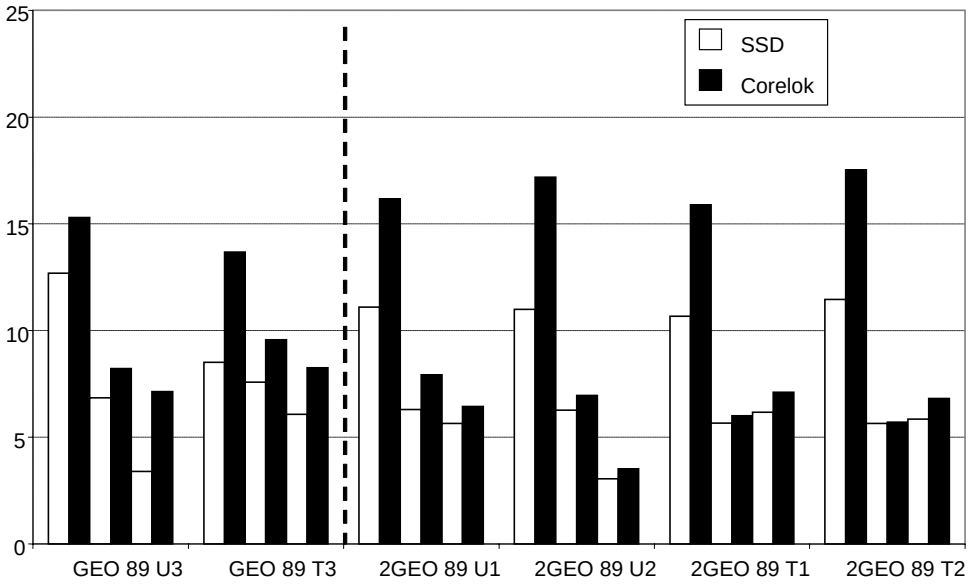

Figure C-21b. Total Air Void of 1st and 2nd Set Georgetown Airport (1989), %

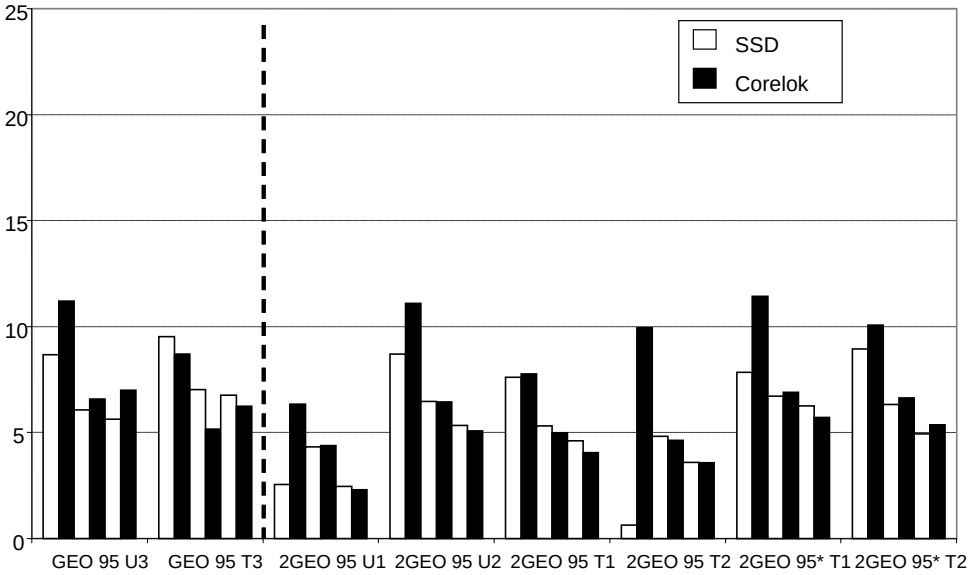

Figure C-22a. Accessible Air Void of 1st and 2nd Set Georgetown Airport (1995), %

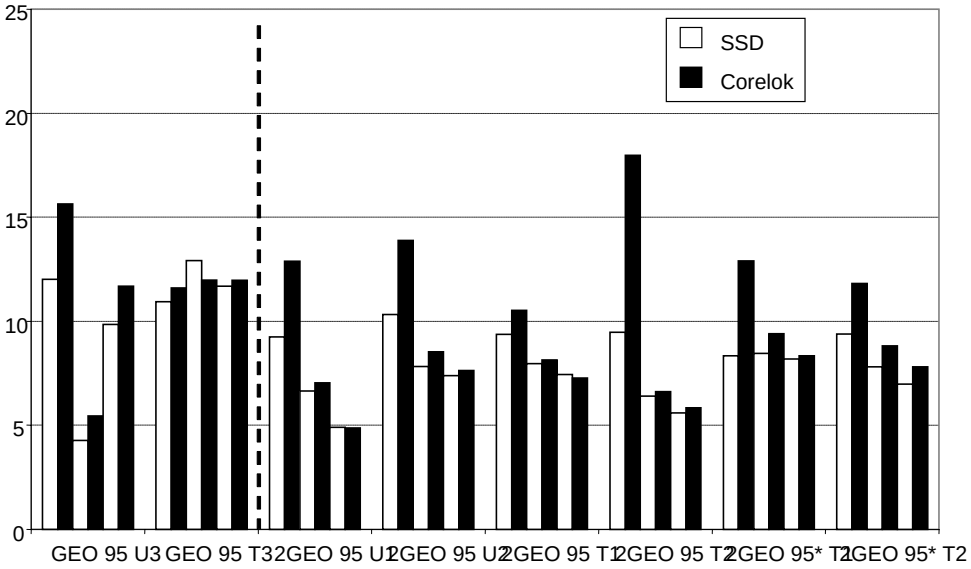

Figure C-22b. Total Air Void of 1st and 2nd Set Georgetown Airport (1995), %

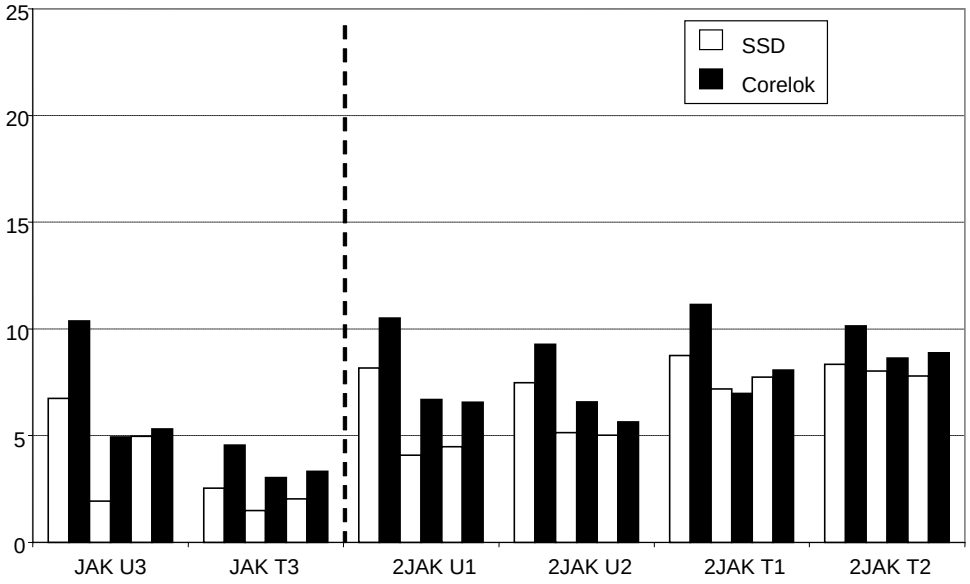

Figure C-23a. Accessible Air Void of 1st and 2nd Set Jacksonville Airport, %

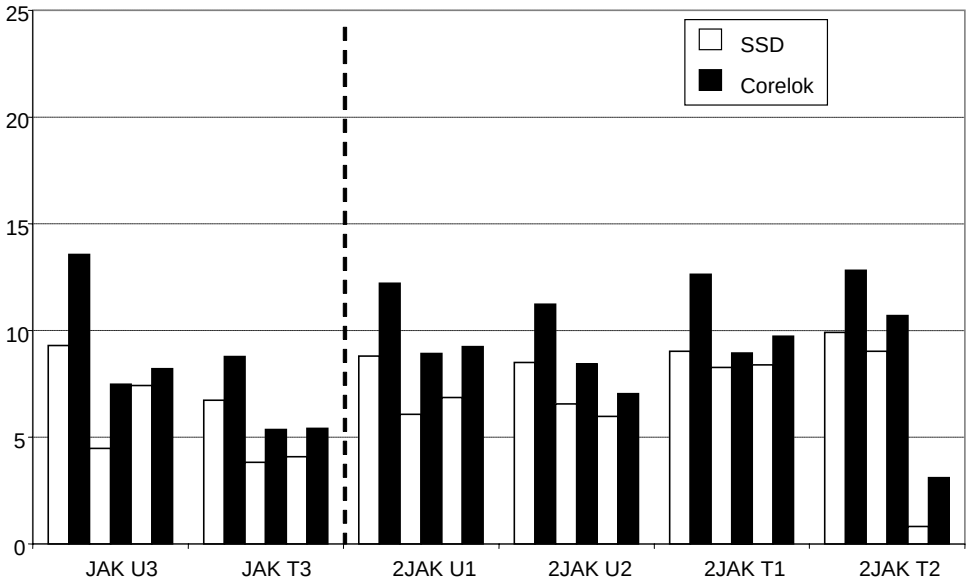

Figure C-23b. Total Air Void of 1st and 2nd Set Jacksonville Airport, %

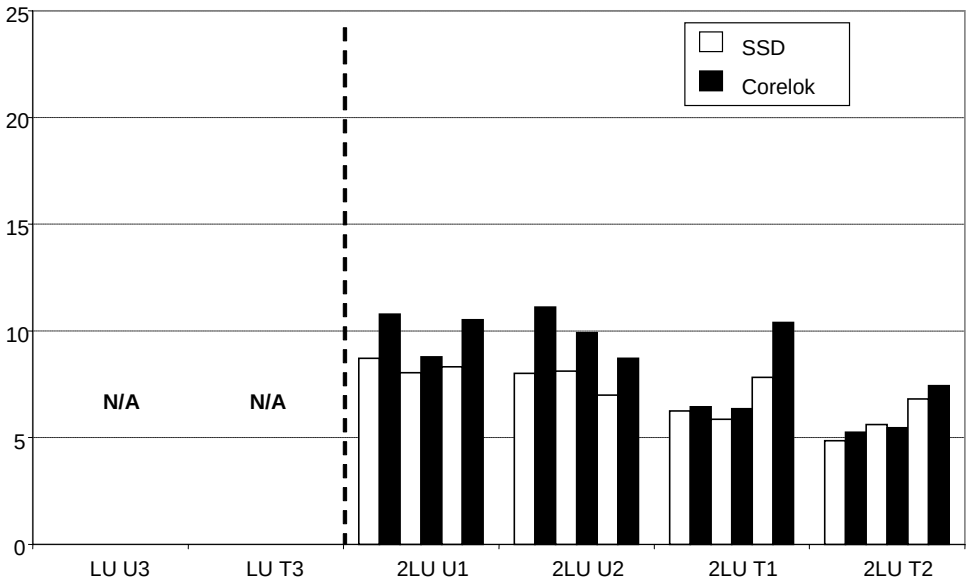

Figure C-24a. Accessible Air Void of 2nd Set Lufkin BUS 59, %

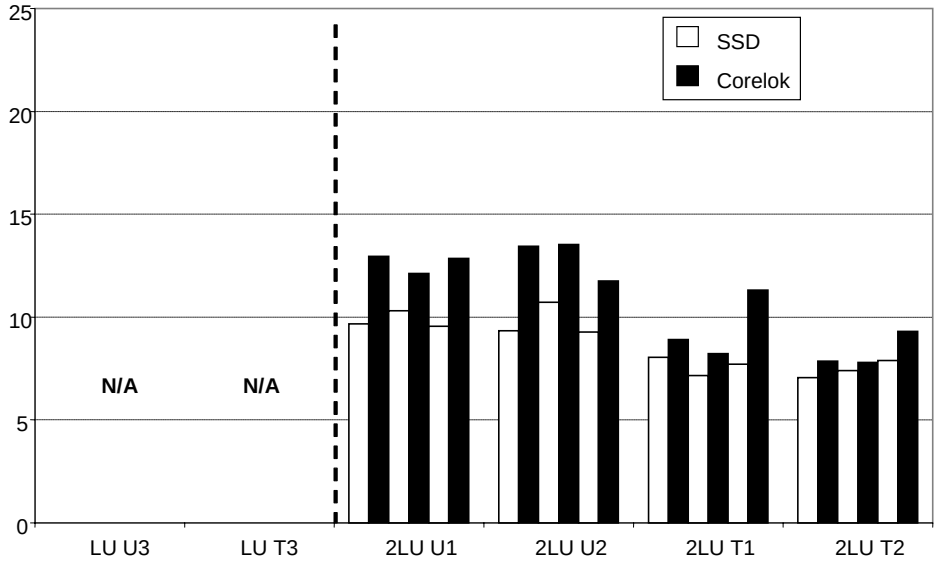

Figure C-24b. Total Air Void of 2nd Set Lufkin BUS 59, %

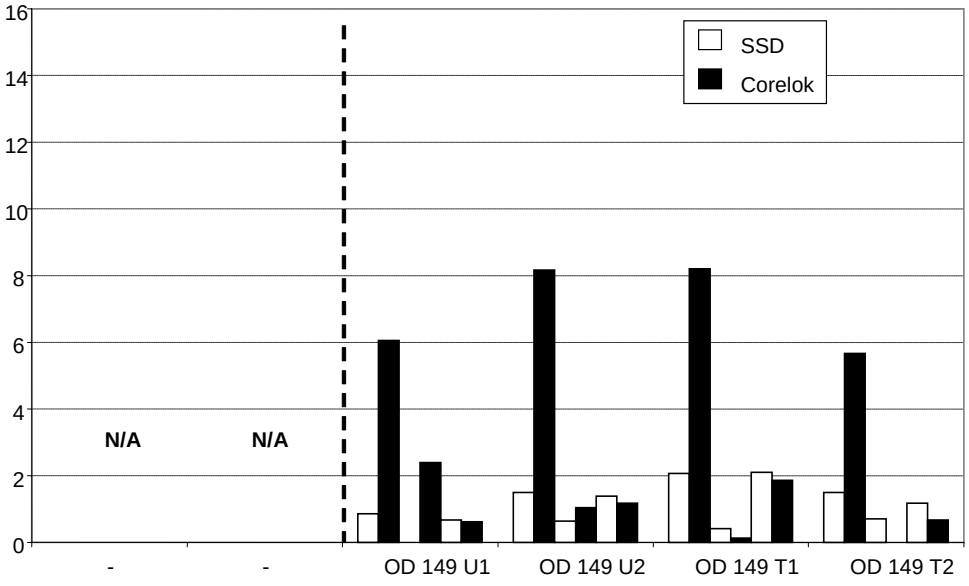

Figure C-25a. Accessible Air Void of Odessa SH 149, %

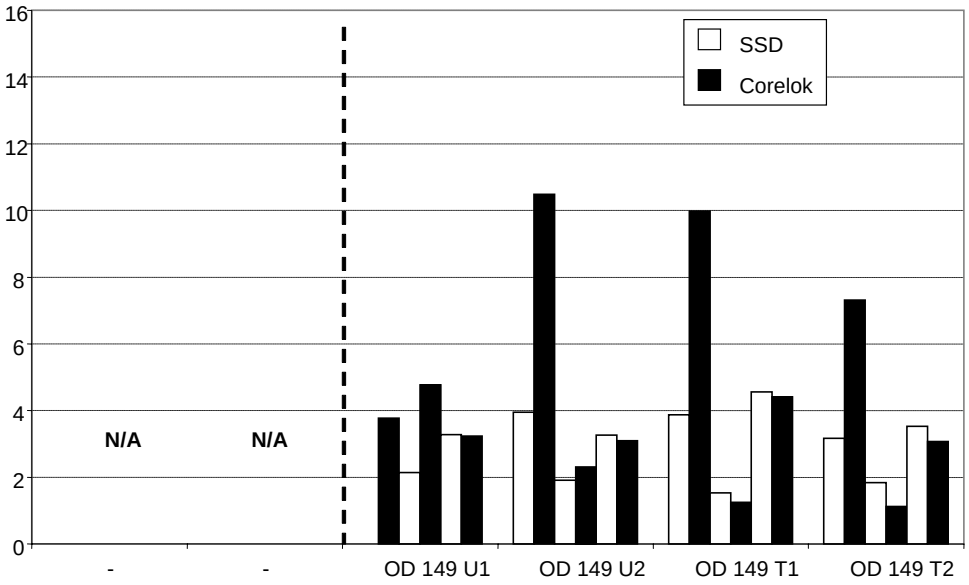

Figure C-25b. Total Air Void of Odessa SH 149, %

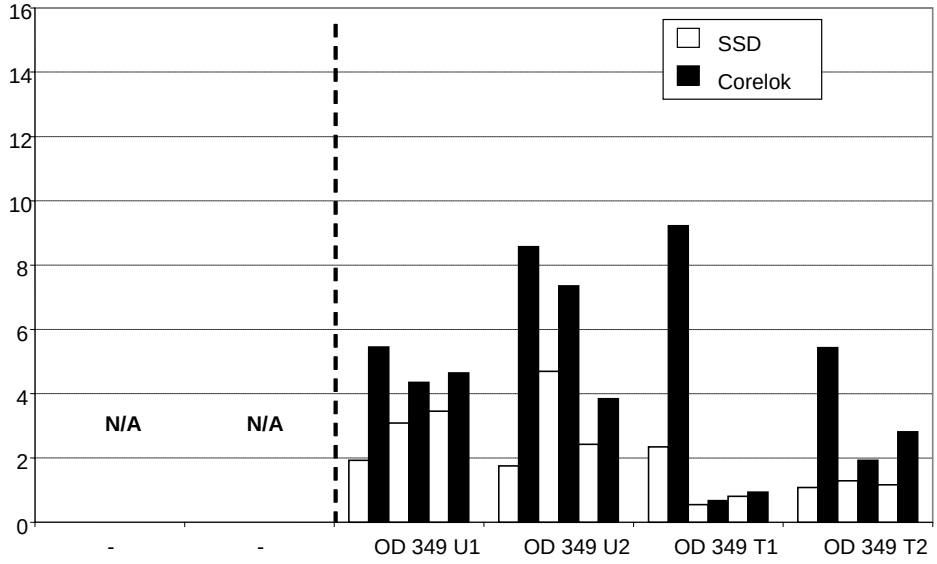

Figure C-26a. Accessible Air Void of Odessa SH 349, %

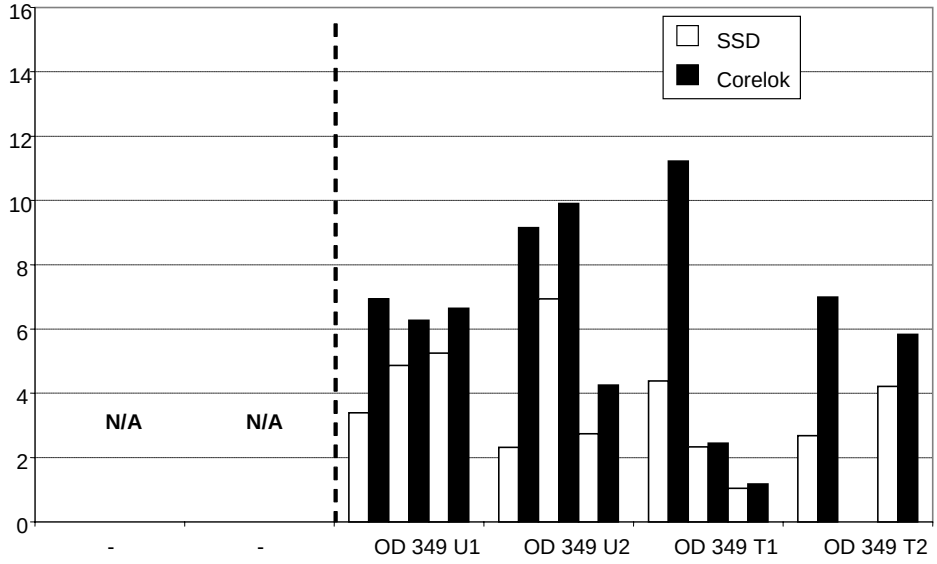

Figure C-26b. Total Air Void of Odessa SH 349, %

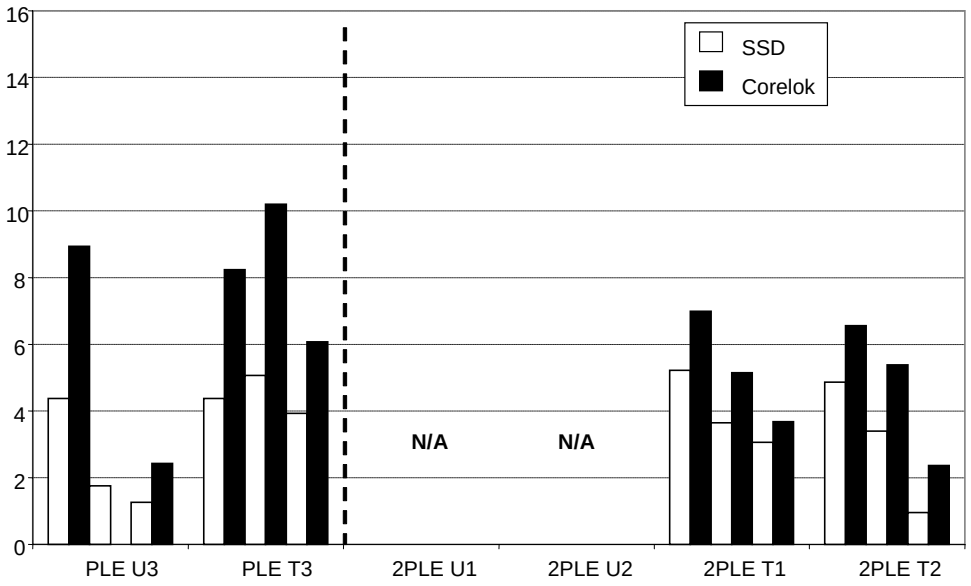

Figure C-27a. Accessible Air Void of 1st and 2nd Set Pleasanton Airport, %

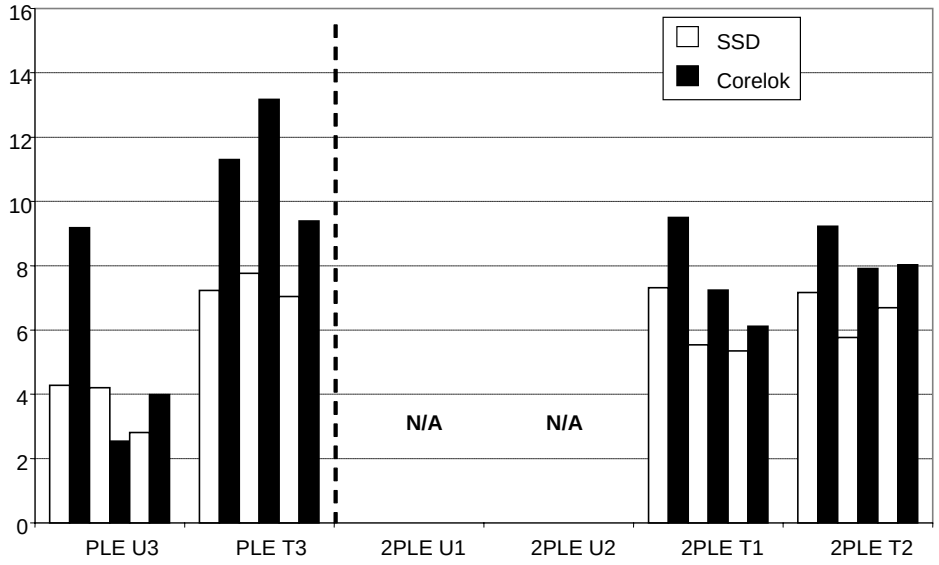

Figure C-27b. Total Air Void of 1st and 2nd Set Pleasanton Airport, %

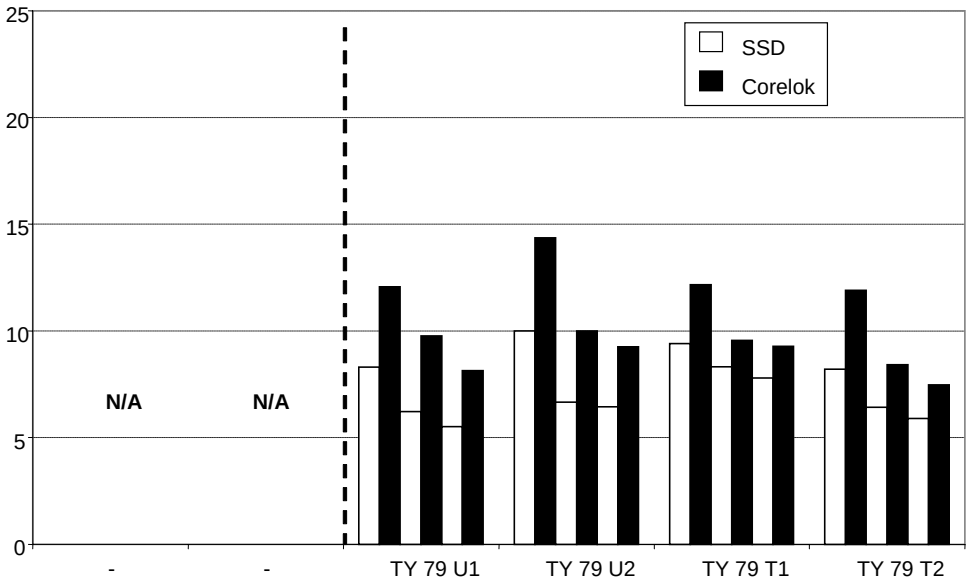

Figure C-28a. Accessible Air Void of Tyler US 79, %

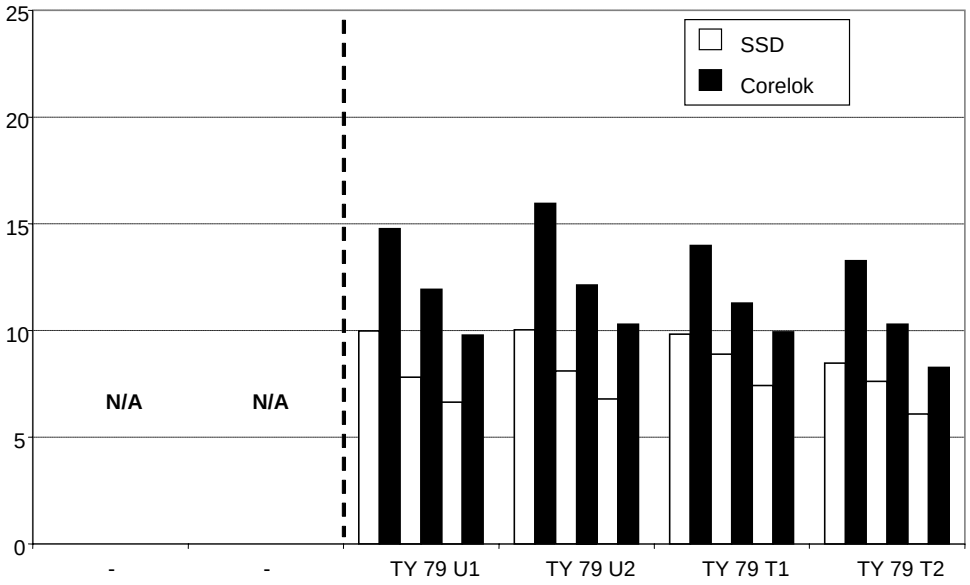

Figure C-28b. Total Air Void of Tyler US 79, %

APPENDIX D

BINDER CONTENT OF CORE SAMPLES FROM CHAPTER II

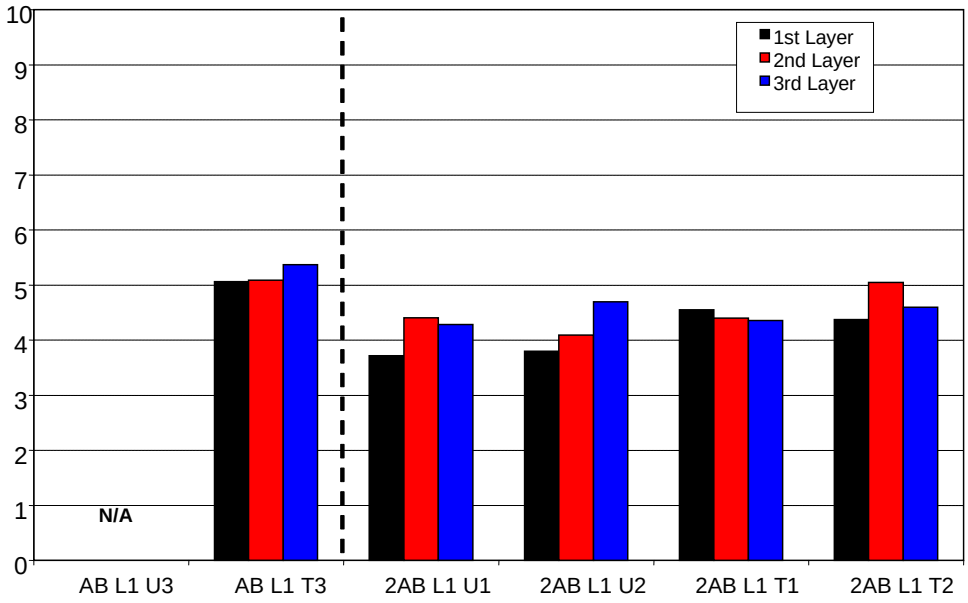

Figure D-2. Binder Content of 1st and 2nd Set Abilene SH 36 L1, %

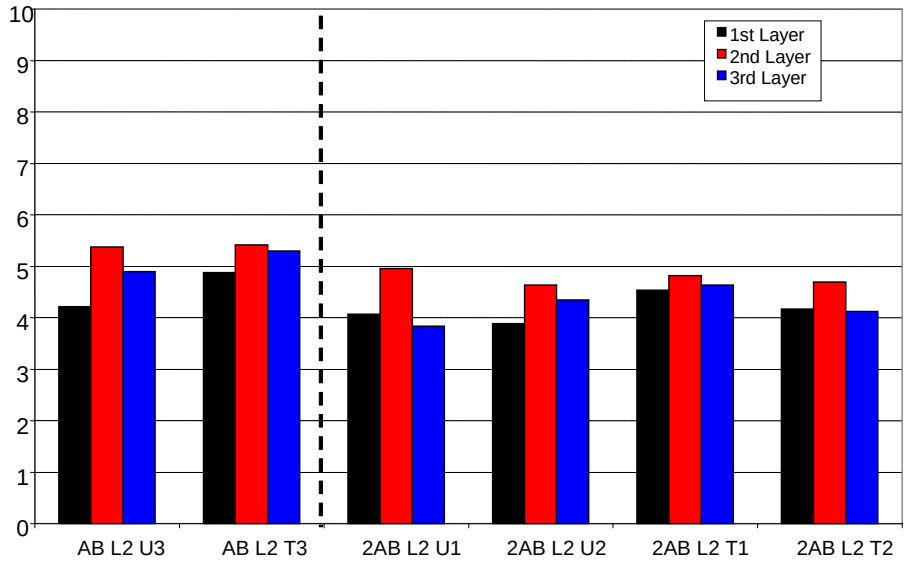

Figure D-3. Binder Content of 1st and 2nd Set Abilene SH 36 L2, %

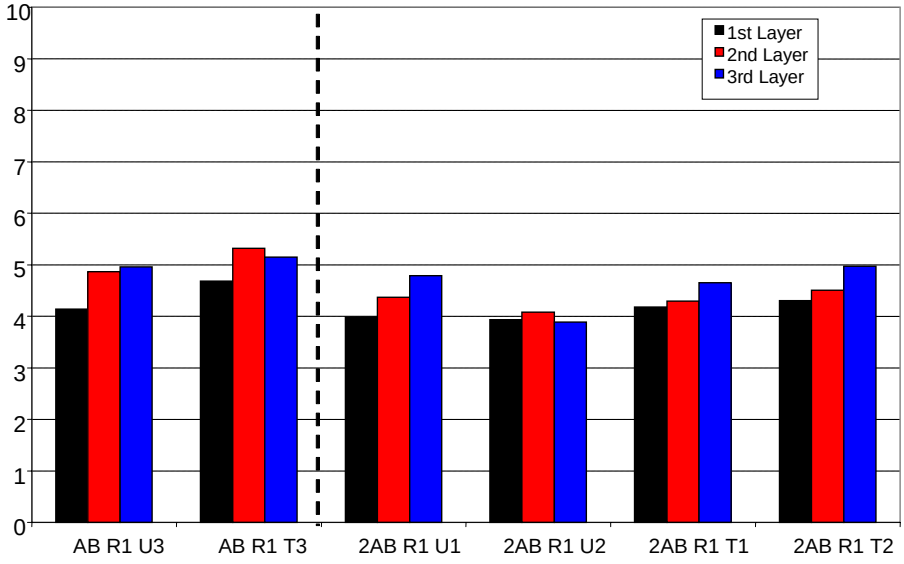

Figure D-4. Binder Content of 1st and 2nd Set Abilene SH 36 R1, %

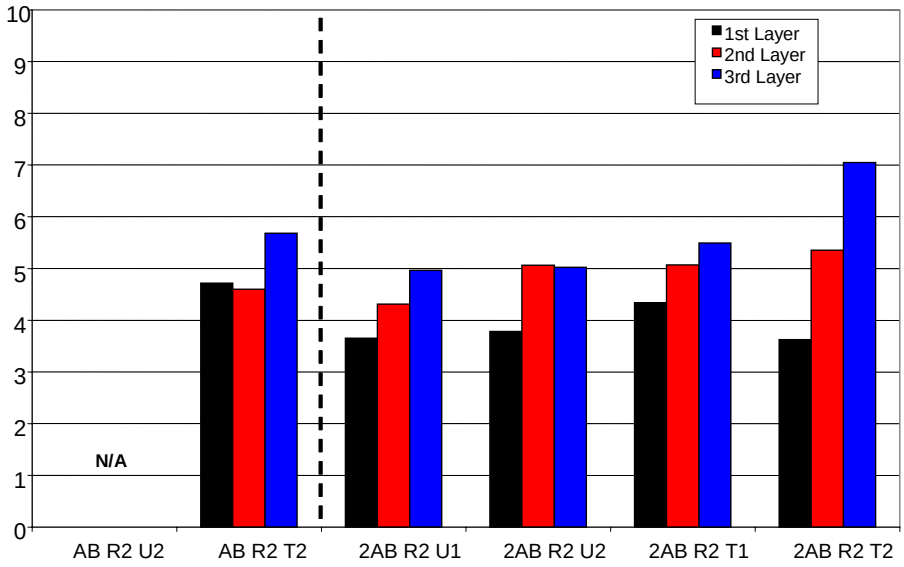

Figure D-5. Binder Content of 1st and 2nd Set Abilene SH 36 R2, %

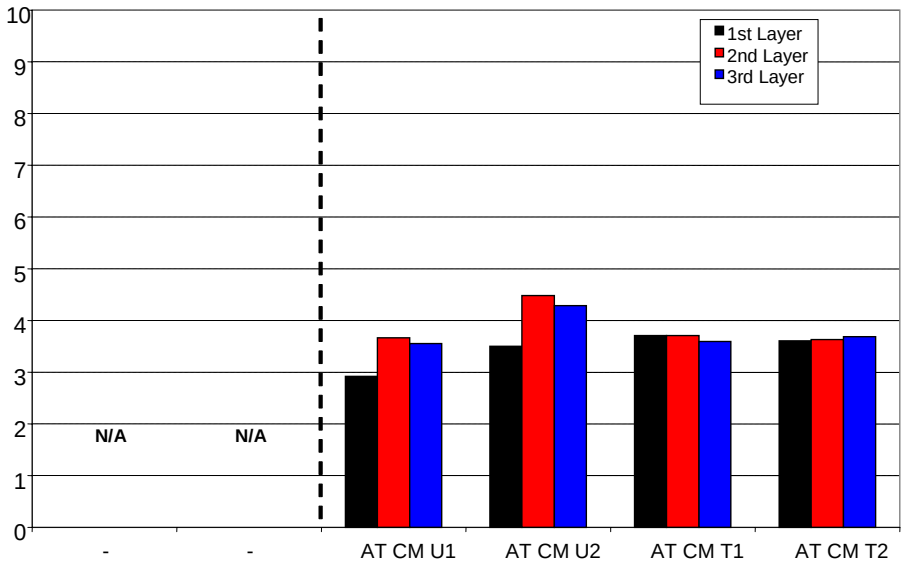

Figure D-6. Binder Content of Atlanta IH 20 CM, %

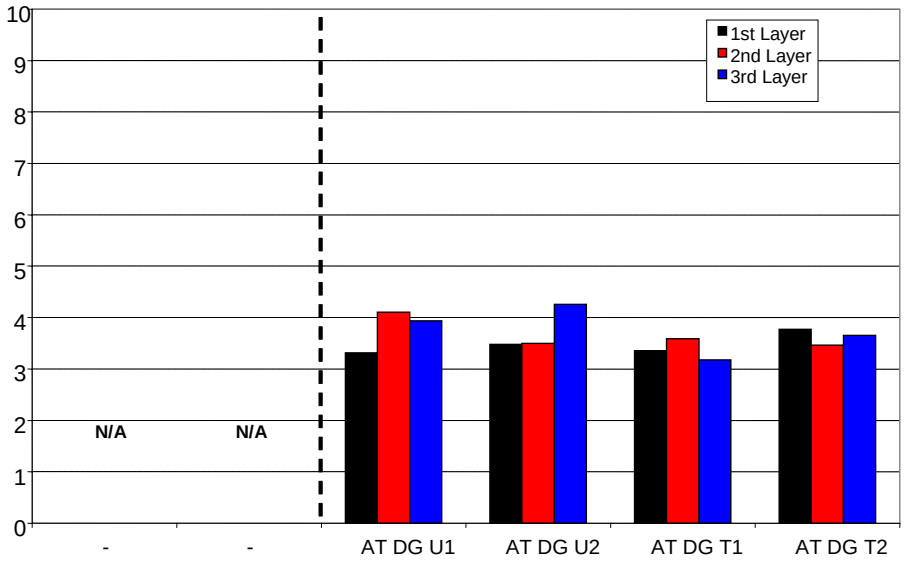

Figure D-7. Binder Content of Atlanta IH 20 DG, %

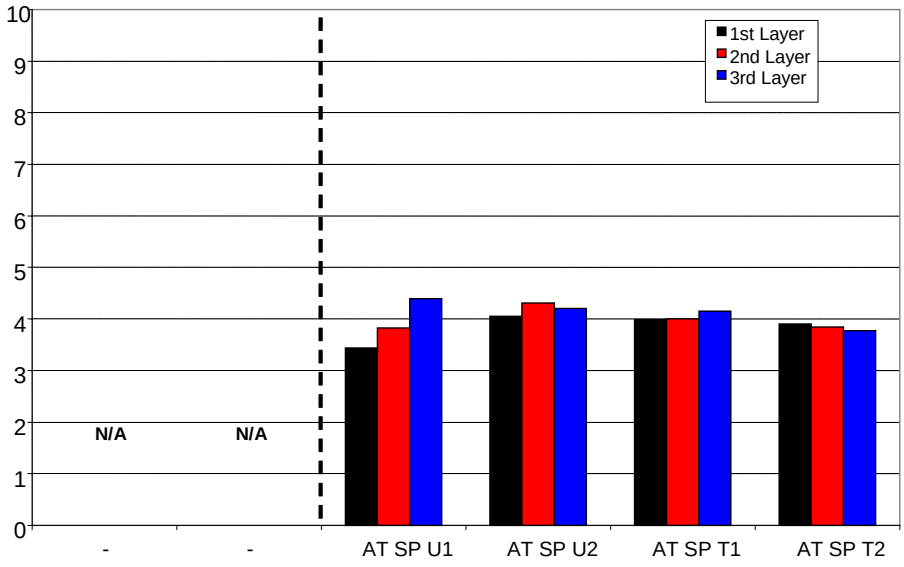

Figure D-8. Binder Content of Atlanta IH 20 SP, %

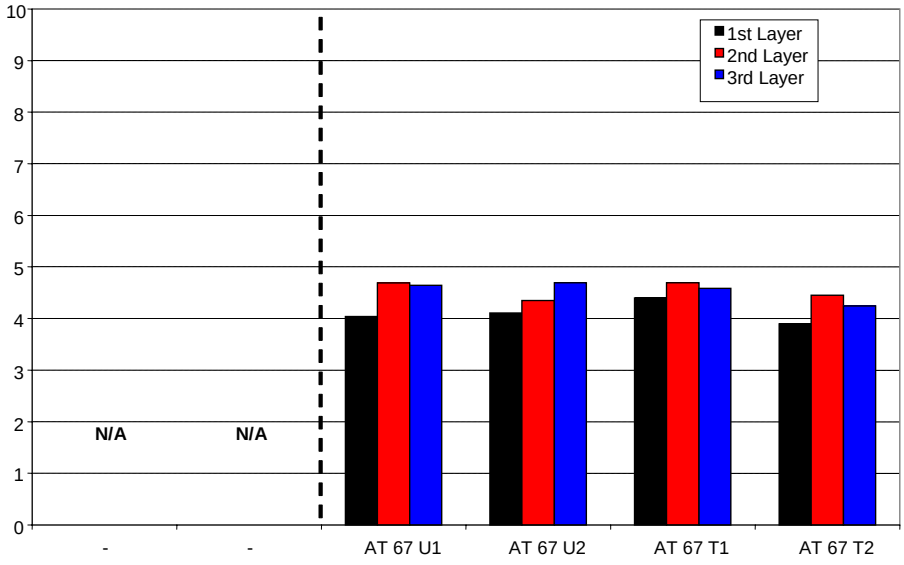

Figure D-9. Binder Content of Atlanta IH 20 67, %

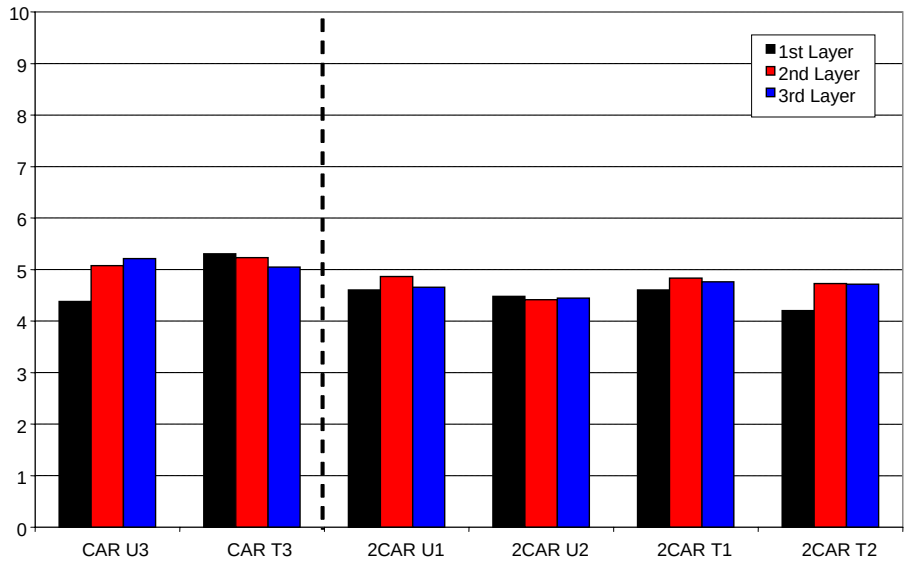

Figure D-10. Binder Content of 1st and 2nd Set Carrizo Springs Airport, %

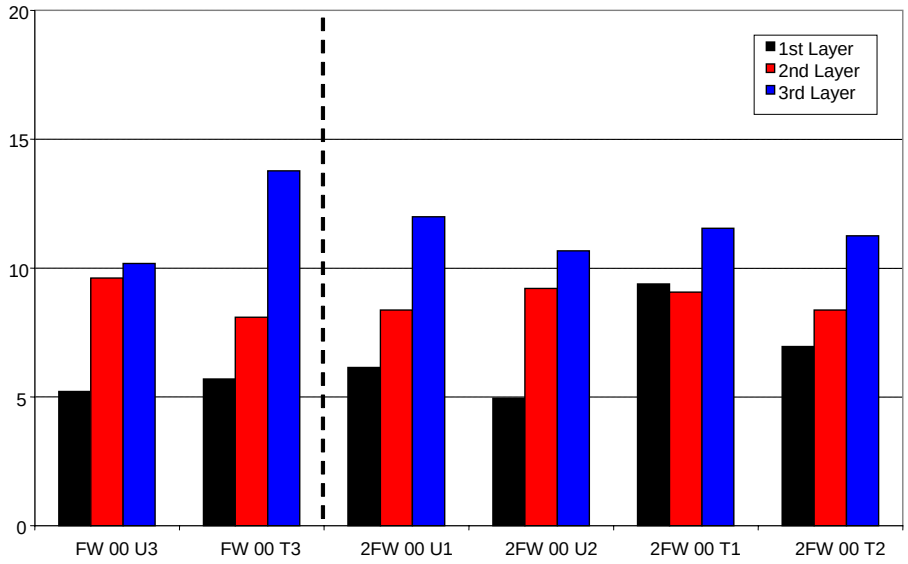

Figure D-11. Binder Content of 1st and 2nd Set Fort Worth FM 4 (2000), %

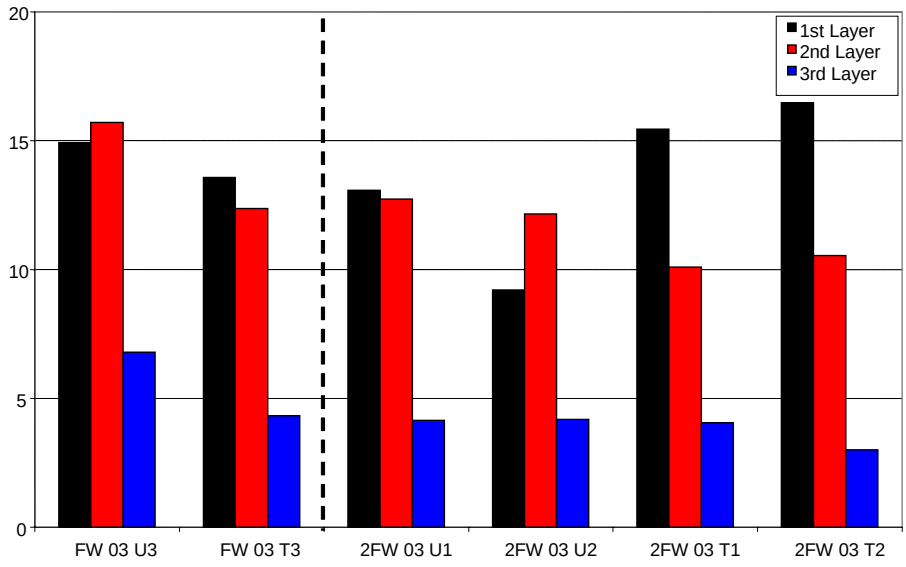

Figure D-12. Binder Content of 1st and 2nd Set Fort Worth FM 4 (2003), %

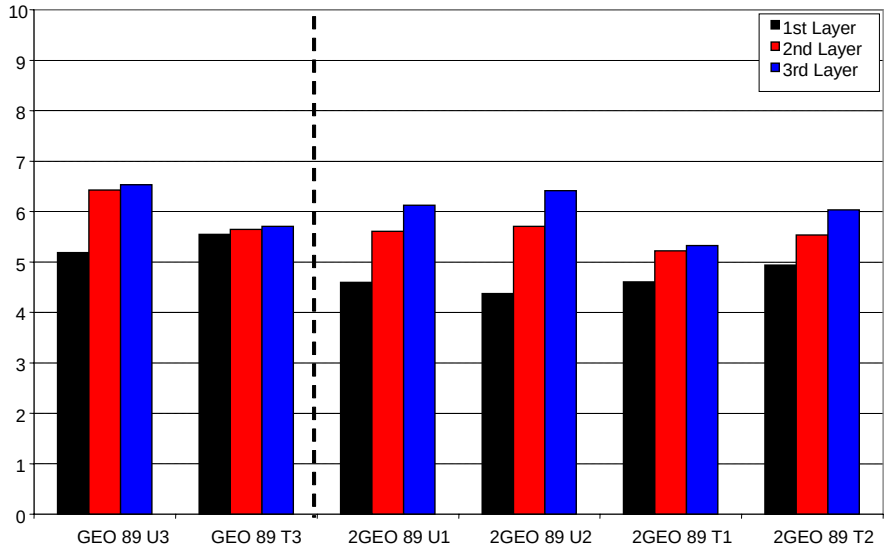

Figure D-13. Binder Content of 1st and 2nd Set Georgetown Airport (1989), %

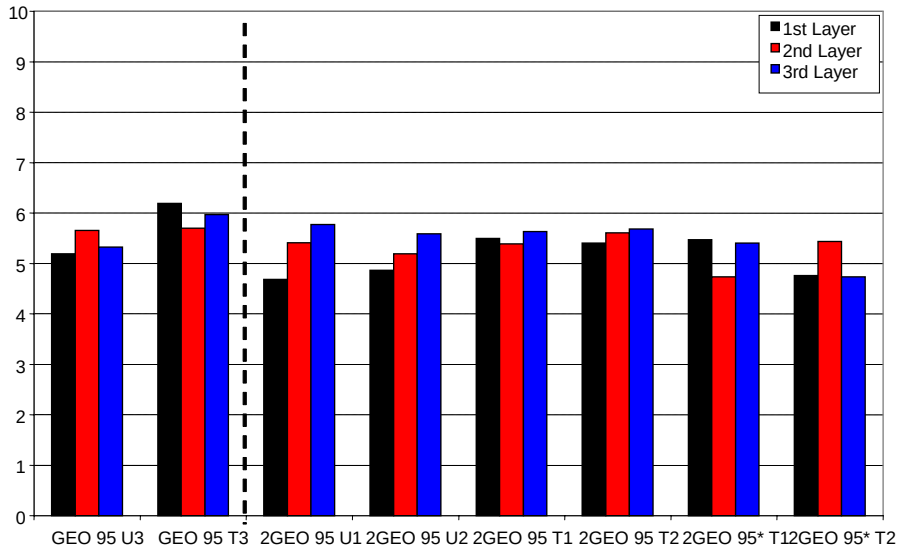

Figure D-14. Binder Content of 1st and 2nd Set Georgetown Airport (1995), %

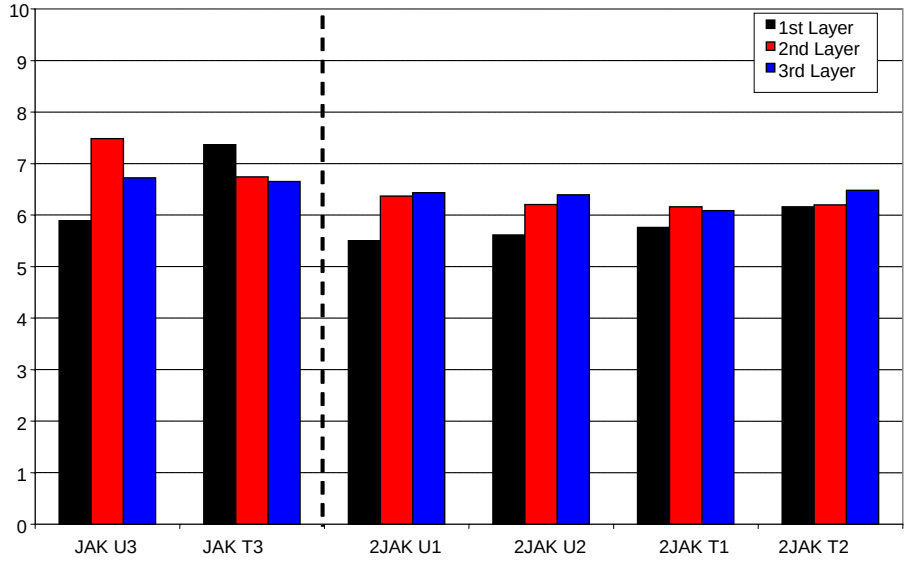

Figure D-15. Binder Content of 1st and 2nd Set Jacksonville Airport, %

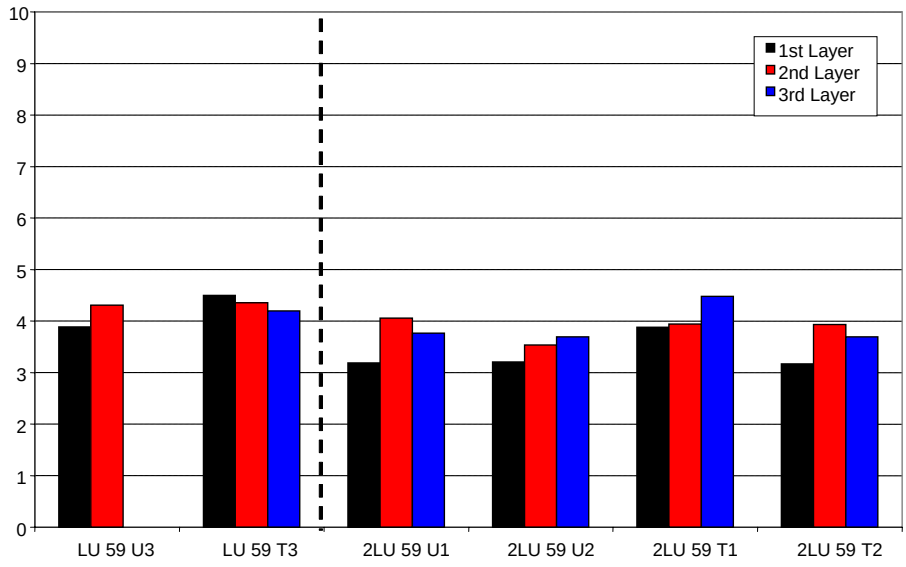

Figure D-16. Binder Content of 1st and 2nd Set Lufkin BUS 59, %

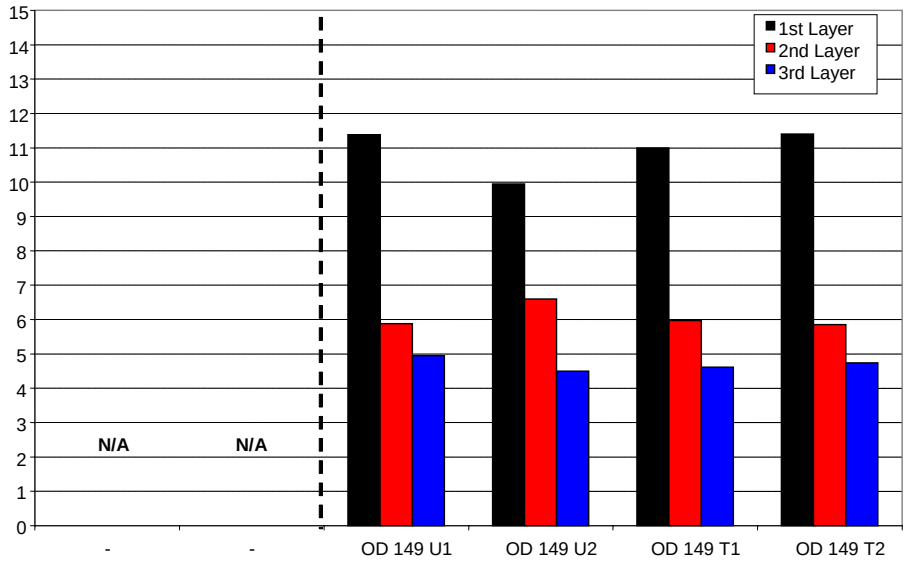

Figure D-17. Binder Content of Odessa SH 149, %

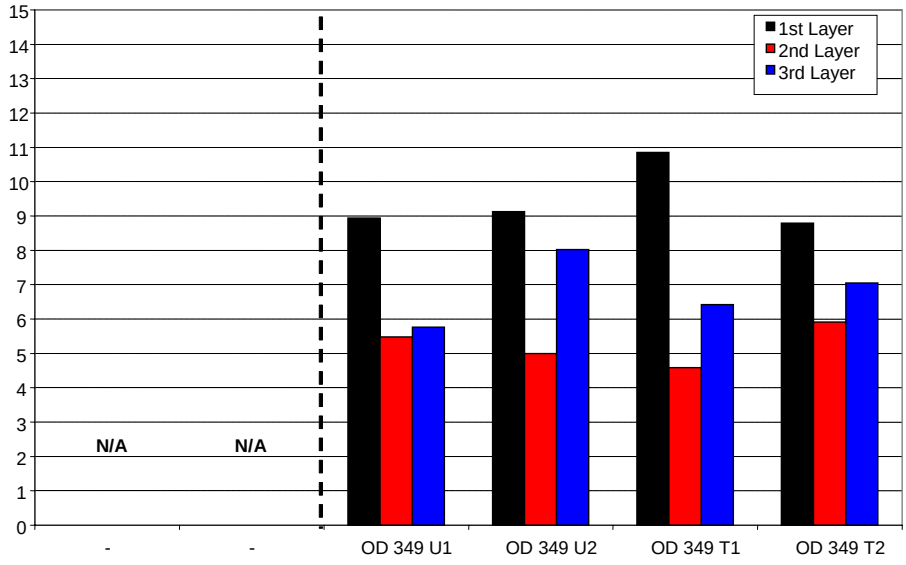

Figure D-18. Binder Content of Odessa SH 349, %

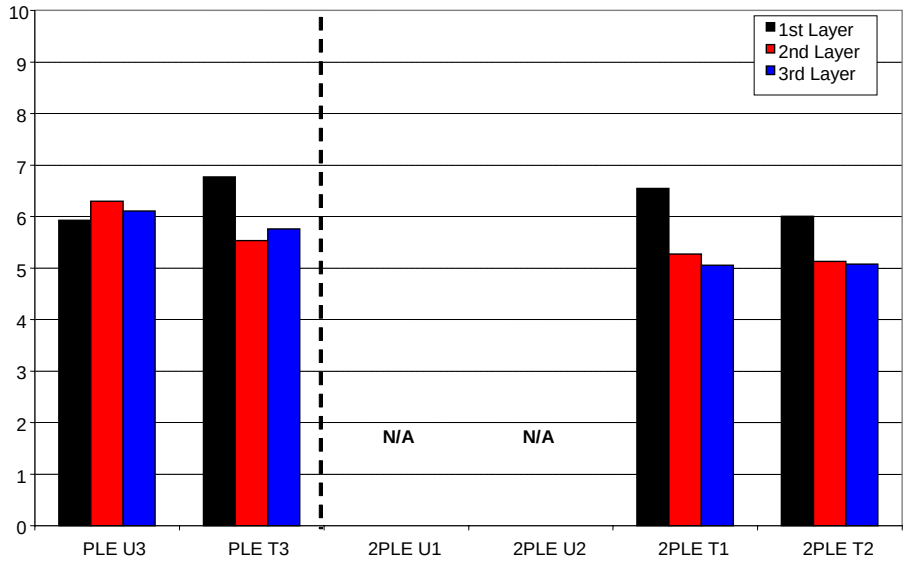

Figure D-19. Binder Content of 1st and 2nd Set Pleasanton Airport, %

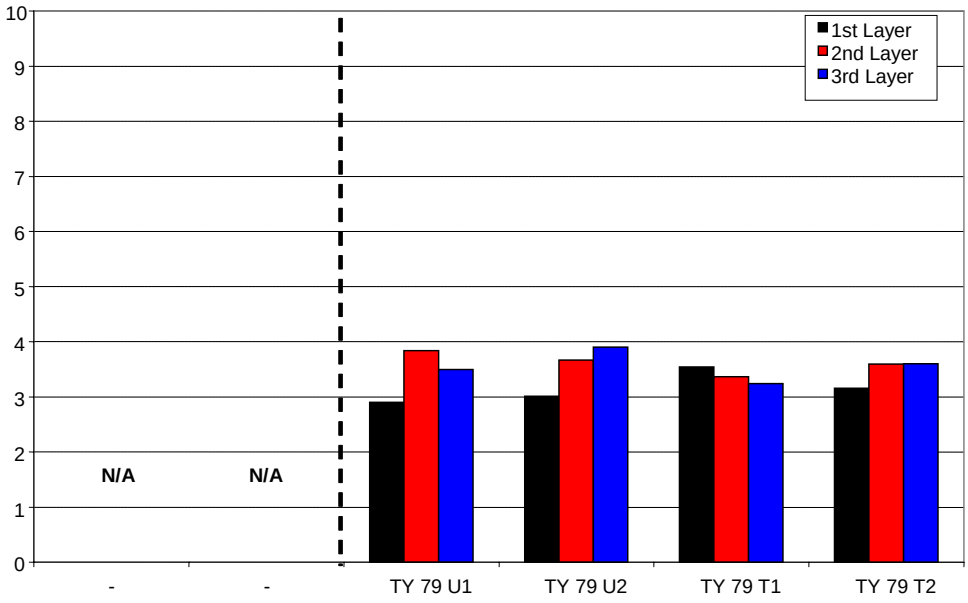

Figure D-20. Binder Content of Tyler US 79, %

APPENDIX E

RESULTS FROM X-RAY CT SCAN FROM CHAPTER III: AVERAGE AIR VOID RADIUS, NO-FLUX BOUNDARY RADIUS, AND AVERAGE DISTANCE BETWEEN TWO ADJACENT AIR VOIDS OF EACH X-RAY CT SCAN LAYER

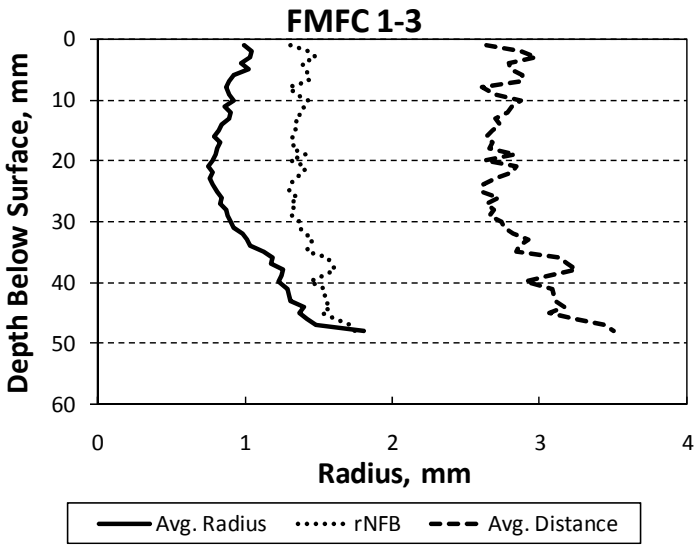

Figure E-1. Results from X-Ray CT Scan for US 259 Core Sample (FMFC Core 1-3): Average Air Void Radius, No-Flux Boundary Radius, and Average Distance between Two Adjacent Air Voids of Each X-Ray CT Scan Layer

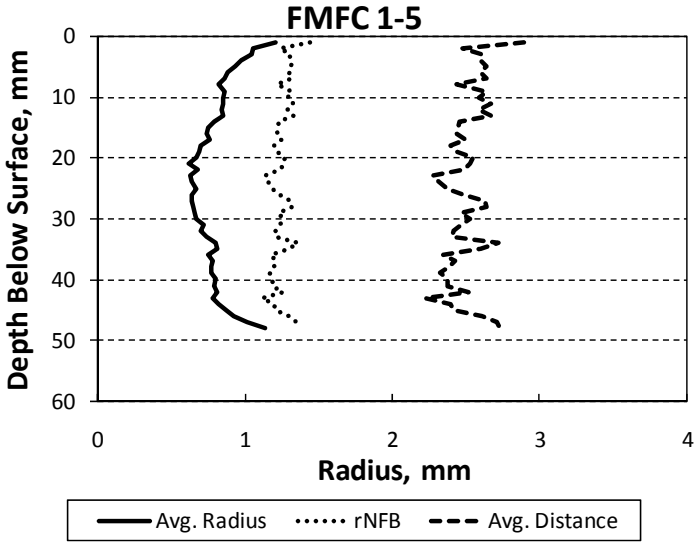

Figure E-2. Results from X-Ray CT Scan for US 259 Core Sample (FMFC Core 1-5): Average Air Void Radius, No-Flux Boundary Radius, and Average Distance between Two Adjacent Air Voids of Each X-Ray CT Scan Layer

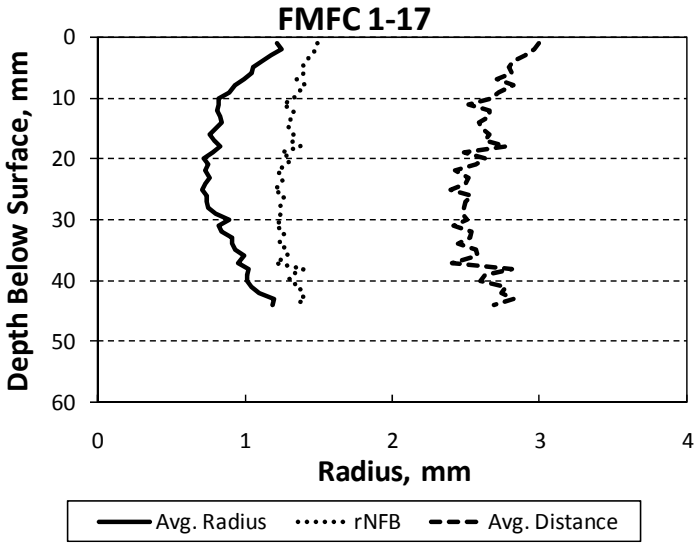

Figure E-3. Results from X-Ray CT Scan for US 259 Core Sample (FMFC Core 1-17): Average Air Void Radius, No-Flux Boundary Radius, and Average Distance between Two Adjacent Air Voids of Each X-Ray CT Scan Layer

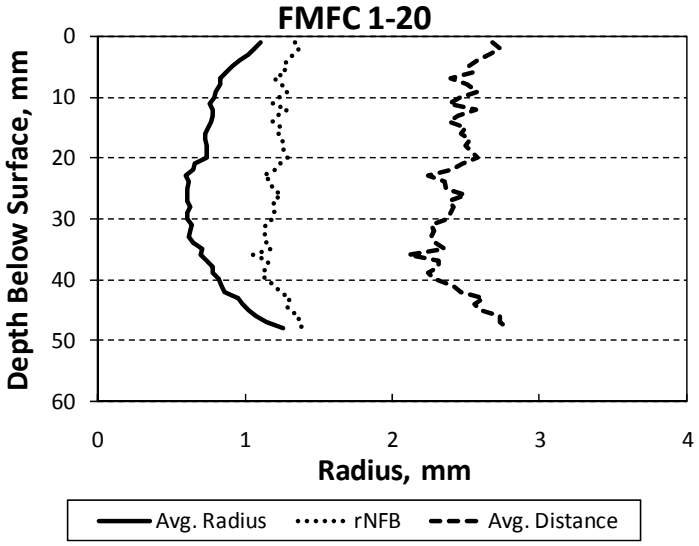

Figure E-4. Results from X-Ray CT Scan for US 259 Core Sample (FMFC Core 1-20): Average Air Void Radius, No-Flux Boundary Radius, and Average Distance between Two Adjacent Air Voids of Each X-Ray CT Scan Layer

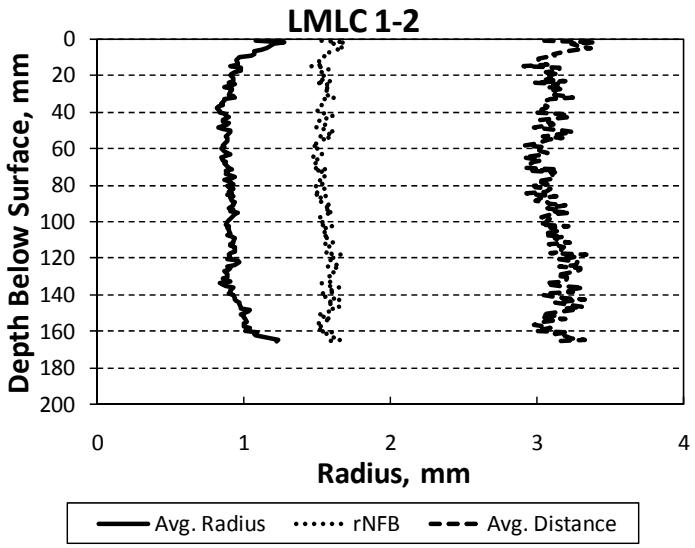

Figure E-5. Results from X-Ray CT Scan for US 59 Core Sample (LMLC Core 1-2): Average Air Void Radius, No-Flux Boundary Radius, and Average Distance between Two Adjacent Air Voids of Each X-Ray CT Scan Layer

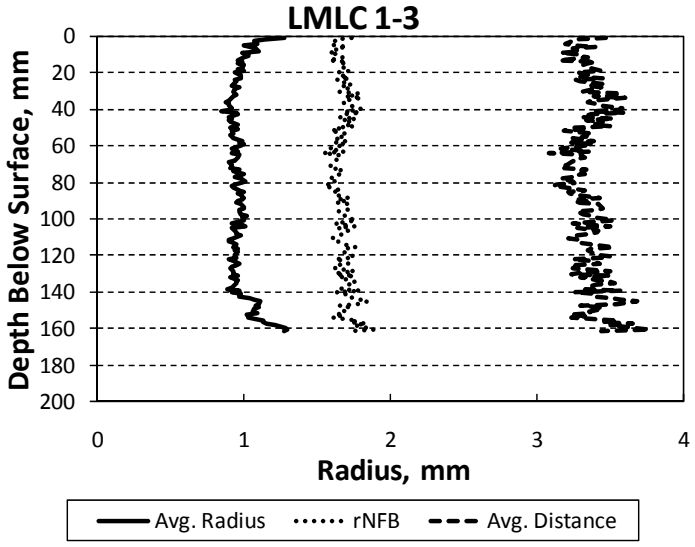

Figure E-6. Results from X-Ray CT Scan for US 59 Core Sample (LMLC Core 1-3): Average Air Void Radius, No-Flux Boundary Radius, and Average Distance between Two Adjacent Air Voids of Each X-Ray CT Scan Layer

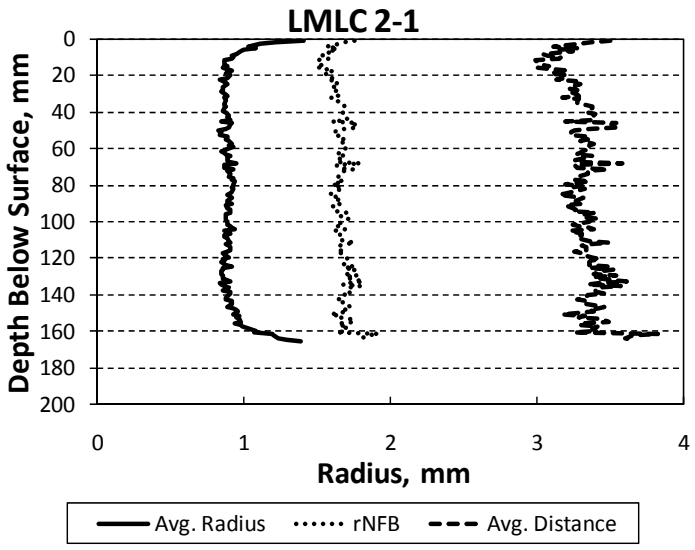

Figure E-7. Results from X-Ray CT Scan for US 59 Core Sample (LMLC Core 2-1): Average Air Void Radius, No-Flux Boundary Radius, and Average Distance between Two Adjacent Air Voids of Each X-Ray CT Scan Layer

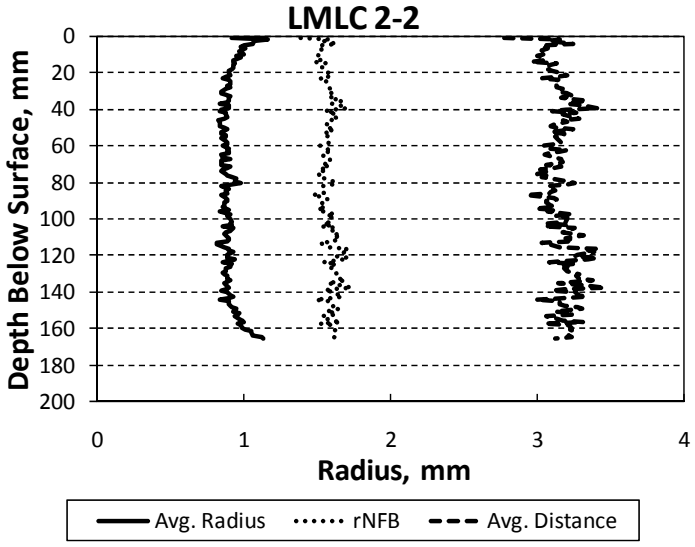

Figure E-8. Results from X-Ray CT Scan for US 59 Core Sample (LMLC Core 2-2): Average Air Void Radius, No-Flux Boundary Radius, and Average Distance between Two Adjacent Air Voids of Each X-Ray CT Scan Layer

APPENDIX F

RESULTS FROM INTEGRATED ASPHALT OXIDATION MODEL IN PAVEMENT WITH THE PAVEMENT TEMPERATURE PREDICTION MODEL FROM CHAPTER VI: CALCULATED CARBONYL AREA GROWTH AT DEPTHS OF 20 MM, 80 MM, AND 160 MM OF PAVEMENTS IN THE STUDY FOR ONE-YEAR AND TEN-YEAR PERIOD

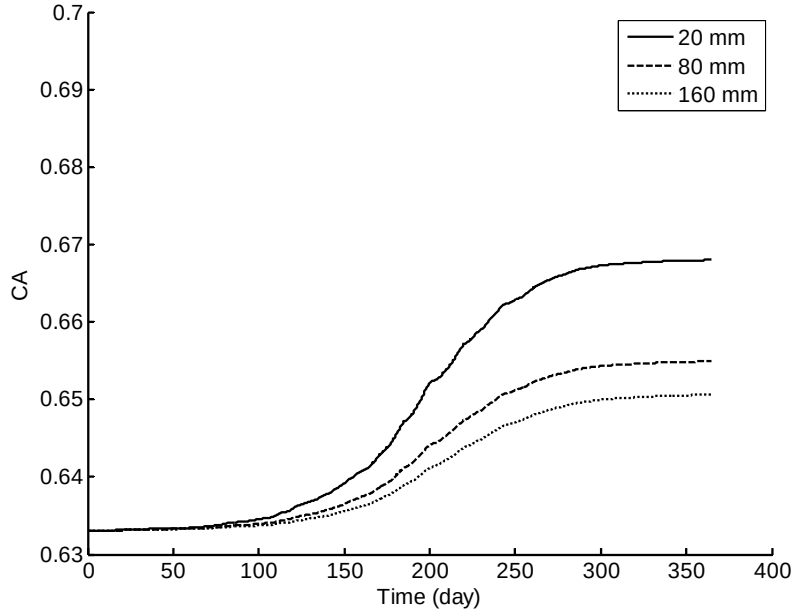

Figure F-1. Calculated Carbonyl Area from Integrated Binder Oxidation Model at Various Depths of Pavement in Arizona (1 Year Period)

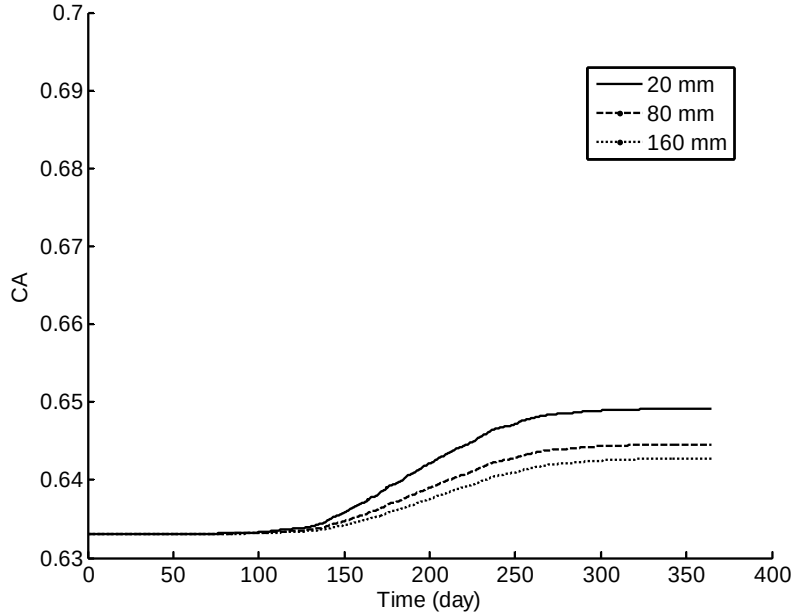

Figure F-2. Calculated Carbonyl Area from Integrated Binder Oxidation Model at Various Depths of Pavement in Minnesota (1 Year Period)

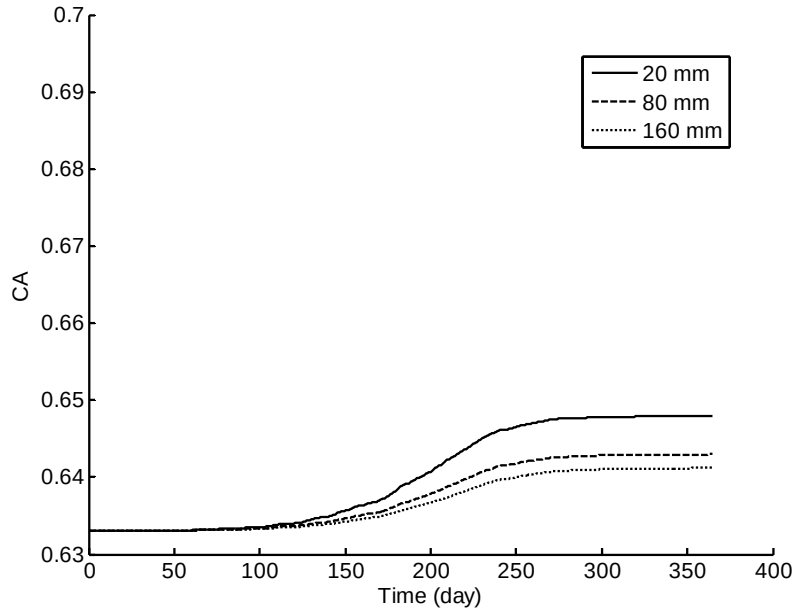

Figure F-3. Calculated Carbonyl Area from Integrated Binder Oxidation Model at Various Depths of Pavement in Montana (1 Year Period)

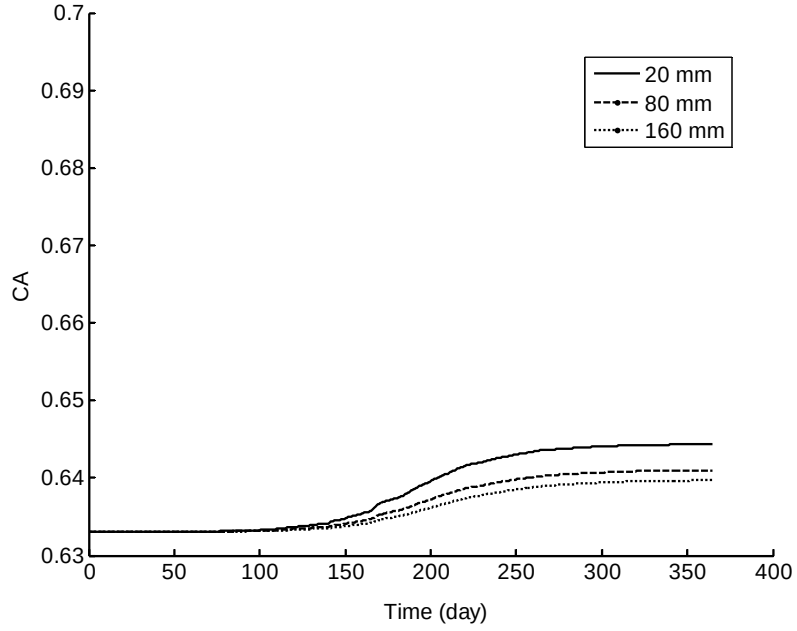

Figure F-4. Calculated Carbonyl Area from Integrated Binder Oxidation Model at Various Depths of Pavement in New York (1 Year Period)

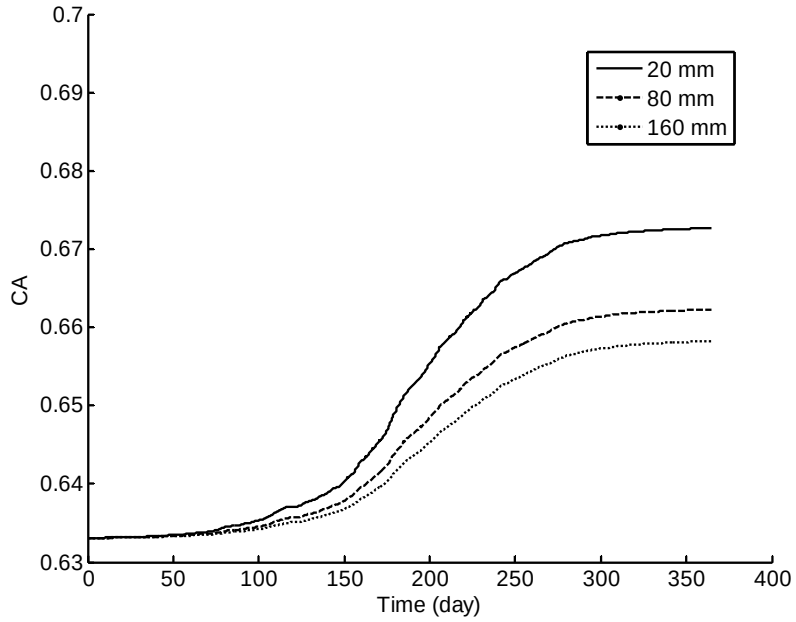

Figure F-5. Calculated Carbonyl Area from Integrated Binder Oxidation Model at Various Depths of Pavement in Amarillo, TX (1 Year Period)

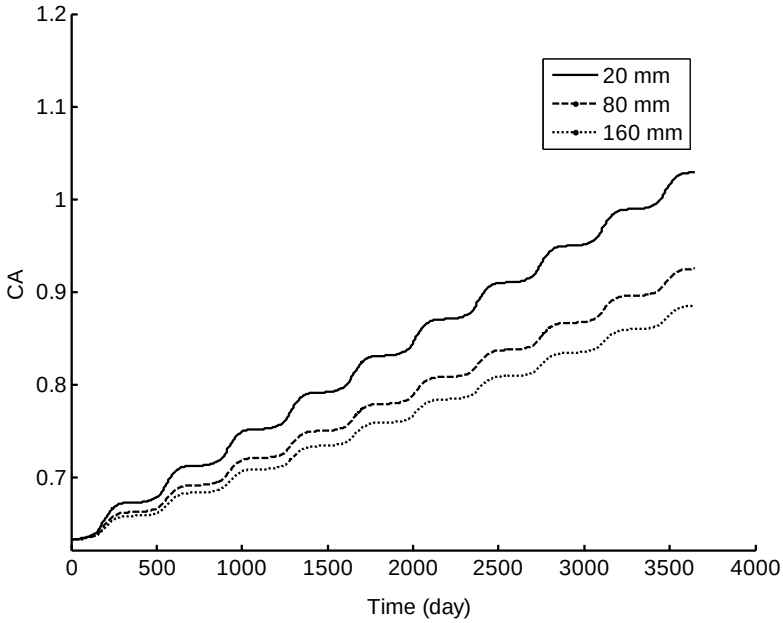

Figure F-6. Calculated Carbonyl Area from Integrated Binder Oxidation Model at Various Depths of Pavement in Amarillo, TX (10 Year Period)

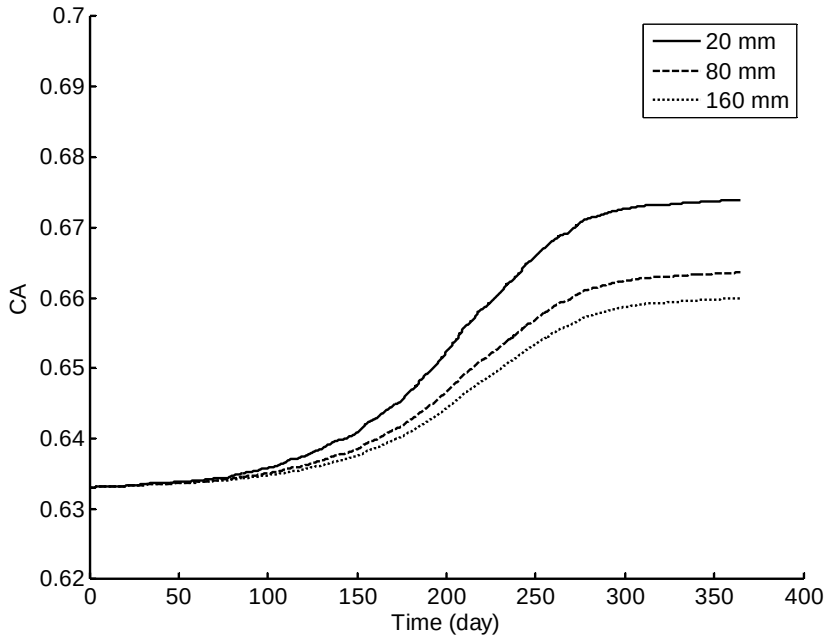

Figure F-7. Calculated Carbonyl Area from Integrated Binder Oxidation Model at Various Depths of Pavement in Bryan, TX (1 Year Period)

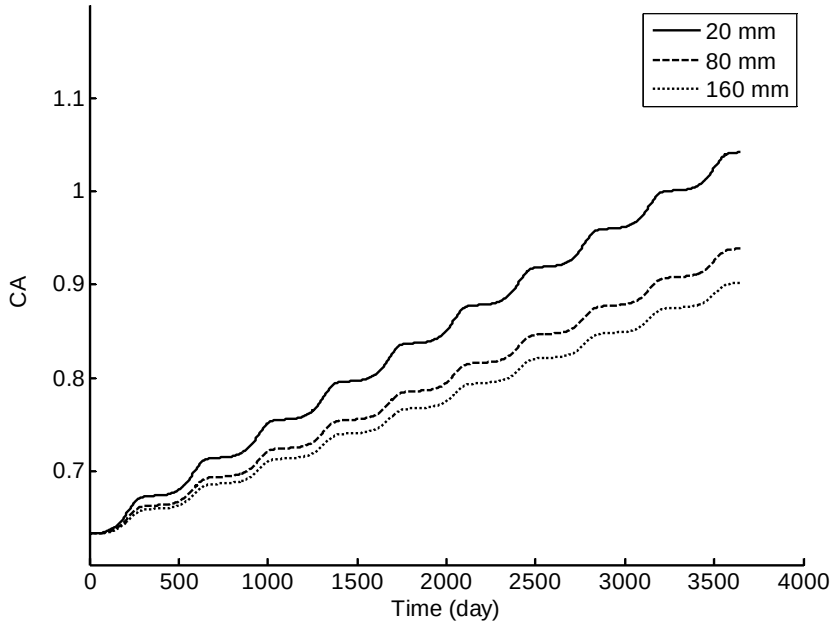

Figure F-8. Calculated Carbonyl Area from Integrated Binder Oxidation Model at Various Depths of Pavement in Bryan, TX (10 Year Period)

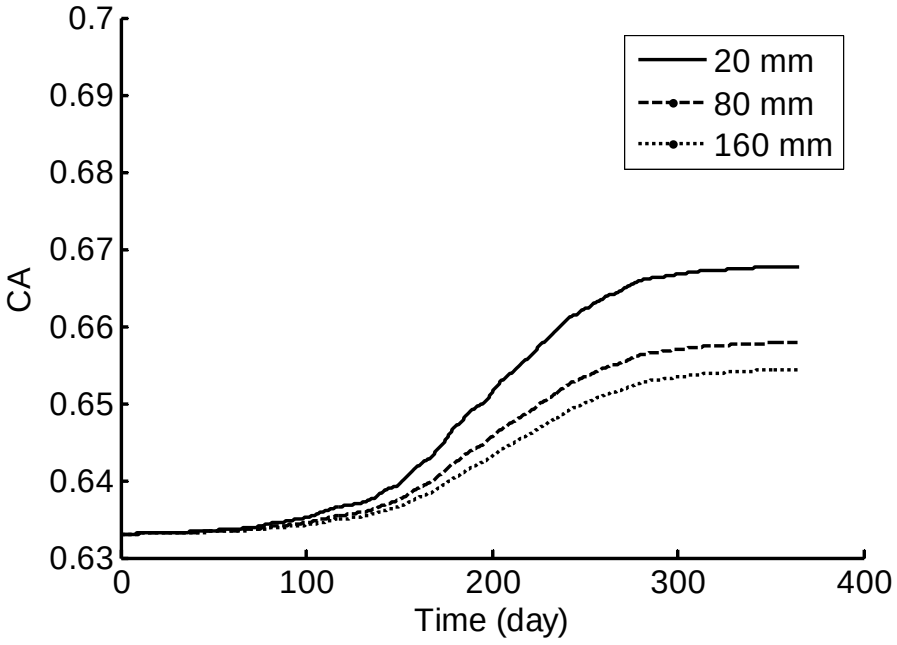

Figure F-9. Calculated Carbonyl Area from Integrated Binder Oxidation Model at Various Depths of Pavement in Dallas, TX (1 Year Period)

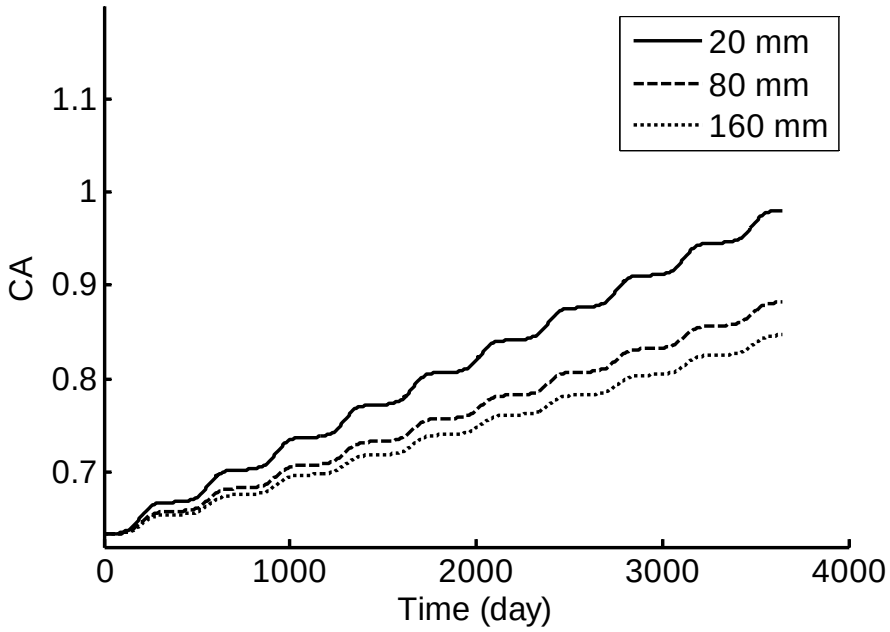

Figure F-10. Calculated Carbonyl Area from Integrated Binder Oxidation Model at Various Depths of Pavement in Dallas, TX (10 Year Period)

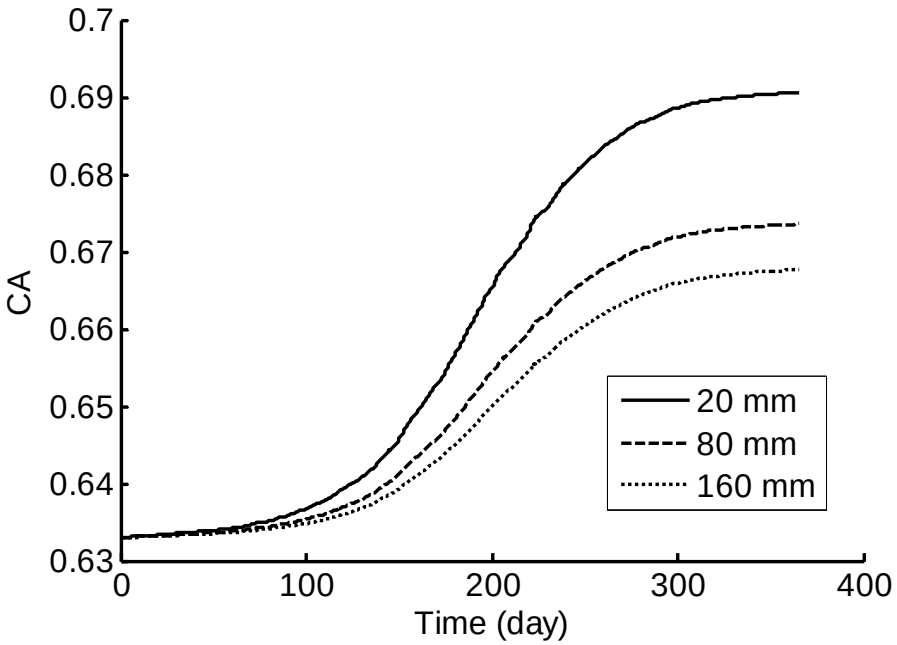

Figure F-11. Calculated Carbonyl Area from Integrated Binder Oxidation Model at Various Depths of Pavement in El Paso, TX (1 Year Period)

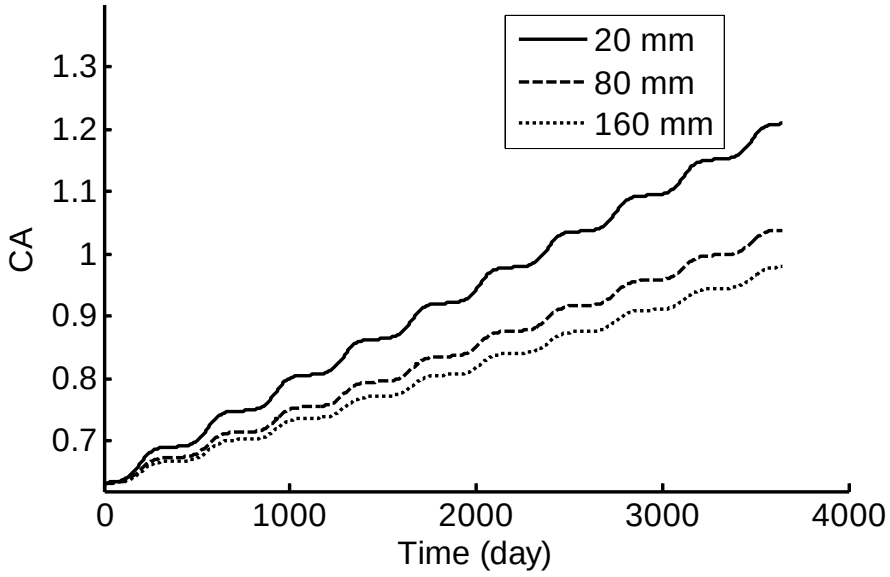

Figure F-12. Calculated Carbonyl Area from Integrated Binder Oxidation Model at Various Depths of Pavement in El Paso, TX (10 Year Period)

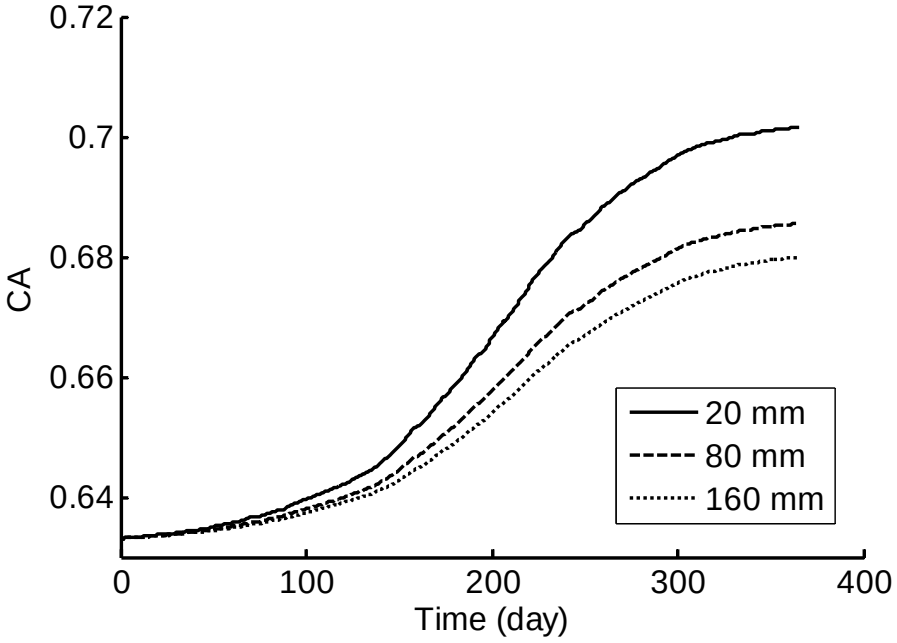

Figure F-13. Calculated Carbonyl Area from Integrated Binder Oxidation Model at Various Depths of Pavement in Hidalgo, TX (1 Year Period)

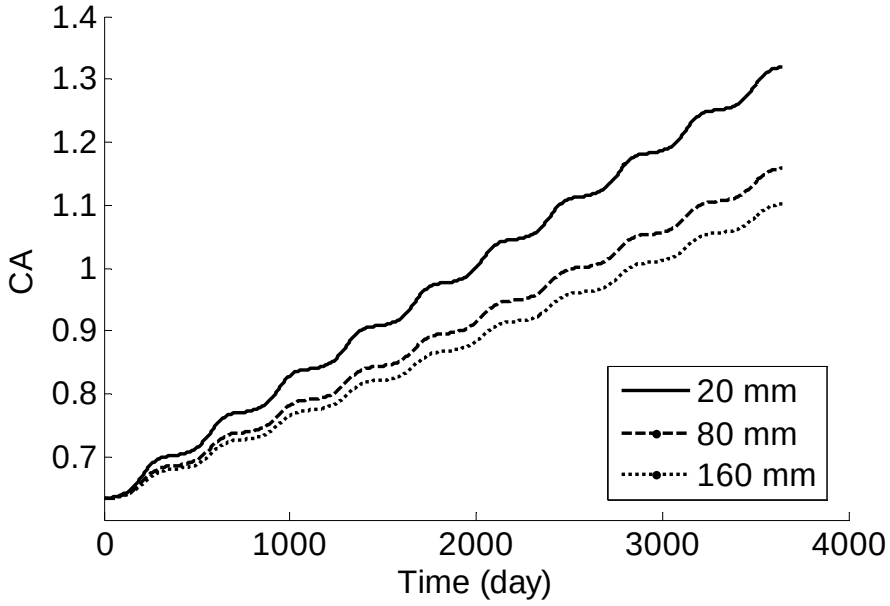

Figure F-14. Calculated Carbonyl Area from Integrated Binder Oxidation Model at Various Depths of Pavement in Hidalgo, TX (10 Year Period)

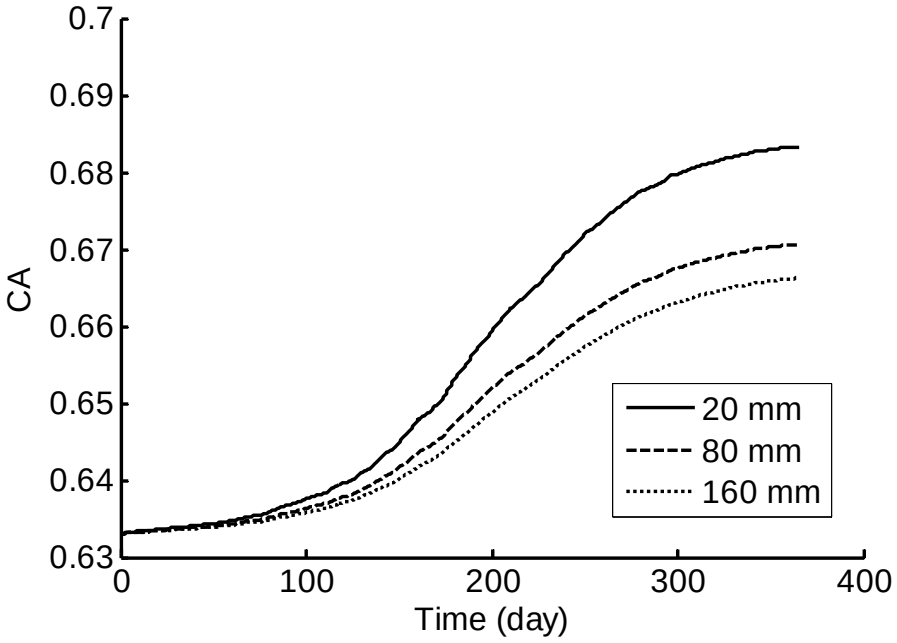

Figure F-15. Calculated Carbonyl Area from Integrated Binder Oxidation Model at Various Depths of Pavement in Kingsville, TX (1 Year Period)

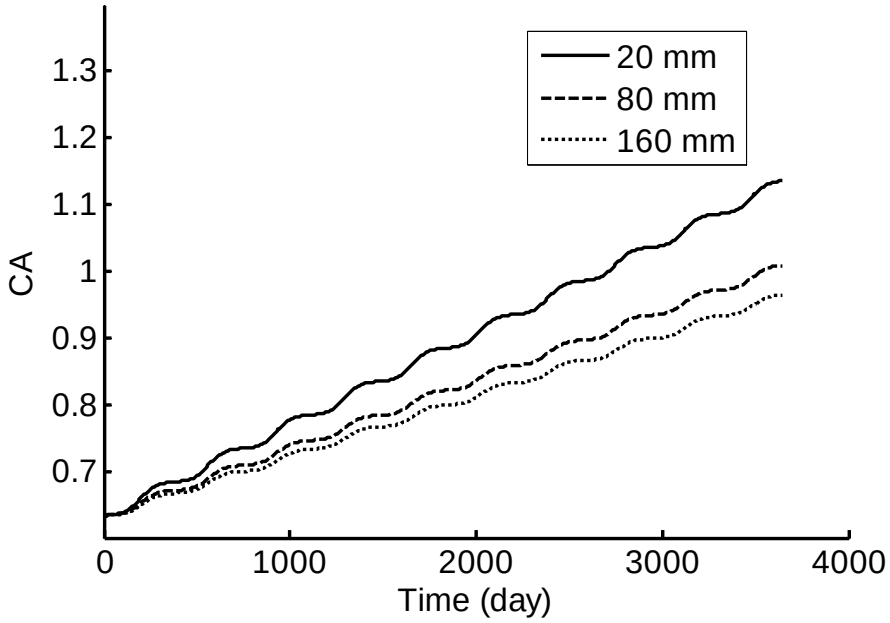

Figure F-16. Calculated Carbonyl Area from Integrated Binder Oxidation Model at Various Depths of Pavement in Kingsville, TX (10 Year Period)

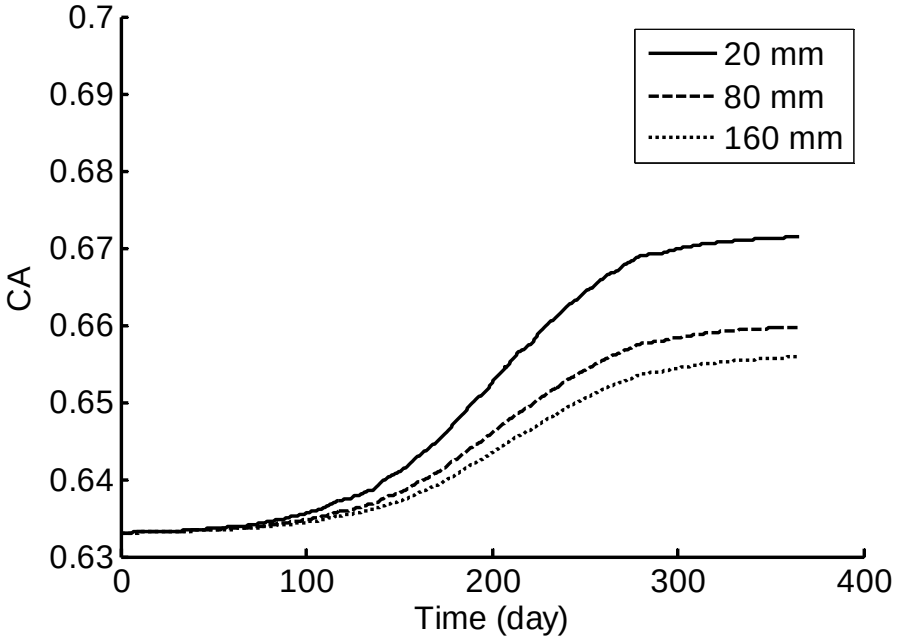

Figure F-17. Calculated Carbonyl Area from Integrated Binder Oxidation Model at Various Depths of Pavement in Lufkin, TX (1 Year Period)

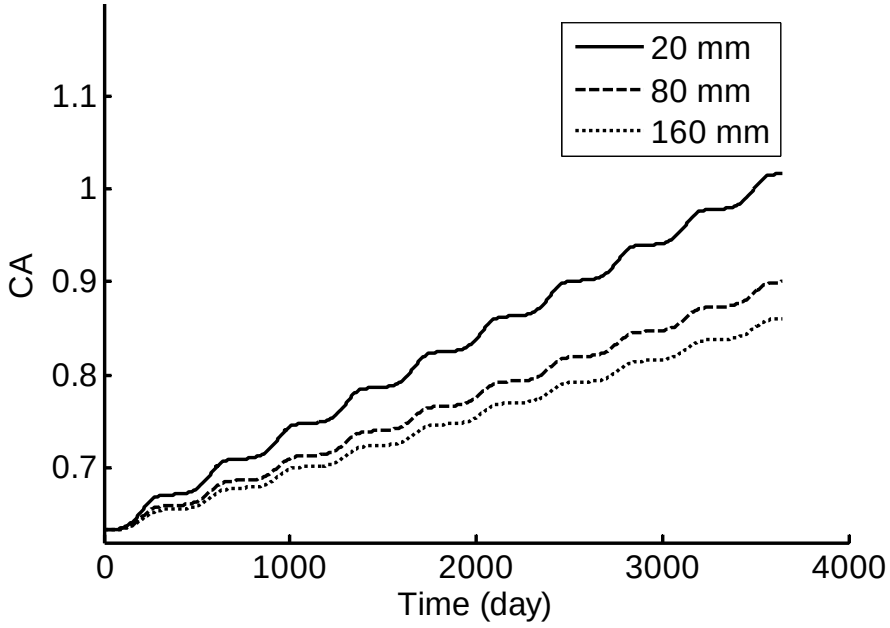

Figure F-18. Calculated Carbonyl Area from Integrated Binder Oxidation Model at Various Depths of Pavement in Lufkin, TX (10 Year Period)

VITA

Nikornpon Prapaitrakul was born to Nopadol Prapaitrakul and Kanokpun Prapaitrakul in Bangkok, Thailand. He received his Bachelor of Engineering in chemical engineering from Chulalongkorn University in Bangkok in July 2001 and his Master of Engineering in chemical engineering from Texas A&M University in College Station, Texas, in December 2002. He graduated with his Ph.D. in chemical engineering from Texas A&M University, College Station, Texas, in December 2009. He can be reached through the following address:

Department of Chemical Engineering, c/o Dr. Charles J. Glover
Texas A&M University
3122 TAMU
College Station, TX, 77843-3122